Synthesis, grain growth and physical properties of nanoparticulate manganese oxides

Dissertation

zur

Erlangung des Doktorgrades

der Naturwissenschaften

(Dr. rer. nat.)

dem

Fachbereich Chemie

der Philipps-Universität Marburg

vorgelegt von

M. Sc. Mohamed Abdel megeed Ibrahim Said

aus Assiut, Ägypten

Marburg an der Lahn 2015

This work was carried out from May 2011 to April 2015 at the Department of Chemistry, Philipps University, Marburg under the supervision of Prof. Dr. B. Harbrecht

Erklärung

Ich erkläre, dass eine Promotion noch an keiner anderen Hochschule als der Philipps-Universität Marburg, Fachbereich Chemie, versucht wurde.

Ich versichere, dass ich meine vorgelegte Dissertation

"Synthesis, grain growth and physical properties of nanoparticulate manganese oxides" selbst und ohne fremde Hilfe verfasst, nicht andere als die in ihr angegebenen Quellen oder Hilfsmittel benutzt, alle vollständig oder sinngemäß übernommenen Zitate als solche gekennzeichnet sowie die Dissertation in der vorliegenden oder einer ähnlichen Form noch bei keiner anderen in- oder ausländischen Hochschule anlässlich eines Promotionsgesuchs oder zu anderen Prüfungszwecken eingereicht habe.

Marburg, 9-4-2015   Unterschrift

                                              (Mohamed Abdel megeed Ibrahim Said)

To the soul of my brother

To my beloved wife Azza and my beautiful

children Salma and Tarek

Acknowledgement

Table of Contents

List of abbreviations and symbols

µm	Micrometer
nm	Nanometer
Å	Angstrom
mg	Milligram
mol	Mole
mol L^{-1}	Mole Liter^{-1}
mL	Milliliter
°C	Celsius temperature
K	Kelvin
Tc	Curie temperature
T$_N$	Néel temperature
kJ	Kilojoule
min	Minute
h	Hour
<d>	Average particle size
ℓ	Length
Φ	Tube diameter
ρ	Density
V	Volume
V/V	Volume/Volume
Eº	Standard electrode potential
XRPD	X-ray powder diffraction
FTIR	Fourier transform infra-red
SEM	Scanning electron microscope
EDX	Energy dispersive X-ray spectroscopy
TEM	Transmission electron microscope

HR-TEM	High resolution TEM
TGA	Thermogravimetric analysis
DTA	Differential thermal analysis
DSC	Differential scanning calorimetry
SAED	Selected area electron diffraction
BET	Brunauer–Emmett–Teller
BJH	Barrett-Joyner-Halenda
S_{BET}	Specific surface area
SQUID	Superconducting quantum interference device
FC	Field-cooled
ZFC	Zero field-cooled
H	Magnetic field strength
M_g	Mass magnetization
χ	Magnetic susceptibility
μ_{eff}	Effective magnetic moment
μ_B	Bohr magneton
θ_{CW}	Curie-Weiss temperature
M_{sat}	Saturation magnetization
Oe	Oersted
emu	Electromagnetic unit
EtOH	Ethanol
iPr	Isopropanol
DMF	Dimethylformamid
CTAB	Cetyltrimethylammonium bromide
SDS	Sodiumdodecylsulphate
SDBS	Sodiumdodecylbenzenesulfonate
PEG	Polyethylene glycol
CMC	Carboxymethylecellulose
Ar	Argon

N_2	Nitrogen
FWHM	Full width at half maximium
SOF	Site occupation factor
GOF	Good of fitness
Wyck.	Wyckoff sites
B	Isotropic displacement parameters
IUPAC	International Union of Pure and Applied Chemistry
Np	Nanoparticles
Nc	Nanocrystals

Chapter 1

Introduction and background

1. Background

Recently, development of metal oxide nanoparticles has attracted enormous attention because of their significant applications in catalysis, energy storage, magnetic data storage, sensors, and biomedical application.[1,2] Variable oxides of manganese are known due to the presence of Mn in different oxidation states (II, III, IV, and VII). The magnetic, structural, and transport properties of these manganese oxides are of considerable interest in understanding their unique properties from a fundamental point of view.[3-5]

Manganese oxide and oxyhydroxide nanostructured materials are of great importance because of their low cost, high natural abundance, and environmental compatibility.[6,7] Manganese oxide materials are widely applied in many fields, such as batteries, catalysts, electrochromic, and magnetic materials.[8-11]

Manganese forms the stable oxides MnO, α-Mn_3O_4, α-Mn_2O_3, and MnO_2 as well as the metastable Mn_5O_8, the structural properties of these oxides are listed in Table 1.[12]

Table 1. Manganese oxides structural data.[12]

Oxide	MnO	α-Mn$_3$O$_4$	Mn$_5$O$_8$	α-Mn$_2$O$_3$	β-MnO$_2$
JCPDS	71-1177	24-0734	39-1218	41-1442	43-1455
Mineral Name	Mangosite	Hausmannite		Bixbyite	Pyrolusite
Valence	+2	+2, +3	+2, +4	+3	+4
Crystal Structure	Cubic	Tetragonal	Monoclinic	Cubic	Tetragonal/ Rutile-type
Space group	$Fm\bar{3}m$	$I4_1/amd$	$C2/m$	$Ia3$	$P4_2/mnm$
Lattice parameters	a= 4.446	a= 5.7621 b= 9.4696	a= 10.392 b= 5.730 c= 4.866, β = 109.62	a= 9.4091	a= 4.3999 c= 2.8740
Formula units/ unit cell	4	4	2	16	2

A more detailed overview about various manganese oxide/hydroxide phases including their structure, synthesis, properties and application will be shown in this chapter. We will focus also on the shortage of the reported studies about manganese oxide/hydroxide nanoparticles that encourage us to do our research project.

1.1. Manganese oxyhydroxides (MnOOH)

1.1.1. Structure

Oxyhydroxides of metals $M^{3+}OOH$ can be divided into two structural groups; one has octahedral coordination and strong hydrogen bonds and in the other M is seven-fold coordinated without strong hydrogen bonds. In the second group (M^{3+} = Ho, Tb, Yb, Lu, Er, Y) there are six oxygen atoms, three of which are hydroxyl groups. These oxygen atoms will form a trigonal coordination prism around M, and the seventh O locates along a normal to a prism face closest to the M center. Oxyhydroxides with octahedral arrangement around M are existing for M^{3+} = Al, Sc, Y, V, Cr, Mn, Fe, Co, Ni, Rh, Ga, and In. Various modifications can exist for this class of oxyhydroxides, commonly labelled by a Greek letter as prefix.[13]

Three polymorphs with distorted octahedral coordination about Mn^{3+}, groutite; α-MnOOH, manganite; γ-MnOOH and feitknechtite; β-MnOOH are well known for MnOOH. Each phase has its own character. Manganite is composed of $Mn^{3+}O_6$ octahedra that are edge- and corner-shared forming a 1×1 tunnelled structure, into these tunnels hydrogen atoms reside. As a result of Jahn-Teller effects the Mn^{3+}- octahedra are distorted; manganite crystallizes in a monoclinic system. The other forms of MnOOH are α-MnOOH (groutite) and β-MnOOH (feitknechtite), both of these are also composed of $Mn^{3+}O_6$ octahedra that are edge- and corner-shared. In case of groutite connection of octahedra will result in a 2×1 tunnels whereas feitknechtite forms an octahedral layered structure.[14]
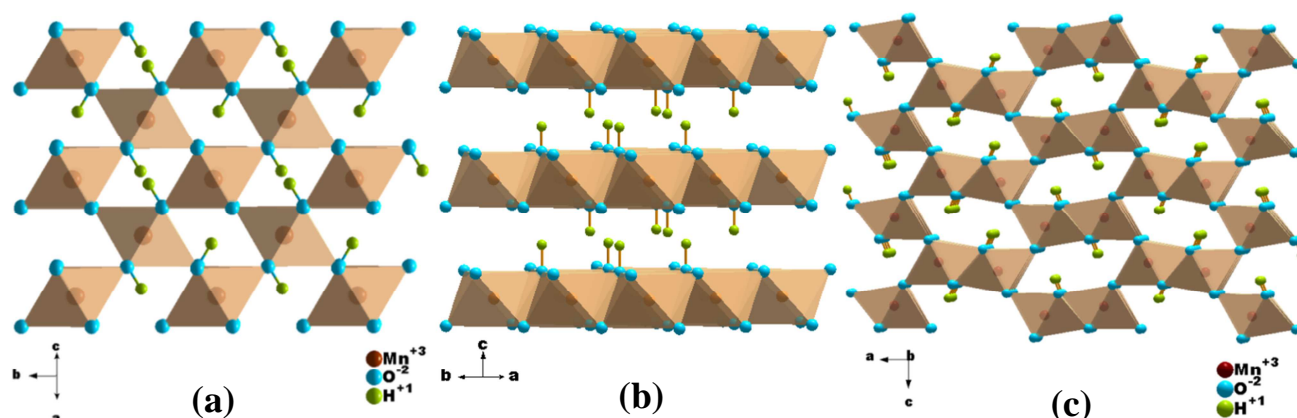
Figure 1. *Crystal structure of the different modifications of MnOOH: a) manganite; γ-MnOOH, b) feitknechtite; β-MnOOH and c) groutite, α-MnOOH.*

As depicted in Figure 1, Feitknechtite, (β-MnOOH) has a lamellar structure and is considered to be a metastable polymorph, while γ-MnOOH is the most stable form of manganese oxyhydroxides.[15]

Most of the published work (as we will see later) was focusing on the studying of manganite synthesis and its variable applications (probably as a result of its structural stability). Few reports were developed on the basis of the other two types.[15-17]

1.1.2. Importance and applications

A lot of valuable technological applications have been reported for manganese oxyhydroxide nanocrystals particularly manganite because of their fabulous structural flexibility associated with novel chemical and physical properties.[18] γ-MnOOH was found to have freaked adsorption capacities for scavenging numerous trace elements from aquatic environments. It has strong oxidizing abilities for natural and xenobiotic organic substances and is considered as a model compound in understanding reactivity of trivalent Mn in many minerals.

Manganite was used as a precursor for the synthesis of complex Mn oxides such as Li-Mn-O for lithium ion batteries as well as a precursor for synthesis of other manganese oxides such as MnO_2, Mn_3O_4, Mn_2O_3 and metastable Mn_5O_8.[19]

A novel non-enzymatic hydrogen peroxide (H_2O_2) sensor was made depending on γ-MnOOH nanowire composite film modified glass carbon electrode (GCE). The biosensor obtained showed outstanding performance for H_2O_2. This unique electrode material has the advantages of good analytical performance, low cost and simple fabrication method making it a promising for the development of effective non-enzymatic hydrogen peroxide sensor.[20]

1.1.3. Synthesis of MnOOH nanoparticles

1.1.3.1. Synthesis of γ-MnOOH

A lot of versatile methods were reported for the preparation of γ-MnOOH nanoparticles with different sizes and morphological shapes such as rods, wires, whiskers and multipods. We will summarize them as follow:

1.1.3.1.1. Hydrothermal methods

γ-MnOOH nanowires with a mean diameter of about 12 nm and lengths of up to several micrometers were synthesized from hydrothermal reaction performed between $KMnO_4$ and toluene in water at 180 °C for 24 h.[21,22]

Y. Zhang et. al.,[23] synthesize single-crystalline γ-MnOOH microrods via hydrothermal reduction of $KMnO_4$ using NH_4Cl, the hydrothermal temperature was set at 150 °C and the reaction lasts 24 h. SEM and TEM observations revealed that the diameters of these microrods ranging from 0.2 to1.2 µm and lengths up to several tens of micrometers. Molar ratio between $KMnO_4$ and NH_4Cl was identified as a key parameter for the production of clean phase γ-MnOOH. The reaction temperature was a critical factor for formation of either clean phase γ-MnOOH or birnessite type manganese oxide, the formation of pure γ-MnOOH needs high reaction temperature.

G. Xi et.al. prepared γ-MnOOH nanorods by reducing $KMnO_4$ with KI at 120 °C for 12 h. SEM images of the as-prepared products revealed that they were uniform and consisted of a large quantity of nanorods with a diameter in range of 50–120 nm and tens of micrometers in length.[24] γ-MnOOH nanorods was then used as a precursor for production of β-MnO_2 nanorods by calcination at 250 °C for 2 h. The impact of calcination time, temperature and heating rate on the quality of β-MnO_2 nanorods was studied.

1.1.3.1.2. Solvothermal methods

γ-MnOOH nanorods and Mn_3O_4 nanoparticles were prepared, respectively, through a solvothermal reaction of $KMnO_4$, where ethanol/water solution was used as a solvent. The ethanol/water ratio and reaction temperature were found to have enormous effects on the phase of the final product. The results indicate that formation of single phase of Mn_3O_4 nanoparticles needs higher reaction temperature and higher volume percent of ethanol (>50%), whereas the formation of single phase of γ-MnOOH nanorods needs lower reaction

temperature and lower volume percent of ethanol (2–10%). TEM investigations revealed that MnOOH has rod-like morphology and the diameter of these rods is in the range 50-500 nm.[25]

Single crystal γ-MnOOH nanorods[26] were prepared through a solvothermal reaction by reduction of $KMnO_4$ by DMF (Dimethylformamide) under temperature of 120 °C for different reaction time. The results showed that the morphology of so obtained γ-MnOOH can be well controlled by simply controlling the reaction time. TEM images of the products which prepared from the reactions performed at 120 °C for 2 h and 4 h showed some lamellar structures besides wire nanostructures which have tendency to curl. Whereas the product obtained at 120 °C for 6 h comprises a large number of nanorods with a diameter range of 5–55 nm and lengths up to hundreds of nanometers, however, there were some impurities in the products. TEM analysis for γ-MnOOH produced at 120 °C for 10 h indicated that it contains a large quantity of nanorods with the average diameter of 9 nm and length reaches hundreds of nanometers. High-resolution TEM (HRTEM) for the last one showed that a fringe spacing of 0.342 nm along the longitudinal axis and 0.287 nm along the latitudinal axis of the nanorod, which correspond to those of ($\bar{1}11$) and (101) planes of γ-MnOOH. γ-MnOOH nanorods prepared by this method exhibited a high specific capacitance and good electrochemical performance as electrode materials for supercapacitor.

1.1.3.1.3.Surfactant-assisted methods

Facile CTAB (cetyltrimethylammonium bromide) assisted hydrothermal method for synthesis of γ-MnOOH single crystalline nanorods was reported. Via hydrothermal treatment of $MnSO_4$ and NaOH in the presence of CTAB at 200 °C for 20 h γ-MnOOH nanorods were obtained. Subsequently, MnOOH was heat-treated at 300 °C for 3 h to produce β-MnO_2. From the TEM images wire-like nanostructures with about 40–100 nm in diameter and tens of microns in length have been observed for both γ-MnOOH and its annealing product β-MnO_2.[27]

γ-MnOOH whiskers[28] were synthesized using $MnSO_4.H_2O$ and ethylamine as the alkali source at 120 °C for 72 h in the presence of cationic surfactant (CTAB). The product is obtained under extremely low surfactant concentrations and under basic conditions. β-MnO_2 whiskers were obtained by subsequent calcination of MnOOH whiskers at 300 ºC for 1 h. XRD analysis for the product obtained showed that beside manganite whiskers few feitknechtite (layered–type manganese oxyhydroxide that is free of interlayer cations) were

observed. For β-MnO$_2$ minor impurities of γ-Mn$_3$O$_4$ were observed as well. TEM and SEM images for the as-synthesized sample indicate a fiber-like morphology, with length between hundreds of nanometers and several micrometers and diameter ranging from several nanometers to tens of nanometers.

A slight modifications for this method was done thereafter,[29] by controlling the amount of CTAB and time of reaction, quite pure phases of γ-MnOOH nanorods as well as of γ-Mn$_3$O$_4$ nanoparticles were produced.

Solid MnO$_x$ nanoparticles (MnOOH, Mn$_2$O$_3$, and MnO$_2$) with different shapes as sphere, wire, rod, and particle[30] were synthesized via a simple one-pot hydrothermal method by reacting Mn(NO$_3$)$_2$ and sodium dodecylbenzenesulfonate (SDBS) in water at 170 °C for 12 h. Surfactant concentration was the key factor that controls phase and shape of MnOx nanocrystals so obtained as shown in the schematic representation depicted in Figure 2.
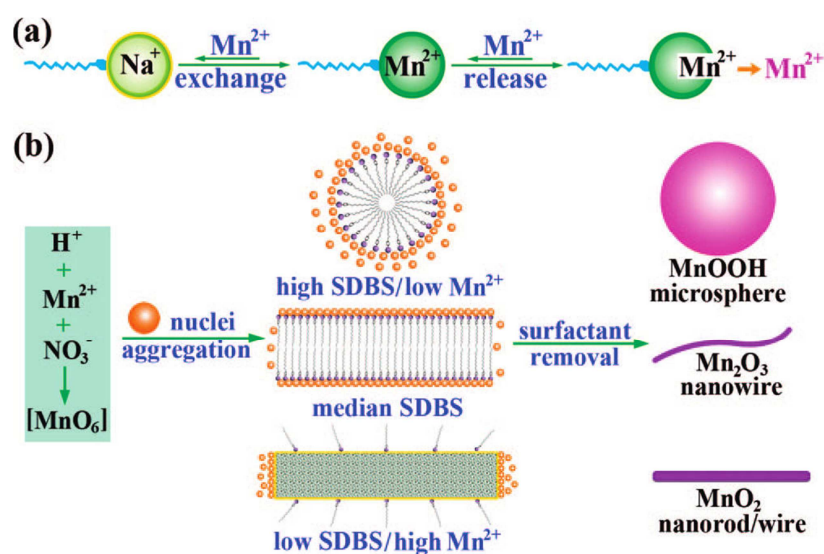
Figure 2. *Schematic illustration for controlled fabrication of MnO$_x$ nanostructures: (a) represents ion exchange between Na$^+$ and Mn^{2+} and (b) represents surfactant assemblies and formation of MnO$_x$ solids with various morphological shapes.[30]*

1.1.3.1.4.Polymer assisted methods

γ-MnOOH nanorods having different diameters were prepared by a simple one-step polymer-assisted hydrothermal method via the reaction of $Mn(NO_3)_2$ solution with polyethylene glycol (PEG-10000). Variation of the volume of $Mn(NO_3)_2$ solution was having significant impact on the diameters of as synthesized γ-MnOOH nanorods.[31] Manganite nanorods were then used as a precursor for synthesis of both β-MnO_2 and α-Mn_2O_3 by calcination at 350 and 600 °C, respectively for 1 h.

γ-MnOOH multipods were fabricated hydrothermally via reduction of $KMnO_4$ using PEG200. Morphological shape was significantly changed by addition of the surfactant CTAB. Addition of CTAB into the starting reactant leads to formation of one-dimensional (1D) MnOOH nanowires instead of multipods. Phase control experiments were achieved by controlling the volume of PEG200. TEM and HRTEM images of γ-MnOOH multipods showed the formation of mixtures of three-, four- and six-armed multipods. The diameter of each arm was variable, ranging from 40 to 120 nm and they were uniform along the length direction, the length of the arms was about 800 to 1200 nm. For γ-MnOOH nanowires, TEM and HRTEM observations showed that the product consists of a large number of nanowires with a diameter in the range of 10–120 nm and length of tens of micrometers and no multipods were observed.[32]

1.1.3.1.5.Comproportionation reaction

The redox reaction between $KMnO_4$ and $Mn(OAc)_2.4H_2O$, was utilized for synthesis of γ-MnOOH nanorods and square-like Mn_3O_4 nanoparticle via a facile hydrothermal method coupled with variation of the pH value of the reaction medium. Variable values were used for pH and temperature in this reaction. The influence of the temperature and the pH value on the final product is shown in Table 2.[33]

Actually, this kind of reactions is a promising one not only because of their simplicity but also because they provide versatile experimental parameters that are most useful for modifying the product phase. In addition to the molar ratio of Mn^{2+}/ MnO_4^{-}, type of manganese salt as well as the type of the alkali metal of the permanganate salt will have significant influence.

Table 2. Impact of reaction temperature and the pH value on the product phase and its particle size \<d\>.[33]

Reactant	Temp. °C	pH	Product	\<d\> / nm
MnO_4^-	210	1-4	γ-MnOOH nanorods	> 50
		4-13	γ-MnOOH and Mn_3O_4	
Mn^{2+}		14	square-like Mn_3O_4 nanoparticles	30-50
	180	1-4	γ-MnOOH nanorods	40-60
		4-14	γ-MnOOH and Mn_3O_4	
	150	1-14	MnOOH nanoparticles	

It is apparent that both the reaction temperature and the pH value played an important role in influencing the crystallographic form of the final products.

HRTEM image of γ-MnOOH obtained at 180 °C revealed that the nanorods have uniform structures and the interlayer distances are ca. 0.34 nm and 0.25 nm that are matched with the lattice space of ($\bar{1}$11) and (111) planes of bulk γ-MnOOH, respectively. The results of HRTEM and SAED of γ-MnOOH nanorods indicated a single crystal nature. The growth direction was identified along [111] crystal direction.[33]

A slight modification was introduced to this method by Xia Caoa et.al.[20] Instead of performing the reaction hydrothermally, the comproportionation reaction between $KMnO_4$ and $Mn(OAc)_2.4H_2O$ was carried out under refluxing conditions for about 12 h. SEM image with higher magnification showed that the diameter of these nanowires is about 20 nm whereas the length can be up to tens of micrometers. HRTEM images indicated that the diameter of the ultra-long nanowires is in the range of 20–25 nm, the lattice fringe spacing was determined to be 0.26 nm which agreed with the d value for monoclinic MnOOH (020) planes (0.2639 nm).

To the best of our knowledge most of the previous reports were utilized mainly for the preparation of manganite nanocrystals with a single particle size, none of them has studied how to manage the various experimental parameters for the purpose of modifying the average particle size (i.e., size-selective experiments). Grain growth for the obtained nanocrystals still obscured.

1.1.3.2. Synthesis of β-MnOOH

Indeed, few reports were issued for feitknechtite nanoparticles.[15,16] Limited synthetic routes were presented for its preparation which might be a normal result of its low stability and difficulty to obtain it in a clean form. These methods comprise the following:

A large scale synthesis of ultrathin β-MnOOH nanofibers[16] were performed via a green chemical method by aging a mixture of very dilute aqueous solution of $Mn(NO_3)_2$ (0.4 mmol L^{-1}) and amino ethanol (0.8 mmol L^{-1}) at room temperature for 1.5 h. Alternatively, it can be obtained by aging a mixture of very dilute aqueous solution of $Mn(NO_3)_2$ (0.4 mmol L^{-1}) and sodium hydroxide (0.8 mmol L^{-1}) for 24 h. The diameter of these nanowires was evaluated by applying Scherrer's formula to the strongest XRD peak and was found 27 nm, which agreed with that observed by SEM and TEM for bundles.
TEM investigations revealed that the nanofibers were uniform and had an average diameter of 25 nm. High-magnification TEM and SEM images illustrated that these nanofibers were bundles consisting of fine nanofibers of 3–5 nm in diameter and are parallel assembled together. The HRTEM results showed as well that these fibers are grown along <010> direction. The specific surface area of these β-MnOOH nanofibers was 104 $m^2\,g^{-1}$.

Evolution of the morphology and phase transition of β-MnOOH nanocrystals (prepared by the same method as above) to γ-MnOOH in water under hydrothermal conditions were studied by X. B. Chen. γ-MnOOH nanowires with a diameter of 40-100 nm were obtained. A synchronous oriented-attachment and dissolution–recrystallization mechanism was used to interpret this transition. Subsequent annealing for β-MnOOH in oxygen atmosphere for 1 h at temperatures of 300 °C, 400 °C and 500 °C resulted in formation of Mn_5O_8, MnO_2 and Mn_2O_3 nanofibers, respectively. These results are different from that is reported for calcination of β-MnOOH under air atmosphere where Mn_3O_4, MnO_2 and Mn_2O_3 were obtained at temperatures of 400 °C, 600 °C and 800 °C, respectively.[15]

Obviously, modest work was reported on single phase feitknechtite. The previously mentioned methods for synthesis of feitknechtite showed a shortage in the characterization. A single reflection in the powder pattern locates at 2θ ≈ 19.2° was observed which is unsatisfactory to relate the pattern to feitknechtite. Really, further characterization methods are necessary to identify feitknechtite.

According to the forgoing reports about manganese oxyhydroxides, we have seen that it is possible to prepare the other manganese oxides e.g., β-MnO₂, Mn₅O₈, Mn₂O₃ and Mn₃O₄

through heat-treatment of manganese oxyhydroxide precursors. In particular, the thermal decomposition of manganite under different atmospheres will give rise to the formation of various manganese oxides. Consequently, it is of importance to clarify the various thermal behaviors that manganite can adopt under different conditions.

1.1.4. Thermal behavior of manganite

Thermal behavior of manganite was studied frequently either in air or under an inert atmosphere (N_2 or argon), different sequences were proposed for its thermal decomposition. Under air conditions several mechanisms were reported.[34,35] The most relevant one which widely spread in literature showed that manganite firstly undergoes oxidative dehydration to pyrolusite (β-MnO_2) which subsequently reduced to bixbite (α-Mn_2O_3) and this finally undergoes further reduction to hausmannite (α-Mn_3O_4).[34]

$$4\,\gamma\text{-MnOOH} + O_2 \xrightarrow[300\,°C]{air} 4\,\beta\text{-MnO}_2 + 2H_2O \tag{1}$$

$$2\,\beta\text{-MnO}_2 \xrightarrow[600\,°C]{air} \alpha\text{-Mn}_2O_3 + \tfrac{1}{2}\,O_2 \tag{2}$$

$$3\,\alpha\text{-Mn}_2O_3 \xrightarrow[1000\,°C]{air} 2\,\alpha\text{-Mn}_3O_4 + \tfrac{1}{2}\,O_2 \tag{3}$$
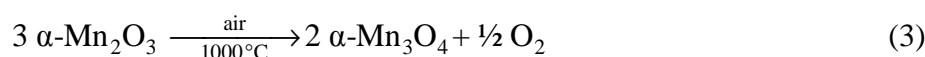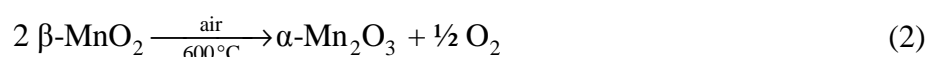
Heating of manganite in nitrogen flow[36] or under vacuum[37] up to 700 °C points to completely different reaction sequences. The first mass loss could be ascribed to the formation of a mixture of the metastable state Mn_5O_8 and α-Mn_3O_4. Mn_5O_8 suffered a reductive decomposition to α-Mn_3O_4 in the second step.

$$8\,\gamma\text{-MnOOH} \xrightarrow[300\,°C]{N_2} Mn_5O_8 + \alpha\text{-Mn}_3O_4 + 4\,H_2O \tag{4}$$

$$Mn_5O_8 \xrightarrow[450–500\,°C]{N_2} 5\,Mn_3O_4 + 2\,O_2 \tag{5}$$
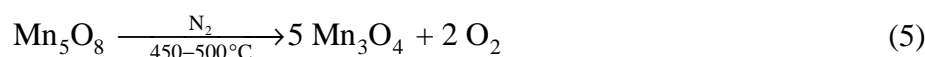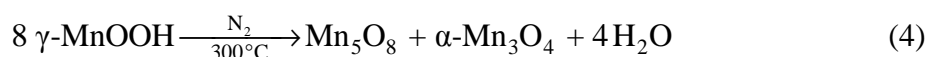
In another scheme it is proposed that γ-MnOOH decomposes directly to α-Mn_3O_4 under argon flow. The second and third steps exhibit small mass losses and could not be interpreted. The residue obtained at the end of the decomposition process was examined by XRD analysis which is characterized as α-Mn_3O_4. Workers accounted this for some chemical changes that take place in the second and third steps. The changes are too small to be monitored by XRD.[34]

$$6\,\gamma\text{-MnOOH} \xrightarrow[320\,°C]{argon} 2\,\alpha\text{-Mn}_3O_4 + 3H_2O + \tfrac{1}{2}\,O_2 \tag{6}$$
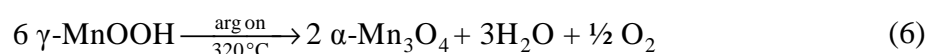
1.2. Manganese dioxide

1.2.1. Structure

Several polymorphs are well known for MnO_2.[38] MnO_2 and its related oxides were recognized as very interesting materials because they possess many crystalline structures and are rich in Mn valence. Generally, manganese dioxide related materials are complex and nonstoichiometric oxides, where foreign cations, physisorbed and structural water molecules and structural vacancies can exist within their structures. As a result of the presence of foreign species, the average valence of Mn generally lies between 3 and 4. The structure of the various MnO_2 related oxides is mainly based on one basic structural unit, MnO_6 octahedron.[39]

We can summarize the structural characteristics of the most important forms of manganese dioxides as follow:

1.2.1.1. One-dimensional structures

1.2.1.1.1. Pyrolusite (β-MnO₂)

The most stable form of all MnO_2 polymorphs has rutile-type structure with tetragonal symmetry $(P4_2/mnm)$[40] in which single chains made from edge-sharing MnO_6 are propagating along the crystallographic c axis. These chains are connected to four neighboring chains by corner-sharing. MnO_6 network forms tunnels with square cross-section, i.e., one octahedron by one octahedron, also represented by 1x1 tunnels (Figure 3a). The size of these tunnels is too small to accommodate other chemical species, except for Li^+ ions.

1.2.1.1.2. Ramsdellite (R-MnO₂) and nsutite (γ-MnO₂)

Ramsdellite (R-MnO₂) has a structure which is close to that of β-MnO₂. The difference between them is that the single chains in pyrolusite are replaced by double chains in ramsdellite. In ramsdellite the two adjacent chains sharing the octahedral edges as well. The eventual structure consists also of tunnels[41] which are of rectangular shape and defined with 1x2 octahedral sides (Figure 3b). This large size of tunnels allows the insertion of water or different cations such as Na^+ or Ca^{2+}. Ramsdellite is a rare mineral and is isostructural with goethite (FeOOH), it can be prepared synthetically from the spinel $LiMn_2O_4$.[42]

The structure of γ-MnO₂ (nsutite minerals) has been considered as an intergrowth of ramsdellite (R) and pyrolusite (r),[43] i.e., as faults r in R (Figure 3c). Two parameters were defined in the structure of nsutite i.e. Pr and Tw. Pr was identified as the fraction of slabs r in the structure of R. The parameter Pr is known as a ''De Wolff defect'' which denotes the

replacement of a single chain of octahedra by double chains. Another parameter which is Tw^{44} (defined later by Mt) is used to identified a percentage of ''microtwinning'' (a change of ca. 60/120° in the c-axis direction). The space group Pbcm is used here for R and this setting is retained for a faulted R.

Chabre and Pannetier,[44] presented defects of ''microtwinning''. They referred to a possibility of continuous evolution (theoretical probability) from a γ-MnO_2 structure with only De Wolff defects to an ϵ-MnO_2 structure. Hexagonal symmetry arises as a result of extreme twinning (the twinning not being dependent on the De Wolff defects). In this case, the double chains of R and/or single chains of r parallel to the c-axis undergo a lot of changes in direction at ca. 60/120° upon twinning leading to a mean hexagonal structure. ϵ-MnO_2 (mineral name, akhtenskite) has a hexagonal very dense packing of oxygen atoms and a statistical distribution of Mn^{4+} over half of the octahedral positions (Figure 3d).

1.2.1.1.3. Hollandite (α-MnO_2)

Another MnO_2 structure with larger size tunnels is α-MnO_2. The corresponding minerals existing in nature are hollandite ($Ba_xMn_8O_{16}$) and cryptomelane ($K_xMn_8O_{16}$). α-MnO_2 has tetragonal symmetry (space group I4/m) with cell parameters: a = 9.8776 Å and c = 2.8654 Å. Insertion of cations distorts the structure, hence, hollandite minerals usually have monoclinic I2/m symmetry. Hollandite structures comprise double chains of edge-sharing MnO_6 octahedra, forming 2x2 tunnels (0.46 nm x 0.46 nm) that propagate along the c axis of the tetragonal unit cell (Figure 3e). The tunnelled structure of α-MnO_2 can stabilize by insertion of Ba^{2+} or K^+, or by water molecules located in the center of the 2x2 tunnels,[38] concomitant with reduction of Mn^{4+} to Mn^{3+} and replacement of O^{2-} by OH^-.

Larger tunnels MnO_2 frameworks can also exist in nature. The best-known examples are romanechite $A_2Mn_5O_{10}.xH_2O$ (A = Ba^{2+}, K^+, . . .; tunnel size 2x3) and todorokite (tunnel size 3x3).[45,46]

1.2.1.2. Two dimensional layered Structures

Birnessite (δ-MnO_2)

Layered structure polymorphs of chemically modified MnO_2 are also known and are named ˝birnessite-type" compounds, after the mineral birnessite. The structure of these compounds consists of layers (Figure 3f) with the interlayer distance about 7Å. It is stabilized by intercalation of cations such as Na^+ or K^+ and significant water content. Generally, it is extremely hard to eliminate the water from the structure without leading to structural

degradation. The synthetic Na-, Mg-, and K-rich birnessites (e.g., $Na_4Mn_{14}O_{27}.9H_2O$) have a structure[47] which is closely related to that of ternary oxides such as chalcophanite $Na_2Mn_3O_7$.[48] Na-containing birnessite almost comprises vacancy-free layers consisting of MnO_6 octahedra. The substitution of Mn^{3+} for Mn^{4+} results in a Jahn–Teller distortion which causes a distortion of the hexagonal symmetry of the layers. The super cell A = 3a parameter (a = 5.172 Å) results from the neat distribution of Mn^{3+}-rich rows parallel to [010] and are away from each other along [100] through the existence of two Mn^{4+} rows between them.[49]

1.2.1.3. Three-dimensional structures

Spinel λ-MnO$_2$

   λ-MnO_2 is a metastable phase of manganese dioxide, it can be produced via extracting lithium from $LiMn_2O_4$ preserving its cubic spinel structure[50] by either acid leaching[50,51] or by electrochemical delithiation.[51,52] The former method produces samples having the composition of $Li_{0.03}MnO_2$.[53] It is ambiguous if the λ-MnO_2 phase can be stabilized without any lithium. The 3-D spinel structure with the above symmetry has the general formula $A_x[B_2]O_4$, where the B cations occupy the octahedral 16d sites, the oxygen anions exist in the 32e sites, and the A cations reside in tetrahedral 8a sites. In $LiMn_2O_4$, a cubic close-packed array of oxide ions incorporates the MnO_6 octahedron sharing two opposing corners with LiO_4 tetrahedra. It was found that the unit cell parameter varies with the lithium content at room temperature, and increases from a = 8.155(1) Å in $Li_{0.27}Mn_2O_4$ to a = 8.225(1) Å in $Li_1Mn_2O_4$.[54]
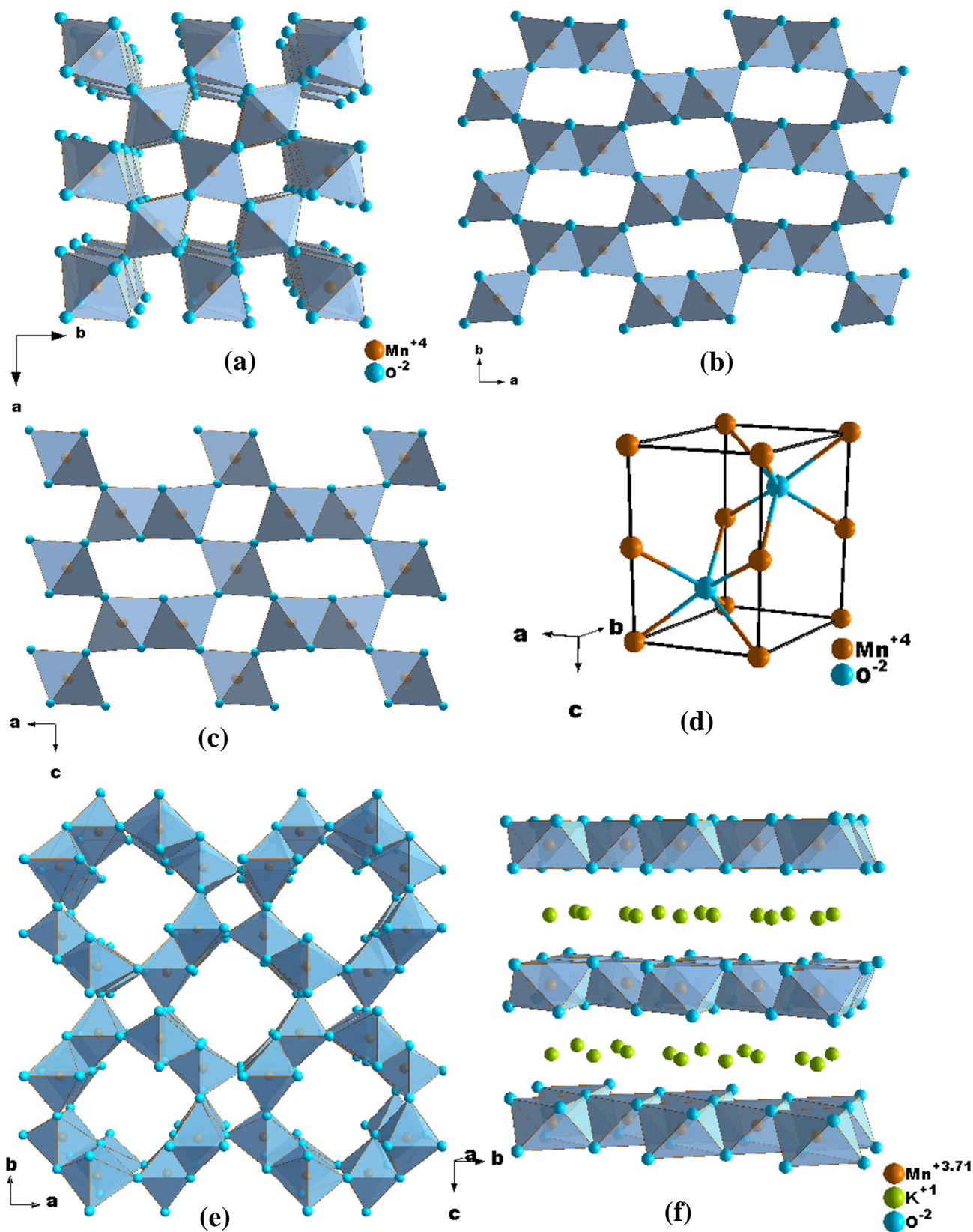
Figure 3. *Polyhedral presentations of the crystal structures of some manganese oxide phases;*
(a) Pyrolusit, (b) Ramsdellite, (c) Nsutite, (d) Akhtenskite, (e) Hollandite and (f) Birnessite.

1.2.2. Synthesis

Manganese oxides were prepared using various molar ratios of $KMnO_4/MnSO_4$,[55-58] and the average oxidation state (AOS) of manganese could be governed by modifying the MnO_4^-/Mn^{2+} ratio.[59]

1.2.2.1. Hydrothermal process

α-MnO_2 nanorods with a diameter ranging from 25 to 40 nm, along with tipped needles β-MnO_2 with a diameter of 100 nm were obtained hydrothermally at 150 °C for 24 h between $MnSO_4$ and $KMnO_4$ using different molar ratios.[60]

The same reaction was performed by Guohong Qiu and coworkers.[61] Pyrolusite was formed hydrothermally at 120 °C from the reaction of $KMnO_4$ and $MnSO_4$ in H_2SO_4 (0.1 mol L^{-1}), the molar ratios of $KMnO_4/MnSO_4$ were 7:18 and 8:17. A mixture of pyrolusite and cryptomelane was obtained by increasing the molar ratio. It was established that potassium ions are playing an essential role in the formation of cryptomelane. The impact of acid concentration on transformation of layered birnessite to the tunnelled structure manganese oxide was studied.[62,63] The concentration of H_2SO_4 is a critical parameter in the hydrothermal reaction of $KMnO_4$ and $MnSO_4$. It was observed that H_2SO_4 with a low concentration (0.1 mol L^{-1}) has no impact on the products whilst the $KMnO_4/MnSO_4$ ratio was increased from 7:18 to 11:14. When the acid concentration increased to 0.2 mol L^{-1}, a mixture of cryptomelane and pyrolusite was formed even when the ratio of $KMnO_4/MnSO_4$ was 7:18. The content of pyrolusite decreased with increasing of the $KMnO_4/MnSO_4$ ratio. Single phase cryptomelane was obtained when the ratios of $KMnO_4/MnSO_4$ were used as 2:3 and 11:14, which suggest that H^+ ions might reside into the tunnel hence, support the framework and inhibit the transformation of cryptomelane to pyrolusite.

α-MnO_2 nanotubes or nanowires and β-MnO_2 nanowires were prepared hydrothermally by the reaction of $KMnO_4$ either with HCl or $MnSO_4$, respectively. They were utilized as catalysts for water oxidation driven by visible light. The as-prepared α-MnO_2 nanotubes were highly uniform; the outer and inner tube diameters were about 100 ± 30 nm and 40 ± 20 nm, respectively. The length of the nanotubes ranges 0.5–3 mm. The nanowires of α-MnO_2 had an average diameter of 30 ± 10 nm and length of 2 ± 1 μm. An SEM image of the β-MnO_2 nanowires indicated that the nanowire morphology occurs throughout this sample, a typical length of 2 ± 1 μm and diameter of 30 ± 20 nm were found.[64]

Xun Wang et.al. have prepared α-, β- and δ-MnO_2 nanowires/nanorods with different aspect ratios by hydrothermal method based on the redox reactions of MnO_4^- and/or Mn^{2+}. δ-MnO_2 nanorods were obtained when pure $KMnO_4$ or a high molar ratio (about 6:1) of a $KMnO_4/MnSO_4$ mixture was hydrothermally treated at 160 °C. When the molar ratio of MnO_4^-/Mn^{2+} was set at about 2.5:1, the products were characterized as α-MnO_2 nanorods with diameter of 20 ± 80 nm and length ranging between 2 and 6 μm. When a molar ratio of about 2:3 was used, the reaction resulted in β-MnO_2 nanorods with diameter of 40 ± 100 nm and length of 0.5 ± 1.0 μm. By changing the type of the oxidant, i.e., $(NH_4)_2S_2O_8$ or $NaClO$, α, β-, and γ-MnO_2 nanowires/ nanorods were obtained by a liquid-phase oxidation method (Table 3).[55]

Table 3. MnO_2 nanowires/nanorods obtained under different reaction conditions.[55]

Oxidant	Exp. conditions		Phase	Morphology	
	T °C	$(NH_4)_2SO_4$		Diameter/nm	Length/μm
$(NH_4)_2S_2O_8$	140	0	β	40-100	2.5-4.0
$(NH_4)_2S_2O_8$	90	0	γ	20-40	0.1-0.2
$(NH_4)_2S_2O_8$	140	0.02	α	5-20	5-10
$(NH_4)_2S_2O_8$	140	0.007	β	20-30	5-10
NaClO	180	0	β	30-40	1-2
NaClO	180	2 mL HCl	β	60-80	0.5-1
NaClO	180	0.02 NH_4Cl	β	20-40	4-8

Layered-type manganese dioxide (δ-MnO_2) was prepared via facile low-temperature hydrothermal method by mixing $KMnO_4$ and epoxypropane at 90 °C for 24 h. The obtained δ-MnO_2 has a layered structure with interlayer spacing of 0.72 nm and long flexible bundles assembled with nanobelts. Epoxypropane played a crucial role for the formation of δ-MnO_2 particles. The as-prepared oxide not only had a large surface area of 188 m^2 g^{-1} but also showed good capacitive behavior and cycling stability in a neutral electrolyte system. Barrett-Joyner-Halenda (BJH) average pore diameter of 11.76 nm confirmed the predominant presence of mesopores in the obtained oxide with a layered structure This electrode material has promising application in supercapacitors because of its advantages of low cost, high capacitance, and good cycling stability.[65]

A catalytic-ion assisted hydrothermal method has been used for the synthesis of hierarchical manganese dioxide nanostructures. Various shapes of hierarchical MnO_2 (nanorod, nanothorn sphere and sphere) were prepared hydrothermally by mixing of $MnSO_4$ and $(NH_4)_2S_2O_8$ aqueous solutions in the presence or absence of Al^{3+}. Single phase of β-MnO_2 was obtained in the absence of Al^{3+} but upon addition of Al^{3+} as a catalytic species, a mixed phase of akhtenskite(ε) and ramsdellite with little α-phase was obtained. It was found that the amount of α-phase increases with increasing Al^{3+} present in the solution. The aspect ratio of aligned nanorods on the nanothorn sphere was controlled by the amount of Al^{3+}.[66]
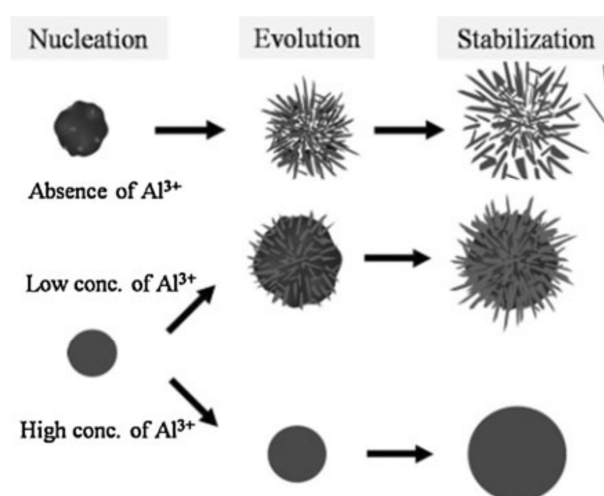
Figure 4. *Schematic illustration of formation stage of MnO_2 prepared in the solution with different amount of Al^{3+} during hydrothermal reaction.*[66]

1.2.2.2. Surfactant assisted method

α-MnO_2 nanowires with diameters of 40-50 nm, and γ-MnO_2 hollow hierarchical microspheres have been prepared by a sodium dodecyl benzenesulfonate (SDBS)-assisted hydrothermal treatment of a mixture of $MnSO_4$ or $MnCl_2$ and $KMnO_4$ in a temperature range 160-180 °C for 6-12 h.[67]

MnO_2 hollow nanospheres were synthesized via liquid co-precipitation approach using different concentrations of cationic surfactant CTAB. The obtained manganese dioxide was characterized as α-MnO_2 and the particle sizes of the samples were between 100 and 300 nm. The synthesized MnO_2 exhibited a specific capacitance of 178 F/g at the current density of 500 mA/g and its BET surface area was 229.8 m^2/g, compared to the 126 F/g and 178.4 m^2/g of the MnO_2 prepared without surfactant.[68]

Microstructures $MnCO_3$ were prepared hydrothermally from manganese chloride and urea with the assistance of sodium dodecyl benzene sulphonate (SDBS) and dodecyl sulfonic acid sodium (SDS). Microplates with diameter ~2.3 μm and thickness of 200 nm as well as 3.1 μm microspheres stacked with 50 nm-thick sheets were obtained, respectively. The as-synthesized $MnCO_3$ precursors were annealed at 400 °C for 4 h resulting in formation of mesoporous γ-MnO_2 microplates and microspheres with pore size of 4–50 nm, which retained the initial shapes. The BET surface areas of the as-prepared γ-MnO_2 microplates and microspheres were 52.1 m^2 g^{-1} and 50.2 m^2 g^{-1}, respectively. The electrochemical property examined over Li^+ batteries revealed that the initial discharge capacity of γ-MnO_2 microplates and microspheres were 1997 mAh g^{-1} and 1533 mAh g^{-1}.[69]

1.2.2.3. Direct precipitation approach

Akhtenskite (ε-MnO_2) with a globular morphology was prepared via a controlled interfacial synthesis in a U-tube using a permeable membrane with different pore sizes. The formation of MnO_2 takes place at the interface between two aqueous solutions of $KMnO_4$ and $Mn(OAc)_2$, the membrane controls the rate of mixing (and therefore the rate of precipitation). Obvious influence of the membrane pore size on both particle size and pore size distribution was found. Consequently, specific surface areas of 50–160 m^2 g^{-1} have been obtained.[70]

1.2.3. Applications

As electrode materials

Nanostructured MnO_2 has been considered as a promising candidate for electrode materials due to its low cost, environmentally friendly nature, and special high capacity.[10,71] Moreover, MnO_2 is superior to the other electrode materials, which should be used in strong acidic or alkaline electrolytes since it can be used in neutral aqueous electrolytes.[72-74] This feature can meet the requirements of a ''green electrolyte'' in supercapacitors.

Catalysis

Porous Manganese dioxide can act as a catalyst for a variety of reactions. It can be used for the decomposition of ozone,[75] reduction of nitric oxide,[76] selective oxidation of carbon monoxide.[77] An even more sophisticated catalysis is the electrochemical assisted epoxidation of Styrene with hydrogen peroxide.[71]

MnO_2 is known as a mild oxidant and has good stability in acidic conditions. These materials exhibit excellent water oxidation activity under visible light by using $Ru(bpy)_3^{2+}$ as a sensitizer and $Na_2S_2O_8$ as a sacrificial electron acceptor.[64]

Birnessite (δ-MnO_2) was used to oxidize organic pollutants including substituted anilines,[78] triclosan, chlorophene,[79] oxyteracycline,[80] and antibacterial agents.[81] Gandhe et al.[82] found that ethyl acetate was completely oxidized by cryptomelane. 2-Mercaptobenzothiazole was effectively degraded by β-MnO_2 suspension.[83]

Technological fields including

Energy-saving,[84] lithium ion energy storage capacities,[85] water treatment[86] and sensors.[87]

Due to the great and wide applicability of manganese dioxide nanoparticles in various interesting areas, the attention to the preparation route is of significance. We have seen from the forgoing survey about manganese dioxide nanoparticles that many synthetic routes were employed, the most common ones are those performed hydrothermally particularly, those employing the comproportionation reaction between Mn^{2+} and $KMnO_4$. Actually, this reaction is a promising one since it presents various synthetic parameters that can modify the phase of the final product.

The problem with the hydrothermal reactions is the sophisticated instrumentation, where much efforts and costs are needed to prepare the oxides under hydrothermal conditions. Accordingly, the necessity to modify a simple reaction system which is valid for formation of various manganese dioxide phases remains a problem.

We have seen also that the formation of single phases of manganese dioxide demands the use of versatile preparative methods. Up to now, there is no common synthetic method that can be utilized for formation of the various manganese dioxide polymorphs.

Although, the self-template effect (by using different MnO_4^- salts) could be a feasible suggestion for such comproportionation reactions that can modify the phase of the so obtained manganese dioxide, nonetheless, it is fairly used in literature.[88]

1.3. Spinel, Mn_3O_4 (Hausmannite)

1.3.1. Structure

Two modifications are well known for Mn_3O_4.[89] Above ~1273 °C, a cubic phase (space group $Fd\overline{3}m$) exists, and below ~1273 °C, one with tetragonal symmetry exists (space group $I4_1$/amd). The latter is named hausmannite and has a distorted spinel structure. The O^{2-} ions form a slightly distorted close packing (16h), while the Mn^{2+} ions occupy 1/8 of the tetrahedral sites (4a) and the Mn^{3+} ions occupy 1/2 of the octahedral sites (8d), as shown in the formula; $Mn^{2+}_{1\ 4a}Mn^{3+}_{2\ 8d}O^{2-}_{4\ 16h}$. The unit cell with lattice constant a = 0.576 nm and c = 0.944 nm consists of four Mn_3O_4 units.[90]

The distribution of manganese ions is based on the principle of maximized self-avoidance, so that all occupied tetrahedrons are surrounded by empty octahedrons and vice versa.[91] The structure is shown in Figure 5. The octahedral sites are tetragonally distorted as a result of the Jahn-Teller effect (four Mn-O distances of 0.193 nm and two of 0.229 nm)[92] thus, changing the crystal structure from cubic to elongated tetragonal.

In an octahedral ligand field the two orbitals directed towards the ligands along the x-, y- and z-axis ($d_{x^2-y^2}$ and d_{z^2}) are energetically raised to give the e_g orbital set, while the three orbitals in between the coordinate axes (d_{xy}, d_{xz} and d_{yz}) are energetically reduced and give the t_{2g} orbital set. In case of Mn^{3+}, the central atom has d^4 electron configuration. These are distributed as $t^3_{2g}e^1_g$. If the one electron in the e_g orbital set occupies the d_{z^2} orbital, the ligand field can be stabilized by enhancement of the distance between the central atom and the two ligands along the z-axis. That way, the orbitals with a z component (d_{z^2}, d_{xz} and d_{yz} are energetically lowered, while d_{xy} and $d_{x^2-y^2}$ are raised.[91] This is schematically shown in the Figure 6.

The stoichiometric hausmannite may be regarded as a normal spinel AB_2O_4. Accordingly, the unit cell comprises 32 oxide ions, 8 Mn^{2+} ions occupying the tetrahedral (A) sites and 16 Mn^{3+} ions located in the octahedral (B) sites.[93-95]
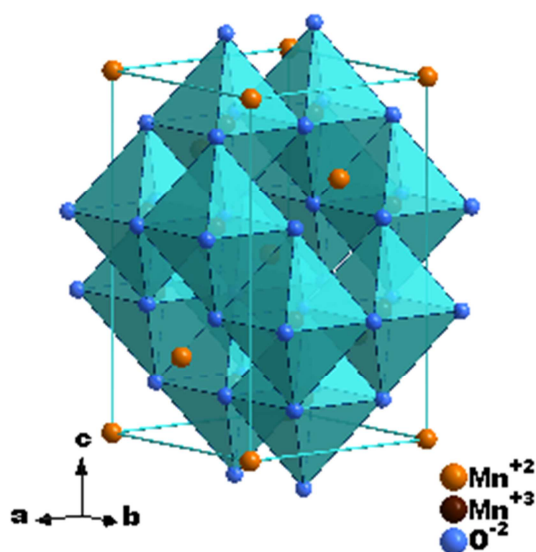
Figure 5. *Crystal structure of the spinel hausmannite, Mn_3O_4.*
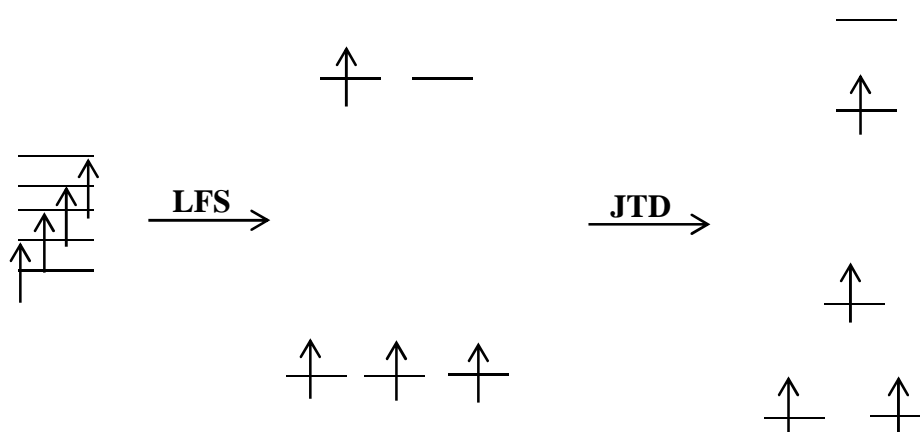
Figure 6. *Schematic representation of ligand field splitting (LFS) and Jahn-Teller distortion (JTD) for Mn(III). Note that the five 3d orbitals in the fictional spherical ligand field (left) are energetically degenerate.*

Actually, many intrinsic properties such as surface, magnetic and electrochemical properties for the materials are function of their structure; therefore, it is significant to investigate the materials according to their structures. In other words, studying the defect chemistry of the materials as a function of their particle size is of importance.

For hausmannite the literature overview (for low temperature modification) revealed that hausmannite has some trends toward nonstoichiometry through the formation of oxygen-rich compounds compared to the normal Mn:O ratio in stoichiometric Mn_3O_4.[96-99] These

deviations from stoichiometry result in a defect structure and substitution of Mn^{3+} for Mn^{2+} result in formation of either interstitial anions or cation vacancies.

Driessens[94] showed a small impact of oxygen pressure on the oxygen content of hausmannite referring to some anionic defects. The oxidation of manganese will be equilibrated by creation of cationic vacancy.

Studying the distribution of Mn^{3+} cations and cationic vacancies in the hydrous hausmannite[100] obtained by the controlled oxidation of $Mn(OH)_2$ revealed for the single-phase product that it has hydroxide groups which are contained in the anionic sublattice. The single-phase product could be then defined as hydrohausmannite. Based on measurements of the integrated intensities of X-ray reflections it has been found that the cationic vacancies in hydrohausmannite are mainly due to the presence of structural OH^- groups. The distribution of vacancies on the tetrahedral and octahedral spinel cationic sublattices they express in the form:

$$Mn^{2+}_{8-3x+y}Mn^{3+}_{5x/2-y}\square_{x/2}\left[Mn^{3+}_{16-x/2}\square_{x/2}\right](OH)_y O_{32-y}$$

Where, x = vacancies/unit-cell and y = hydroxyl groups/unit-cell.

1.3.2. Synthesis

Several synthetic routes were utilized for preparation of nanoscaled Mn_3O_4. Via thermal decomposition of a manganese-benzoic acid complex at 500 °C, Hosny and Dahshan prepared spherical manganese spinel nanoparticles with particle sizes ranging from 39 to 90 nm, depending on whether the precursor was prepared from manganese chloride or sulfate and if it was coordinated by one or two benzoic acid molecules.[101]

Mn_3O_4 nanoparticles (NPs) were prepared via sonication of manganese chloride in ethanol/water solution, estimated crystallite size was about 17 ± 5 nm.[102]

By precipitating a manganese (II) hydroxide gel with ammonium hydroxide and aging the gel at 85 °C for 12 h in aqueous solution, Baykal et. al. obtained Mn_3O_4 nanocrystals with an average particle size of 32 nm.[103]

Wang et. al. synthesized Mn_3O_4 nanocrystals with a particle size of 4-5 nm in a similar fashion. Instead of water, they used ethanol as solvent, precipitated the hydroxide with KOH and heated to 60 °C for 24 h. The obtained nanocrystals were ordered in a pattern of regular walls and are reported to possess an unusual high anisotropy field and coercivity.[104]

Controlled synthesis of Mn_3O_4 of octahedral shapes with a rhombic length of about 300–500 nm was done using the redox reaction between $KMnO_4$ and CMC (sodium carboxymethyl cellulose). Adjusting the experiment conditions such as molar ratio of the reactants, reaction temperature, and the reaction time is the key for synthesis of various manganese oxides.[105]

1.3.3. Applications

The biggest advantages of Mn_3O_4 compared to other metal oxides are that it is non-toxic, available in large amounts and inexpensive (about 1% of the price of cobalt oxide). It can be used as a redox catalyst for various reactions. For treatment of air pollutions, Mn_3O_4 can be used as a catalyst for decomposition of nitric oxides into the elements or for the reduction of CO_2 which represent effective pollutants in the air. It can be utilized as a catalyst for some chemical changes, e.g., reduction of nitrobenzene or oxidation of methane.[106,107]

In electrochemistry, manganese oxides are promising candidates as anode materials for lithium-ion accumulators. Mn_3O_4 can also be used in the synthesis of Li–Mn–O electrode materials for rechargeable lithium batteries.[108,109]

Another important application of Mn_3O_4 is the usage as raw a material for the synthesis of soft magnetic materials such as manganese zinc ferrite, which is powerful for magnetic cores in transformers for power supply.[110]

1.4. Metastable Mn_5O_8

According to studies of Oswald et al.,[111] the crystal structure of Mn_5O_8 was introduced as isostructural to monoclinic $Cd_2Mn_3O_8$,[112] the compositional formula of Mn_5O_8 could be written as $Mn_2^{2+}Mn_3^{4+}O_8$.

Mn_5O_8 has a layer-type structure as appeared in Figure 7a. Its structure composed of 2D octahedral layers in bc planes formed form the basic units $[Mn_3^{4+}O_8]^{4-}$, Mn^{2+} ions are located between these layers. Obviously, one fourth of the cationic sites in the octahedral sheets which are occupied by Mn^{4+} ions are vacant as shown in Figure 7b, above and below the empty Mn^{4+} sites are Mn^{2+} ions that coordinate to six oxygen atoms, three from one octahedral layer and three from the next, forming trigonal prisms in the interlayer space.[36]

Many interesting applications have been suggested for Mn_5O_8. It has been used as ionic conductor for fuel cells or batteries, where the interlayer and/or intralayer defects may facilitate the ion transport at suitable conditions.[113] It was introduced also as a promising catalyst.[114]
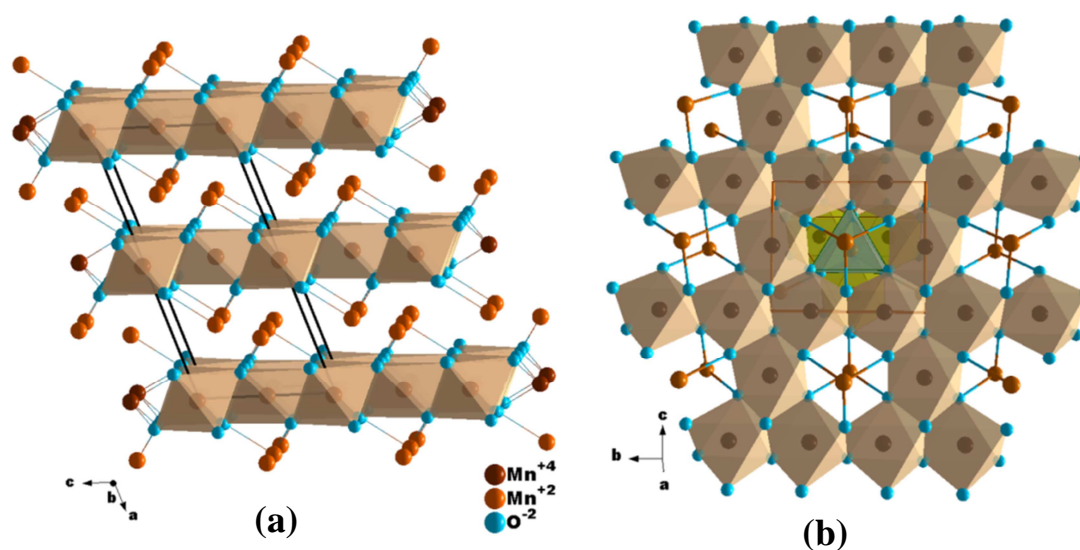
Figure 7. Crystal structure of Mn₅O₈.

Norby et.al.[36] have prepared Mn_5O_8 (14 nm) by topotactic conversion of γ-MnOOH under N_2 flow at 400 °C. Raman scattering studies were made for the product, ten of eighteen Raman-active modes (10 A_g + 8 B_g) were recognized and which are characteristic for monoclinic Mn_5O_8. The most intensive A_g mode locates at 647 cm^{-1} and is used for identifying evidently the monoclinic Mn_5O_8 materials. Magnetic studies for Mn_5O_8 sample

revealed that the electronic spins are ordered antiferomagnetically with Néel temperature of 133 K. Impurities of spinel were identified by coexistence of a sharp peak in χ in the vicinity of ~40 K which is consistent with T_c for spinel hausmannite. The effective magnetic moment for this sample was 4.803 μ_B which matches with calculated value of 4.79 μ_B considering the spin only contributions. Curie–Weiss temperature was determined and the results indicate that its value is located at -144 K.

M. S. Seehra et.al.[115] have studied the magnetic properties for Mn_5O_8 sample (14 nm) synthesized via the reaction of manganese nitrate and sodium hydroxide at pH ~12 and heating the product at 400 °C for 3 h. Measuring the temperature variations of the magnetic susceptibility showed antiferromagnetic ordering with Néel temperature T_N ~128 K, sharp peak is observed near 40 K coinciding with T_c of ferrimagnetic Mn_3O_4.

From the previous knowledge about Mn_5O_8 nanocrystals, we are able to identify the following research problems:

⇨ It is claimed that Mn_5O_8 nanorods (yet, not clean according to XRPD) can be produced via the calcination of manganite under nitrogen flow. No attention has been paid to the importance of oxygen pressure in the formation of Mn_5O_8 from manganite.

⇨ Moreover, the magnetic behavior of such Mn_5O_8 nanocrystals, revealed the presence of a significant amount of spinel impurities. In addition, the presence of such impurities has neither quantified nor clearly interpreted.

⇨ Structural investigations of Mn_5O_8 did not receive an adequate interest.

The former works on manganese oxide/hydroxide nanoparticles have showed that the various reactions that are used for their synthesis from solution are performed either in water or organic solvent. No attention has been paid to the role of the oxygen dissolved in the reaction solutions. Actually, none of the forgoing studies on manganese oxides/hydroxides has refer to or clarify the impact of dissolved oxygen DO (mild oxidizing agent) in the reaction medium on the reaction pathway. Consequently, it is worth to know firstly the factors affecting the amount of DO in the solutions, reaction solvent and temperature are the most significant parameters.

1.5. Solubility of oxygen in ethanol-water mixtures

The report of Shchukarev et.al.,[116] about the solubility of oxygen in ethanol-water mixtures revealed that, the amount of dissolved oxygen significantly affected by the content of ethanol in water. Solutions with high ethanol contents can dissolve oxygen much easier than those with low ethanol content. The quantity ι (Ostwald distribution coefficient, i.e., the volume of gas dissolved in a given volume of solvent) for dissolved oxygen in pure water, pure ethanol and in a mixture of both was determined experimentally. The distribution coefficient was dependent on the temperature (Figure 8); the corresponding coefficients at 25 ℃ were found for pure water 0.031 and 0.283 for pure ethanol.
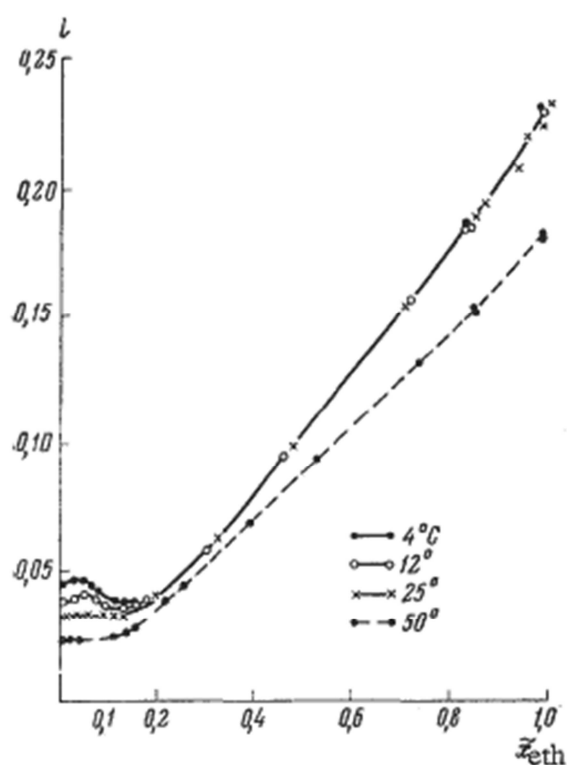
Figure 8. Solubility isotherms for oxygen in ethanol-water mixtures at temperatures of 4, 12, 25, and 50 ℃.[116]

1.6. Motivations

According to our literature survey, we identified some research problems that motivate us to do such a research project:

- Development and manipulation of simple, economic and safe synthetic route valid for the production of versatile manganese oxides/hydroxides nanocrystals.

- Size-selective synthesis of manganese oxide/hydroxide nanocrystals through variation of the reaction parameters e.g. time, temperature, total manganese concentration in the solution and the polarity of the reaction solvent (most interesting one).

- Size-dependent physical properties such as thermal stability and surface properties (surface area, pore size distribution curves and total pore volume) will be studied, these properties are of importance for various applications.

- According to the former reports on γ-MnOOH, it is not so obvious, why and how the decomposition of γ-MnOOH can pursue various pathways upon heating under different conditions. Hence, rationalization of the thermal behavior of manganite under air and in an inert gas atmosphere is of significance.

- In accordance with Norby's et.al. report who studied the magnetic properties of nc-Mn_5O_8, the results showed that it has a high content of spinel contaminations. Therefore, the present study aims to investigate the magnetic properties of nearly clean phase nc-Mn_5O_8 prepared in different ways, as well as to identify the reasons that influence the presence of tiny impurities of spinel in its content and trying to avoid them.

- Finally, as many intrinsic properties are function of the material's structure so detailed studies of the defect chemistry and structural analysis for some selected MnO_x structures are of significance in our project. Size-dependent structural analyses for the hausmannite will be studied as well.

References

1. Schmid, G. Large clusters and colloids. Metals in the embryonic state. *Chem. Rev.* **1992,** *92* (8), 1709-1727.

2. Andres, R. P.; Bielefeld, J. D.; Henderson, J. I.; Janes, D. B.; Kolagunta, V. R.; Kubiak, C. P.; Mahoney, W. J.; Osifchin, R. G. Self-assembly of a two-dimensional superlattice of molecularly linked metal clusters. *Science* **1996,** *273* (5282), 1690-1693.

3. Nayak, S. K.; Jena, P. Giant magnetic moments and magnetic bistability of stoichiomatric MnO clusters. *Phys. Rev. Lett.* **1998,** *81* (14), 2970-2973.

4. Erik Lidström and Ola Hartmann Paramagnetic fluctuations in MnO. *J. Phys. : Condens. Matter* **2000,** *12* (23), 4969.

5. Pask, J. E.; Singh, D. J.; Mazin, I. I.; Hellberg, C. S.; Kortus, J. Structural, electronic, and magnetic properties of MnO. *Phys. Rev. B* **2001,** *64* (2), 024403.

6. Wu, M. S. Electrochemical capacitance from manganese oxide nanowire structure synthesized by cyclic voltammetric electrodeposition. *Appl. Phys. Lett.* **2005,** *87* (15), 153102-153103.

7. Chang, J. K.; Tsai, W. T. Material characterization and electrochemical performance of hydrous manganese oxide electrodes for Use in electrochemical pseudocapacitors. *J. Electrochem. Soc.* **2003,** *150* (10), A1333-A1338.

8. Shen, Y. F.; Zerger, R. P.; Deguzman, R. N.; Suib, S. L.; McCurdy, L.; Potter, D. I.; O'Young, C. L. Manganese oxide octahedral molecular sieves: preparation, characterization, and applications. *Science* **1993,** *260* (5107), 511-515.

9. Feng, Q.; Kanoh, H.; Ooi, K.; Tani, M.; Nakacho, Y. Synthesis of hollandite−type manganese dioxide with H^+ form for lithium rechargeable battery. *J. Electrochem. Soc.* **1994,** *141* (10), L135-L136.

10. Armstrong, A. R.; Bruce, P. G. Synthesis of layered $LiMnO_2$ as an electrode for rechargeable lithium batteries. *Nature* **1996,** *381* (6582), 499-500.

11. Còrdoba De Torresi, S. I.; Gorenstrein, A. Electrochromic behaviour of manganese dioxide electrodes in slightly alkaline solutions. *Electrochim. Acta* **1992,** *37* (11), 2015-2019.

12. Pike, J.; Hanson, J.; Zhang, L.; Chan, S. W. Synthesis and redox behavior of nanocrystalline Hausmannite (Mn_3O_4). *Chem. Mater.* **2007,** *19* (23), 5609-5616.

13. Kohler, T.; Armbruster, T.; Libowitzky, E. Hydrogen bonding and Jahn-Teller distortion in groutite, alpha-MnOOH, and manganite, gamma-MnOOH, and their

relations to the manganese dioxides ramsdellite and pyrolusite. *J. Solid State Chem.* **1997,** *133* (2), 486-500.

14. Crisostomo, V. M.; Ngala, J.; Alia, S.; Dobley, A.; Morein, C.; Chen, C. H.; Shen, X.; Suib, S. L. New synthetic route, characterization, and electrocatalytic activity of nanosized manganite. *Chem. Mater.* **2007,** *19* (7), 1832-1839.

15. Chen, X.; Wang, C.; Ye, F.; Zhu, Q.; Du, G.; Zhong, Y.; Peng, X.; Jiang, J. Phase transition of manganese (oxyhydr) oxides nanofibers and their applications to lithium ion batteries and separation membranes. *Cryst. Eng. Comm.* **2012,** *14* (9), 3142-3148.

16. Peng, X.; Ichinose, I. Green-chemical synthesis of ultrathin beta-MnOOH nanofibers for separation membranes. *Adv. Funct. Mater.* **2011,** *21* (11), 2080-2087.

17. Ocana, M. Uniform particles of manganese compounds obtained by forced hydrolysis of manganese(II) acetate. *Colloid. Polym. Sci.* **2000,** *278* (5), 443-449.

18. Yuan, Z. Y.; Ren, T. Z.; Du, G. H.; Su, B. L. Facile preparation of single-crystalline nanowires of gamma-MnOOH and beta-MnO_2. *Appl. Phys. A Mater. Sci.* **2005,** *80* (4), 743-747.

19. Gao, T.; Krumeich, F.; Nesper, R.; Fjellvag, H.; Norby, P. Microstructures, surface properties, and topotactic transitions of manganite nanorods. *Inorg. Chem.* **2009,** *48* (13), 6242-6250.

20. Cao, X.; Wang, N.; Wang, L.; Mo, C.; Xu, Y.; Cai, X.; Lin, G. A novel non-enzymatic hydrogen peroxide biosensor based on ultralong manganite MnOOH nanowires. *Sens. Actuators, B* **2010,** *147* (2), 730-734.

21. Zhang, Y. C.; Qiao, T.; Hu, X. Y. Preparation of Mn_3O_4 nanocrystallites by low-temperature solvothermal treatment of gamma-MnOOH nanowires. *J. Solid State Chem.* **2004,** *177* (11), 4093-4097.

22. Zhang, Y. C.; Qiao, T.; Hu, X. Y.; Zhou, W. D. Simple hydrothermal preparation of gamma-MnOOH nanowires and their low-temperature thermal conversion to beta-MnO_2 nanowires. *J. Cryst. Growth* **2005,** *280* (3-4), 652-657.

23. Zhang, Y. G.; Liu, Y.; Guo, F.; Hu, Y. H.; Liu, X. Z.; Qian, Y. T. Single-crystal growth of MnOOH and beta-MnO_2 microrods at lower temperatures. *Solid State Commun.* **2005,** *134* (8), 523-527.

24. Xi, G. C.; Peng, Y. Y.; Zhu, Y. C.; Xu, L. Q.; Zhang, W. Q.; Yu, W. C.; Qian, Y. T. Preparation of beta-MnO_2 nanorods through a gamma-MnOOH precursor route. *Mater. Res. Bull.* **2004,** *39* (11), 1641-1648.

25. Zhang, W. X.; Yang, Z. H.; Liu, Y.; Tang, S. P.; Han, X. Z.; Chen, M. Controlled synthesis of Mn_3O_4 nanocrystallites and MnOOH nanorods by a solvothermal method. *J. Cryst. Growth* **2004,** *263* (1-4), 394-399.

26. Li, Z.; Bao, H.; Miao, X.; Chen, X. A facile route to growth of gamma-MnOOH nanorods and electrochemical capacitance properties. *J. Colloid Interface Sci.* **2011,** *357* (2), 286-291.

27. Wu, J.; Zhang, H.; Ma, X.; Li, J.; Sun, F.; Du, N.; Yang, D. Synthesis and characterization of single crystalline MnOOH and MnO$_2$ nanorods by means of the hydrothermal process assisted with CTAB. *Mater. Lett.* **2006,** *60* (29-30), 3895-3898.

28. Sun, X. D.; Ma, C. L.; Wang, Y. D.; Li, H. D. Preparation and characterization of MnOOH and beta-MnO$_2$ whiskers. *Inorg. Chem. Commun.* **2002,** *5* (10), 747-750.

29. Sun, X. D.; Kong, X. D.; Wang, Y. D.; Ma, C. L.; Cui, F. Z.; Li, H. D. Formation of manganite fibers under the directing of cationic surfactant. *Mater. Sci. Eng. , C* **2006,** *26* (4), 653-656.

30. Cheng, F.; Shen, J.; Ji, W.; Tao, Z.; Chen, J. Selective synthesis of manganese oxide nanostructures for electrocatalytic oxygen reduction. *ACS Appl. Mater. Interfaces* **2009,** *1* (2), 460-466.

31. Zhou, F.; Zhao, X.; Yuan, C.; Xu, H. Synthesis of gamma-MnOOH nanorods and their isomorphous transformation into beta-MnO$_2$ and alpha-Mn$_2$O$_3$ nanorods. *j. Mater. Sci.* **2007,** *42* (24), 9978-9982.

32. Mi, Y.; Zhang, X.; Yang, Z.; Li, Y.; Zhou, S.; Zhang, H.; Zhu, W.; He, D.; Wang, J.; Van Tendeloo, G. Shape selective growth of single crystalline MnOOH multipods and 1D nanowires by a reductive hydrothermal method. *Mater. Lett.* **2007,** *61* (8-9), 1781-1784.

33. Fang, Z.; Tang, K.; Gao, L.; Wang, D.; Zeng, S.; Liu, Q. Facile and large-scale synthesis of single-crystalline manganese oxyhydroxide/oxide nanostructures. *Mater. Res. Bull.* **2007,** *42* (9), 1761-1768.

34. Folch, B.; Larionova, J.; Guari, Y.; Guerin, C.; Reibel, C. Synthesis of MnOOH nanorods by cluster growth route from [Mn$_{12}$O$_{12}$(RCOO)(16)(H$_2$O)(n)] (R = CH$_3$, C$_2$H$_5$). Rational conversion of MnOOH into Mn$_3$O$_4$ or MnO$_2$ nanorods. *J. Solid State Chem.* **2005,** *178* (7), 2368-2375.

35. Chen, W.; Wang, N.; Liu, L.; Cui, Y.; Cao, X.; Chen, Q.; Guo, L. Facile synthesis of manganite nanowires: phase transitions and their electrocatalysis performance. *Nanotechnol.* **2009,** *20* (44), 445601-445608.

36. Gao, T.; Norby, P.; Krumeich, F.; Okamoto, H.; Nesper, R.; Fjellvag, H. Synthesis and properties of layered-structured Mn$_5$O$_8$ nanorods. *J. Phys. Chem. C* **2010,** *114* (2), 922-928.

37. Hernan, L.; Morales, J.; Tirado, J. L. Relationships between composition and surface properties of the dehydration products of synthetic manganite. *Surf. Coat. Technol.* **1986,** *27* (4), 343-350.

38. Umek, P.; Zorko, A.; Arcon, D. Magnetic properties of transition-metal oxides: From bulk to nano. In *Ceramics Science and Technology*, Wiley-VCH Verlag GmbH & Co. KGaA: 2010; pp 791-833.

39. Mao-wen X.; Shu-Juan B. Nanostructured MnO_2 for Electrochemical Capacitor. In *Energy Storage in the Emerging Era of Smart Grids*, Prof.Rosario Carbone, Ed.; InTech: 2011; pp 251-278.

40. Baur, W. H. Rutile-type compounds. V. Refinement of MnO_2 and MgF_2. *Acta Cryst. B* **1976,** *32* (7), 2200-2204.

41. Bystrom, A. M. The crystal structure of ramsdellite, an orthorhombic modification of MnO_2. *Acta Chem. Scand.* **1949,** *3*, 163-173.

42. Thackeray, M. M.; Rossouw, M. H.; Gummow, R. J.; Liles, D. C.; Pearce, K.; De Kock, A.; David, W. I. F.; Hull, S. Ramsdellite-MnO_2 for lithium batteries: the ramsdellite to spinel transformation. *Electrochim. Acta* **1993,** *38* (9), 1259-1267.

43. De Wolff, P. M. Interpretation of some γ-MnO_2 diffraction patterns. *Acta Cryst.* **1959,** *12* (4), 341-345.

44. Chabre, Y.; Pannetier, J. Structural and electrochemical properties of the proton / γ-MnO_2 system. *Prog. Solid State Chem.* **1995,** *23* (1), 1-130.

45. Turner, S. H. I. R.; Buseck, P. R. Todorokites: a new family of naturally occurring manganese oxides. *Science* **1981,** *212* (4498), 1024-1027.

46. Turner, S.; Siegel, M. D.; Buseck, P. R. Structural features of todorokite intergrowths in manganese nodules. *Nature* **1982,** *296* (5860), 841-842.

47. Post, J. E.; Veblen, D. R. Crystal structure determinations of synthetic sodium, magnesium, and potassium birnessite using TEM and the Rietveld method. *Am. Mineral.* **1990,** *75* (5-6), 477-489.

48. Chang, F. M.; Jansen, M. Darstellung und kristallstruktur von $Na_2Mn_3O_7$. *Z. Anorg. Allg. Chem.* **1985,** *531* (12), 177-182.

49. Drits, V. A.; Silvester, E.; Gorshkov, A. I.; Manceau, A. Structure of synthetic monoclinic Na-rich birnessite and hexagonal birnessite; I, Results from X-ray diffraction and selected-area electron diffraction. *Am. Mineral.* **1997,** *82* (9-10), 946-961.

50. Hunter, J. C. Preparation of a new crystal form of manganese dioxide:λ-MnO_2. *J. Solid State Chem.* **1981,** *39* (2), 142-147.

51. Greedan, J. E.; Raju, N. P.; Wills, A. S.; Morin, C.; Shaw, S. M.; Reimers, J. N. Structure and magnetism in λ-MnO_2. geometric frustration in a defect spinel. *Chem. Mater.* **1998,** *10* (10), 3058-3067.

52. Jang, Y. I.; Huang, B.; Chou, F. C.; Sadoway, D. R.; Chiang, Y. Magnetic characterization of λ-MnO_2 and $Li_2Mn_2O_4$ prepared by electrochemical cycling of $LiMn_2O_4$. *J. Appl. Phys.* **2000,** *87* (10), 7382-7388.

53. Mosbah, A.; Verbaere, A.; Tournoux, M. Phases $Li_xMnO_{2\lambda}$ rattachees au type spinelle. *Mater. Res. Bull.* **1983,** *18* (11), 1375-1381.

54. Berg, H.; Rundlöv, H.; Thomas, J. O. The $LiMn_2O_4$ to λ-MnO_2 phase transition studied by in situ neutron diffraction. *Solid State Ionics* **2001,** *144* (1−2), 65-69.

55. Wang, X.; Li, Y. D. Synthesis and formation mechanism of manganese dioxide nanowires/nanorods. *Chem. Eur. J.* **2003,** *9* (1), 300-306.

56. Deguzman, R. N.; Shen, Y. F.; Neth, E. J.; Suib, S. L.; O'Young, C. L.; Levine, S.; Newsam, J. M. Synthesis and characterization of octahedral molecular sieves (OMS-2) having the hollandite structure. *Chem. Mater.* **1994,** *6* (6), 815-821.

57. Schurz, F.; Bauchert, J. M.; Merker, T.; Schleid, T.; Hasse, H.; Gläser, R. Octahedral molecular sieves of the type K-OMS-2 with different particle sizes and morphologies: Impact on the catalytic properties in the aerobic partial oxidation of benzyl alcohol. *Appl. Catal. , A* **2009,** *355* (1-2), 42-49.

58. Portehault, D.; Cassaignon, S.; Baudrin, E.; Jolivet, J. P. Morphology control of cryptomelane type MnO_2 nanowires by soft chemistry. growth mechanisms in aqueous medium. *Chem. Mater.* **2007,** *19* (22), 5410-5417.

59. Cui, H.; Qiu, G.; Feng, X.; Tan, W.; Liu, F. Birnessites with different average manganese oxidation states synthesized, characterized, and transformed to todorokite at atmospheric pressure. *Clays Clay Miner.* **2009,** *57* (6), 715-724.

60. Kalubarme, R. S.; Cho, M. S.; Yun, K. S.; Kim, T. S.; Park, C. J. Catalytic characteristics of MnO_2 nanostructures for the O_2 reduction process. *Nanotechnol.* **2011,** *22* (39), 395402.

61. Qiu, G.; Huang, H.; Dharmarathna, S.; Benbow, E.; Stafford, L.; Suib, S. L. Hydrothermal synthesis of manganese oxide nanomaterials and their catalytic and electrochemical properties. *Chem. Mater.* **2011,** *23* (17), 3892-3901.

62. Zhang, Q.; Xiao, Z.; Feng, X.; Tan, W.; Qiu, G.; Liu, F. α-MnO_2 nanowires transformed from precursor δ-MnO_2 by refluxing under ambient pressure: The key role of pH and growth mechanism. *Mater. Chem. Phys.* **2011,** *125* (3), 678-685.

63. Shen, X. F.; Ding, Y. S.; Liu, J.; Cai, J.; Laubernds, K.; Zerger, R. P.; Vasiliev, A.; Aindow, M.; Suib, S. L. Control of nanometer-scale tunnel sizes of porous manganese oxide octahedral molecular sieve nanomaterials. *Adv. Mater.* **2005,** *17* (7), 805-809.

64. Boppana, V. B. R.; Jiao, F. Nanostructured MnO_2: an efficient and robust water oxidation catalyst. *Chem. Commun.* **2011,** *47* (31), 8973-8975.

65. Zhang, X.; Chang, X.; Chen, N.; Wang, K.; Kang, L.; Liu, Z. H. Synthesis and capacitive property of δ-MnO$_2$ with large surface area. *J. Mater. Chem.* **2012,** *47* (2), 999-1003.

66. Ryu, W. H.; Han, D. W.; Kim, W. K.; Kwon, H. S. Facile route to control the surface morphologies of 3D hierarchical MnO$_2$ and its Al self-doping phenomenon. *J. Nanopart. Res.* **2011,** *13* (10), 4777-4784.

67. Chen, Y.; Duan, Z.; Min, Y.; Shao, M.; Zhao, Y. Synthesis, characterization and catalytic property of manganese dioxide with different structures. *J. Mater. Sci. : Mater. Electron.* **2011,** *22* (8), 1162-1167.

68. Zhang, H.; Wang, Y.; Liu, C.; Jiang, H. Influence of surfactant CTAB on the electrochemical performance of manganese dioxide used as supercapacitor electrode material. *J. Alloys Compd.* **2012,** *517*, 1-8.

69. Li, J.; Xi, B.; Zhu, Y.; Li, Q.; Yan, Y.; Qian, Y. A precursor route to synthesize mesoporous γ-MnO$_2$ microcrystals and their applications in lithium battery and water treatment. *J. Alloys Compd.* **2011,** *509* (39), 9542-9548.

70. Roberts, A. J.; Slade, R. C. T. Controlled synthesis of ε-MnO$_2$ and its application in hybrid supercapacitor devices. *J. Mater. Chem.* **2010,** *20* (16), 3221-3226.

71. Espinal, L.; Suib, S. L.; Rusling, J. F. Electrochemical catalysis of styrene epoxidation with films of MnO$_2$ nanoparticles and H$_2$O$_2$. *J. Am. Chem. Soc.* **2004,** *126* (24), 7676-7682.

72. Wu, M. S.; Lee, R. H. Nanostructured manganese oxide electrodes for lithium-ion storage in aqueous lithium sulfate electrolyte. *J. Power Sources* **2008,** *176* (1), 363-368.

73. Qu, Q.; Zhang, P.; Wang, B.; Chen, Y.; Tian, S.; Wu, Y.; Holze, R. Electrochemical performance of MnO$_2$ nanorods in neutral aqueous electrolytes as a cathode for asymmetric supercapacitors. *J. Phys. Chem. C* **2009,** *113* (31), 14020-14027.

74. Zhang, H.; Cao, G.; Wang, Z.; Yang, Y.; Shi, Z.; Gu, Z. Growth of manganese oxide nanoflowers on vertically-aligned carbon nanotube arrays for high-rate electrochemical capacitive energy storage. *Nano Lett.* **2008,** *8* (9), 2664-2668.

75. Radhakrishnan, R.; Oyama, S. T. Ozone decomposition over manganese oxide supported on ZrO$_2$ and TiO$_2$: A kinetic study using in situ laser Raman spectroscopy. *J. Catal.* **2001,** *199* (2), 282-290.

76. Qi, G.; Yang, R. T. Low-temperature selective catalytic reduction of NO with NH$_3$ over iron and manganese oxides supported on titania. *Appl. Catal. , B* **2003,** *44* (3), 217-225.

77. Xia, G. G.; Yin, Y. G.; Willis, W. S.; Wang, J. Y.; Suib, S. L. Efficient stable catalysts for low temperature carbon monoxide oxidation. *J. Catal.* **1999,** *185* (1), 91-105.

78. Klausen, J.; Haderlein, S. B.; Schwarzenbach, R. Oxidation of substituted anilines by aqueous MnO$_2$: Effect of Co-solutes on initial and quasi-steady-state kinetics. *Environ. Sci. Technol.* **1997,** *31* (9), 2642-2649.

79. Zhang, H. C.; Huang, C. H. Oxidative transformation of triclosan and chlorophene by manganese oxides. *Environ. Sci. Technol.* **2003,** *37* (11), 2421-2430.

80. Rubert; Pedersen, J. A. Kinetics of oxytetracycline reaction with a hydrous manganese oxide. *Environ. Sci. Technol.* **2006,** *40* (23), 7216-7221.

81. Zhang, H.; Chen, W. R.; Huang, C. H. Kinetic modeling of oxidation of antibacterial agents by manganese oxide. *Environ. Sci. Technol.* **2008,** *42* (15), 5548-5554.

82. Gandhe, A. R.; Rebello, J. S.; Figueiredo, J. L.; Fernandes, J. B. Manganese oxide OMS-2 as an effective catalyst for total oxidation of ethyl acetate. *Appl. Catal. , B* **2007,** *72* (1−2), 129-135.

83. Li, F.; Liu, C.; Liang, C.; Li, X.; Zhang, L. The oxidative degradation of 2-mercaptobenzothiazole at the interface of β-MnO$_2$ and water. *J. Hazard. Mater.* **2008,** *154* (1−3), 1098-1105.

84. Tang, Z.; Kotov, N. A. One-dimensional assemblies of nanoparticles: Preparation, properties, and promise. *Adv. Mater.* **2005,** *17* (8), 951-962.

85. Liu, D.; Garcia, B. B.; Zhang, Q.; Guo, Q.; Zhang, Y.; Sepehri, S.; Cao, G. Mesoporous hydrous manganese dioxide nanowall arrays with large lithium ion energy storage capacities. *Adv. Funct. Mater.* **2009,** *19* (7), 1015-1023.

86. Fei, J. B.; Cui, Y.; Yan, X. H.; Qi, W.; Yang, Y.; Wang, K. W.; He, Q.; Li, J. B. Controlled preparation of MnO$_2$ hierarchical hollow nanostructures and their application in water treatment. *Adv. Mater.* **2008,** *20* (3), 452-456.

87. Xia, C.; Ning, W.; Lin, G. Facile synthesis of novel MnO$_2$ hierarchical nanostructures and their application to nitrite sensing. *Sens. Actuators, B* **2009,** *137* (2), 710-714.

88. Santos, V. P.; Pereira, M. F. R.; Órfão, J. J. M.; Figueiredo, J. L. Synthesis and characterization of manganese oxide catalysts for the total oxidation of ethyl acetate. *Top. Catal.* **2009,** *52* (5), 470-481.

89. Bousquet-Berthelin, C.; Stuerga, D. Flash microwave synthesis of Mn$_3$O$_4$-hausmannite nanoparticles. *j. Mater. Sci.* **2005,** *40* (1), 253-255.

90. Kaczmarek, J.; Wolska, E. Cation and vacancy distribution in nonstoichiometric hausmanite. *J. Solid State Chem.* **1993,** *103* (2), 387-393.

91. Holleman, A. F.; Wiberg, E.; Wiberg, N. *Lehrbuch Der Anorganischen Chemie;* de Gruyter: 2007.

92. Norrestam, R. α–Manganese (III) Oxide —— a C-type sesquioxide of orthorhombic symmetry. *Acta Chem. Scand.* **1967,** *21* (10), 2871-2884.

93. Chardon, B.; Vigneron, F. Mn_3O_4 commensurate and incommensurate magnetic structures. *J. Magn. Magn. Mater.* **1986,** *58* (1–2), 128-134.

94. Driessens, F. C. M. Place and valence of the cations in Mn_3O_4 and some related manganates. *Inorg. Chim. Acta* **1967,** *1* (0), 193-201.

95. Burns, R. G. *Mineralogical applications of crystal field theory;* Cambridge University Press: 1970.

96. Feitknecht, W.; Marti, W. Über die oxydation von mangan(II)-hydroxyd mit molekularem sauerstoff. *Hev. Chim. Acta* **1945,** *28* (1), 129-148.

97. Feitknecht, W.; Brunner, P.; Oswaldw, H. R. Über den einfluß der feuchtigkeit auf die oxydation von manganhydroxid durch molekularen sauerstoff. *Z. Anorg. Allg. Chem.* **1962,** *316* (3-4), 154-160.

98. Hem, J. D. Rates of manganese oxidation in aqueous systems. *Geochim. Cosmochim. Acta* **1981,** *45* (8), 1369-1374.

99. Murray, J. W.; Dillard, J. G.; Giovanoli, R.; Moers, H.; Stumm, W. Oxidation of Mn(II): Initial mineralogy, oxidation state and ageing. *Geochim. Cosmochim. Acta* **1985,** *49* (2), 463-470.

100. Kaczmarek, J.; Wolska, E. The defect structure and vacancy distribution in the low-temperature hausmanite. *Solid State Ionics* **1993,** *63–65* (0), 633-638.

101. Hosny, N. M.; Dahshan, A. Facile synthesis and optical band gap calculation of Mn_3O_4 nanoparticles. *Mater. Chem. Phys.* **2012,** *137* (2), 637-643.

102. Baykal, A.; Kavas, H.; Durmus, Z.; Demir, M.; Kazan, S.; Topkaya, R.; Toprak, M. S. Sonochemical synthesis and chracterization of Mn_3O_4 nanoparticles. *Cent. Eur. J. Chem.* **2010,** *8* (3), 633-638.

103. Baykal, A.; Koeseoglu, Y.; Senel, M. Low temperature synthesis and characterization of Mn_3O_4 nanoparticles. *Cent. Eur. J. Chem.* **2007,** *5* (1), 169-176.

104. Wang, N.; Guo, L.; He, L.; Cao, X.; Chen, C.; Wang, R.; Yang, S. Facile synthesis of monodisperse Mn_3O_4 tetragonal nanoparticles and their large-scale assembly into highly regular walls by a simple solution route. *Small* **2007,** *3* (4), 606-610.

105. Yin, J.; Gao, F.; Wu, Y.; Wang, J.; Lu, Q. Synthesis of Mn_3O_4 octahedrons and other manganese-based nanostructures through a simple and green route. *Cryst. Eng. Comm.* **2010,** *12* (11), 3401-3403.

106. Stobbe, E. R.; de Boer, B. A.; Geus, J. W. The reduction and oxidation behaviour of manganese oxides. *Catal. Today* **1999,** *47* (1–4), 161-167.

107.　Zwinkels, M. F. M.; Järås, S. G.; Menon, P. G.; Griffin, T. A. Catalytic materials for high-temperature combustion. *Catal. Rev.* **1993,** *35* (3), 319-358.

108.　Sanchez, L.; Farcy, J.; Pereira-Ramos, J. P.; Hernan, L.; Morales, J.; Tirado, J. L. Low-temperature mixed spinel oxides as lithium insertion compounds. *J. Mater. Chem.* **1996,** *6* (1), 37-39.

109.　Thackeray, M. M.; David, W. I. F.; Bruce, P. G.; Goodenough, J. B. Lithium insertion into manganese spinels. *Mater. Res. Bull.* **1983,** *18* (4), 461-472.

110.　Pan'kov, V. V. Interaction of (MnZn)O solid solutions with Fe_2O_3 as intermediate stage of formation of MnZn ferrites. *Ceram. Int.* **1988,** *14* (2), 87-91.

111.　Oswald, H. R.; Wampetich, M. J. Die Kristallstrukturen von Mn_5O_8 und $Cd_2Mn_3O_8$. *Hev. Chim. Acta* **1967,** *50* (7), 2023-2034.

112.　Oswald, H. R.; Feitknecht, W.; Wampetich, M. J. Crystal data of Mn_5O_8 and $Cd_2Mn_3O_8$. *Nature* **1965,** *207* (4992), 72.

113.　Park, Y. J.; Doeff, M. M. Synthesis and electrochemical characterization of $M_2Mn_3O_8$ (M= Ca, Cu) compounds and derivatives. *Solid State Ionics* **2006,** *177* (9–10), 893-900.

114.　Tian, Z. R.; Tong, W.; Wang, J. Y.; Duan, N. G.; Krishnan, V. V.; Suib, S. L. Manganese oxide mesoporous structures: Mixed-valent semiconducting catalysts. *Science* **1997,** *276* (5314), 926-930.

115.　Punnoose, A.; Magnone, H.; Seehra, M. S. Synthesis and antiferromagnetism of Mn_5O_8. *Ieee Trans. Magn.* **2001,** *37* (4), 2150-2152.

116.　Shchukarev, S. A.; Tolmacheva, T. A. Solubility of oxygen in ethanol - water mixtures. *J. Struct. Chem.* **1968,** *9* (1), 16-21.

Chapter 2

Experimental part and physical methods

2.1. Materials

All reagents used in the experiments were analytically pure these are: Permanganate salts; $KMnO_4$, $NaMnO_4$ ($\geq 97\%$) and $CsMnO_4$ (98%) as well as Manganese salts; $Mn(OAc)_2.4H_2O$, $MnCl_2.4H_2O$ or $MnSO_4.H_2O$) were purchased from Sigma-Aldrich - Sodium hydroxide; NaOH (99%) and Ammonia; NH_3 (25%) were purchased from Grüssing GmbH - Hydrochloric acid, HCl from Merk - Organic solvents; Ethanol and acetone were of analytical grade and purchased from Fisher Scientific GmbH. All chemicals were used without further purifications.

2.2. Synthesis of oxide/hydroxide nanoparticles

2.2.1. Synthesis of γ-MnOOH nanorods with smallest accessible particle size

Among wide variety of the preparative methods reported for synthesis of manganite nanorods, the most effective ones those lead to the formation of single phase of manganite nanorods with smallest diameter were those including the production of manganite via reduction of $KMnO_4$ either by toluene (12 nm diameter)[1,2] or DMF (~9 nm).[3] We used the redox reaction between potassium permanganate and divalent manganese salts in aqueous medium for the following reasons:

❖ Economically, manganese salts are cheaper than toluene and DMF.

❖ Relative toxicity of toluene and DMF, inhaling toluene has potential to cause severe neurological harm. Long term toluene exposure is often associated with effects such as: psychoorganic syndrome;[4] visual evoked potential (VEP) abnormality;[4] toxic polyneuropathy, cerebellar, cognitive, and pyramidal dysfunctions;[4,5] optic atrophy; and brain lesions. DMF has been linked to cancer in humans, it is thought to cause birth defects and the long-term exposure may damage the liver and kidneys.[6]

❖ The reaction between MnO_4^- and Mn^{2+} has been proved to be a promising and versatile route since it provides many experimental parameters to modify the reaction pathway.[7]

Manganite nanorods prepared by two different methods:

• Comproportionation reaction reported before between $KMnO_4$ and manganese acetate ($Mn(OAc)_2.4H_2O$) in an aqueous medium,[8] followed by our size-selective experiments.

• Successfully, a new synthetic method for the preparation of manganite nanorods was developed through performing the redox reaction between $KMnO_4$ and variable manganese salts, e.g., $MnCl_2.4H_2O$ or $MnSO_4.H_2O$. These reactions were reported

frequently for the hydrothermal synthesis of different forms of MnO_2[9,10] associated with modification of initial pH of the reaction medium. This process leads to formation of γ-MnOOH nanorods.

Using manganese acetate

In a typical experimental procedures, 0.60 g (2.45 mmol) of $Mn(CH_3COO)_2 \cdot 4H_2O$ and 0.075 g (0.47 mmol) of $KMnO_4$ (molar ratio about 5:1) were dissolved in 150 mL of pure water to form a light brown solution, the initial pH for this mixture was ~6. The mixture was refluxed under constant agitation for about 17 h, and then cooled to room temperature naturally. The final precipitate was collected by centrifugation, washed with deionized water for several times to remove unreacted ions, and dried in air at 60 °C. The yield of manganite samples prepared under reflux was high approximately 92-95%.

Grain growth and size control experiments were performed afterward by variation of either the reaction time or the total manganese concentration in the solution. Grain growth can be managed via governing the reaction temperature and time. For this purpose the same reaction was repeated but this time under hydrothermal conditions (better control over the reaction temperature). By this way, 0.075 g $KMnO_4$ (0.47 mmol) and 0.60 g $Mn(CH_3COO)_2.4H_2O$ (2.45 mmol) were mixed into 70 mL distilled water. The resulting light brown solution was transferred into a Teflon-lined stainless steel autoclave of 100 mL capacity. The autoclave was maintained at 85–160 °C for 1-72 h. After the autoclave was sealed, cooled to room temperature naturally, the products were filtered off and washed with de-ionized water for several times and then dried in air at 60 °C. Low yield was obtained under hydrothermal conditions; around 70% manganite was produced.

Using manganese chloride or sulphate

To the best of our knowledge this is the first time that manganite nanoparticles are prepared via comproportionation reaction between manganese chloride/sulphate and potassium permanganate. The same experimental procedures as above were used except that manganese acetate was replaced either by manganese chloride or sulphate keeping the same molar ratio of 5:1 for Mn^{2+}/MnO_4^- couple. Typically, 0.41 g (2.43 mmol) of $MnSO_4.H_2O$ (or 0.48 g, 2.43 mmol of $MnCl_2.4H_2O$) and 0.075 g of $KMnO_4$ were introduced in 500 mL round flask. 125 mL of distilled water was added to the mixture. The initial pH of the aqueous solution was about 3. In order to rise the pH to ~6-8 (optimum pH values for formation of γ-MnOOH

known from our work) NaOH (1.0 mol L^{-1}) was added. The volume of the solution was then adjusted to 150 mL by adding distilled water. Thereafter, the same steps as above were followed for separation of γ-MnOOH nanorods (about 96% yields).

2.2.2. Synthesis of various manganese oxide/hydroxide phases

Synthesis of α-, γ-, ε-, δ-MnO$_2$, β-MnOOH and α-Mn$_3$O$_4$ nanocrystals with variable morphological shapes was accomplished by performing the former reaction between Mn^{2+} and MnO$_4^-$ salts and modification of the experimental parameters as follow:

- Reaction solvent (Ethanol/water, acetone/water mixtures or pure organic solvents were used instead of pure water, keeping the total volume of the solution at 70 mL), pure acetone is necessary for **Feitknechtite synthesis** (β-MnOOH) under solvothermal conditions (the same procedures as mentioned before, acetone was used instead of water, 50% yield).

- Reaction temperature (room temperature **synthesis of ε-MnO$_2$**, 95% yield),

- Initial pH of the reaction medium was adjusted in both acidic and basic media using either HCl (1.0 mol L^{-1}) or NaOH (1.0 mol L^{-1}), respectively,

- Molar ratio of the redox couple Mn^{2+}/MnO$_4^-$

- The counter ion of manganese salt (OAc$^-$, Cl$^-$ and SO$_4^{-2}$) and

- Type of alkali metal cation of the permanganate salt (template effect).

2.2.3. Synthesis of Mn$_5$O$_8$ and β-MnO$_2$ nanorods

Mn$_5$O$_8$ and β-MnO$_2$ nanorods were prepared by calcination of definite amounts (~30 mg) of manganite precursor (26 nm) in open air (isothermally) at different temperatures. The calcination process was carried out using aluminium block mounted over a hot plate with temperature controller and fitted with a thermo-couple to get the proper temperature for calcination. Glass tubes with different sizes (length (ℓ) = 10 or 20 cm and diameter (Φ) =1 or 3 cm) were utilized for such calcination. We observed that the size of the tube has pronounced impact on the calcination pathway.

For the preparation of β-MnO$_2$, the size of the tube is not significant as long as the calcination process occurs at low temperatures of 225-265 °C (the tube maintained to 1 h). At higher annealing temperatures ≥ 350 °C the size of the tube is a crucial parameter. Large size tubes are necessary for the production of single phase of nc-MnO$_2$.

Mn_5O_8 can be prepared by calcination of γ-MnOOH in a narrow tube at a temperature in the range of 350-520 °C for 1 h. No Mn_5O_8 can be obtained using a large size tube irrespective of the temperature of calcination.

Non-isothermal decomposition of manganite precursor was made using TGA/DSC for purpose of comparison. TGA was run up to two different temperatures 400 °C (optimum temperature for synthesis of Mn_5O_8) and 600 °C. Calcinations for the as-prepared MnO_2 and Mn_5O_8 were carried out in open air at a temperature near to 600 °C, the results obtained are compared with those produced from TGA at a temperature of 600 °C.

2.2.4. Synthesis of the spinel, Mn_3O_4

<u>In aqueous solution</u>

All reactions were performed in 500 mL Schlenk flasks. Samples were prepared by dissolving 4.1 mmol of $Mn(OAc)_2.4\,H_2O$ in a definite volume of water. After that, 8.3 mmol of ammonia (25%) or sodium hydroxide was added as a precipitant, then water volume adjusted to 100 mL. The molar ratio of manganese(II) to the precipitant was chosen to be about 1:2 in order to ensure quantitative precipitation of manganese(II) hydroxide (slight excess of the base was added). Upon addition of the base, the color of the reaction solutions turned from light pink to brown within seconds. Thereafter, the whole mixture was put into an oil bath kept at a temperature of about 40 °C, fitted with a reflux condenser and stirred for different reaction times. After cooling to room temperature the precipitate was centrifuged (9000 rpm, 15 min) and washed with water several times. The samples were dried in an oven at 60 °C for several hours. Hausmannite with yield around 82% was obtained using NaOH as a precipitant whereas about 58% hausmannite yield was produced using ammonia.

<u>In ethanol-water mixture</u>

The former experimental steps were repeated, this time with replacing water partially by ethanol. Different volume ratios of $EtOH/H_2O$ (v/v) were used to study the effect of such solutions on the product phase, average grain size, excess mass and structure, keeping the other experimental parameters unchanged.

Another set of experiments was performed to investigate the impact of the base concentration (i.e., pH of the medium) on the product phase and its mean particle size. The molar ratio between manganese salt and the precipitant (NH_3 solution or NaOH) was increased up to 1:4 and 1:6.

The impact of the reaction temperature and time on the crystallite size and the phase purity was examined; different times of 1, 6, 24 and 72 h were used, various reaction temperatures were chosen, i.e., room temperature, 40, 60 and 80 °C.

2.3. Physical measurements

2.3.1. XRD-measurement [11,12]

The crystals are formed mainly from periodical arrangement of atoms that are extending in the three dimensions. The smallest repeated unit in the crystal is called unit cell, which bear all structural information of the crystal. X-rays can be considered as waves of electromagnetic radiation, when they strike the atoms, diffraction of x-ray waves takes place (mainly through electrons of the atoms).

The diffracted beams can interfere constructively or destructively, in limited specific directions they can add constructively. These specific directions can be seen as spots on the diffraction pattern called reflections. Bragg identified the condition for the constructive interference by the following law:

$$2d \sin \theta = n\lambda$$

Where, λ is the wavelength of the X-rays, d is the distance between the lattice planes, θ is the angle of the x-ray beam incident to the sample and n is a whole number.

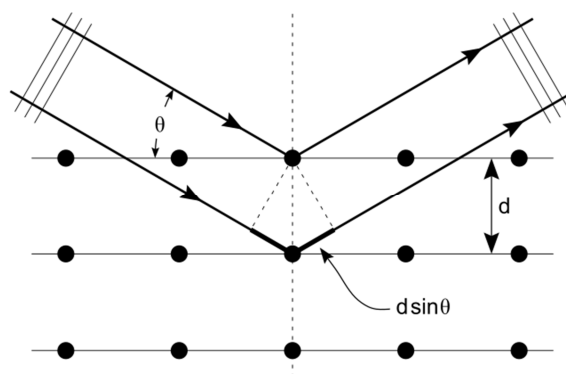*Figure 1: Bragg reflection on adjacent lattice planes.*[12]

XRD spectra of the bulk-materials display distinct peaks (reflections) locate at the angles 2θ where constructive interferences occur. For materials with smaller particles in the range of nanometres, the peaks get broader. Scherrer's equation can be used for the calculation of the particle sizes smaller than 100 nm as given by the following equation:[13]

$$<d> = k\lambda/\ \beta \cos \theta$$

<d> is the average size of the ordered (crystalline) regions, which may be smaller or equal to the grain size. K is a dimensionless shape factor; its value is close to unity, typically ~0.9. This value can be changed with the actual shape of the crystallite. λ is the wavelength of X-ray. β is the line broadening at half the maximum intensity (FWHM), after subtracting the instrumental line broadening, in radians. This quantity is also sometimes denoted as $\Delta(2\theta)$; θ is the Bragg angle.

Rietveld Refinement[14]

Rietveld refinement is a method contrived by Hugo Rietveld to be used in the investigation of the crystalline materials. The results of neutron and x-ray diffraction for powder samples appear as patterns formed from reflections (peaks in intensity) locate at fixed positions. The height, width and position of these reflections are of importance for determination of several features of the material's structure. The refinement in Rietveld method is based on the least squares approach, the refinement proceeds till matching the theoretical line profile with the measured one.

•Peak shape

There are some factors affecting the profile of powder diffraction reflection among them the characteristics of the beam, the experimental setup, size and shape of the sample. For the monochromatic neutron sources the sophistication of the numerous effects leads to a reflex almost Gaussian in shape. The contribution of a given reflection to the profile y_i at position $2\theta_i$ is then:

$$y_i = I_k \exp\left[\frac{-4\ln(2)}{H_k^2}(2\theta_i - 2\theta_k)^2\right]$$

Where H_k is full-width half-maximum, $2\theta_k$ is the midpoint of the reflex, and I_k is the calculated intensity of the reflex (obtained from the structure factor, the Lorentz factor, and multiplicity of the reflection).

At very low diffraction angles the reflections might have an asymmetry owing to the vertical difference of the beam. A semi-empirical correction factor A_S was used to explain such asymmetry:

$$A_s = 1 - [\frac{sP(2\theta_i - 2\theta_k)^2}{tan\,\theta_k}]$$

P is the asymmetry factor and s is an integer (+1, 0,-1) relying on the difference of $2\theta_i$-$2\theta_k$ being +ve, zero or –ve, respectively.

The profile may consist of more than one diffraction peak located at a given position. The intensity is merely the summation of all reflections contributing at the point $2\theta_i$.

- **Peak width**

At higher Bragg angles the width of the diffraction peaks is found to broaden. This angular dependency was formulated by

$$H_k^2 = U\,tan^2\,\theta_k + V\,tan\theta_k + W$$

Where U, V and W are the half width parameters and probably refined during the fit.

- **Preferred orientation**

For powder samples with plate- or rod-like crystallites there is an affinity to line up themselves laterally to the axis of a cylindrical sample holder. For polycrystalline samples the fabrication of the material may lead to larger volume fraction of certain crystal orientations (referred to as texture). Therefore, the reflex intensities will differ from those expected for a completely random distribution. Rietveld permitted for moderate cases of the previous through presenting a correction factor:

$$I_{corr} = I_{obs}\,exp(-G\alpha^2)$$

Where I_{obs} is the expected intensity for a random sample, G is the preferred orientation parameter and α is the acute angle between the scattering vector and the normal of the crystallites.

- **Refinement**

In principle Rietveld method is act to minimize the function M which investigates the difference between a calculated profile y(calc) and the observed data y(obs). M can be given by the following equation:

$$M = \sum_i W_i \left\{ y_i^{obs} - \frac{1}{c} y_i^{calc} \right\}^2$$

Where W_i is the statistical weight and c is an overall scale factor such that $y^{calc} = cy^{obs}$

Instrumentation

The powder XRD analyses in our work were performed using a Philips powder X'Pert MPD X-ray diffractometer equipped with a graphite monochromator (Cu Kα radiation, λ = 0.1542 nm), operated at 40 kV and 40 mA and were used to identify the phase constitutions and crystallite sizes of the obtained products by application of Scherrer's equation.

2.3.2. Infrared spectroscopy[15]

IR spectroscopy deals with the infrared region of the electromagnetic spectrum. It comprises a variety of techniques, mostly based on absorption spectroscopy. It is useful for identification and studying of chemicals. The infrared part of the electromagnetic spectrum can be divided to three regions; the near-, mid- and far- infrared (relative to the visible spectrum). Near-IR region has a higher-energy ~14000–4000 cm^{-1} (0.8–2.5 μm wavelength). The mid-IR, locates in the range of about 4000–400 cm^{-1} (2.5–25 μm) and can be used to study the fundamental vibrations and related rotational-vibrational structure. Finally, the region of far-IR locates in the range of 400–10 cm^{-1} (25–1000 μm) and has low energy.

In IR-spectrometers the absorbance or transmission of the infrared radiation through the sample is measured. The obtained IR spectrum is basically a plot of the absorbed infrared light (or transmited) on the vertical axis vs. frequency or wavelength on the horizontal axis. The frequency used in IR spectra has a unit of cm^{-1} (sometimes called wave numbers).

In IR spectroscopy molecules absorb particular frequencies that are characteristic of their structure. These absorptions are result of resonant frequencies (there is a matching between the frequency of the absorbed radiation and the transition energy of the bond or group that vibrates).

Investigation of the transmitted light gives information about how much energy was absorbed at each frequency (or wavelength). This can be accomplished by using a monochromator which enable the scanning of the wavelength range. Today usually FT-IR-spectrometers are used where the wave numbers are not detected step by step but all wavelengths are irradiated at the same time and the transmission is measured. In those spectrometers a Michelson interferometer is used. The resulting spectrum is Fourier transformed to a classical spectrum. This technique has the advantage of saving time since it is not necessary to measure wavenumber by wavenumber. Consequently, the measurement

can be repeated several times to get better spectra with a better signal to noise ratio. Analysis of the position, shape and intensity of the peaks in this spectrum reveals details about the molecular structure of the sample.

Vibrational modes

Only the vibrational modes in a molecule associated with changes in the dipole are "IR active". The molecule can vibrate in several manners; each is called a vibrational mode. For linear molecules, 3N–5 degrees of vibrational modes are possible (N number of atoms in the molecule), whereas for nonlinear molecules 3N – 6 degrees of vibrational modes are exist.

Stretching Vibrations

Symmetric   Asymmetric

Bending Vibrations

In-plane   Out-of-plane

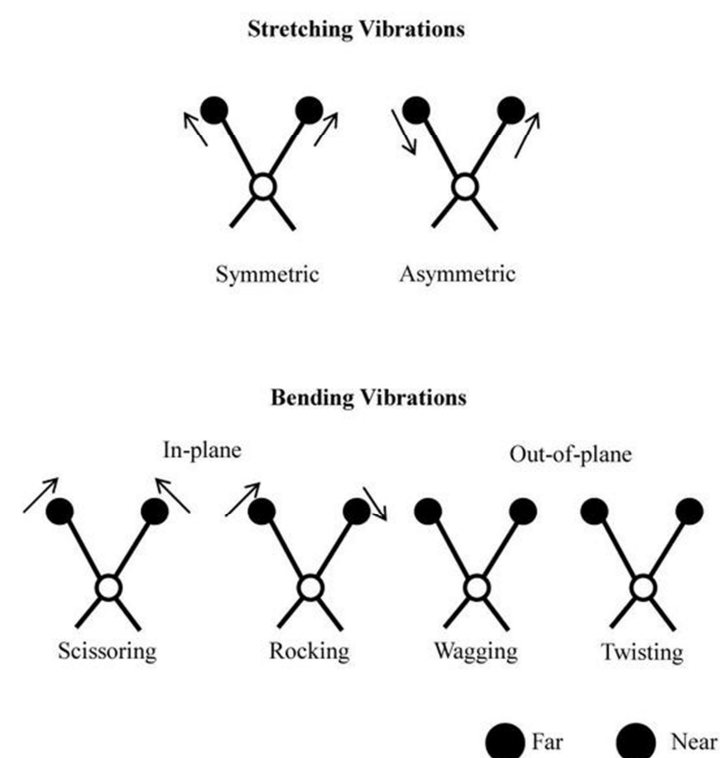Scissoring   Rocking   Wagging   Twisting

● Far   ● Near

Figure 2: *Various molecular vibration modes.*[16]

Instrumentation

In our work Fourier transform infrared (FT-IR) spectra were recorded in the wavenumber range 4000–400 cm^{-1} with a TENSOR 37 (Bruker Optics) spectrometer.

2.3.3. Raman spectroscopy[17]

Basically, in Raman spectroscopy the sample is exposed to intense laser beams in the UV-visible region (υ_o), the scattered light is ordinarily seen in the direction at right angles to the incident beam. The scattered light comprises two types: one, named Rayleigh scattering (strong) which has the identical frequency as the incident beam (υ_o). The other, called Raman scattering, (very weak about 10^{-5} of the incident beam) has frequencies $\upsilon_o \pm \upsilon_m$ where υ_m is a vibrational frequency of a molecule. The $\upsilon_o - \upsilon_m$ and $\upsilon_o + \upsilon_m$ lines are termed the Stokes and anti-Stokes lines, respectively. Consequently, in Raman spectroscopy, we determine the vibrational frequency (υ_m) as a shift from the incident beam frequency (υ_o).

Compare to IR spectra, Raman spectra are detected in the UV-visible region since both the excitation and Raman lines appear.

Raman spectrometer consists of the following components:

(1) Excitation source, which is a continuous-wave (CW) laser

(2) Sample illumination and collection system

(3) Wavelength selector

(4) Detection and computer control/processing systems

A Raman spectrum can be represented by a plot of the intensity versus Raman shift ($\Delta \upsilon = \upsilon_o \pm \upsilon$). $\Delta\upsilon$ is often written as υ for brevity.

As shown in the energy level diagram (Figure 3),[18] a molecule at relaxation exists in the ground vibrational and electronic states. The energy of the system is raised for an instantaneous by the electric field of the laser which induces a polarization in the chemical species. The polarized state is not a true energy state and is commonly called a "virtual state". Decay from the virtual state happens almost immediately and predominantly back to the initial ground state. This process leads to the Rayleigh scattering. Decay to the first excited vibrational level gives rise to a Stokes-Raman shift. The energy of Stokes-Raman shift scattering is lower (longer wavelength) compared to that of the laser light. For the systems possess a small population in the excited vibrational state, decay to the ground state is probable, resulting in a scattering of higher energy (shorter wavelength) compared to the laser light. This form of scattering is named anti-Stokes-Raman scattering.
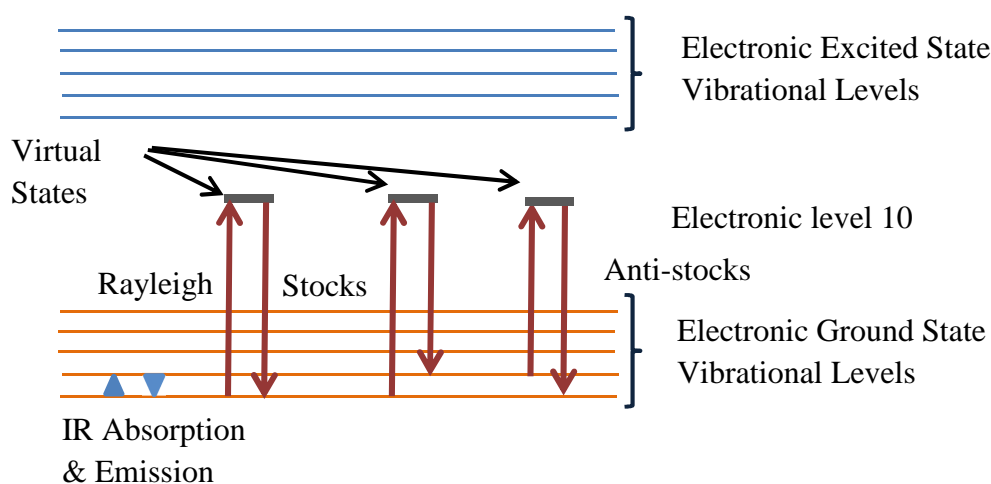
Figure 3. Energy-level diagram showing the states involved in Raman signal.[18]

The vibrational states explored by Raman spectroscopy are similar to those included in infrared spectroscopy. Both Raman spectroscopy and Fourier transform infrared (FT-IR) spectroscopic technique are very similar. In fact, the two vibrational spectroscopy techniques are complementary. The strong vibrations in an infrared spectrum (those resulting in strong dipole moments) are usually weak in a Raman spectrum. Similarly, vibrations of non-polar functional group that provide very strong Raman bands usually gives rise to weak infrared signals.

Vibrational spectroscopy affords significant data on the structure of the molecules. For instance, the position and intensity are useful to study the molecular structure or to define the chemical identity of the sample.

By noticing the positions and intensity of the Raman bands, it is possible to identify the chemical compounds or to study intermolecular interactions.

Instrumentation

Raman spectra for the manganite samples were measured using a LabRAM HR 800 system equipped with a He–Ne laser. The wavelength of the laser beam is 632.8 nm and the light power 5 mW. Long-working distance 50xobjective lens was used (working distance = 50 mm).

2.3.4. Scanning electron microscope (SEM)

Scanning electron microscopes permits surface imaging of particles too small for conventional light microscopes. Instead of electromagnetic radiation, these microscopes rely on electrons accelerated to several KeV with very small wavelengths to make structures on the submicrometer scale visible. A beam of electrons is emitted by a tungsten or LaB_6 cathode and focused by electromagnetic lenses. To avoid the interaction of the beam with atoms other than the sample, the measurement is performed under vacuum. The interaction of electrons with matter is divided into elastic and inelastic scattering. Electrons scattered inelastically loose energy in favor of excitation of electronic or vibrational states in the sample depending on the energy of the incident electron. If the energy is large enough, secondary electrons can be ejected due to ionization. Electrons ejected by surface atoms can be detected. The narrow beam of electrons in the microscope scans the sample. The image is then obtained by recording the secondary electron current of multiple beam positions.[19]

Instrumentation

Scanning electron microscopy was carried out using a JEOL JSM-7500F field emission scanning electron microscope at an accelerating voltage of 2-5 kV. All samples were sputtered with platinum prior to observation.

2.3.5. Transmission electron microscopy (TEM)

For microstructural analysis, TEM is the most commonly used method. It necessitates electron transparent samples, less than 100 nm thick. A high energy electron beam (100–1000 keV) is focused on the specimen by electromagnetic lenses similar to SEM. Whereas the scanning electron microscope generates an image from elastically backscattered electrons, in TEM the intensity of transmitted electrons is measured. The intensity is inversely proportional to the atomic number, and so discriminating between different elements present in different microdomains. Another contribution to image contrast is diffraction, highly sensitive to changes in the orientation of crystals, when lattice plans are close to Bragg orientation. If the microscope is adequately equipped, selected area electron diffraction (SAED) can be performed on individual crystallites. Unlike SAED, X-ray diffraction of powders always shows an average diffractogram of crystallites possibly of different sizes, shapes and composition. High resolution TEM (HRTEM) allows for resolution of columns of individual atoms. Columns are the result of interference between incident and scattered electron waves.[19]

Instrumentation

The transmission electron micrographs were picked out using, JEM-3010 of JEOL. The samples were suspended in ethanolic solution. Thereafter, a small portion of this suspension was mounted with a pipette to a copper grid (3.05 mm), then the grid should be left for while till evaporates the ethanol.

2.3.6. Energy dispersive X-ray spectroscopy (EDX)

EDX device usually coupled to SEM machines and is useful for elemental analysis. In EDX the high energy electron beam is used to ionize atoms by removing core level electrons. The resulting ions are highly unstable and decay within 10^{-13}–10^{-8} s. The electron deficiency in the core orbital is compensated by an electron from an upper level. Excessive energy is emitted as an X-ray photon and/or auger electron. The photon energy is equivalent to the energy difference of the electronic states of the transition. These energies are characteristic for every element therefore allows a qualitative analysis of the sample.

The radiation is converted into electrical signals of energy proportional to the X-ray photons via a semiconductor detector. This technique allows the elements from Be to U to be measured simultaneously. The quantity of an element is determined by comparison of intensities of the sample and a reference. Limitation to EDX is the resolution of about 140 eV in energy. Also the accuracy of quantification is between 1% and 10% depending on the applied correction procedures. With decreasing atomic numbers elements are increasingly difficult to determine quantitatively due to matrix effect.[19]

Instrumentation

EDX measurements for the samples were done using a CamScan scanning electron microscope equipped with EDX system from Noran instruments. The samples were mounted on a holder coated with a carbon film; quantitative measurements for the constituents of the sample were done by single point measurement. Several measurements were done thereafter. For each constituent atom the average of the measurements was then estimated. Either atomic percent or elemental percent for the atomic constituents can be determined.

2.3.7. Adsorption-desorption properties[20]

Adsorption is defined as the selective accumulation and concentration of certain molecules within a vapor or gas flow onto the solid surfaces. Therefore, the adsorbed vapors or gases are referred to as adsorbates and the solid surfaces are called adsorbent.

There are two types of adsorption, physical adsorption (electrostatic attraction between the adsorbate and adsorbent via weak forces, e.g., Van der Waals forces). Chemical adsorption (chemisorption) in which electrons are transferred between the adsorbent and the adsorbate giving rise to formation of chemical bonds through a chemical reaction resulting in an adhesion of the adsorbate molecules.

Porosity: The word pore has a Greek origin; it originates from 'poros', which means passage. A pore represents a pathway between the external and the internal surfaces of a solid, through which materials like gases and vapours can influx into, through or out of the solid. Pores are small cavities exist in the solids allowing vapours and gases to pass. Porosity is a comprehensive term for these pores and their allocation in the structure of a solid.

Table 1. Comparison between physical and chemical adsorption.[21]

	Physical adsorption	*Chemical adsorption*
Heat of adsorption / kJmol^{-1}	20 - 40 c.f. heats of liquefaction	> 80 c.f. bulk-phase chemical reactions
Rate of adsorption (at 273 K)	Fast	Slow
Temperature dependence of uptake (with Increasing T)	Decreases	Increases
Desorption	Easy- by reduced pressure or increased temperature	Difficult - high temperature required to break bonds
Desorbed species	Adsorbate unchanged	May be different to original adsorptive
Specificity	Non-specific	Very specific
Monolayer coverage	Mono or multilayer condition dependent	Monolayer

There are four types of pores (see Figure 4):

- Open pore: is a pore associated with the external surface of a solid and permits the adsorbate to pass through the solid.

- Closed pore: an isolated void into the solid which is not linked to the external surface.

- Transport pores: these acts to link the inner microporosity to the various parts of the external surface of the solid.

- Blind pores: these are linked to the transport pores without leading to any other pore or surface.

Internal and external surfaces can be explained as:

- Internal surface: consists of the area surrounding the closed pores along with all cracks which permeate intensely into the internal of the adsorbent which are profounder than they are wide, and

- External surface: composed of the protrusions and superficial cracks which in this case are wider than they are deep.

o- Open pores

c- Closed pores

t- Transport pores

b- Blind pores

Figure 4. Different types of porosity.[20]

Classification of pores

- ♦ According to IUPAC pores are classified relative to their width as follows:[22]
  - o Micropores: < 2 nm
  - o Mesopores: 2 - 50 nm
  - o Macropores: > 50 nm
- ♦ Microporosity may be subdivided into three categories:[23]
  - o Ultramicropores: < 0.5 nm
  - o Micropores: 0.5 - 1.4 nm
  - o Supermicropores: 1.4 - 2.0 nm

Classification of adsorption isotherms (see Figure 5)[24]

Six types of adsorption isotherms are known including:

   Type I isotherm. This is characteristic of the adsorbents having a mostly microporous structure, since the most of the filling for such micropore occurs at relative pressures less than 0.1. At a partial pressure of ~0.5 normally the adsorption process complete. As an example for this type the adsorption of nitrogen on carbon at 77 K and ammonia on charcoal at 273 K.

   Type II isotherm. This type represents the case of the physical adsorption of gases over the surfaces of non-porous solids. Coverage of the monolayer occurs at first thereafter at high relative pressures coverage with multilayers occurs subsequently, e.g., adsorption on carbons having mixed micro- and meso-porosity.
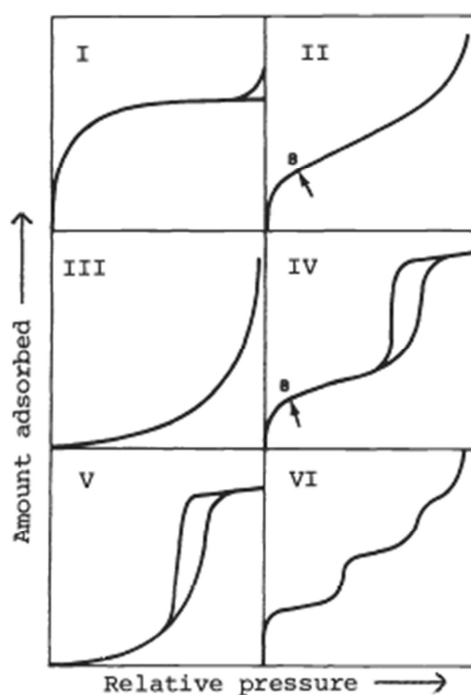

Figure 5. Diagrammatic representation of isotherm types.[24]

   Type III isotherm. The obtained plot is cambered to the relative pressure axis. This type is typical for weak adsorbate-adsorbent interactions[25] and is widely related to both non-porous and microporous adsorbents. Low uptakes at low relative pressures will be the result of the weak interactions between the adsorbate and the adsorbent. Nevertheless, after the adsorption of a molecule on the primary sites, the adsorbate-adsorbate interaction (much stronger) gets the driving force of the adsorption process. Consequently, acceleration of the uptakes will occur at higher relative pressure. At high partial pressures this complementary type of

adsorption represents a cluster, e.g., the adsorption of water molecules over carbon where the primary adsorption sites are oxygen based.

Type IV isotherm. This type is characterized by presence of a hysteresis loop, which is usually connected with the presence of mesoporosity. The shape of which is unique to each adsorption system, hysteresis loop is a result of the capillary condensation.[24] As well as these isotherms show a limited uptake at high relative pressures. Figure 6 demonstrates the various shapes of hysteresis loops that can be seen within this type of isotherm.
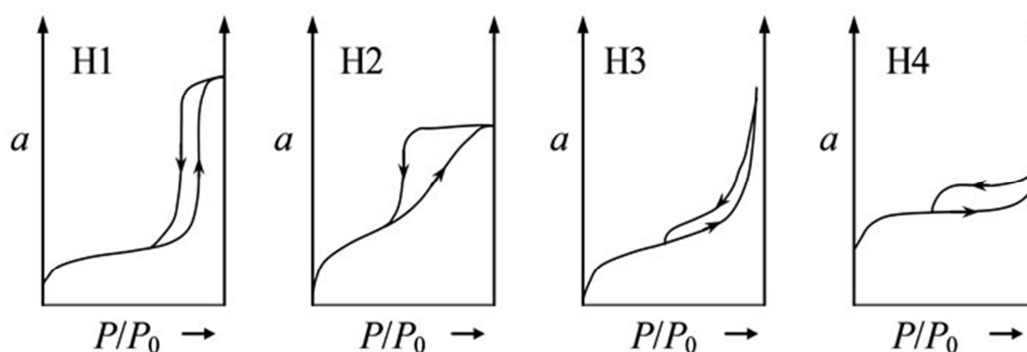

Figure 6. *Hysteresis loops in type IV isotherms according to the IUPAC classification.[26]*

Hysteresis loop: two reverse procedures are included in the adsorption process, i.e., condensation and evaporation of condensed gas. In fine pores, evaporation of the condensed gas does not happen as readily as its condensation. This is a result of the higher possibility of re-condensing a molecule evaporating from a highly curved meniscus than one evaporating from a plane surface. There are four different types of hysteresis:[24]

Type H1 loops characterize the porous materials known to comprise agglomerates or compacts of almost uniform spheres in totally regular array. Therefore, they will have narrow distributions of pore size.

Type H2 loops can be represented by some corpuscular systems (e.g., silica gels), the distribution of pore size and shape is not well-defined. Really, the H2 loop is principally difficult to interpret. In the past it was ascribed to the divergence in the mechanism of condensation and evaporation processes taking place in pores possessing narrow necks and wide bodies (normally referred to as 'ink bottle' pores). However, now it is realized that this gives an over-simplified picture and the role of network impacts must be taken into account.

Type H3 loops these types do not show any limiting adsorption at high p/p°. They can be seen with aggregates of plate-like particles leading to slit-shaped pores.

Type H4 loops are associated with narrow slit-like pores, however in these cases the Type I isotherm character is indicative of microporosity.

Type V isotherm. This characterize also weak adsorbate-adsorbent interactions.[25] The isotherms are convex to the relative pressure axis. These isotherms are suggestive of microporous or mesoporous solids. The shape of this class of isotherms can be explained on the basis of the same reasons as those for Type III and can also exemplify by water adsorption on carbon.

Type VI isotherm. This type presented firstly as a hypothetical isotherm. The shape of which arises from the complete coverage of monomolecular layers prior to the evolution to a subsequent layer. It has been suggested, by Halsey,[27] that the isotherms originate from the adsorption on tremendously homogeneous, non-porous surfaces where the monolayer capacity relates to the step height. The only example recognized for this type is the adsorption of krypton on carbon black (graphitized at 3000 K) at 90 K.[28]

Measurement of surface area[24]

The Brunauer-Emmett-Teller (BET) gas adsorption technique has come to be the most commonly used standard procedure for the determination of the surface area of finely-divided and porous materials, despite the oversimplification of the model on which the theory is based. It is customary to apply the BET equation in the linear form

$$\frac{p}{n^a \cdot (p^o - p)} = \frac{1}{n^a_m \cdot C} + \frac{(C-1)}{n^a_m \cdot C}\frac{p}{p^o}$$

Where n^a is the amount adsorbed at the relative pressure p/p^o, n^a_m is the monolayer capacity and C is the BET constant.

The BET equation requires a linear relation between p/n^a (p^o—p) and p/p^o (i.e., the BET plot). The range of linearity is restricted to a limited part of the isotherm, usually not outside the p/p^o range of 0.05—0.30. The second stage in the application of the BET method is the calculation of the surface area (often termed the BET area) from the monolayer capacity. This requires knowledge of the average area, a_m (molecular cross-sectional area), occupied by the adsorbate molecule in the complete monolayer. Thus

$$A_s \text{ (BET)} = n^a_m \cdot L \cdot a_m$$

and

$$a_s \, (\text{BET}) = A_s \, (\text{BET}) \, / m$$

where A_s (BET) and a_s (BET) are the total and specific surface areas, respectively, of the adsorbent (of mass m) and L is the Avogadro constant.

Instrumentation

All BET measurements in our work were performed on a Micromeritics ASAP 2020 automated system. After degasing of the samples using a mixture of N_2-He gases for appropriate time and under suitable temperature, nitrogen adsorption-desorption behaviors were studied.

Densities of the pre-weighted materials were measured using Micromeritics AccuPyc II 1340. He gas was employed for this purpose.

2.3.8. Thermal analysis[29]

Thermal Analysis (TA) represents techniques in which the properties of materials are studied as a function of temperature. Thermal analysis can be classified according to the property that changes with temperature to:

- Thermogravimetric analysis (TGA): mass
- Differential thermal analysis (DTA): temperature difference
- Differential scanning calorimetry (DSC): heat difference
- Pressurized TGA (PTGA): mass changes as function of pressure
- Thermo mechanical analysis (TMA): deformations and dimension
- Dilatometry (DIL): volume
- Evolved gas analysis (EGA): gaseous decomposition products

In TGA mass changes are recorded as a function of temperature. The measured thermogram gives information on changes in sample composition, thermal stability and kinetic parameters for chemical reactions in the sample. Mass changes can be monitored with some process, e.g., physically; gas adsorption, gas desorption and phase transitions (vaporization or sublimation) or chemically; decomposition, break down reactions, gas reactions and chemisorption. TGA can be used for determination of thermal stability, material purity and humidity, as well as for corrosion studies and for examination of gasification processes.

The temperature at which the decomposition of the sample occurs can be affected by heating rate and sample size, whereas, the progress of the reaction can be influenced by particle size of sample, packing, crucible shape and gas flow rate.

In DTA the temperature difference between sample and reference material is recorded as a function of temperature or time. Thermogram in DTA consists of peaks that appear as exothermic or endothermic ones.

The processes give rise to changes in heat / temperature can be physical process such as adsorption (exothermic), desorption (endothermic), a change in crystal structure (endo – or exothermic), crystallization (exothermic), melting (endothermic), vaporization (endothermic) and sublimation (endothermic). Chemical phenomena such as oxidation, reduction, break down reactions (endo – or exothermic), chemisorption (exothermic) and solid state reactions (endo – or exothermic) can be studied with DTA.

Coupled techniques such as (TGA-DTA) give rise to a comprehensive study of a materials thermal behavior.

The idea of DSC is similar to that of DTA, the difference between them is that DTA measures a difference in temperature while DSC allows for the direct measurement of a change in enthalpy. DTA as mentioned before measures the variation in temperature between the sample and reference (which suffers no phase changes) as the furnace goes through a computer controlled temperature program. Firstly, the temperatures of both the sample and reference material change (increase or decrease) uniformly till the sample reaches a point that it undergoes a phase change, which is either endothermic or exothermic. Secondly, the difference in temperature is recorded. Although useful information is gained using DTA, there are several drawbacks to the technique which result in making it difficult to quantify the results and obtain information regarding the enthalpy of the sample transitions.[30] These difficulties were overcome with the development of DSC. DSC is defined as a technique where the heat flow rate difference into a sample and reference material is measured.

Instrumentation

TGA/DTA were carried out using NETZSCH-TGA/ STA 409 CD device, under air atmosphere as well as under Argon flow from ambient temperature to 1000 °C and 800 °C, respectively, at heating rate of 5 K/min. The sequence of decomposition under both conditions was elucidated by running the chemical analysis after termination of the TG analysis at the end of each mass loss.

2.3.9. Magnetism[31]

Magnetism arises mainly from the orbital and spin motions of electrons and the way how these electrons interact with one another.

The magnetic behavior of materials can be classified into five major groups; diamagnetism, paramagnetism, ferromagnetism, ferrimagnetism and antiferromagnetism.
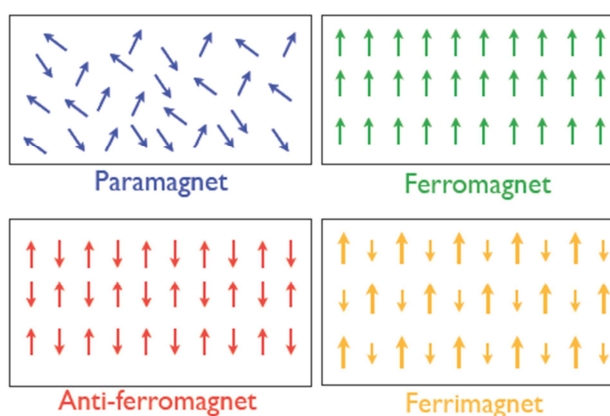

Figure 7. *A graphical summary of the different types of magnetic phenomena.[32]*

Diamagnetic substances consist of atoms which have no net magnetic moments (all orbital are fully occupied and no unpaired electrons can exist). Nevertheless, when subjected to a field, a negative magnetization is created and therefore the susceptibility is negative. From the plot M vs H, we can see:
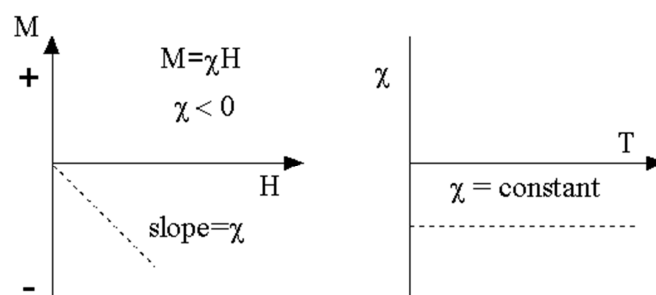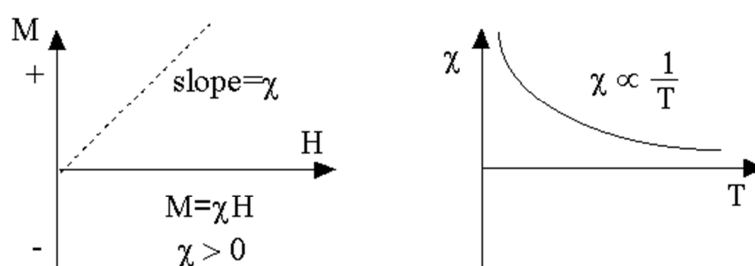

Diamagnetism[31]

Note that the magnetization is zero when the applied field is zero. In diamagnetic materials the susceptibility does not depend on the temperature.

Paramagnetism: as a result of the presence of unpaired electrons in partially filled orbitals, some of the atoms or ions in the material possess a net magnetic moment. Nevertheless, the discrete magnetic moments do not exhibit magnetic interaction. In the absence of external

field the magnetization is zero. As the field is applied, a partial alignment of the atomic magnetic moments arises in the direction of the field, resulting in a net positive magnetization and positive susceptibility. Moreover, the efficacy of the field in aligning the moments is counteracted by the randomizing impacts of temperature. This leads to a temperature dependent susceptibility (Curie Law).

The paramagnetic susceptibility is small at normal temperatures and in moderate fields (but larger than the diamagnetic contribution). Except for the cases at which either the temperature is very low (<<100 K) or the field is very high, paramagnetic susceptibility is independent of the applied field.


Paramagnetism[31]

Ferromagnetism: in these materials the atomic moments are interacting very strongly. The interactions arise from electronic exchange forces and lead to a parallel or antiparallel alignment of atomic moments. Exchange forces are enormous, comparable to a field in order of 1000 Tesla, or just about a 100 million times the strength of the earth's field. The exchange force (quantum mechanical phenomenon) arises from the relative orientation of the spins of two electrons. Ferromagnetic materials show parallel alignment of moments causing a large net magnetization even in the lack of a magnetic field.

Ferromagnetic materials are characterized by presence of three distinguished features:

(1) Spontaneous magnetization,

(2) Existence of magnetic ordering temperature and

(3) Hysteresis

Spontaneous magnetization

Spontaneous magnetization represents the net magnetization that occurs into a uniformly magnetized microscopic volume in the lack of a field. At 0 K, the magnitude of this magnetization is depending on the spin magnetic moments of electrons.


Ferromagnetism[31]
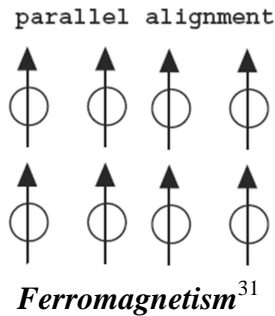
Saturation magnetization

Represents the maximum induced magnetic moment that can be produced in a magnetic field (Hsat); no further increase in magnetization occurs beyond this field. Saturation magnetization is a substantial property, does not depend on the particle size and depend on temperature.

Hysteresis

After the removal of the applied field ferromagnets can preserve some of it, this behavior is termed hysteresis. The plot of the relation of the variation of magnetization versus the magnetic field is called a   hysteresis loop.
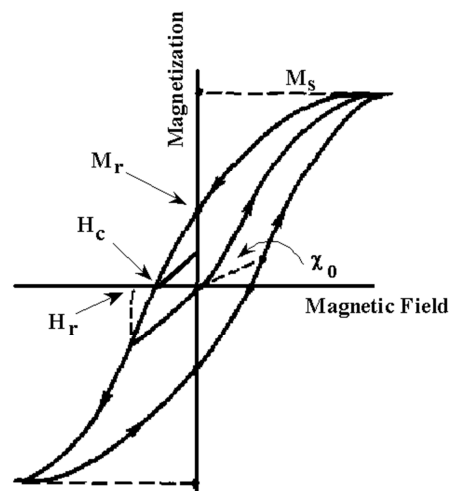
Hysteresis loop[31]

Saturation magnetization (Ms) can be measured by applying a magnetic field of very high strength, which is generally adequate to saturate most magnetic minerals.

When the field is removed, the magnetization does not fall to zero but keep it up as a **saturation remanence (Mr)**. By decreasing the field, the induced magnetization decreases.

Coercivity (Hc), represents the field where the induced magnetization is zero. Further decrease of the field results in saturation again but in the negative direction.

Coercivity of remanence (Hr): This is the reverse field which, when applied and then removed, reduces the saturation remanence to zero (always Hr >Hc).

The initial susceptibility (χ_0) represents the magnetization detected in low fields, as low as of the earth's field (50-100 μT).

The different hysteresis parameters are not merely intrinsic properties; they depend on the grain size, domain state, stresses, and temperature.

Curie temperature[33,34]

Curie temperature (Tc), or Curie point, is the temperature where a material's permanent magnetism changes to induced magnetism or the critical point where a material's intrinsic magnetic moments change direction.

For low levels of magnetization, the magnetization of paramagnets follows what is known as Curie's law, at least approximately. This law indicates that the susceptibility of paramagnetic materials is inversely proportional to their temperature, i.e., materials become more magnetic at lower temperatures. The mathematical expression is:

$$M = \chi H = \frac{C}{T} H$$

M : The resulting magnetization

χ : Magnetic susceptibility

H : Auxiliary magnetic field, measured in ampere/meter

T : Absolute temperature, measured in kelvin

C : A material-specific Curie constant

For a paramagnetic ion with non-interacting magnetic moments with angular momentum J, the Curie constant is related the individual ions' magnetic moments,

$$C = \frac{N_A}{3k_B}\mu_{eff}^2 \text{ where } \mu_{eff} = g\mu_B\sqrt{J(J+1)}$$

μ_{eff} is interpreted as the effective magnetic moment per paramagnetic ion. N_A Avogadro's number, k_B Boltzmann's constant, μ_B the Bohr Magneton and g is the Landé g-factor.

When orbital angular momentum contributions to the magnetic moment are small, as occurs for most organic radicals or for octahedral transition metal complexes with d^3 or high-spin d^5 configurations, the effective magnetic moment takes the form (g = 2.0023... ≈ 2),

$$\mu_{eff} \simeq 2\sqrt{S(S+1)}\mu_B = \sqrt{n(n+2)}\mu_B$$

Where n is the number of unpaired electrons and S is the spin quantum number.

Curie's law is valid under the commonly encountered conditions of low magnetization ($\mu_BH \lesssim k_BT$), but does not apply in the high-field/low-temperature regime where saturation of magnetization occurs ($\mu_BH \gtrsim k_BT$) and magnetic dipoles are all aligned with the applied field. When the dipoles are aligned, increasing the external field will not increase the total magnetization since there can be no further alignment.

The Curie point is seen as a phase transition between a ferromagnet and a 'paramagnet'. The word paramagnet now merely refers to the linear response of the system to an applied field, the temperature dependence of which requires an amended version of Curie's law, known as the **Curie–Weiss law**:

$$M = \frac{C}{T-\theta}H$$

θ describes the exchange interaction that is present albeit overcome by thermal motion. The sign of θ depends on whether ferro- or antiferromagnetic interactions dominate and it is seldom exactly zero, except in the dilute, isolated cases.

Ferrimagnetism: The moments are aligned oppositely (in the absence of an applied magnetic field) and have different magnitudes due to being made up of two different paramagnetic ions. Materials are only ferrimagnetic below their materials corresponding Curie temperature.

Antiferromagnetism: The moments are aligned oppositely and have the same magnitudes resulting in a zero magnetic moment and a net magnetism of zero at all temperatures below the Néel temperature. Materials are only antiferromagetic below their corresponding Néel

temperature. This is similar to the Curie temperature as above the Néel temperature the material undergoes a phase transition and becomes paramagnetic.
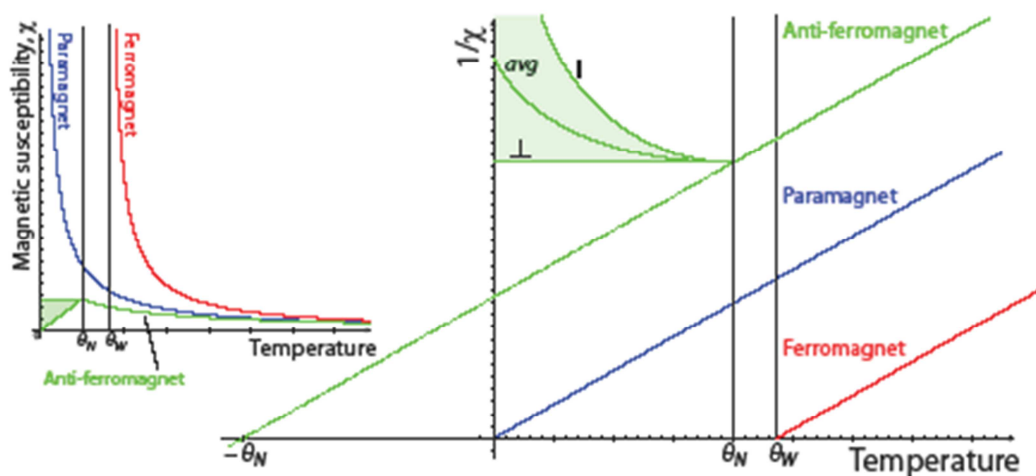

Figure 8. *Magnetic susceptibility as a function of temperature for different types of magnetic material.[32]*

Instrumentation

The magnetic measurements were performed on the SQUID magnetometer using Quantum Design MPMS and generally carried out in a temperature range of 5-350 K and field strengths from 50 to 20,000 Oersted.

For the field-dependent measurements, a definite amount of the sample is fixed between two Scotch-tape strips. To determine the magnetic moment a greater amount of sample (up to 100 mg) was transferred into a gelatine capsule and then measured magnetically.

All the magnetic measurements were done by Clemens Pietzonka.

References

1. Zhang, Y. C.; Qiao, T.; Hu, X. Y. Preparation of Mn_3O_4 nanocrystallites by low-temperature solvothermal treatment of gamma-MnOOH nanowires. *J. Solid State Chem.* **2004,** *177* (11), 4093-4097.

2. Zhang, Y. C.; Qiao, T.; Hu, X. Y.; Zhou, W. D. Simple hydrothermal preparation of gamma-MnOOH nanowires and their low-temperature thermal conversion to beta-MnO_2 nanowires. *J. Cryst. Growth* **2005,** *280* (3-4), 652-657.

3. Li, Z.; Bao, H.; Miao, X.; Chen, X. A facile route to growth of gamma-MnOOH nanorods and electrochemical capacitance properties. *J. Colloid Interface Sci.* **2011,** *357* (2), 286-291.

4. Urban, P.; Lukás, E.; Pelclová, D.; Fenclová, Z.; Dlasková, Z. 485 Neurological and neurophysiological follow-up on workers with severe chronic exposure to toluene. *Toxicol. Lett.* **2003,** *144, Supplement 1* (0), s130.

5. Miyagi, Y.; Shima, F.; Ishido, K.; Yasutake, T.; Kamikaseda, K. Tremor induced by toluene misuse successfully treated by a Vim thalamotomy. *J. Neurol. Neurosurg. Psychiatry* **1999,** *66* (6), 794-796.

6. Hazardous Substance Fact Sheet. *http://nj.gov/health/eoh/rtkweb/documents/fs/0759. pdf* **2011**. (**Last access 21-10-2014**)

7. Portehault, D.; Cassaignon, S.; Baudrin, E.; Jolivet, J. P. Structural and morphological control of manganese oxide nanoparticles upon soft aqueous precipitation through MnO_4^-/Mn^{2+} reaction. *J. Mater. Chem.* **2009,** *19* (16), 2407-2416.

8. Cao, X.; Wang, N.; Wang, L.; Mo, C.; Xu, Y.; Cai, X.; Lin, G. A novel non-enzymatic hydrogen peroxide biosensor based on ultralong manganite MnOOH nanowires. *Sens. Actuators, B* **2010,** *147* (2), 730-734.

9. Wang, X.; Li, Y. D. Synthesis and formation mechanism of manganese dioxide nanowires/nanorods. *Chem. Eur. J.* **2003,** *9* (1), 300-306.

10. Kalubarme, R. S.; Cho, M. S.; Yun, K. S.; Kim, T. S.; Park, C. J. Catalytic characteristics of MnO_2 nanostructures for the O_2 reduction process. *Nanotechnol.* **2011,** *22* (39), 395402.

11. X-ray Diffraction. *http://web. pdx. edu/~pmoeck/phy381/Topic5a-XRD. pdf* **2015**. (**Last access 27-1-2015**)

12. X-ray crystallography. *http://en.wikipedia.org/wiki/X-ray_crystallography#X-ray_analysis _of_crystals* **2015**. (**Last access 28-1-2015**)

13. Scherrer, P. Bestimmung der größe und der inneren struktur von kolloidteilchen mittels Röntgenstrahlen. *Göttinger Nachrichten Gesell.* **1918,** *2*, 98.

14. Rietveld refinement. *http://en.wikipedia.org/wiki/Rietveld_refinement* **2014**. **(Last access 27-1-2015)**

15. Infrared spectroscopy. *http://en. wikipedia. org/wiki/Infrared_spectroscopy* **2015**. **(Last access 28-1-2015)**

16. Christy, A. A.; Ozaki, Y.; Gregoriou, V. G. *Modern Fourier Transform Infrared Spectroscopy;* Elsevier: 2001; Vol. Bd. 35.

17. Ferraro, J. R.; Nakamoto, K.; Brown, C. W. *Introductory Raman Spectroscopy;* Academic Press: 2003.

18. Introduction to Raman Spectroscopy. *http://www.nicoletcz.cz/userfiles/file/Aplikace/ Introduction to Raman. pdf* **2003**. **(Last access 3-9-2014)**

19. Mermet, J. M.; Otto, M.; Kellner, R.; Cases, M. V. *Analytical chemistry: a modern approach to analytical science;* Wiley-VCH: 2004.

20. Porosity and sorption behaviour. *http://personal.strath.ac.uk/ashleigh.fletcher/ adsorption. htm* **2008**. **(Last access 2-9-2014)**

21. Atkins, P. W. *Physical Chemistry;* 5th ed.; Oxford University Press: Oxford: 1994.

22. Everett.D.H. Manual of symbols and terminology for physicochemical quantities and units. Appendix II. Definitions, terminology, and symbols in colloid and surface chemistry. *Pure Appl. Chem.* **1972,** *31* (4), 577-638.

23. Köchling, K. H.; McEnaney, B.; Müller, S.; Fitzer, E. International committee for characterization and terminology of carbon. *Carbon* **1985,** *23* (5), 601-603.

24. Sing, K. S. W.; Everett, D. H.; Haul, R. A. W.; Moscou, L.; Pierotti, R. A.; Rouquerol, J.; Siemieniewska, T. Reporting physisorption data for gas/solid systems with special reference to the determination of surface area and porosity. *Pure Appl. Chem.* **1985,** *57* (4), 603-619.

25. Kiselev, A. V. Adsorption properties of hydrophobic surfaces. *J. Colloid Interface Sci.* **1968,** *28* (3–4), 430-442.

26. Weilun Wang; Peng Liu ; Ming Zhang; Jiashan Hu; Feng Xin The pore structure of phosphoaluminate cement. *J. Compos. Mater.* **2012,** *2* (3), 104-112.

27. Halsey, G. Physical adsorption on nonuniform surfaces. *J. Chem. Phys.* **1948,** *16*, 931-937.

28. Krätschmer, W.; Rathouský, J.; Zukal, A. Adsorption of krypton at 77K on fullerene C60, graphitized carbon black and diamond. *Carbon* **1999,** *37* (2), 301-305.

29. Hatakeyama, T.; Quinn, F. X. *Thermal analysis: fundamentals and applications to polymer science;* Wiley: 1999.

30. Sesták, J. *Thermal Analysis (Vol. XII, Part D)/Thermophysical Properties of Solids;* Elsevier: 1984.

31. Bruce M. M. Hitchhiker's Guide to Magnetism. *http://www. irm. umn. edu/hg2m/hg2m. pdf* **1991**. **(Last access 13-10-2014)**

32. John JL M. Magnetic properties of materials. *http://www. ucl. ac. uk/qsd/people/ teaching/MPM-Part2* **2012**. **(Last access 13-10-2014)**

33. Curie temperature. *http://en. wikipedia. org/wiki/Curie_temperature* **2014**. **(Last access 13-10-2014)**

34. Paramagnetism. *http://en. wikipedia. org/wiki/Paramagnetism* **2014**. **(Last access 13-10-2014)**

Chapter 3

Synthesis, grain growth and physical properties of manganese

oxyhydroxide nanocrystals

3. Introduction

One of the most significant problems associated with the synthesis of manganese oxide/ hydroxide nanoparticles is the phase control over the final product. This problem arises mainly from the presence of various oxidation states for manganese, hence, many oxide/hydroxide phases are available. Diverse structural arrangements of the basic units in the structure of such oxides will result in various polymorphs. These polymorphs can be distinguished simply by denoting the oxide/hydroxide phase Greek letters, i.e., α-, β-, γ-, δ-, ε- and λ.[1,2]

Although, numerous reports were issued for the synthesis and applications of manganite nanoparticles (γ-form manganese oxyhydroxide), nevertheless, few work was reported for feitkenchtite (β-form). Actually, limited synthetic routes were presented for the preparation of feitknechtite.[3,4]

Accordingly, our research study in this chapter will focus on how to manage a simple and reliable reaction for synthesis of various manganese oxyhydroxide polymorphs, particularly, feitknechtite and manganite.

As previously mentioned in chapter 1 many preparative methods were reported for the synthesis of single-size manganite nanoparticles. Yet, there is no method described for the achievement of a systematic variation of their particle size.

Consequently, size-selective experiments will be accomplished here with the purpose of synthesis of manganite nanocrystals with variable grain size by carrying out the comproportionation reaction between Mn^{2+} and MnO_4^- in aqueous media. The molar ratio will be chosen as 5:1, a slight excess of Mn^{2+} salt will be used (in comparison with the following equation) to ensure the formation of single phase of manganite.

$$4\,Mn^{2+} + MnO_4^- + 6\,H_2O \rightarrow 5\,\gamma\text{-MnOOH} + 7\,H^+$$
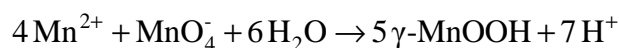
So far, no study reveals the impact of the anion of manganese salt on the morphological shape of the so obtained manganite nanorods. In this chapter we will display how the usage of different manganese salts can affect the rod shapes of as-prepared manganite. In our work and for the first time (to the best of our knowledge) ultra-long manganite nanorods are synthesized from the comproportionation reaction of either manganese chloride or sulphate with $KMnO_4$. Crystallographic data for manganese oxyhydroxide polymorphs are shown in Table 1.

Table 1. Crystallographic data of manganese oxyhydroxide polymorphs.

Compound	*Mineral name*	*Crystal system*	*Z*	*Cell parameters / Å*	*Features*
γ-MnOOH	Manganite	Monoclinic $P2_1/c$	4	a = 5.304 b = 5.277 c = 5.304 $\beta = 114.38°$	1x1 tunnels
α-MnOOH	Groutite	Orthorhombic Pnma	4	a = 10.667 b = 2.871 c = 4.554	1x2 tunnels
β-MnOOH	Feitknechtite	Hexagonal $P\bar{3}m1$	1	a = 3.32 c = 4.71	1x∞ layers

3.1. Sample characterization

3.1.1. XRD analysis

The obtained γ-MnOOH nanoparticles were examined preliminary by means of XRPD analysis. XRD pattern (Figure 1) of the sample SM1 prepared by method 1 (see experimental part) from $Mn(OAc)_2$ under reflux conditions for 17 h indicates that all reflections as compared to ICSD-84949 are well indexed to x-ray single phase manganite. The lattice parameters for this sample a = 5.309(1) Å, b = 5.2903(3) Å, c = 5.319(1) Å and β= 114.424(4)° are consistent with those found in literature as a = 5.304(1) Å, b = 5.277(1) Å, c = 5.304(1) Å and β = 114.38(2)°.[1] From the pattern it can be seen that the reflections are sharp and intense, reflecting high crystallinity for the obtained product. The mean particle size was calculated from the full width at half maximum (FWHM) and line positions (2θ) using Scherrer's equation. Reflection (11-1), (020), (220) and (131) were used for calculation of the mean particle size <d> which was found to be 21.5 nm. To the best of our knowledge this is the first time that nc γ-MnOOH are synthesized utilizing method 2 through modification of the initial pH of the reaction (by refluxing of either $MnCl_2$ or $MnSO_4$ and $KMnO_4$ in aqueous medium and modifying the reaction pH to 6 using NaOH). Manganite samples SM2 (prepared using $MnCl_2$) and SM3 (prepared using $MnSO_4$) were checked also by XRD. The patterns (Figure 2) indicate that pristine manganite samples are obtained, with average particle size <d> of ~24 nm.
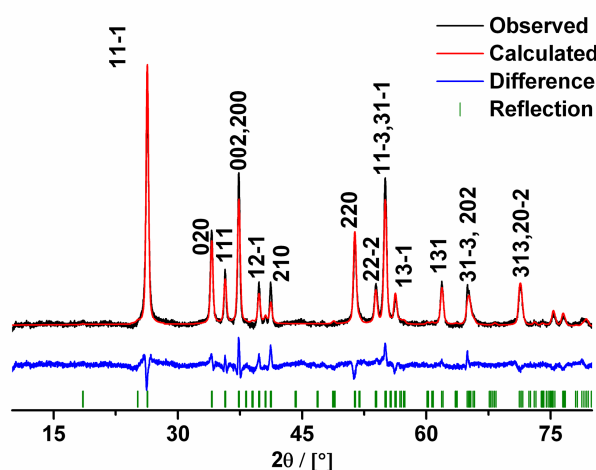

Figure 1. *Rietveld refinement and Laue indices for γ-MnOOH sample (SM1) obtained by refluxing $Mn(OAc)_2.4H_2O$ and $KMnO_4$ (5:1) in aqueous medium for 17 h at 110 °C, total Mn concn. of 13 mmol L^{-1} was used. <d> = 21.5 nm.*

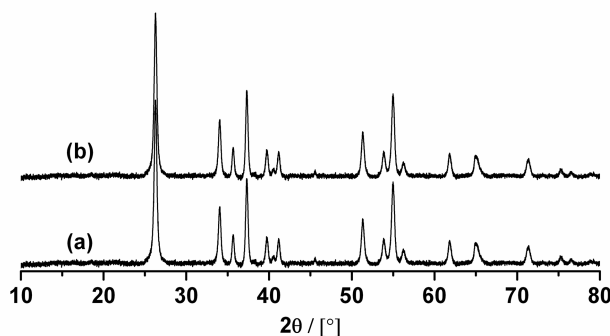***Figure 2.*** *XRD patterns of γ-MnOOH samples obtained by refluxing a) MnCl₂.4H₂O (SM2) or b) MnSO₄.H₂O (SM3) with KMnO₄ (5:1) in aqueous medium (17 h, 110 °C, total Mn concn. of 13 mmol L⁻¹ and pH ~8). <d> = 24 nm.*

3.1.2. IR spectroscopy

   The samples of γ-MnOOH were further characterized by means of IR spectroscopy. IR spectra (Figures 3&4) show two sets of bands between 400-700 and 1000-1200 cm⁻¹ which are assigned to Mn-O stretching vibrations and O-H bending modes (γ-OH, δ-2-OH, δ-1-OH), respectively.[5] The broad bands at 2550 - 2680 cm⁻¹ are attributed to OH stretching vibration weakened due to hydrogen bonds O—H…O, whereas the peak located in the range 2065-2075 cm⁻¹ could be considered as a combination band of the OH-stretching mode at 2550-2680 cm⁻¹ (f_1) and the excited lattice mode at 589 cm⁻¹ (f_2). Thus, by $f = f_1 - f_2$; i.e., 2661 – 589 = 2072 cm⁻¹, the value obtained is close to the reported 2060 cm⁻¹ by Kohler and coworkers.[1]

   IR spectrum of SM1 shows tiny absorption bands in the range of 1350-1670 cm⁻¹. These can be assigned to symmetric and asymmetric carbonyl stretching vibrations of residual acetate groups.[6] This observation can be attributed to the presence of subtle excess of unreacted manganese acetate adsorbed over the surface of manganite nanocrystals. IR spectrum of the sample SM2 displays a sharp absorption band locates at ~3400 cm⁻¹. This band is attributed to OH stretching vibration of the residual NaOH used for pH modification.[7]

   Comparison of the IR data for the obtained manganite samples with those found in literature was done and the data are placed in Table 2. Good agreement between both is obvious.[8] The remarkable shifts in Mn-O and O-H stretching vibrations from that shown in literature are attributed to the nano-size effect.
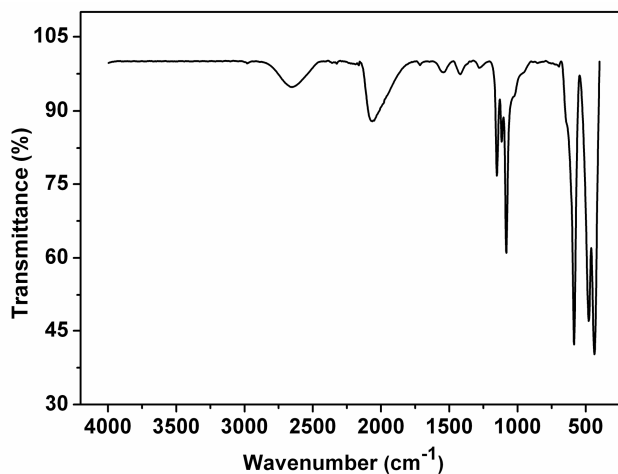
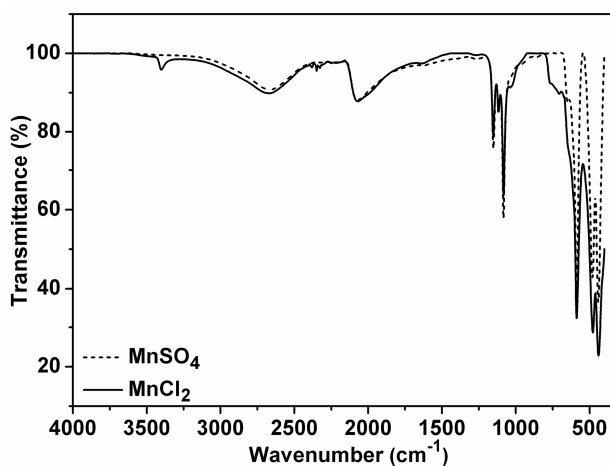***Figure 3.*** *IR spectrum of γ-MnOOH (SM1) prepared by redox reaction between Mn(OAc)$_2$ and KMnO$_4$.*

Figure 4. *IR spectra of γ-MnOOH samples (SM2 and SM3) prepared via redox reaction between MnCl$_2$ or MnSO$_4$ and KMnO$_4$.*

Table 2. Comparison of IR vibrations of manganite samples with those found in literature.

Assignment	*Peak position (cm^{-1})*			
	SM1	*SM2*	*SM3*	*Literature*[8]
Mn-O str.	437, 477, 589	441, 480, 588	440, 470, 588	446, 488, 592
O—H…O bending	1083, 1116, 1152	1083, 1117, 1152	1083, 1117, 1153	1085, 1119, 1152
OH str.	2661	2659	2659	2680
f = f1 – f2	2072	2071	2071	2083

3.1.3. Raman spectroscopy

Further confirmation for the phase purity of so obtained manganite samples was done using Raman spectroscopy. From Raman spectrum of SM1 which is shown in Figure 5, about nine Raman scattering modes located at 149, 220, 260, 288, 360, 389, 530, 558, and 623 cm^{-1} are clearly seen and are matching with those found in literature.[9,10]

γ-MnOOH crystallizes in the monoclinic C_{2h}^5-P2$_1$/c space group and contains four MnOOH formula units per unit cell. All atoms occupy positions with Wyckoff site 4e having site symmetry C_1. The relation between the C_1 site group and the C_{2h} factor group produces 45 optical phonons (after subtracting the K = 0 acoustic modes) of symmetry 12 A_g + 11 A_u +12 B_g + 10 B_u. Practically, not all expected Raman-active modes (12 A_g+12 B_g) can be seen for polycrystalline samples because of low polarizabilities as well as spectral overlap of modes.[11] Moreover, some of the Raman modes might have too little intensity to be observed.[12]
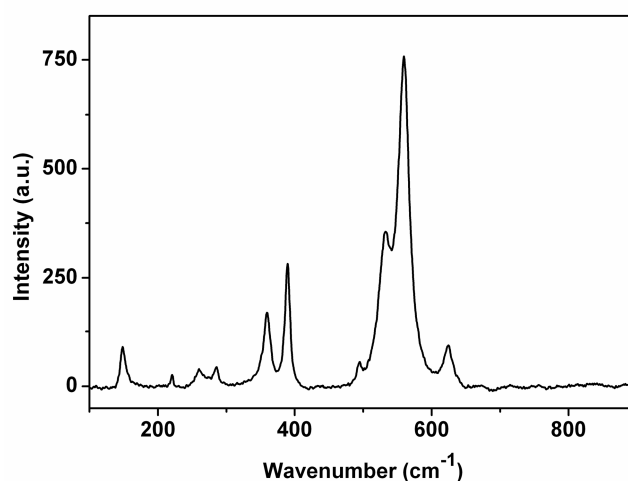

Figure 5. *Raman spectrum of γ-MnOOH (SM1) sample.*

3.1.4. Morphology investigation

3.1.4.1. Scanning electron microscopy (SEM)

Morphological shape of the as-prepared manganite samples was investigated by SEM. From SEM images (Figure 6) a rod-like structure is identified for the samples. It can be seen that the nanorods of SM2 (Figure 6c-d) are much thicker and longer than those of SM1 (Figure 6a-b). The estimated aspect ratio of SM1 sample is in the range 10-20 which is smaller than that of SM2 falling in the range of 40-60. This means that ultra-long nanorods are produced via the second preparative method. The fibrous morphology of the products suggests an anisotropic growth behavior under present experimental conditions. High magnification SEM (Figure 6f) for the manganite sample prepared by refluxing MnSO$_4$ with KMnO$_4$ in aqueous

medium via pH adjustment revealed that it has also rod-like morphology. These rods are uniform throughout their entire length and are longer in length and thicker in diameter than those of SM1. It is worth to mention that SEM is not accurate method for the determination of the diameter of the nanorods. Most of the rods are stacked together and are difficult to be seen separately under the scanning electron microscope, for such purpose TEM is most relevant.
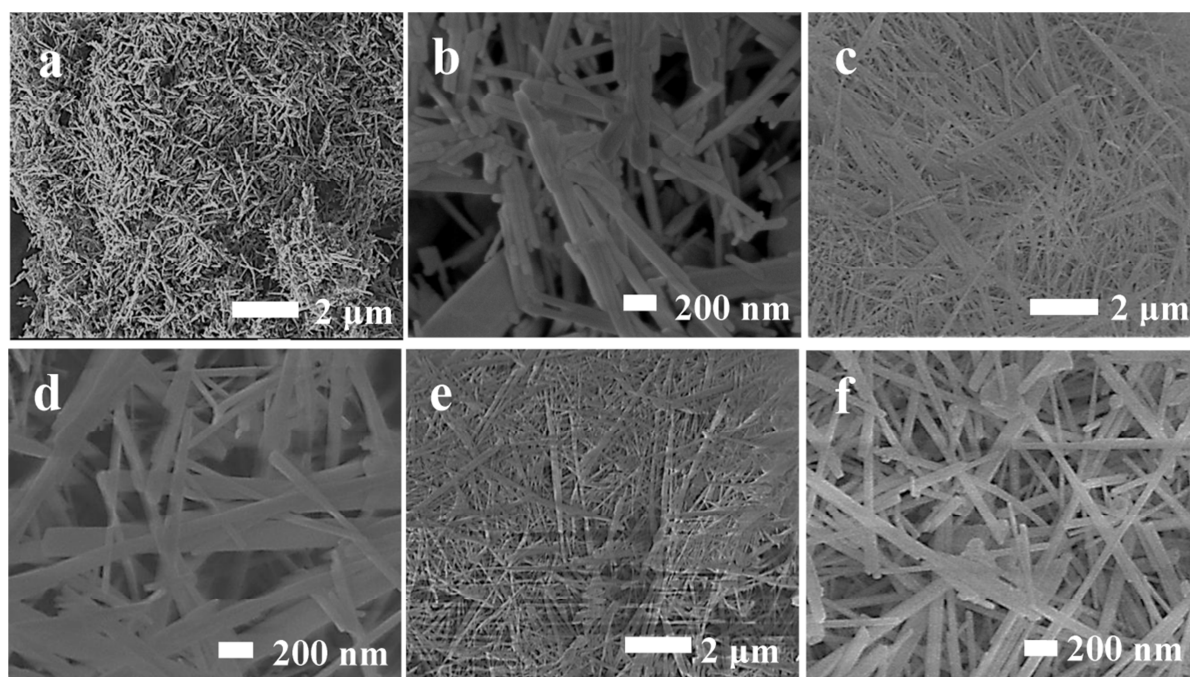

Figure 6. *SEM images of γ-MnOOH samples: a-b) low and high magnification SEM of SM1, c-d) low and high magnification SEM of SM2 and e-f) low and high magnification SEM of SM3.*

3.1.4.2. Transmission electron microscopy (TEM)

Detailed morphological investigation was carried out using TEM and HRTEM. TEM image of the sample SM1 (Figure 7a) reveals a rod-like structure. TEM observations reveal that the nanorods have typical diameters ranging from 5 to 30 nm and lengths of hundreds of nanometers. The average diameter of these nanorods was estimated from size-distribution curve and it is found to be ca. 17 nm. It is apparent from TEM image that manganite nanorods have essentially a uniform diameter throughout their entire lengths. TEM image of SM3 (Figure 7b) shows also a rod-like morphology. From the size distribution curve the average diameter of these nanorods is ~25 nm. Table 3 shows a comparison of the mean particle sizes of SM1 and SM3 estimated from XRD reflections mentioned before with their sizes estimated from the reflection (11-1) and the mean diameters of their rods obtained from TEM analyses. This comparison reveals that the average diameters obtained from TEM analyses are

consistent with the sizes estimated from the reflection (11-1), which corresponds to the growth direction of the diameter of manganite nanorods. Figure 7c depicts HRTEM image of a single γ-MnOOH nanorod from SM3 (aspect ratio ~50) implying its monocrystalline structure. It has a uniform structure with a periodic fringe spacing of 0.346 nm parallel to the longitudinal axis of the nanorod, which corresponds to the interplanar spacing between the (11-1) planes of the monoclinic γ-MnOOH. Therefore, the longitudinal axis of the manganite nanorods corresponds to the b axis of the monoclinic unit cell.
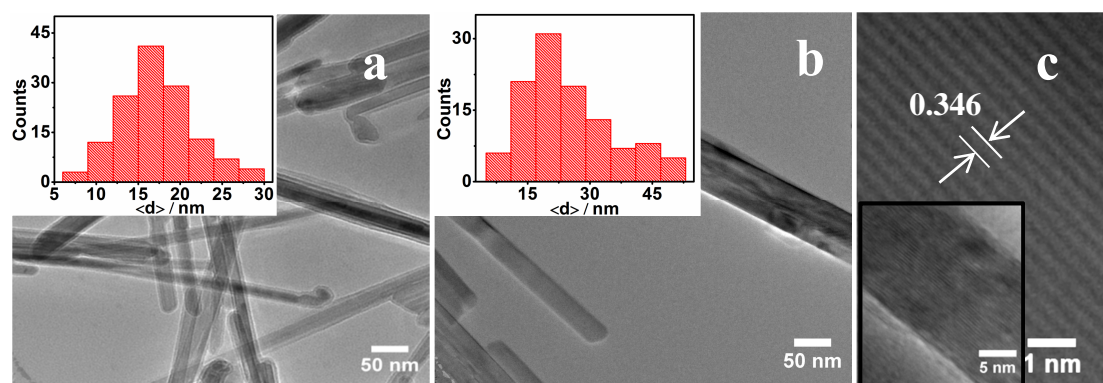

Figure 7. *TEM images of a) SM1 and b) SM3 samples, the insets are their size distribution curves for the rod diameters. c) HRTEM of SM3 sample.*

Table 3. Mean particle sizes of SM1 and SM3 samples estimated from XRD versus the mean diameters of their rods obtained from TEM.

Sample	*Mean size estimated from XRD $<d>$ / nm*	*Size estimated from (11-1) reflection / nm*	*Average diameter from TEM / nm*
SM1	21.5	15	17
SM3	24	22	25

3.1.5. Energy-dispersive X-ray analysis

Compositional analyses were performed for manganite samples which confirm that the structure of nanorods is composed of O and Mn only (H not detectable by EDX). As proven from EDX graphs (not shown here) no corresponding peaks indicating the presence of either Na or K cations. This means that there is no Na or K incorporated into the 1x1 tunnelled (0.24 nm x 0.24 nm) structure of γ-MnOOH. The size of these tunnels is too small to accommodate the large size Na and K cations (K from permanganate salt and Na from sodium hydroxide used for pH modification). For SM2 sample tiny amount of Na cations exists (Table 4) as a result of presence of residual NaOH accumulated over the surface of this sample. Comparison

between the average values obtained for atomic weight percent of O and Mn with those calculated via molecular weight consideration was done. We can notice from Table 4 an agreement between the obtained and theoretical values implying phase purity of the as-prepared samples.

Table 4. Elemental analysis data obtained for SM1 and SM2 samples (from EDX analysis) and their comparison with theoretical values made according to atomic weight percent, standard deviations are shown in parentheses.

Element	*%Found*		*%Theoretical*
	SM1	*SM2*	
Mn	64(6)	61(7)	62.50
O	36(5)	38(5)	36.36
Na	–	0.7(3)	–

3.2. Studying the effect of experimental parameters

The influence of variation of various experimental parameters such as time, temperature, manganese concentration, molar ratio of Mn^{2+}/MnO_4^-, pH of the reaction medium and reaction solvent on phase purity, morphological shape and grain size of the so obtained manganese oxide/hydroxide nanocrystals was studied for the redox reaction between $Mn(OAc)_2$ and $KMnO_4$.

3.2.1. Effect of reflux time

3.2.1.1. On phase purity

The impact of the reflux time on the reaction of $Mn(OAc)_2$ and $KMnO_4$ performed in aqueous medium (molar ratio of Mn^{2+}/MnO_4^- about 5:1, total Mn concn. of 13 mmol L^{-1} and temperature of 110 °C) was studied. After 1 h, large amounts of trivalent manganese are formed in the solution, precipitating in form of oxyhydroxide (γ-MnOOH). Some impurities of tetravalent manganese (MnO_2) coexist. It is seen from XRD pattern shown in Figure 8; few and less intense reflections appear at 2θ ~19, 22 and 24°. These are assigned to MnO_2.

This observation is confirmed by IR analysis. IR spectrum depicted in Figure 9 shows the absorption bands related to manganese oxyhydroxide structure except those located at 761 and 1036 cm^{-1} which are assigned to the presence of MnO_2.[13] When the reaction mixture is refluxed for a time of 3 h, all manganese is precipitated from solution as γ-MnOOH, as

indicated by XRD patterns. The final pH of the reaction solution measured after the separation of the product was found to be ~4.6 (the initial pH value ~6) which is matched with the release of acetic acid as shown in equation 3.

At a reaction time of 3 h, the half redox reactions (1) and (2) are expected to occur. The standard electrode potentials are given.[14]

$$MnO_4^- + 5H^+ + 4e^- \rightarrow \gamma\text{-}MnOOH + 2H_2O \qquad (1) \quad E° = 1.51\ V$$

$$Mn^{2+} + 2H_2O \rightarrow \gamma\text{-}MnOOH + 3H^+ + e^- \qquad (2) \quad E° = -1.51\ V$$

The overall reaction is accordingly:

$$4Mn^{2+} + MnO_4^- + 6H_2O \rightarrow 5\gamma\text{-}MnOOH + 7H^+ \qquad (3)$$

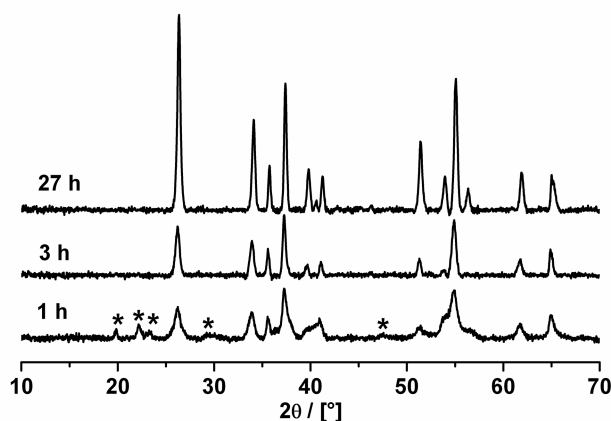***Figure 8.*** *XRD patterns of the samples obtained from the reaction of Mn(OAc)$_2$ with KMnO$_4$ (~5:1) in aqueous medium at 110 °C, total Mn concn. of 13 mmol L^{-1} was used. The reaction mixture was refluxed for different times of 1, 3 and 27 h, <d> = 12, 16 and 23 nm, respectively. Stars: γ-MnO$_2$.*
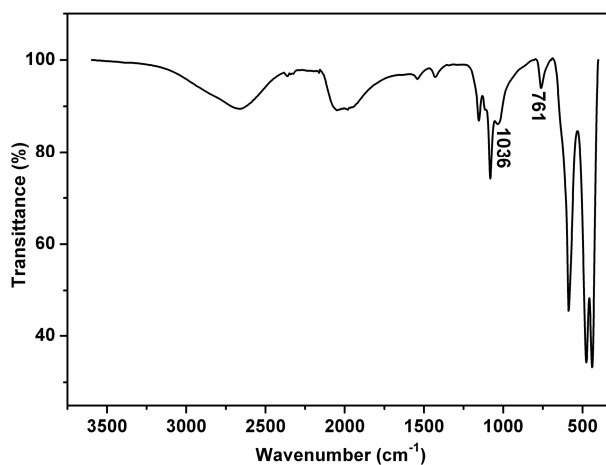

Figure 9. *IR spectrum of the sample (mixture of γ-MnOOH+MnO$_2$) obtained at lower reaction time of 1 h.*

SEM investigation for the as-prepared sample at 1 h (Figure 10) indicates rod-like morphology with few cones present together with those nanorods. The obtained nanorods are too short and thin compared to those of manganite sample prepared at higher reaction time as shown before (Figure 6b).
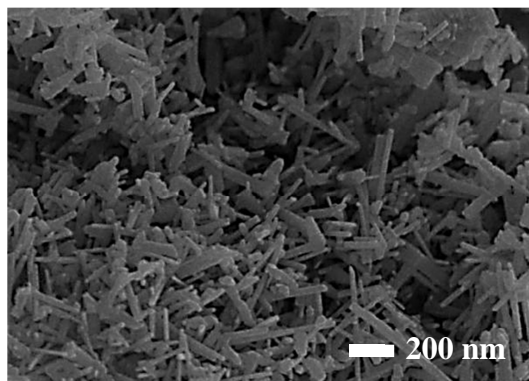

Figure 10. SEM image of the sample obtained after 1 h.

3.2.1.2. On grain size

Starting the redox reaction at a time (reflux time) suitable for the formation of single phase manganite samples further increase in the reaction time leads to grain growth. The other experimental conditions are kept unchanged (temperature of 110 °C and molar ratio of about 5:1 for Mn^{2+}/MnO_4^-). Larger size manganite samples are produced. It is clear from XRD patterns (Figure 8) that the reflections corresponding to the manganite obtained at shorter time are broad and less intense and get narrower and sharper with increasing time. Undeniably grain growth is a time-dependent process, enlargement of the crystallite size occurs via prolongation of the reflux time resulting in manganite samples with larger particle size (i.e., thicker in diameter).

The same effect occurs by variation of the total concentration of manganese in the reaction solution whilst time and temperature of the reaction are kept unchanged. From Figure 11 we can observe that two parameters affect the particle size; reflux time and total manganese concentration in the aqueous solution. Indeed, the growth process is affected by the concentration of the reactants, a lot of nuclei can be formed in this case that can be aggregated readily hence, accelerating the rate of growth and leading to the formation of products with larger size.
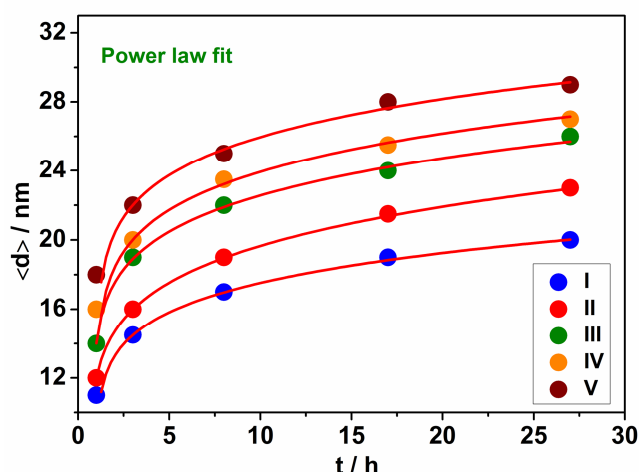
Figure 11. *Variation of the mean particle size <d> (estimated from XRD) of manganite with reflux time and total Mn concentration. The samples were prepared from the redox reaction between Mn(OAc)$_2$ and KMnO$_4$ (5:1) using the same temperature of 110 °C, different times of 1, 3, 8, 17 and 27 h were used. Various total Mn concentrations of I) 5, II) 13, III) 39, IV) 78 and IV) 156 mmol L^{-1} were employed.*

Table 5. Impact of time and total Mn concentration on the mean particle size <d> of manganite samples.

Time / h	Total Mn concn. / mmol L^{-1}				
	5	13	39	78	156
1	11	12	14	16	18
3	14.5	16	19	20	22
8	17	19	22	23.5	25
17	19	21.5	24	25.5	28
27	20	23	26	27	29

Through control of the time and total Mn concentration in the solution, single phase manganite samples with lower particle size of 14 nm (1 h, 39 mmol L^{-1}) are obtained, as well as manganite samples with larger size of 29 nm (27 h, 156 mmol L^{-1}) are produced (Table 5). The power law fit applied to the data obtained for the variation of the mean particle size <d> with time showed that, manganite particles grow with time t (whilst the other parameters are held at constant) according to the equation:

$$<d> = k(t+a)^{1/n}$$

where <d>: the average particle size, t: the reaction time, k: temperature-dependent time constant, a: additional parameter, corresponding to the quotient d_0^n/k with d_0 as particle size at time t = 0 and n: the order of growth of particles with time (ranging from ~6-9). The fit parameters are shown in Table 6.

Table 6. Fit parameters of the data (according to power law function) obtained for variation of the mean particle size of manganite with time using various total Mn Concn.

	n	k	d_0
I	7.95	8.72E+08	10.30
II	6.68	4.69E+08	11.20
III	8.07	9.24E+09	12.69
IV	8.41	4.5E+10	14.46
V	9.15	9.61E+11	16.44

TEM was used to investigate the influence of time on the morphological shape for the as-prepared manganite samples. From TEM images (Figure 12), picked for two manganite samples prepared under reflux for two different times of 3 and 27 h, it can be noticed that changing the time does not result in a change in the morphological shape. The same rod-like structure persists by rising the time instead an increase in the diameter of these nanorods occurs with increasing of the time. An agreement between the average particle size estimated from XRD and the mean diameter obtained from TEM is obvious for both manganite samples (Table 7). In the same way, increasing of the total Mn concentration in the reaction solution results in an increase of the mean diameter of the as-prepared manganite nanorods.
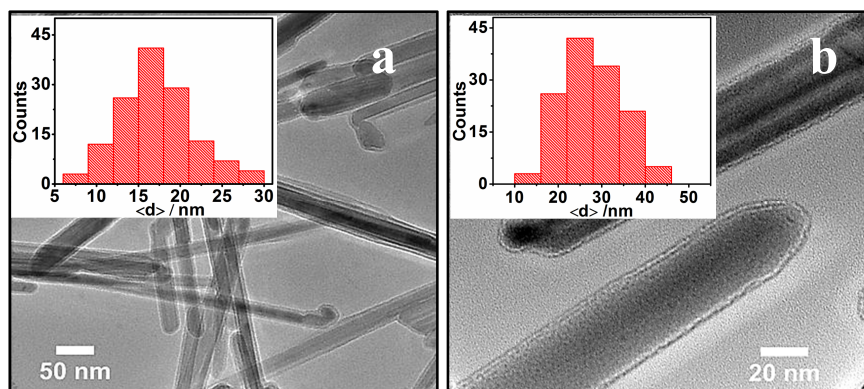

Figure 12. *TEM images of two manganite samples prepared using total Mn concentration of 13 mmol L^{-1} and the same molar ratio of Mn^{2+}/MnO_4^- at two different times of (a) 3 h and (b) 27 h, respectively. Insets represent size distribution curves for the diameters of their rods.*

Table 7. Comparison of the mean particle size <d> (estimated from XRD) of manganite nanorods prepared at two different times with their mean diameters obtained from TEM.

Time / h	*Mean size estimated from XRD <d> / nm*	*Size estimated from (11-1) reflection / nm*	*Average diameter from TEM / nm*
3	16	13	17
27	23	22	25

3.2.2. Influence of reaction temperature

In order to enable a wide range variation of the reaction temperature, the redox reaction between $Mn(OAc)_2$ and $KMnO_4$ was carried out under hydrothermal conditions keeping the same molar ratio for Mn^{2+}/MnO_4^-. The impact of temperature on phase purity, grain size and morphological shape was studied.

3.2.2.1. On phase purity

Starting the reaction at very low temperature of 60 °C while keeping the other experimental parameters unchanged (time of 3 h, molar ratio of 5:1 for Mn^{2+}/MnO_4^- and total Mn concn. of 41.8 mmol L^{-1}) results in reduction of MnO_4^- to Mn^{4+} and oxidation of Mn^{2+} to $Mn^{2.67}$ leading to formation of a mixture of MnO_2 and Mn_3O_4 (Figure 13). By rising the temperature up to 80 °C, manganese oxyhydroxide precipitates as a major phase and minors of MnO_2 are present as contaminants. Sufficiently high temperature ($\geq$ 85 °C) of the reaction results in a single phase of γ-MnOOH.

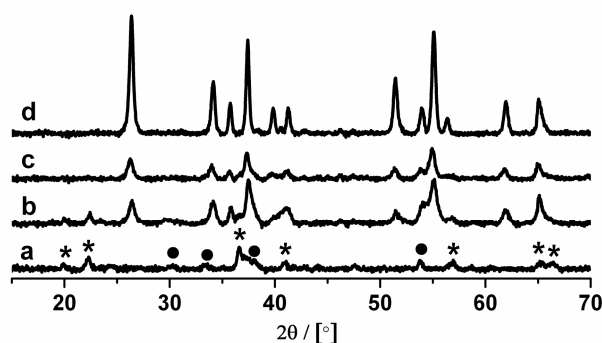**Figure 13.** *Effect of temperature on the products of the reaction of $Mn(OAc)_2$ and $KMnO_4$ (5:1) performed hydrothermally for 3 h at different temperatures of a) 60 ºC, b) 80 ºC; <d> = 11 nm, c) 85 ºC; <d> = 15 nm and d) 140 ºC; <d> = 25 nm. Stars refer to γ-MnO_2 and circles represent Mn_3O_4.*

Two parameters control the precipitation of manganese oxide/hydroxide nanocrystals, i.e., the redox potential of the corresponding redox couples and the solubility product of the precipitated oxide/hydroxide phase. Both of course are affected by variation of the reaction temperature. Table 8 shows the influence of the reaction temperature on the lattice parameters of three manganite samples obtained at different reaction temperatures. Enlargements of the monoclinic unit cell take place with decreasing of the reaction temperature.

**Table 8.** Variation of the lattice parameters of manganite samples with temperature.

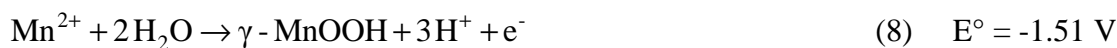|	*80 ºC*	*85 ºC*	*115 ºC*	*140 ºC*	*ICSD-84949 [1]*
a / Å	5.329(6)	5.319(4)	5.315(2)	5.311(1)	5.304(1)
b / Å	5.309(4)	5.302(3)	5.2951(9)	5.2889(6)	5.277(1)
c / Å	5.336(3)	5.328(2)	5.3215(8)	5.318(1)	5.304(1)
β / º	114.67(4)	114.62(3)	114.44(1)	114.423(6)	114.38(2)

Discussion:

❖ At lower reaction temperature the half redox reactions (4) and (5) are expected to take place. The standard electrode potentials are provided.[14]

$$MnO_4^- + 4H^+ + 3e^- \rightarrow MnO_2 + 2H_2O \qquad\qquad (4) \quad E° = 1.70 \text{ V}$$

$$3Mn^{2+} + 4H_2O \rightarrow Mn_3O_4 + 8H^+ + 2e^- \qquad\qquad (5) \quad E° = -1.82 \text{ V}$$

The overall reaction after balancing the number of the lost and gained electrons will be

$$9Mn^{2+} + 2MnO_4^- + 8H_2O \rightarrow 3Mn_3O_4 + 2MnO_2 + 16H^+ \qquad (6)$$
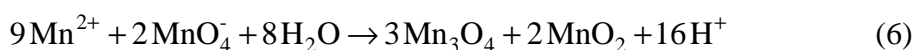
❖ By increasing the reaction temperature a different reaction seems to be run that can be expressed by the following half redox reactions:

$$MnO_4^- + 4H^+ + 3e^- \rightarrow MnO_2 + 2H_2O \qquad\qquad (7) \quad E° = 1.70 \text{ V}$$

$$Mn^{2+} + 2H_2O \rightarrow \gamma\text{-}MnOOH + 3H^+ + e^- \qquad\qquad (8) \quad E° = -1.51 \text{ V}$$

The overall reaction will be

$$3Mn^{2+} + MnO_4^- + 4H_2O \rightarrow 3\gamma\text{-}MnOOH + MnO_2 + 5H^+ \qquad (9)$$

At a temperature of 85 °C, the reaction corresponding to the formation of x-ray single phase of γ-MnOOH can be represented by equation (3).

IR analysis was used as a tool to prove the former assumptions. At a temperature of 60 °C a mixture of Mn_3O_4 and MnO_2 is formed. For this sample the absorption bands located in the range of 400-600 cm^{-1} are assigned to Mn-O stretching vibrations of both oxide phases that are overlapped in this region. The most characteristic bands are located at 730 and 945 cm^{-1} which are related to γ-MnO_2.[13] As we have seen by increasing the temperature to 80 °C a mixture of γ-MnOOH (main product and so most of absorption bands coincide with those of γ-MnOOH), γ-MnO_2 (characteristics band at 945 cm^{-1}) is produced as we can see from Figure 14.
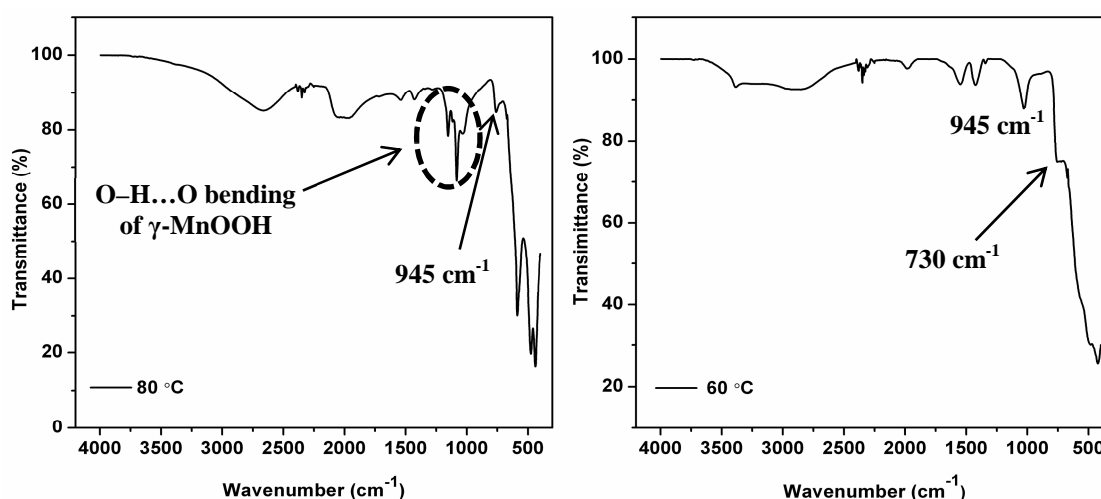

Figure 14. IR spectra of the samples prepared hydrothermally at the same time of 3 h and different reaction temperatures of 60 °C and 80 °C.

3.2.2.2. On grain size

The relationship between reaction time and particle size at constant reaction temperature is shown in Figure 15. Increasing time at fixed reaction temperature results in an increase in the size of manganite particles. Similarly, rising the reaction temperature at fixed reaction time leads to the same result (Table 9). According to the power law fit applied to the data obtained for the variation of the particle size as a function of time, it is found that manganite particles grow with time t (whilst the reaction temperature kept unchanged) according to the equation:

$$<d> = k(t+a)^{1/n}$$

where, $<d>$: the average particle size, t: the reaction time, k: temperature-dependent time constant, a: additional parameter, corresponding to the quotient d_0^n/k with d_0 as particle size at time t = 0 and n: the order of growth of particles with time (ranging from ~6-9). The fit parameters are shown in Table 10.

Different case exists at much higher temperatures where no further growth takes place; instead, a dissolution process commences resulting in drop in the particle size.
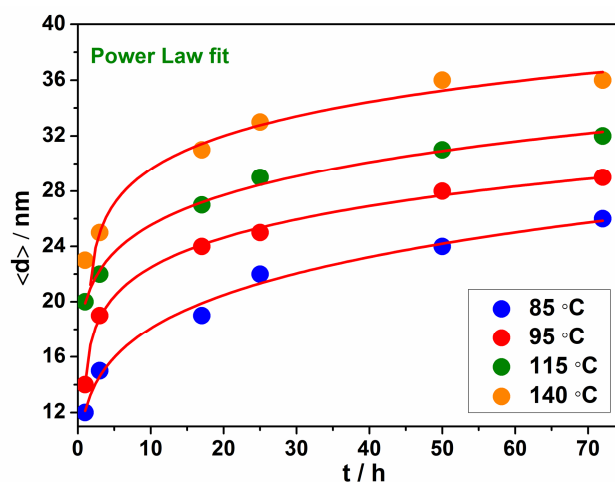

Figure 15. *Change of particle size with time and temperature for nc-manganite prepared hydrothermally from redox reaction between Mn(OAc)$_2$ and KMnO$_4$ of given molar ratio of Mn^{2+}/MnO$_4^-$ and total Mn concentration of 41.8 mmol L^{-1}.*

Table 9. Variation of the mean particle size of manganite samples with temperature and time.

Time / h	Temperature / °C			
	85	95	115	140
1	12	14	20	23
3	15	19	22	25
17	19	24	27	31
25	22	25	29	33
50	24	28	31	36
72	26	29	32	36

Table 10. Fit parameters of the data obtained for variation of the mean particle size of manganite with reaction time at various reaction temperatures.

Temp. / °C	n	k	d$_0$
85	5.48	7.59E+06	8.30
95	8.02	7.74E+09	12.56
115	8.30	4.70E+10	16.67
140	9.92	4.59E+13	22.64

The effect of temperature on the grain growth process of nc-manganite was investigated by TEM analysis. TEM images captured for two manganite samples prepared at different temperatures while the other synthetic parameters held constant revealed that with increasing reaction temperature an increase in the diameter of manganite nanorods takes place. It is clear from Figure 16a-b that manganite nanorods prepared at 85 °C are thinner (mean diameter of 19 nm) compared to those obtained at higher temperature of 140 °C (mean diameter of 37 nm). Size distribution curves were constructed for these samples (Figure 16c-d). Obviously, the mean diameters of the manganite nanorods differ significantly as a function of reaction temperature. Matching between the average particle sizes calculated from XRD and the average rod diameters obtained from TEM for both manganite samples is noticeable as one can see from Table 11.
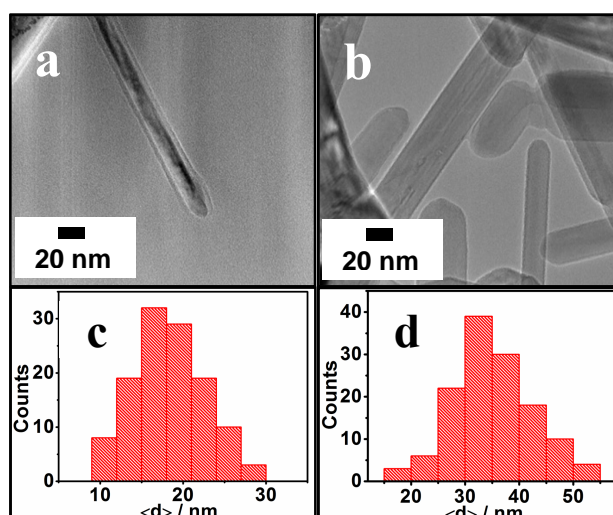

Figure 16. *a-b) TEM images of two manganite samples prepared hydrothermally using two different reaction temperatures of 85 °C and 140 °C, respectively, at 25 h. Figures c-d) represent the corresponding size distribution curves for the diameters of nanorods.*

Table 11. Comparison of the mean particle sizes <d> of manganite nanorods prepared at two different temperatures with their mean diameters obtained from TEM.

Temp. / °C	Mean size estimated from XRD <d> / nm	Size estimated from (11-1) reflection / nm	Average diameter from TEM / nm
85	21	19	19
140	36	39	37

3.2.3. Type of alkali metal cation of the permanganate salt

The impact of alkali metal cation on phase, particle size and morphological shape of the as-obtained product was studied. The redox reaction between manganese acetate and different permangante salts, i.e., $KMnO_4$, $NaMnO_4$ and $CsMnO_4$ was carried out, 5:1 molar ratio for the redox couple Mn^{2+}/MnO_4^- was used (SM1, SM4 and SM5 samples, respectively). Changing the alkali metal cation does not affect the product at this molar ratio, all products are assigned to pure phases of manganite. These observations come at variance to use of a higher molar ratio of 1:1 for Mn^{2+}/MnO_4^- at which different phases of MnO_2 are obtained using various permangante salts (see chapter 5).

Elemental analyses were performed for such manganite samples (SM1, SM4 and SM5, respectively) to ensure that there is no excess of the alkali metal cations adsorbed over their surfaces, also to investigate the posssibilty of their accommodation into 1x1 tunnels (0.24 nm x 0.24 nm) of the manganite structure. Hence, modifying the reaction path toward the formation of different phases of manganese oxyhydroxide. Although Na^+ has low ionic radius of about 0.102 nm (Na–O distance of ~0.242 nm),[15,16] the tunnels can not accommodate Na ions insertion. This is confirmed by EDX analysis for the sample SM4 (see Table 12) where there is no peak corresponding to its presence in the EDX graph (not shown here). For large Cs^+ cations (sample SM5) that have an ionic radius of 0.167 nm,[9] the insertion into 1x1 tunnels is not expected as confirmed by EDX analysis. Indeed, the small size tunnels are occupied with small size hydrogen atoms with O–H bond length 0.098 nm.[1]

Table 12. Atomic weight percent values obtained from EDX analyses for γ-MnOOH samples prepared using different permanganate salts.

Sample	*%Atomic weight*		
	Mn	*O*	*X*
SM4	61(4)	39(5)	0.15(5)[a]
SM5	67(1)	33(1)	0.0[b]
Expected	62.5	36.36	0.0

a; X = Na and b; X = Cs

IR spectra for these samples are shown in Figure 17 in which all absorptions occur as typical for γ-MnOOH (see Figure 3). No impact on the peak positions in IR spectra could be seen. Merely, a slight increase in the intensities of the absorption bands is observed and this could relate to some difference in particle size of the prepared manganite samples.
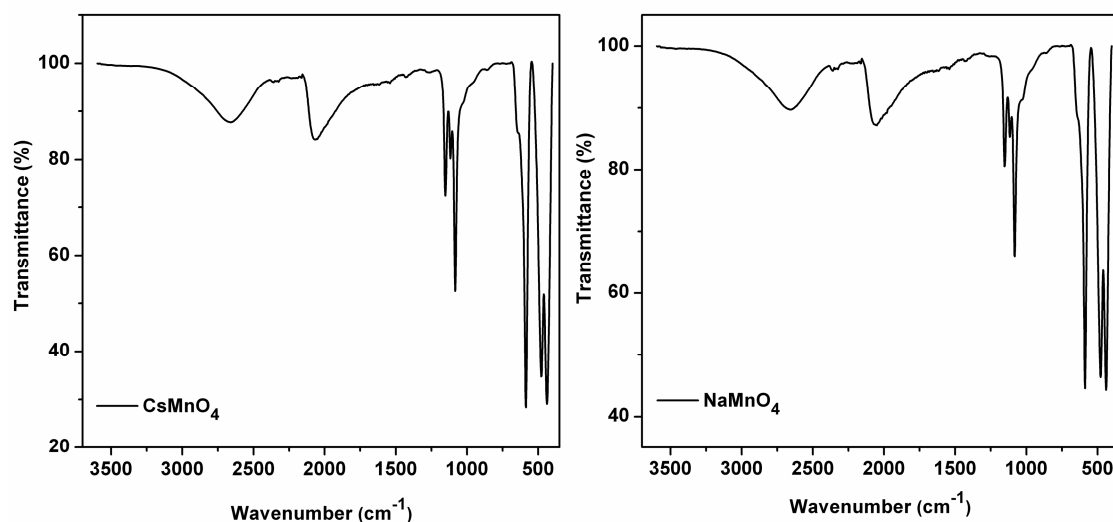

Figure 17. IR spectra of γ-MnOOH samples prepared from the reaction between Mn(OAc)$_2$ and NaMnO$_4$ (SM4) or CsMnO$_4$ (SM5) under reflux for 17 h.

We have seen that manganite nanocrystals (X-ray single phases) are produced regardless of the type of parmanganate salts. These results were demonstrated by IR analyses. Nevertheless, SEM investigations for such products revealed an vast impact of alkali metal cations on the morphological shape of nc-manganite. Different images were taken for each sample. For SM4 sample we can see a rod-like morphology (Figure 18a). The nanorods are thicker than those of SM1, some nanoparticles coexist beside nanorods. These seem to be deformed in shape or nanorods at intial stage of formation. The same observation can be seen for the sample SM5 but in this case much of these nanoparticles are spread over the nanorods (Figure 18b).

We can conclude from these results that Na and Cs may hinder the uniform growth of manganite nanorods. They are not appropriate candidates for formation of manganite samples with well shaped and uniform rod-like morphology.
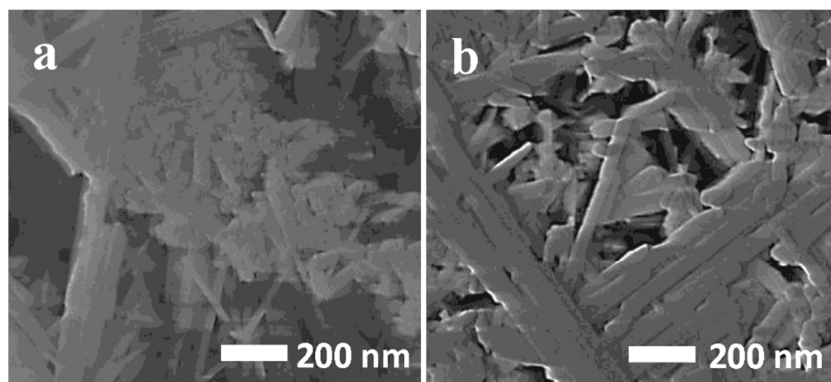
Figure 18. *SEM pictures of nc γ-MnOOH: a) SM4 and b) SM5.*

3.2.4. Solvent effect

It was established that solvents with different polarities and tendencies to participate in a side reaction with the reactans have an influence on the product phase as well as on its grain size.[8,17] In the current study, we will implement this finding as an alternative approach in order to achieve a control over the size and phase of the so obtained manganse oxide/ hydroxide nanocrystals.

For such purpose the comproportionation reaction between $Mn(OAc)_2$ and $KMnO_4$ was performed solvothermally at 160 °C for 3 h. Water was mixed partially with ethanol in an attempt to understand the influence of solvent polarity on the reaction product as well as its grain size. The other experimental conditions were kept constant (molar ratio of 5:1 for Mn^{2+}/MnO_4^- and total Mn concn. of 41.8 mmol L^{-1}). Starting from pure water to pure ethanol, the products of such reaction were characterized by XRPD as shown in Figure 19.
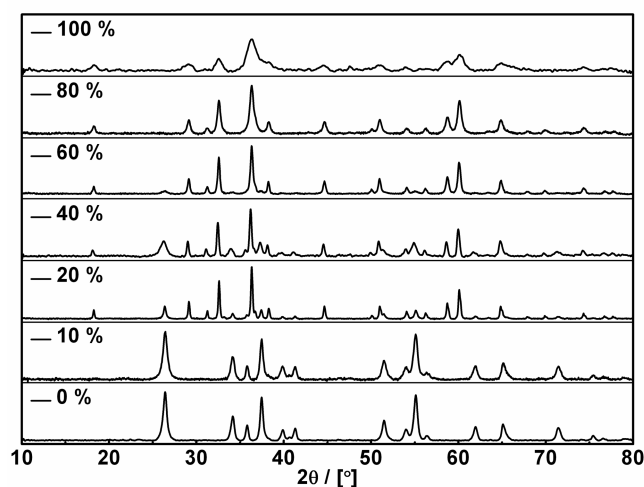

Figure 19. *Impact of %EtOH on the reaction of $Mn(OAc)_2$ and $KMnO_4$, 70 mL solution was used, reaction temperature holded at 160 °C for 3 h.*

In pure water, γ-MnOOH with a particle size of 27 nm is produced. Replacing water partially with 10% EtOH, γ-MnOOH is still formed as the prevalent product. The average grain size <d> for this sample drops to 24 nm. With increasing of EtOH content up to 20% a new phase appears, the powder pattern for the product shows additional reflections that can be indexed to the spinel, α-Mn_3O_4.

This result can be explained by taking into considerations that part of $KMnO_4$ is involved in a side redox reaction with ethanol which consumes some of $KMnO_4$, hence reducing its concentration. Actually, the product of the reduction of $KMnO_4$ by ethanol could not be established. It may be reduced to γ-MnOOH or Mn_3O_4, the product phase depends on the experimental parameters.[8] Tiny impurties of γ-MnOOH are present in case of 40 and 60% EtOH with formation of spinel as a major product.

Clean phase Mn_3O_4 is obtained when 80% EtOH is used, since the amount of $KMnO_4$ remaining after consumption in the side reaction with ethanol is merely enough for oxidation of Mn^{2+} to Mn_3O_4. The calculated average particle size for this sample is ~26 nm (estimated from band broadening and line positions using Scherrer's formula). The lattice parameters of this sample are a = 5.7658(1) Å and c = 9.4573(5) Å.

Further increase in the EtOH content results in a shrinkage of the particle size of Mn_3O_4 samples. Spinel with average particle size of 9 nm is obtained utilizing 100% EtOH. The calculated lattice parameters for this sample are a = 5.767(7) Å and c = 9.47(1) Å. By increasing of %EtOH (shrinkage in grain size) elongation of the unit cell occurs in the c direction.

IR analysis was done for the sample obtained in pure ethanol (Figure 20), the spectrum shows three absorption peakes at 399, 478 and 599 cm^{-1} which are assigned to Mn-O strectching vibrations in the spinel, Mn_3O_4.[18] Additional absorption bands are located at 3362 and 1634 cm^{-1}, these bands are attributed to stretching and bending vibrations of the –OH group of absorbed and/or crystallization water molecules.[19]
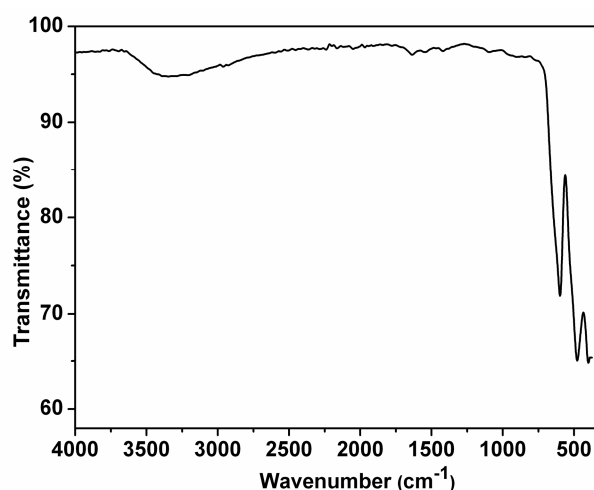

Figure 20. *IR spectrum of spinel sample Mn_3O_4 (<d> = 9 nm) prepared in pure ethanol.*

TEM investigations for the two spinel samples obtained using 80% and 100% EtOH (Figure 21a-b) reveal nearly sphere-like morphologies (i.e., shape-isotropic particles) with average diamters of 26 nm and 8 nm, respectively. These results coincide with those obtained from XRD calculation.

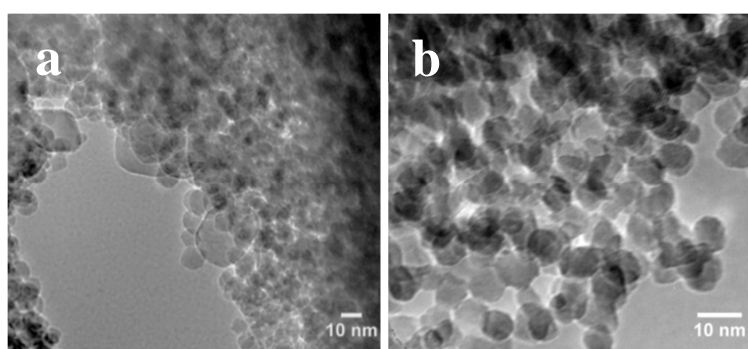**Figure 21.** *TEM images of two Mn_3O_4 samples prepared using different ethanol contents: a) 80% EtOH and b) 100% EtOH.*

In a conclusion, ethanol has a significant influence on the grain size of the obtained manganite and spinel nanocrystals. The remarkable fall of the particle size with increasing the content of ethanol can be explained as follow: Ethanol is a less polar solvent than water, thus

the solvation energy of the oxide/hydroxide phase is lower than in pure water. This leads to a higher initial energy of the oxide/hydroxide before nucleation, so decreasing the energy barrier that has to be overcome for crystallization.[20] Consequently, the nucleation rate is higher in ethanol-rich solutions, so the available manganese oxide is consumed quickly, which prevents the growth of bigger crystallites.

The main influence of ethanol on the reaction products comes from its role as a reducing agent participating in a side redox reaction hence, consuming part of $KMnO_4$ thus, leading to formation of a product with lower oxidation state, i.e., MnOOH or Mn_3O_4.

3.2.5. Synthesis and characterization of feitknechtite (β-MnOOH)

A survey about feitknechtite revealed that modest work has been done.[21-24] Limited preparative methods were reported for feitknechtite synthesis.

The relative structural instability of the layered-structure feitknechtite (with a lamellar structure) compared to that of manganite place it under the risk of structural modification toward the most stable polymorph manganite with 1x1 tunnels.[4,25] Much efforts are necessary for synthesis of single phase feitknechtite, this could be the reason for the limitations of feitknechtite synthesis in literature.

Here, a novel method is developed for the preparation of feitkenchtite based on the former aspect of the influence of the solvent on the comproportionation reaction between manganese acetate and $KMnO_4$. Pure acetone is used as a solvent instead of ethanol (95 ºC, 1 h and 70 mL acetone). Actually, the oxidation of acetone is not as readily as that of ethanol. It is oxidized hardly by $KMnO_4$, the oxidation occurs essentially via C-C bond repture under vigrous conditions resulting in formation of a mixture of formic acid and acetic acid.[26] Therefore, a slight amount of permangante is consumed in the side reaction with acetone (relative to that consumed by ethanol).

The results obtained whilst solvents of different polarties were used, i.e., water, ethanol and acetone showed a change in the reaction product. In pure water the product is identified as γ-MnOOH and in pure ethanol as spinel (Figure 19), whereas the product obtained in pure acetone is characterized as feitknechtite; β-MnOOH (Figure 22).[25] The average particle size for this sample is ~39 nm. Feitknechtite has a trigonal symmetry (space group $P\overline{3}m1$ (164)) with cell parameters as a = 3.428(3) Å, c = 4.919(1) Å and β = 120º. Peak list for this sample is shown in Table 13.

Indeed, the Mineralienatlas database for feitknechtite reported 4 reflections that can be seen at d-spacing = 4.62, 2.64, 2.36 and 1.96.[27] These reflections match well with our pattern of feitknechtite for which the reflections are seen at d-spacing ≈ 4.60, 2.69, 2.38, 2.06, 1.85 and 1.58, taking into account that we have shifts in the positions of the lines as a result of using Co-radiation. Indexation of the powder pattern of this feitknechtite sample is not possible, specially with appreciable shifts in peak positions which can be ascribed to some structural changes.
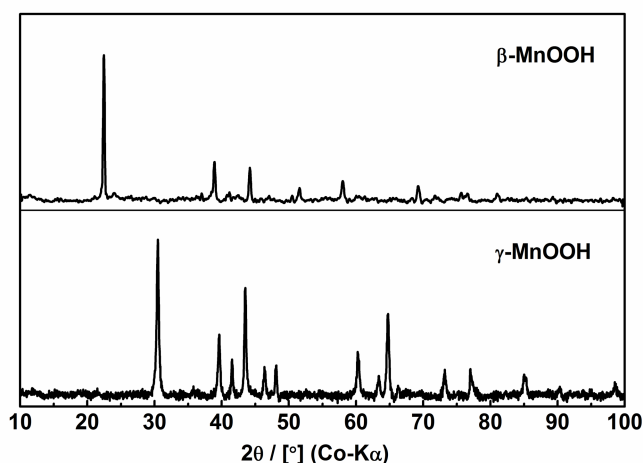
Figure 22. *Diffractograms of γ-MnOOH (<d> = 19 nm, 3 h) and β-MnOOH (<d> = 39 nm, 1 h) samples prepared in pure water and pure acetone solutions, respectively.*

Table 13. Peak list of feitknechtite sample.

Peak No.	Pos. [°2Th.]	d-spacing [Å]	FWHM [°2Th.]
1	22.453	4.59788	0.4093
2	38.94	2.68562	0.307
3	41.1598	2.54657	0.614
4	44.2002	2.3793	0.307
5	51.5608	2.05819	0.307
6	58.0246	1.84569	0.307
7	69.2864	1.57355	0.4992

IR analysis for feitknechtite sample (Figure 23) revealed two sets of absorption peaks. In the range of 400-700 cm^{-1} the absorption peaks are related to Mn-O stretching vibrations. The other set locates at 745, 947 and 1070 cm^{-1} and are assigned to O—H...O deformation vibrations of β-MnOOH.[28]

It is clear that IR spectrum of feitknechtite differs from that of manganite (see Table 14) although both have basically the same constituent atomic bonds. This can be ascribed to the divergence in the structural arrangement of MnO_6 octahedral. In manganite they are connected in away, so 1x1 tunnels are produced in which H atoms are residing. In feitknechtite the octahedral MnO_6 are arranged in layers and H atoms locate in the interlayer spacing (4.7 Å).[29]
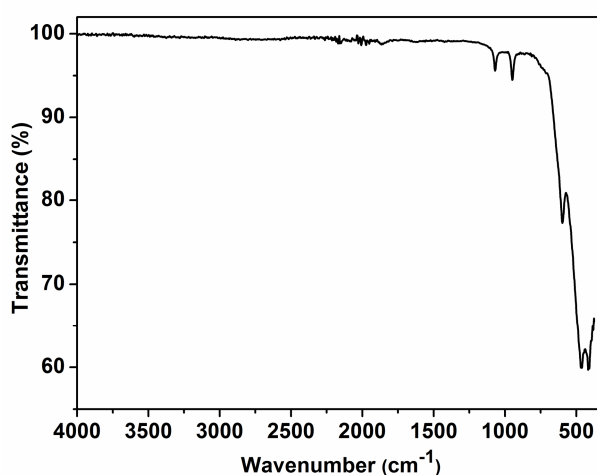

Figure 23. IR spectrum of β-MnOOH sample prepared solvothermally in pure acetone at 95 ºC, 1 h.

Table 14 shows the comparison between Mn-O and O—H...O vibrations for both manganite and feitknechtite. The most significant observation is that O—H...O bending modes of manganite are more energetic which can be explained by a stronger hydrogen bonding in manganite structure compared to that in feitknechtite structure.

Table 14. Comparison of the positions of the absorption bands obtained from IR spectra of manganite and feitknechtite.

Sample	Mn-O			OH bending			OH str.
Manganite	436	476	587	1082	1116	1153	2660
Feitknechtite	414	465	597	745	947	1068	1865

Density measurements for this sample revealed that it has a density of ~3.7 g/cm^3 which is consistent with the calculated one of 3.8 g/cm^3.[30,31] This result reflects that we have a clean phase feitknechtite by all indications. The synthesis of feitknechtite sample was repeated twice using the same conditions. Density measurements were done for the as-prepared samples, density values in the range of 3.69-3.72 were found.

EDX analysis for this sample revealed that the main constituent atoms are Mn and O. TEM investigation for the as-prepared feitknechtite sample showed that this sample has a rod-like morphology (Figure 24) with average diameter of ~10 nm.
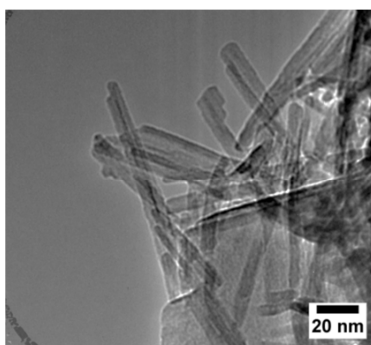
Figure 24. TEM image of β-MnOOH sample prepared in pure acetone.

In conclusion we can accentuate that a novel preparative method for sythesis of the spinel, with controllable grain size has been settled in our work via accomplishment of the reaction between manganese acetate and KMnO$_4$ in ethanol-water solutions. Sample with smallest crystallite size is obtained in pure ethanol. Furthermore, an innovative preparative method is developed for synthesis of feitknechtite using acetone as a reaction solvent.

3.2.6. Molar ratio of Mn²⁺/ MnO₄⁻

The influence of the molar ratio of Mn^{2+} salt to $KMnO_4$ was studied using 2.5 mmol of manganese salt and different mmoles of $KMnO_4$, i.e., 6.3×10^{-2}, 0.19, 0.41, 0.63 and 2.5 mmol. The corresponding molar ratios are 39:1, 13:1, 6:1, 4:1 and 1:1, respectively. The other experimental parameters are kept unchanged, i.e., time, temperature and the volume of water (225 mL). The solid products were then characterized by XRD analysis. The XRPD diffractograms are shown in Figure 25. It is obvious that the ratio has a significant impact on the product, indicating that the relative amount of $KMnO_4$ is a curcial parameter for formation of various manganese oxide/hydroxide phases.
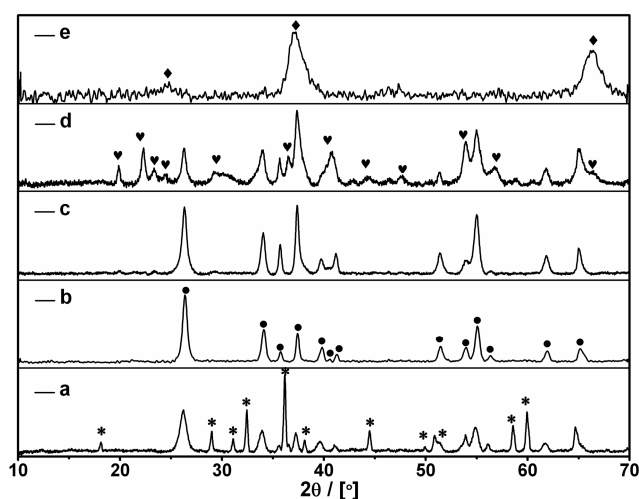

Figure 25. *Impact of variation of Mn^{2+}/ MnO_4^- ratio on the purity of the obtained products prepared via refluxing the mixture for 3 h in 225 mL H_2O. The corresponding molar ratios of Mn^{2+}/ MnO_4^- are a) 39:1, b) 13:1, c) 6:1, d) 4:1 and e) 1:1. Stars: α-Mn_3O_4, closed circles: γ-MnOOH, hearts: γ-MnO_2 and diamonds: δ-MnO_2.*

At very high molar ratio of 39:1 a low concentration of $KMnO_4$ is involved into the redox reaction, therefore full oxidation of all Mn^{2+} existing in the reaction medium to Mn^{3+} by $KMnO_4$ can not take place. The relatively high concentration of Mn^{2+} salt (acting as a reducing agent) has the ability to reduce the low concentration of $KMnO_4$ to manganese oxide with lowest possible oxidation state. As a result the spinel, Mn_3O_4 with average oxidation state of 2.67 is produced as a major phase. γ-MnOOH (oxidation state of 3+) is formed as a minor phase (Figure 25a).

Lowering the molar ratio to 13:1 (higher concentration of $KMnO_4$ is included into the redox reaction) has an impact on the capability of $KMnO_4$ to oxidize Mn^{2+} to Mn^{3+}.

Simultaneously reduction of $KMnO_4$ to Mn^{3+} takes place. γ-MnOOH is obtained as a single phase. The same process occurs when the molar ratio of Mn^{2+}/MnO_4^- is adjusted to 6:1 (Figure 25b-c).

With molar ratio of 4:1, $KMnO_4$ is able to oxidize Mn^{2+} to Mn^{4+}, precipitated as γ-MnO$_2$. Minors of Mn^{3+} are still formed in the form of γ-MnOOH. Finally, using a very low molar ratio of 1:1 results in δ-MnO$_2$ (K-birnessite) due to presence of excess K^+ concentration (K-template effect). Low quality powder pattern (Figure 25e) is obtained with considerably broad reflections which may indicate the turbostratic disorder in the birnessite structure, i.e., each layer is translated and/or rotated randomly in relation to adjacent layers.[32]

The forgoing study was subsequently followed by another study of the influence of the reaction time on the product phase. The results showed that the most distinct effect is observed when molar ratio of 1:1 is used. Carrying out the reaction under reflux for 3 h leads to formation of δ-MnO$_2$ (layered type MnO$_2$). By extending the reflux time to 17 h, the layers are collapsed to 2x2 tunnels. α-MnO$_2$ (2x2 tunnelled structure) is produced (Figure 26). For the molar ratios of 13:1 and 6:1 characterized by formation of manganite nanocrystals, extending the reaction time leads to enlargement of the crystallite size.
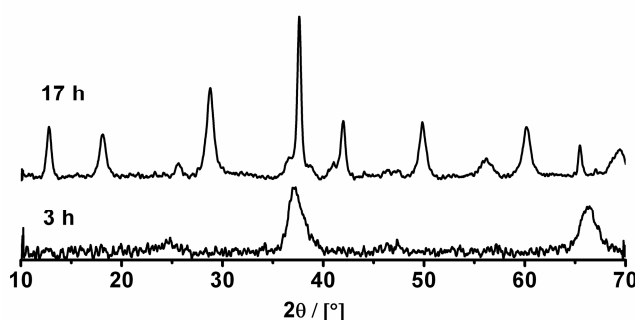

Figure 26. *Effect of reaction time on the product phase when the molar ratio of 1:1 is used for the redox couple Mn^{2+}/MnO_4^-. δ-MnO$_2$ (<d> = 8 nm) is produced at 3 h and α-MnO$_2$ (<d> = 14 nm) is obtained at 17 h.*

3.2.7. Variation of the reaction pH

The pH value is a decisive parameter that can significantly alter the reaction pathway. In order to investigate the impact of variation of the reaction pH, a set of hydrothermal reactions was performed between manganese acetate and $KMnO_4$ at low temperature of 95 ºC for 3 h. The reaction was done in aqueous medium using 70 mL distilled water, the pH was about 6. Formation of single phase γ-MnOOH is prevailing in this case. Manganite can be formed in a pH range of 6-8, the reaction proceeds according to eqn. 3. The final pH value of the reaction solution measured after the separation of manganite was approximately 4.5. XRD patterns of the products obtained by pH modifications are shown in Figure 27. Table 15 shows the various products formed as a function of variation of the initial pH of the reaction medium.
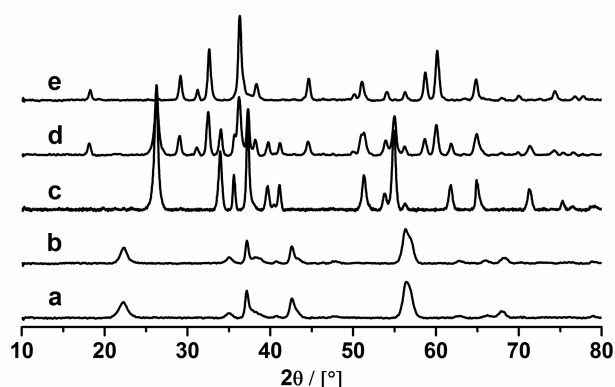
Figure 27. *Impact of variation of pH of the medium on the products of the reaction of Mn(OAc)$_2$ with KMnO$_4$ performed under hydrothermal conditions at 95 °C for 3 h. a) pH ~2; γ-MnO$_2$, b) pH ~4; γ-MnO$_2$, c) pH ~6; γ-MnOOH, d) pH ~9; γ-MnOOH + Mn$_3$O$_4$ and e) pH ~11; Mn$_3$O$_4$.*

Table 15. Influence of the change of the reaction pH on the product phase and its grain size.

pH_i	~2	~4	~6	~9	~11
Phase	γ-MnO$_2$	γ-MnO$_2$	γ-MnOOH	γ-MnOOH + Mn$_3$O$_4$	Mn$_3$O$_4$
<d> / nm	12.0	12.7	19.0	–	21.0
pH_f	1.4	2.2	4.5	8.5	10.5

The initial pH of the medium was then lowered by adding drops of HCl solution (0.1 mol L^{-1}) preserving the total volume of the reaction solution at 70 mL. At pH ~2, nsutite, γ-MnO$_2$ (ICSD-78331) is formed. By raising the pH up to 4, there is no change in the reaction product, i.e., γ-MnO$_2$ is still formed. These results reflect the fact that nsutite is preferably formed in acidic media. Nevertheless, these findings come at variance to what is reported,[33] where at low pH values of ~1-4 and temperatures of 150-210 °C γ-MnOOH is formed. This has an indication that in combination with the pH change, the reaction temperature is a crucial parameter for variation of the reaction pathway under hydrothermal conditions. Formation of nsutite in acidic medium can be represented by the equation:

$$2\,MnO_4^- + 3\,Mn^{2+} + 2\,H_2O \rightarrow 5\,MnO_2 + 4\,H^+ \qquad\qquad (10)$$

In basic medium, by addition of NaOH solution (0.1 mol L^{-1}) variation of the reaction product is apparent. At pH ~9, a mixture of γ-MnOOH and Mn$_3$O$_4$ is produced while raising the pH up to ~11 results in formation of single phase spinel, Mn$_3$O$_4$. In comparison to what is reported,[33] we are able to prepare the spinel at lower temperature of 95 °C (spinel was obtained at higher hydrothermal temperature of 210 °C). According to the report,[33] the estimated particle size for the spinel sample was ~30-50 nm which is larger than that we obtained (21 nm) by the same method at lower hydrothermal temperature. Formation of Mn$_3$O$_4$ in basic medium can be represented by the following equation:

$$2\,MnO_4^- + 13\,Mn^{2+} + 24\,OH^- \rightarrow 5\,Mn_3O_4 + 12\,H_2O \qquad\qquad (11)$$

Variation of the product phase with the reaction pH can be explained on two bases: firstly, the redox potentials for the corresponding redox species which change significantly with the variation of pH; secondly, the solubility product of the precipitated manganese oxide/hydroxide phases which changes also with the reaction pH.

For nsutite, SEM images (Figure 28a) showed that it has a plate-like morphology. The plates are shapeless with plate thickness of 12 nm which matchs with the average particle size estimated by Scherrer's formula. For the spinel, TEM is the best analysis tool for the morphology where SEM does not give detailed information about the shape. From TEM picture shown in Figure 28b one can see that the spinel particles have octahedron shapes in most cases, some deformed octahedrons can be seen as well. The shorter axis for these

octahedrons has a diameter in the range of 20-40 nm whereas the longer one is approximately 40-60 nm large.
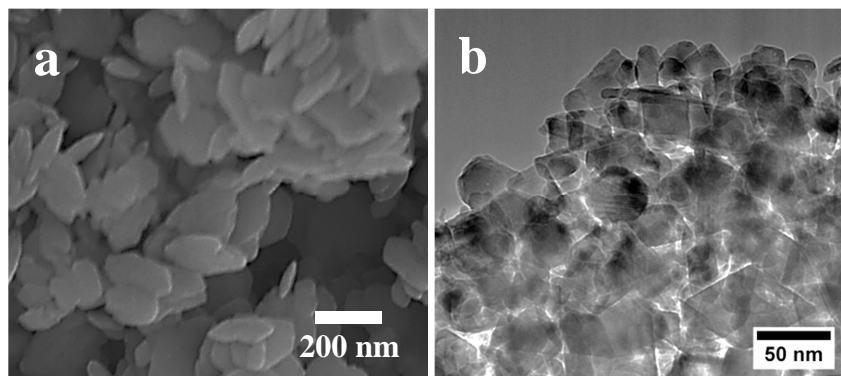

Figure 28. *Morphological investigations of the products obtained via pH modification: a) SEM image of γ-MnO$_2$ sample and b) TEM image of the α-Mn$_3$O$_4$ sample.*

3.3. Size dependent physical properties

3.3.1. Vibrational properties

IR spectroscopy

To study the effect of particle size variation on the absorption properties, IR analyses were performed of three manganite samples with different sizes (Figure 29). It is obvious from IR spectra that the particle size affects only the intensity of the absorption bands, where the intensity increases with increasing particle size. Magnifications for two spectral ranges 400-700 and 1000-1200 cm^{-1} were done (inset of Figure 29) to see the influence of size on the intensity of Mn-O stretching bands as well as on those corresponding to OH bending modes. It is clear from IR spectra that the size has no significant effect on the peak position; non appreciable shifts take place with increasing size. No excess mass can exist over the surface of manganite samples (even for manganite with the lowest particle size), since no absorption bands characteristic to presence of water can be seen. The corresponding peak positions are listed in Table 16 that depicts a little or no shifts in the location of absorption bands.

Table 16. Comparison of the positions of the absorption bands obtained from IR spectra for three manganite samples with different sizes.

<d> / nm	*Mn-O*			*OH bending*			*OH str.*
16	438	476	588	1081	1115	1154	2656
23	436	476	587	1082	1116	1153	2660
28	437	478	589	1083	1116	1151	2656

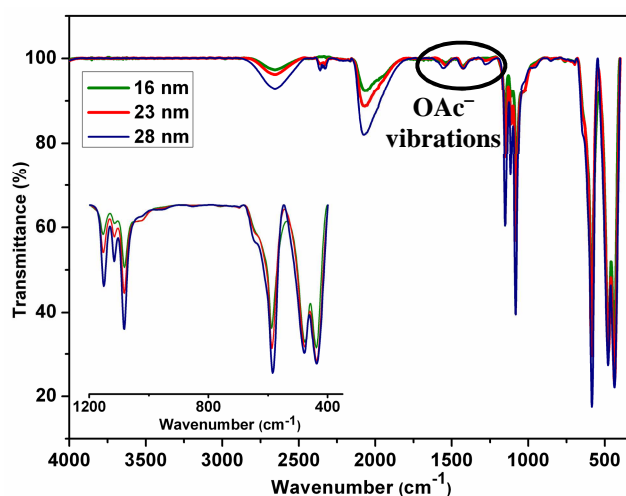***Figure 29.*** *IR spectra of three manganite samples of different particle sizes.*

3.3.2. Thermal stability

Thermogravimetric analysis was used to identify the thermal behavior of γ-MnOOH under air atmosphere from ambient temperature to 1000 °C. The corresponding TGA curves are illustrated in Figure 30, four steps of mass losses are observed within the temperature range. The first mass loss corresponds to loss of adsorbed water over the surface of manganite. The second step corresponds to a dehydration coupled with oxidation of γ-MnOOH to β-MnO$_2$ (rutile type structure) which has a similar tunnelled structure as γ-MnOOH except that the tunnels are vacant in case of β-MnO$_2$ and occupied with H atoms in case of γ-MnOOH. In the third step the weight loss indicates the decomposition of β-MnO$_2$ to α-Mn$_2$O$_3$ (Bixbyite) which undergoes a subsequent decomposition in the last step to α-Mn$_3$O$_4$ (Hausmannite).
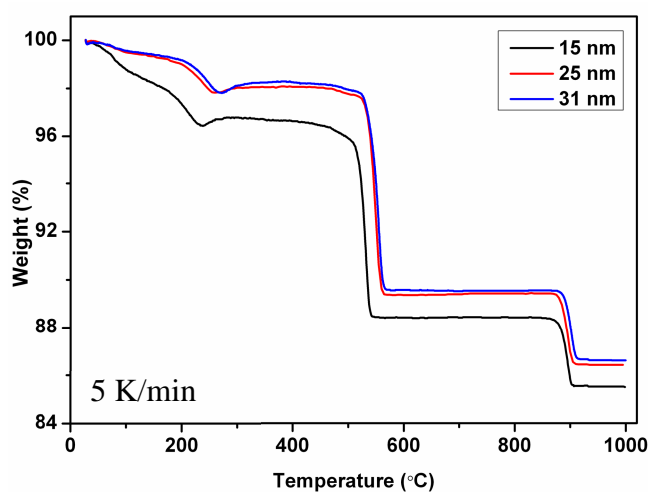
Figure 30. *TGA of three manganite samples with different sizes performed under air flow.*

This scheme of decomposition was elucidated by two means; firstly by comparing weight loss of each decomposition step with that calculated (Table 17), secondly by XRD analysis (Figure 31) of the products obtained at the end of each decomposition step.

Table 17. Mass losses for three manganite samples with different sizes compared to the calculated mass changes and assignment of phases.

Step	15 nm	25 nm	31 nm	Assignment	Calcd.
I	2.0	0.9	0.6	H$_2$O	-
II	1.8	1.2	1.4	β-MnO$_2$	1.1
III	7.9	8.4	8.4	α-Mn$_2$O$_3$	9.1
IV	2.8	3.0	3.0	α-Mn$_3$O$_4$	3.4

Figure 31. *XRD analysis of manganite sample and its decomposition products under air: a)*
γ-MnOOH, b) 400 °C; β-MnO₂, c) 600 °C; α-Mn₂O₃ and d) 1000 °C; α-Mn₃O₄.

From the forgoing results, the proposed sequence of decomposition will be as follow:[34]

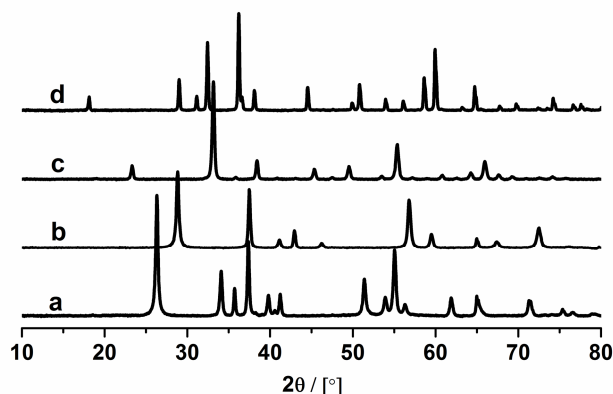$$4\,\gamma\text{-MnOOH} + O_2 \rightarrow 4\,\beta\text{-MnO}_2 + 2\,H_2O \tag{12}$$

$$3\,\alpha\text{-Mn}_2O_3 \rightarrow 2\,\alpha\text{-Mn}_3O_4 + \tfrac{1}{2}\,O_2 \tag{13}$$

$$2\,\beta\text{-MnO}_2 \rightarrow \alpha\text{-Mn}_2O_3 + \tfrac{1}{2}\,O_2 \tag{14}$$

The effect of grain size on the kinetics of decomposition was investigated by studying the decomposition of three manganite samples of different size under the same conditions (heating rate 5 K/min, 25-1000 °C and under air flow). From TG curves (Figure 30) one can see that the inflection points at which the decomposition starts T_i (initial temperature of decomposition) are markedly affected by grain size and it is obvious that these temperatures shift toward higher values with increasing of grain size. We can conclude that increasing the particle size results in a more stable MnOOH as well MnO_x.

This can be explained depending on two bases: firstly, smaller nanoparticles with larger surface-to-volume ratio usually exhibit higher surface energy. Therefore, they require less enthalpy for lattice distortions, resulting in decreased phase transition temperatures.[11] Secondly, with the decrease of the particle sizes the ratio of the number of surface atoms to the total number of atoms increases rapidly.[11] These atoms are in general chemically more active and possess high diffusion mobility at elevated temperatures. To observe how the particles size affects the stability of MnOOH and MnO_x, plots of T_i vs. particle size were constructed for 1st, 2nd and 3rd decomposition steps and shown in Figure 32.
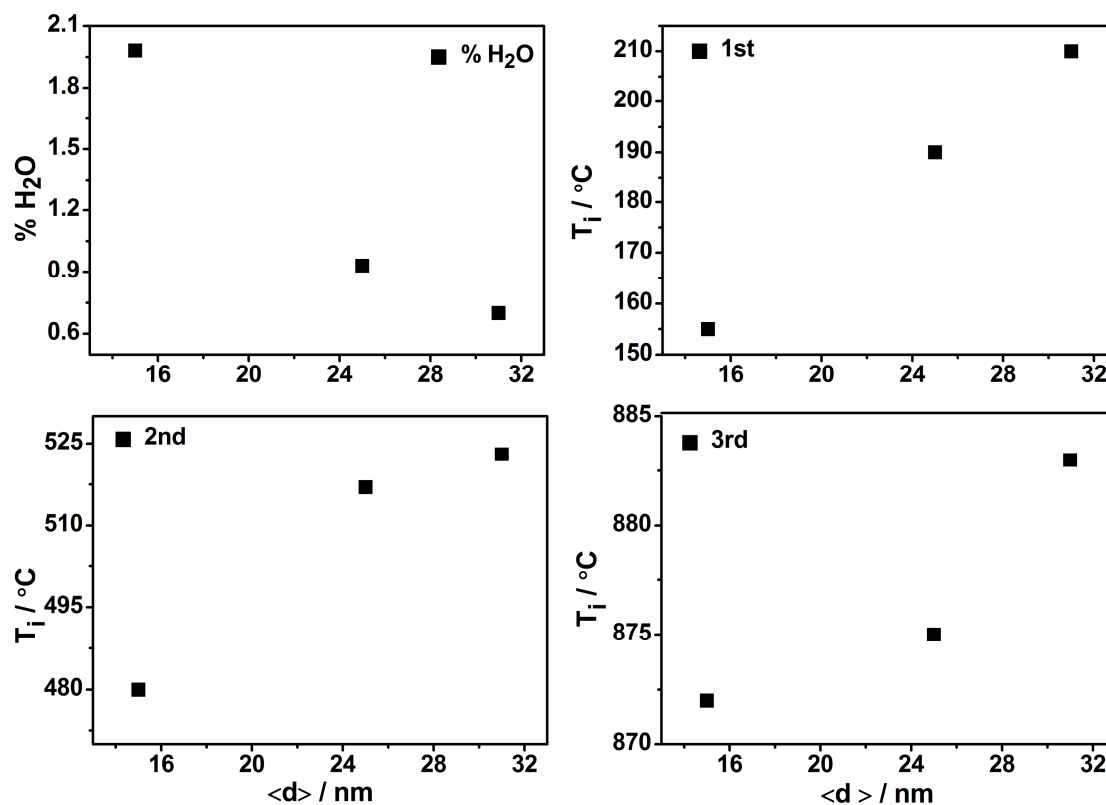
Figure 32. *Influence of mean particle size on the initial temperature of decomposition (T_i) of manganite and its decomposition products as well as the effect of size on the amount of adsorbed water on manganite surface.*

3.3.3. Surface area and pore size distribution

Nitrogen adsorption-desorption isotherms (Figure 33) were monitored for four manganite samples of different average particle size to study the impact of mean particle size on the surface area and pore size distribution. These isotherms correspond to type IV characterized by distinct hysteresis loops indicating mesoporous (2 - 50 nm) structures.[35] The loops follow H3 type isotherms, which do not exhibit any limiting adsorption at high p/p°. This type is characteristic to slit-shaped pores.[36] It is derived from these isotherms that the surface area decreases with increasing particle size. The corresponding Barrett–Joyner–Halenda (BJH) pore size distribution curves are shown in Figure 34. The average pore width for the samples is found as ~10-12 which is indicative for mesoporous structure. The values of surface area and average pore width are listed along with the corresponding particle size in Table 18. Figure 35 displays the relationship between the specific surface area S_{BET} and the inverse of the average particle size 1/<d>.

Table 18. Surface areas, average pore width and total pore volume for four manganite samples with different sizes.

<d> / nm	S_{BET} (m^2/g)	Average pore width / nm	Total pore volume / cm^3/g
15	47.6	10.9	0.13
22	23.3	11.7	0.068
26	15.6	12.1	0.047
29	13.0	10.3	0.037

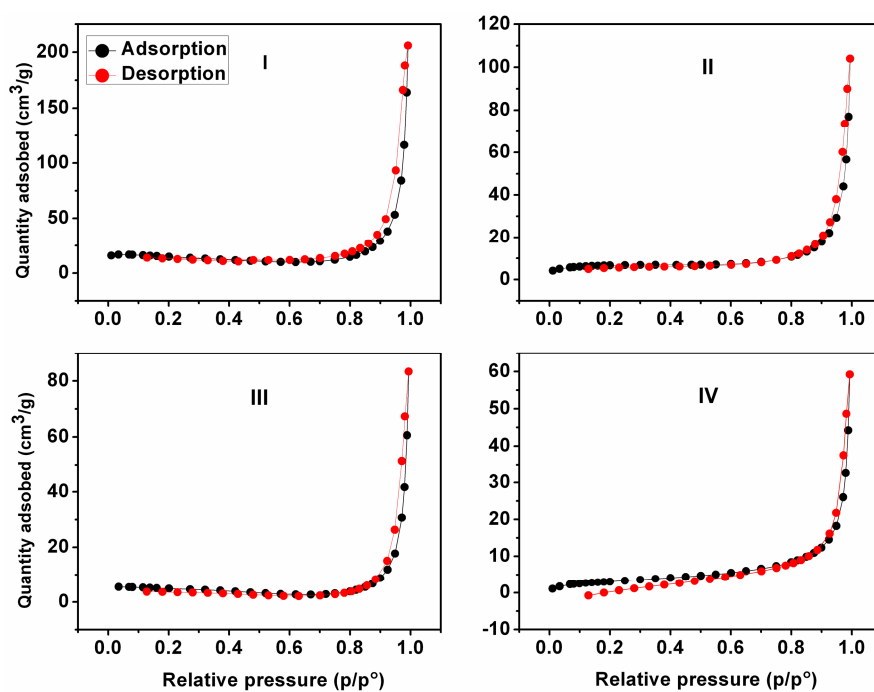**Figure 33.** *Nitrogen adsorption-desorption isotherms for four samples of manganite with different particle size: I) 15 nm, II) 22 nm, III) 26 nm and IV) 29 nm.*
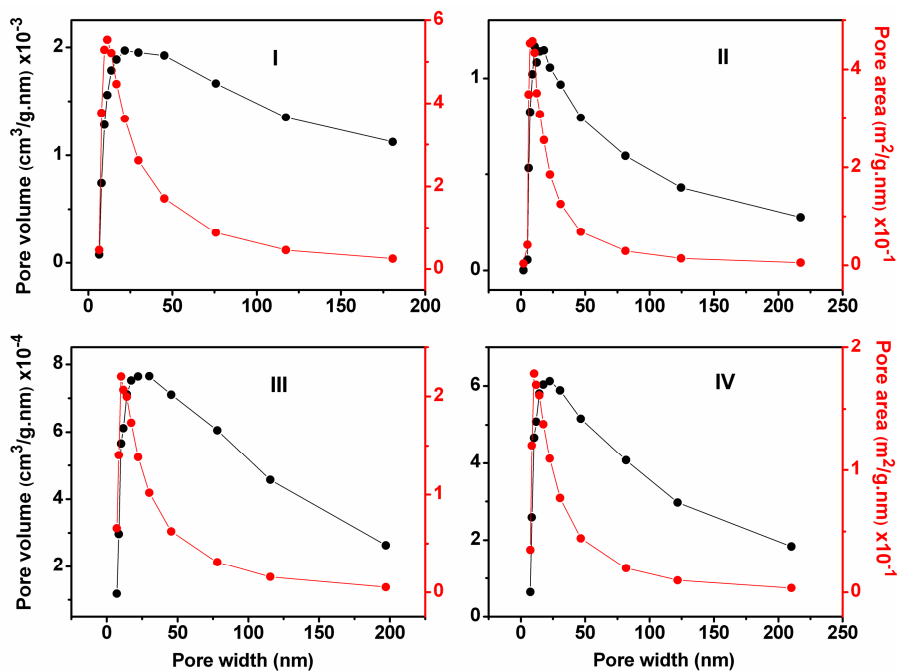
Figure 34. *Pore width-pore volume and pore width-pore area relationships constructed for four different size γ-MnOOH samples: I) 15 nm, II) 22 nm, III) 26 nm and IV) 29 nm.*
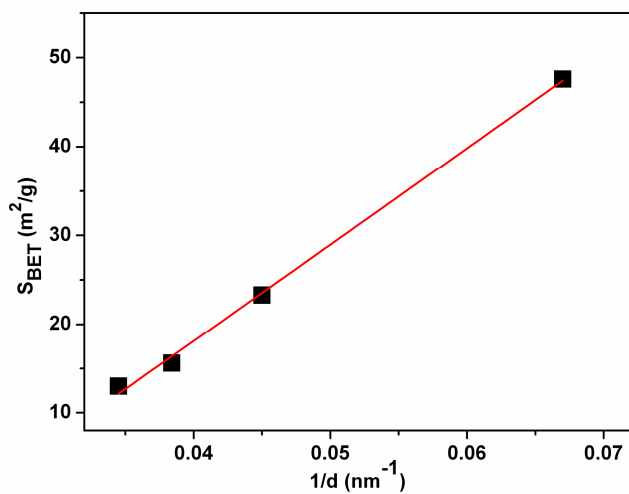

Figure 35. *BET surface area as a function of the grain size of γ-MnOOH samples.*

3.4. Summary and conclusions

♦ Size-selective experiments of γ-MnOOH nanorods were carried out by modifying the experimental parameters (time, temperature and total Mn concentration in the solution), as a result γ-MnOOH samples with average grain size <d> as low as 14 nm and as large as 36 nm are produced.

♦ The pH of the reaction medium, time, temperature as well as the molar ratio of Mn^{2+}/ MnO_4^- are crucial parameters in the reaction that change the reaction pathway giving rise to formation of various manganese oxide/hydroxide phases.

♦ Significant impact of the anion of the manganese salt (OAc^-, SO_4^{-2} and Cl^-) on the morphological shape of the as-prepared manganite nanorods is established by SEM investigations. For the first time ultra-long γ-MnOOH nanorods are prepared in this work via the redox reaction of either $MnCl_2$ or $MnSO_4$ with $KMnO_4$ through modifying the pH of the reaction medium.

♦ The alkali metal cation of the permanganate salt (K, Na and Cs) was proven to have an enormous influence on the morphology of as-synthesized manganite nanorods. The results showed that usage of $KMnO_4$ leads to formation of regular shape manganite nanorods. However, Na or Cs permanganate hinders the uniform growth of such nanorods, consequently, manganite samples with deformed rod-like morphology are obtained.

♦ Reaction solvent is an important parameter that can result in varying both of the reaction pathway and the grain size of the so obtained manganese oxide/hydroxide phases.

❖ In Pure water single phase manganite (1x1 tunnelled structure) are synthesized from the redox reaction between manganese acetate and $KMnO_4$.

❖ A new synthetic route is developed for feitknechtite synthesis (layer type manganese oxidehydroxide) for the first time on the basis of replacement of water entirely by acetone.

❖ Using pure ethanol, manganese spinel (lower oxidation state) is formed as a result of consumption of part of $KMnO_4$ in a side redox reaction with ethanol.

❖ Size-control over the synthesized manganese oxide/hydroxide nanoparticles is achieved by replacement of water partially with ethanol. Shrinkage of the size takes place by increasing of ethanol content in water.

♦ The results showed that many important physical properties are size-dependent:

    ❖ Significantly, the thermal stability of the manganite nanoparticles (as well as its decomposition products) increases with increasing its particle size. This feature is important for application purposes.

    ❖ Surface properties were studied, the results revealed that the surface area increases with decreasing grain size which is important for purpose of catalysis.

References

1. Kohler, T.; Armbruster, T.; Libowitzky, E. Hydrogen bonding and Jahn-Teller distortion in groutite, alpha-MnOOH, and manganite, gamma-MnOOH, and their relations to the manganese dioxides ramsdellite and pyrolusite. *J. Solid State Chem.* **1997,** *133* (2), 486-500.

2. Umek, P.; Zorko, A.; Arcon, D. Magnetic properties of transition-metal oxides: From bulk to nano. In *Ceramics Science and Technology*, Wiley-VCH Verlag GmbH & Co. KGaA: 2010; pp 791-833.

3. Peng, X.; Ichinose, I. Green-chemical synthesis of ultrathin beta-MnOOH nanofibers for separation membranes. *Adv. Funct. Mater.* **2011,** *21* (11), 2080-2087.

4. Chen, X.; Wang, C.; Ye, F.; Zhu, Q.; Du, G.; Zhong, Y.; Peng, X.; Jiang, J. Phase transition of manganese (oxyhydr) oxides nanofibers and their applications to lithium ion batteries and separation membranes. *Cryst. Eng. Comm.* **2012,** *14* (9), 3142-3148.

5. Novak, A. Hydrogen bonding in solids correlation of spectroscopic and crystallographic data. In *Large Molecules*, 18 ed.; Springer Berlin Heidelberg: 1974; pp 177-216.

6. Spectral Database for Organic Compounds SDBS. *http://sdbs. db. aist. go. jp/sdbs/cgi-bin/direct_frame_top. cgi* **2015**.

7. Greenberg J.; Hallgren L.J. Infrared Spectra of NaOH Above and Below the Melting Point. *J. Chem. Phys.* **1961,** *35* (1), 180-182.

8. Zhang, W. X.; Yang, Z. H.; Liu, Y.; Tang, S. P.; Han, X. Z.; Chen, M. Controlled synthesis of Mn_3O_4 nanocrystallites and MnOOH nanorods by a solvothermal method. *J. Cryst. Growth* **2004,** *263* (1-4), 394-399.

9. Bernard, M. C.; Goff, A. H. L.; Thi, B. V.; Detorresi, S. C. Electrochromic reactions in manganese oxides : Raman analysis. *J. Electrochem. Soc.* **1993,** *140* (11), 3065-3070.

10. Julien, C. M.; Massot, M.; Poinsignon, C. Lattice vibrations of manganese oxides: Part I. Periodic structures. *Spectrochim. Acta, Part A* **2004,** *60* (3), 689-700.

11. Gao, T.; Krumeich, F.; Nesper, R.; Fjellvag, H.; Norby, P. Microstructures, surface properties, and topotactic transitions of manganite nanorods. *Inorg. Chem.* **2009,** *48* (13), 6242-6250.

12. Gao, T.; Glerup, M.; Krumeich, F.; Nesper, R.; Fjellvåg, H.; Norby, P. Microstructures and spectroscopic properties of cryptomelane-type manganese dioxide nanofibers. *J. Phys. Chem. C* **2008,** *112* (34), 13134-13140.

13. Abbas, H.; Nasser, S. A. Hydroxyl as a defect of the manganese dioxide lattice and its applications to the dry cell battery. *J. Power Sources* **1996,** *58* (1), 15-21.

14. Rausch R. Das Periodensystem der Elemente online. *http://www. periodensystem-online. de/index. php?el=25&id=redox* **2015**.

15. Brown, I. D.; Shannon, R. D. Empirical bond-strength-bond-length curves for oxides. *Acta Cryst. A* **1973,** *29* (3), 266-282.

16. Shannon, R. D. Revised effective ionic radii and systematic studies of interatomic distances in halides and chalcogenides. *Acta Cryst. A* **1976,** *32* (5), 751-767.

17. Liang, X.; Wang, X.; Zhuang, J.; Chen, Y.; Wang, D.; Li, Y. Synthesis of nearly monodisperse iron oxide and oxyhydroxide nanocrystals. *Adv. Funct. Mater.* **2006,** *16* (14), 1805-1813.

18. Ishii, M.; Nakahira, M.; Yamanaka, T. Infrared absorption spectra and cation distributions in (Mn, Fe)$_3$O$_4$. *Solid State Commun.* **1972,** *11* (1), 209-212.

19. Nakamoto, K. *Infrared and Raman Spectra of Inorganic and Coordination Compounds: Applications in coordination, organometallic, and bioinorganic chemistry;* Wiley: 1997.

20. Rollett, A.; Humphreys, F. J.; Rohrer, G. S. *Recrystallization and Related Annealing Phenomena;* Elsevier Science: 2004.

21. Strunz, H. Beitrag zum Pyrolusitproblem. *Naturwissenschaften* **1943,** *31* (7-8), 89-91.

22. Feitknecht, W.; Marti, W. Über die oxydation von mangan(II)-hydroxyd mit molekularem sauerstoff. *Hev. Chim. Acta* **1945,** *28* (1), 129-148.

23. Feitknecht, W.; Brunner, P.; Oswaldw, H. R. Über den einfluß der feuchtigkeit auf die oxydation von manganhydroxid durch molekularen sauerstoff. *Z. Anorg. Allg. Chem.* **1962,** *316* (3-4), 154-160.

24. Meldau, R.; Newesely, H.; Strunz, H. Zur kristallchemie von feitknechtit, β-MnOOH. *Naturwissenschaften* **1973,** *60* (8), 387.

25. Portehault, D.; Cassaignon, S.; Baudrin, E.; Jolivet, J. P. Evolution of nanostructured manganese (oxyhydr)oxides in water through MnO$_4^-$ reduction. *Cryst. Growth & Des.* **2010,** *10* (5), 2168-2173.

26. Oxidation reactions of aldehydes and ketones. *http://www. tutorvista. com/ content / chemistry/chemistry-iv/oxygen-ii/oxidation-aldehydes-ketones. php* **2014**.

27. Feitknechtite.*https://www.mineralienatlas.de/lexikon/index.php/MineralData?mineral =Feitknechtite* **2014**.

28. Feng, X.; Tan, W.; Liu, F.; Huang, Q.; Liu, X. Pathways of birnessite formation in alkali medium. *Sci. China Ser. D-Earth Sci.* **2005,** *48* (9), 1438-1451.

29. Auerbach, S. M.; Carrado, K. A.; Dutta, P. K. *Handbook of Layered Materials;* CRC Press: 2004.

30. Pansu, M.; Gautheyrou, J. *Handbook of Soil Analysis: Mineralogical, Organic and Inorganic Methods;* Springer Berlin Heidelberg: 2007.

31. Cöelfen, H.; Antonietti, M. *Mesocrystals and Nonclassical Crystallization;* Wiley: 2008.

32. Holland, K. L.; Walker, J. R. Crystal structure modeling of a highly disordered potassium birnessite. *Clays Clay Miner.* **1996,** *44* (6), 744-748.

33. Fang, Z.; Tang, K.; Gao, L.; Wang, D.; Zeng, S.; Liu, Q. Facile and large-scale synthesis of single-crystalline manganese oxyhydroxide/oxide nanostructures. *Mater. Res. Bull.* **2007,** *42* (9), 1761-1768.

34. Folch, B.; Larionova, J.; Guari, Y.; Guerin, C.; Reibel, C. Synthesis of MnOOH nanorods by cluster growth route from $[Mn_{12}O_{12}(RCOO)(16)(H_2O)(n)]$ (R = CH_3, C_2H_5). Rational conversion of MnOOH into Mn_3O_4 or MnO_2 nanorods. *J. Solid State Chem.* **2005,** *178* (7), 2368-2375.

35. Everett.D.H. Manual of symbols and terminology for physicochemical quantities and units. Appendix II. Definitions, terminology, and symbols in colloid and surface chemistry. *Pure Appl. Chem.* **1972,** *31* (4), 577-638.

36. Sing, K. S. W.; Everett, D. H.; Haul, R. A. W.; Moscou, L.; Pierotti, R. A.; Rouquerol, J.; Siemieniewska, T. Reporting physisorption data for gas/solid systems with special reference to the determination of surface area and porosity. *Pure Appl. Chem.* **1985,** *57* (4), 603-619.

Chapter 4

Controlled synthesis of Mn$_5$O$_8$ and β-MnO$_2$ nanorods via thermal decomposition of γ-MnOOH precursor: Characterization and magnetic properties

4. Introduction

Manganite was frequently used as a precursor for synthesis of other manganese oxides, i.e., β-MnO_2, Mn_5O_8, Mn_2O_3 and Mn_3O_4. The corresponding oxides can be obtained via calcination of the precursor under different atmospheres.[1-3]

Many reports have discussed the thermal behavior of manganite, several decomposition sequences were proposed under different atmospheres.[1-3] According to these reports, it is not so obvious, why and how the decomposition of γ-MnOOH can pursue various pathways upon heating under different conditions. Therefore, we will present in this chapter a clarification of the thermal behavior of manganite in air and inert gas atmosphere.

Focusing on Mn_5O_8 and β-MnO_2, the effect of calcination parameters on the decomposition of manganite and subsequent formation of such products will be studied. Especially, the influence of calcination temperature and accessibility of oxygen to the manganite (in terms of the size of the glass tube in which calcination process takes place) will be examined. For this purpose manganite will be heat-treated isothermally and non-isothermally.

According to the work of Norby et.al.,[3] it is claimed that Mn_5O_8 nanorods (yet, not clean according to XRPD) can be produced via calcination of manganite under nitrogen flow. No attention has been paid to the importance of oxygen pressure in the formation of Mn_5O_8 from manganite. Moreover, the magnetic behavior of such Mn_5O_8 nanocrystals revealed the presence of a significant amount of spinel impurities. In addition, the presence of such impurities has not been clearly interpreted.

In our work we will present a modified preparation method of Mn_5O_8 by calcination of manganite just in air, with a rationalization of the formation of minute spinel impurities. X-ray single phase Mn_5O_8 nanoparticles are accessible by the described method. Magnetic behaviour for different Mn_5O_8 samples will be studied in more details. Details of the structure of Mn_5O_8 will be discussed in this chapter.

4.1. Isothermal heat treatment of manganite

Initially, the solid product obtained from refluxing of $Mn(OAc)_2$ and $KMnO_4$ in aqueous medium for 27 h was identified by means of XRD analysis as shown in Figure 1. All observed reflections are consistently indexed to single phase γ-MnOOH with monoclinic unit cell and space group $P2_1/c$. The lattice parameters are a = 5.3130(3) Å, b = 5.2842(2) Å, c = 5.3059(3) Å and β = 114.404(3)°. Estimation of the mean particle size from band broadening using Scherrer's formula was done. An approximate grain size of 28 nm was found.

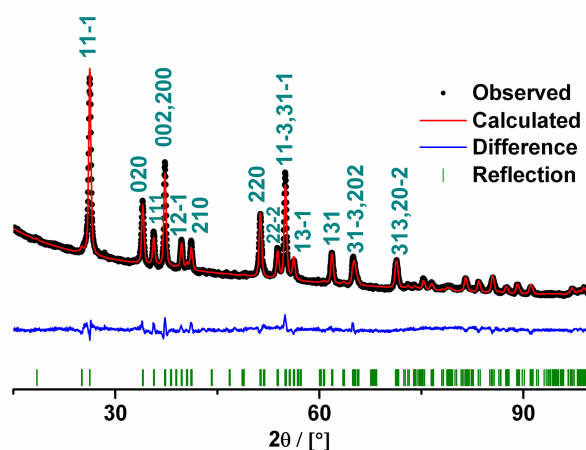***Figure 1.*** *Rietveld refinement for the as-prepared γ-MnOOH precursor (~28 nm), Laue indices are shown.*

The precursor was then investigated using IR analysis. In the IR spectrum (previously shown in chapter 3) two groups of bands, located between 400-700 and 1000-1200 cm^{-1}, are pronounced which are assigned to Mn-O stretching vibrations and OH bending modes (γ-OH, δ-2-OH, δ-1-OH), respectively.[4] The wide band at 2656 cm^{-1} can be ascribed to OH stretching vibration due to hydrogen bond O—H…O, whereas the band located at 2072 cm^{-1} is considered as a combination band of the OH-stretching mode at 2656 cm^{-1} (f1) and the excited lattice mode at 589 cm^{-1} (f2). Thus, by f = f1 – f2; i.e., 2656 – 589 = 2067 cm^{-1}. The value obtained is close to the reported 2060 cm^{-1} by Kohler et.al.[5]

Calculation of SOF (Site Occupancy Factor) of Mn^{3+} from Rietveld analysis done for the precursor (Figure 1) indicates that all Wyckoff sites containing Mn^{3+} are occupied which refer to ideal γ-MnOOH structure without any recognizable defects (the refinement data are listed in Table 1&2). The refinement was based on the assumption that all oxygen sites are fully occupied. This observation was further confirmed by TGA analysis, where excess mass of about 0.5% was found. This mass is essentially attributed to water. Density measurements for

the precursor revealed that it has a density of 4.39(0.05) g/cm^3 compared to 4.31 g/cm^3 calculated from Rietveld refinement, indicating a non-defected manganite structure.

Table 1. Refinement data of manganite precursor prepared under reflux, <d> ~28 nm (refined according to 84949-ICSD).

	Manganite	*Literature[7]*
Space group (No.)	P 2_1/c (14)	P 2_1/c (14)
a / Å	5.3127(2)	5.2983(3)
b / Å	5.2846(2)	5.2782(2)
c / Å	5.3064(4)	5.3067(3)
β / •	114.410(3)	114.401(2)
V/ 10^6 pm^3	135.664	135.148(12)
ρ / g/cm^3	4.31	4.32
Z	4	4
R (expected) / %	1.377	
R (profile) / %	1.033	
R (weighted profile) / %	1.316	
R (Bragg) / %	0.971	
GOF	0.914	

Radiation is Cu-$K\alpha$ and the type of profile fit is Pseudo-Voigt

Table 2. Wyckoff positions, atomic fractional coordinates and isotropic displacement parameters B of manganite precursor refined according to 84949-ICSD.

Atom	*Wyck.*	*x*	*y*	*z*	*B/ 10^4 pm^2*
Mn1	4e	0.248(3)	0.5150(5)	0.243(3)	0.87(3)
O1	4e	0.161(5)	0.110(3)	0.385(5)	1.37(3)
O2	4e	0.632(4)	0.366(3)	0.390(4)	0.94(3)

Isothermal heat treatment was performed by calcination of the manganite precursor in air at varied calcination temperatures. A calcination time of 1 h was chosen. Using the same amount of the precursor (~30 mg) and the same size for the glass tube (length (ℓ) = 10 cm and diameter (Φ) = 1 cm) in which the calcination process was performed, distinctive products were obtained. XRD analyses were made for the corresponding calcination products, the results are shown in Figure 2. Table 3 lists the various decomposition products of manganite and their corresponding average particle sizes <d>.
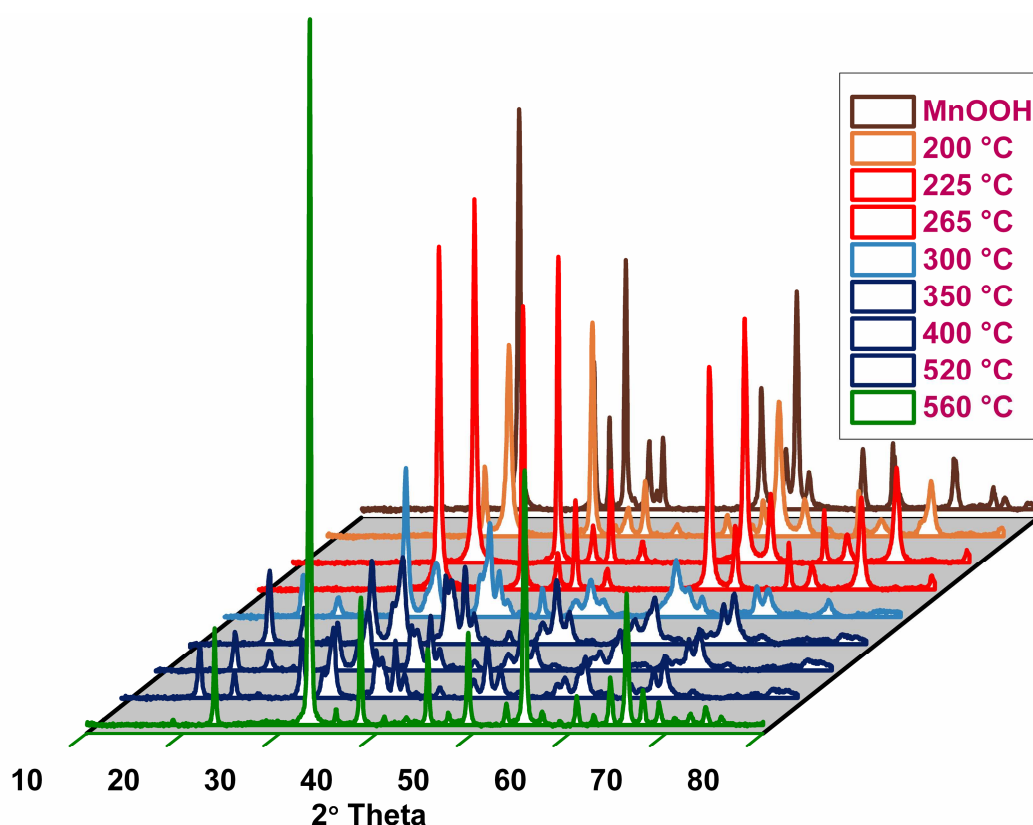
Figure 2. *XRD patterns of γ-MnOOH and its annealing products obtained via isothermal heat treatment (t = 1 h) at various calcination temperatures. At 200 °C; a mixture of MnOOH+β-MnO₂, 225-265 °C; β-MnO₂, 300 °C; mixture of β-MnO₂ + Mn₅O₈, 350-520 °C; Mn₅O₈ and 560 °C; α-Mn₂O₃. The same amounts of the precursor (~30 mg) were used, calcination occurs in the same size glass tubes each with ℓ = 10 cm and Φ = 1 cm.*

Table 3. Decomposition products produced by calcination of manganite precursor at different temperatures along with their particle sizes estimated using Scherrer's equation.

Temp. / °C	*225-265*	*350-520*	*560*	*1000*
Product	β-MnO₂	Mn₅O₈	α-Mn₂O₃	α-Mn₃O₄
<d> / nm	23-24	16-19	30	44

From 3D representation of XRD patterns we can see that, by calcination at 200 °C manganite transforms to pyrolusite (β-MnO_2). Minor impurities related to γ-MnOOH could be recognized which implies that some of manganite is still un-decomposed at this low temperature. XRD-clean β-MnO_2 (space group P $4_2$/m n m (136)) is obtained by rising the temperature up to 225 °C (equation 1). The lattice parameters for this β-MnO_2 sample are a = 4.4030(2) Å and c = 2.8742(1) Å that match with those found in literature (a = 4.3983(3) Å and c = 2.8730(3) Å).[6] Moreover, a single phase of β-MnO_2 is still obtained by increasing the calcination temperature up to 265 °C. By elevating the annealing temperature to about 300 °C manganite transforms directly to Mn_5O_8, though minute impurities of β-MnO_2 coexist.

$$4\,\gamma\text{-MnOOH} + O_2 \rightarrow 4\,MnO_2 + 2\,H_2O \tag{1}$$
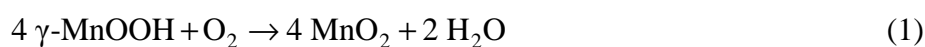
XRD single phase Mn_5O_8 samples (monoclinic, space group C 1 2/m 1 (12)) are obtained by heating the precursor in a temperature range of 350 °C - 520 °C. This process can be described by the following equation:

$$20\,\gamma\text{-MnOOH} + O_2 \rightarrow 4\,Mn_5O_8 \ + \ 10\,H_2O \tag{2}$$
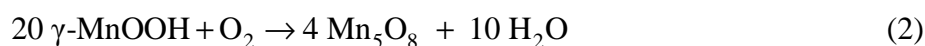
Heat treatment of the precursor at 560 °C leads to formation of bixbyite, α-Mn_2O_3. By calcination of manganite at 1000 °C, hausmannite; α-Mn_3O_4 is produced (Figure 3).
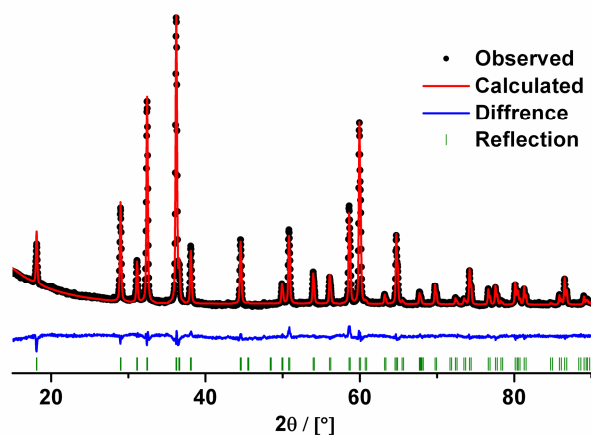
Figure 3. *Rietveld refinement of the calcination product of γ-MnOOH precursor obtained at 1000 °C in open air, Mn₃O₄ (refined according to ICSD-31094).*

It is noteworthy that the former results do not represent decomposition sequences for manganite; the whole approach can be described by Figure 4 which means that manganite is used as starting material for the synthesis of the corresponding manganese oxides depending on the calcination temperature.
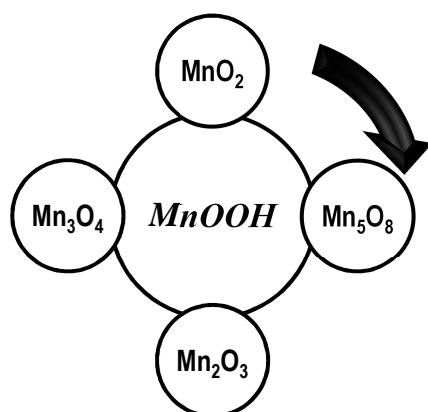
Figure 4. *Schematic representation of the calcination products of manganite by rising calcination temperature.*

    The former results were further confirmed by IR analyses performed for the decomposition products obtained at different calcination temperatures. The magnified sections for the IR spectra of the products in the range of 400-1200 cm^{-1} are shown in Figure 5. The positions of the absorption bands taken from IR spectra are listed in Table 4 along with their assignments.
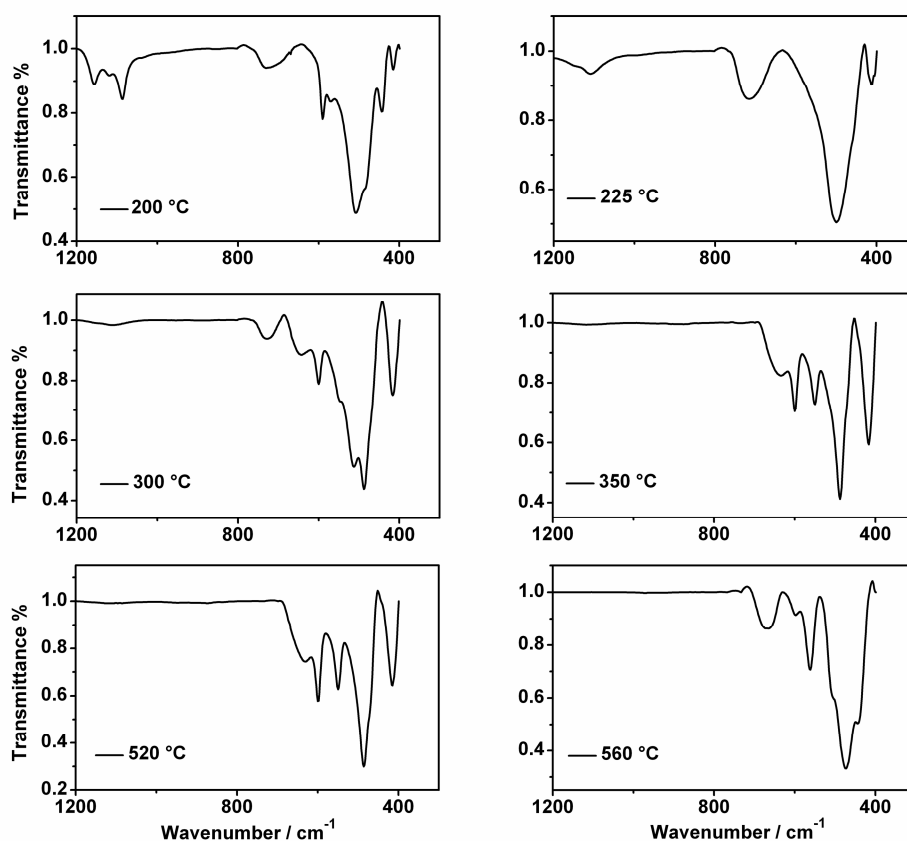
Figure 5. *IR spectra of the calcination products of γ-MnOOH magnified in the range of 400-1200 cm^{-1}: 200 °C; β-MnO$_2$ + γ-MnOOH, 225 °C; β-MnO$_2$, 300 °C; Mn$_5$O$_8$ + β-MnO$_2$, 350-520 °C; Mn$_5$O$_8$, 560 °C; α-Mn$_2$O$_3$.*

Table 4. IR absorption bands for manganite and its decomposition products, positions and assignments.

	$\upsilon(Mn\text{–}O)$ /cm^{-1}	OH bending / cm^{-1}	OH str./ cm^{-1}
γ-MnOOH	437, 476 and 587	1082, 1116 and 1152	2667
β-MnO$_2$	409, 499 and 722	–	–
Mn$_5$O$_8$	417, 488, 550, 600 and 634	–	–
α-Mn$_2$O$_3$	562, 598 and 666	–	–

Interestingly, three absorption bands are detected in the IR spectrum of the sample obtained by calcination at 200 °C situated in 1000-1200 cm^{-1} range (Figure 5), these can be assigned to O–H···O bending modes of γ-MnOOH (ν-OH, δ-2-OH and δ-1-OH),[4] implying the presence of γ-MnOOH as impurities admixed to the β-MnO$_2$ sample. Three absorption peaks at 722, 499 and 409 cm^{-1} are observable in the IR spectrum of the sample prepared by calcination of the precursor at 225 °C which are typical for single phase β-MnO$_2$ and arising from the Mn-O stretching, bending and wagging modes, respectively.[8,9]

The spectrum of the sample obtained by annealing at 300 °C exhibits an absorption peak located at 720 cm^{-1} which is ascribed to the presence of impurities related to β-MnO$_2$. IR spectra for the samples obtained at temperatures of 350-520 °C are typical ones for Mn$_5$O$_8$ and match very well with those reported before for Mn$_5$O$_8$.[10] The absorption bands for the sample produced by calcination at 560 °C coincide with Mn-O stretching modes for α-Mn$_2$O$_3$.[10]

4.2. Non-isothermal heat treatment of manganite

Non-isothermal heat treatment was made by running TGA/DSC for manganite precursor (~28 nm) from ambient temperature to 1000 °C under air flow (Figure 6).
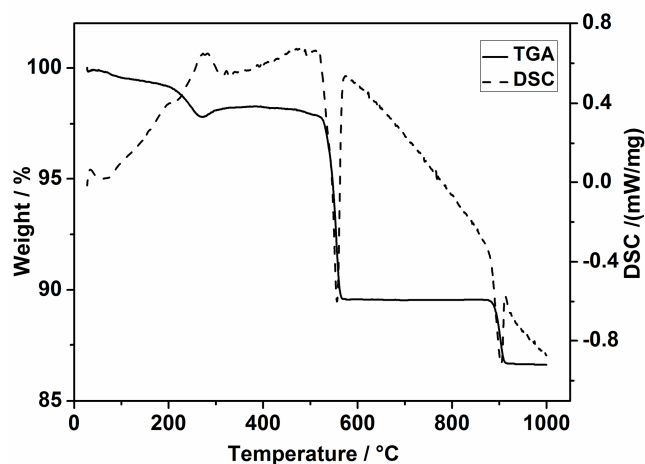
Figure 6. *TGA/DSC of γ-MnOOH (~28 nm) under ambient air flow, heating rate of 5 K/min was used.*

From the TG curve depicted in Figure 6 and according to the theoretical expectations manganite loses adsorbed water firstly at ~130 °C. The second mass loss at ~275 °C is ascribed to decomposition of manganite giving rise to formation of β-MnO$_2$. In the third decomposition step occurs at ~575 °C pyrolusite is reduced to bixbyite, α-Mn$_2$O$_3$ which finally undergoes further reduction at 920 °C to hausmannite. These expectancies were evidenced by comparison of the calculated and found mass losses. The results are presented in Table 5. Moreover, XRD analyses (Figure 7) were made for the products obtained at the end of each decomposition step revealing that we have the sequence as proposed which is in accordance with that reported before.[2]

Table 5. Calculated, found mass losses and their assignments of the decomposition products of manganite under air flow.

Mass loss step	I	II	III	IV
Calcd. / %	–	1.1	9.2	3.4
Found / %	0.5	1.2	8.3	3.0
Assignment	H$_2$O	β-MnO$_2$	α-Mn$_2$O$_3$	α-Mn$_3$O$_4$
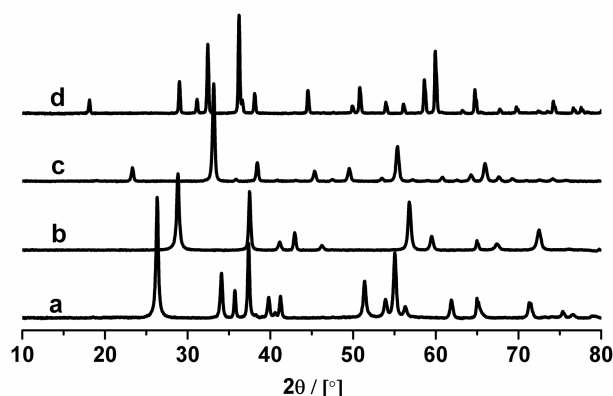
Figure 7. *XRD patterns of γ-MnOOH and its decomposition products obtained at the end of each mass loss extracted from thermogravimetric analysis: a) γ-MnOOH, b) 400 ºC; β-MnO₂, c) 600 ºC; α-Mn₂O₃ and d) 1000 ºC; α-Mn₃O₄.*

We have submitted such results of TGA in this work for two purposes: firstly to show the consistency of our results with those reported in literature,[11] and secondly to depict the difference between isothermal and non-isothermal heat treatments for manganite.

4.3. Isothermal and non-isothermal heat treatment of β-MnO₂ and Mn₅O₈

Non-isothermal analysis was carried out for β-MnO₂ sample (~20 nm) via TGA from room temperature up to 400 °C and repeated once again by elevating the temperature up to 600 °C under air flow. The isothermal annealing (1 h) was done utilizing the same amount of pyrolusite (~30 mg) in the same size glass tube at two different temperatures near to 400 and 600 °C. These studies were implemented to substantiate whether or not Mn_5O_8 could be produced as an intermediate between β-MnO₂ and α-Mn₂O₃.[12] The products obtained in both cases at various temperatures were examined by XRD analysis (Figure 8 and 9).

Figure 8. *XRD patterns of a) β-MnO₂ sample (prepared by calcination of manganite at 265 °C, ~20 nm) and its heating products obtained by TGA at b) 400 °C; β-MnO₂ persists and c) 600 °C; α-Mn₂O₃) using heating rate of 5 K/min.*

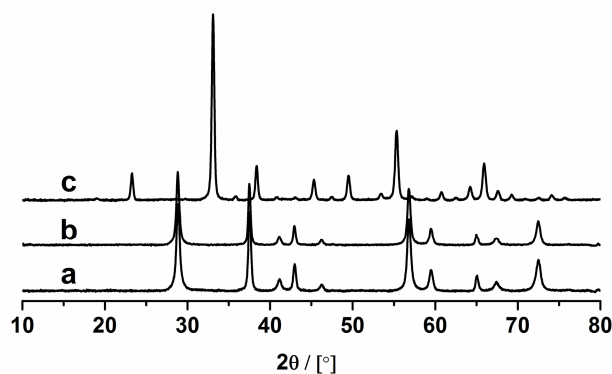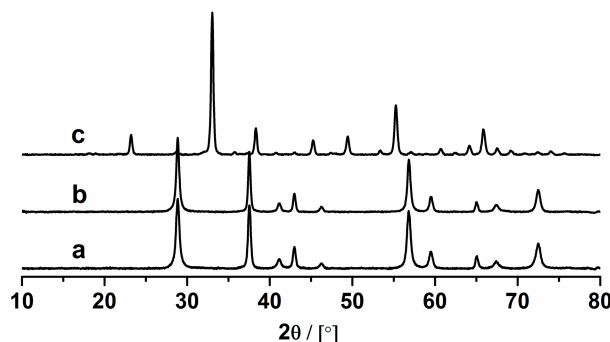***Figure 9.*** *XRD patterns of a) β-MnO₂ and its annealing products obtained by isothermal heat treatment for 1 h in air at b) 375 °C; β-MnO₂ persists and c) 560 °C; α-Mn₂O₃.*

Seemingly, neither isothermal nor non-isothermal heat treatment of β-MnO$_2$ (at 400 °C) leads to formation of Mn$_5$O$_8$ in contrast to what was reported before.[12] Instead, enlargement of the grain size of β-MnO$_2$ sample from 20 to 25 nm takes place in both cases. Upgrading the temperature of annealing up to 600 °C leads to reduction of β-MnO$_2$ to α-Mn$_2$O$_3$. Consequently, we can infer that Mn$_5$O$_8$ is not an intermediate product in such processes and is formed right away from manganite by annealing in open air atmosphere under conditions which enable low accessibility of oxygen to the precursor.

Mn$_5$O$_8$ sample was then heat-treated under either isothermal or non-isothermal conditions at 480 and 560 °C in air. At a temperature of ~480 °C no phase transition is observed whereas annealing of Mn$_5$O$_8$ at 560 °C gives rise to formation of α-Mn$_2$O$_3$ as evidenced by XRD results illustrated in Figure 10.
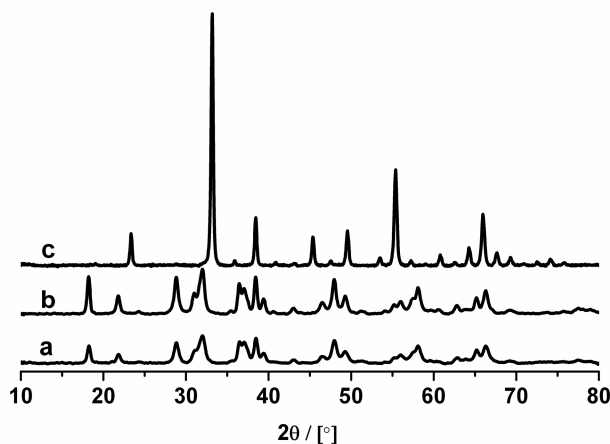
Figure 10. *XRD diffractograms of a) Mn₅O₈ prepared by calcination of the manganite precursor at 350 ºC for 1 h and its annealing products obtained (isothermal heat treatment for 1 h) at b) 480 °C; Mn₅O₈ persists and c) 560 °C; α-Mn₂O₃.*

The above results came at variance to what is reported before.[12] According to that report, Mn_5O_8 is considered as an intermediate product between β-MnO_2 and α-Mn_2O_3 through heating at or above 300 °C. It was considered that the coexistence of some β-MnO_2 intergrown with Mn_5O_8 as an evidence for the production of Mn_5O_8 from β-MnO_2. A possible interpretation for this formation is by taking into the account the amount of oxygen in contact with manganite that influences unequivocally the oxidation pathway, leading to a variety of oxidation products.

The following sequences for both isothermal and non-isothermal heat treatment of manganite depending on the accessibility of oxygen are constructed on the basis of the presented results.
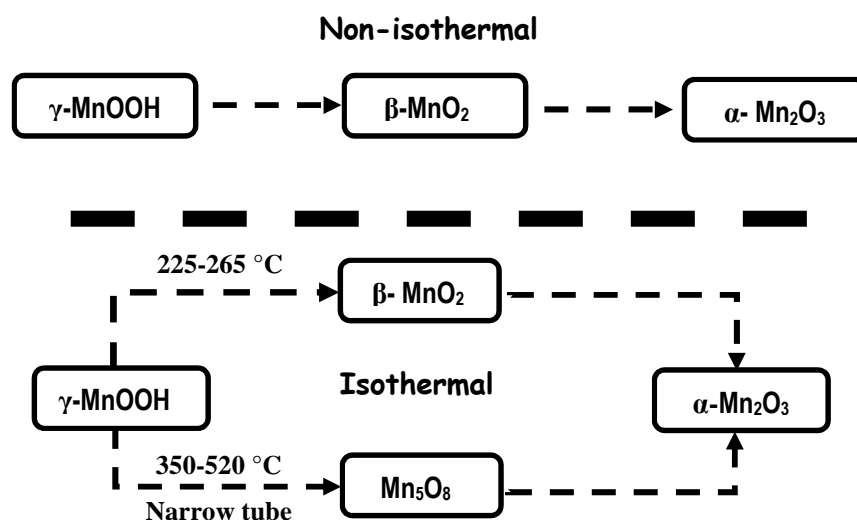
Figure 11. *Schematic representation for the different pathways adopted during the decomposition of γ-MnOOH under isothermal and non-isothermal heat treatment at various temperatures.*

In spite of the fact that both of these processes were performed under air atmosphere however, there is a pronounced difference between them. The question now arises what is the provenance of this divergence between isothermal and non-isothermal heat treatment of γ-MnOOH? In order to answer this question very simple experiments were carried out. Two parallel calcinations for manganite precursor at the same temperature of 400 °C and for the same time of 1 h were performed using two glass tubes of different sizes; one is shorter in length and narrower in diameter (ℓ = 10 cm, Φ = 1 cm) and the second is wider and longer (ℓ = 20 cm, Φ = 3 cm). XRD was used to examine the products obtained (Figure 12).
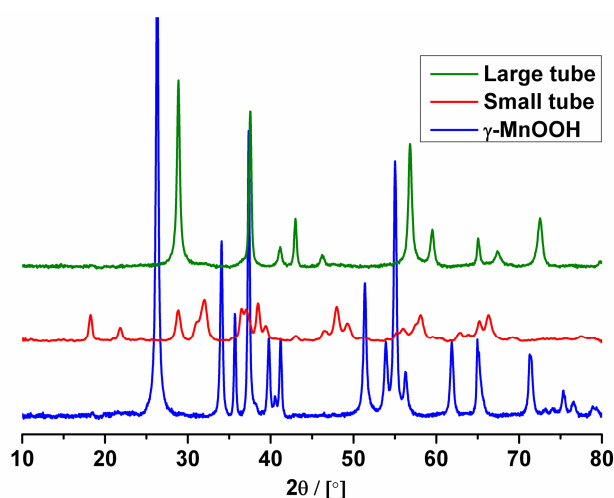
Figure 12. *XRD diffractograms of γ-MnOOH and its products obtained by isothermal heat treatment at 400 °C for 1 h, using small size glass tube (Mn_5O_8) and large size tube (β-MnO_2).*

Seemingly, calcination in narrow tubes leads to formation of Mn_5O_8 and that performed in a wide tube results in formation of β-MnO_2. This can be explained by taking into the account that the amount of oxygen accessible to the precursor in the narrow tube is much less than that for the wide one. Taking into consideration equations 1 and 2 we can realize that each one mole of manganite needs 1/20 mole oxygen to produce Mn_5O_8 whereas 1/4 mole of oxygen is necessary for production of β-MnO_2. Non-isothermal heat treatment of manganite unequivocally results in formation of MnO_2 where a stream of air rich in oxygen flows over manganite precursor implying a higher partial oxygen pressure exerted over the surface of manganite. So we can draw the conclusion that the partial pressure of oxygen is the key factor that governs these transformation, higher pressure is exerted in case of air flow rich in oxygen, the case of non-isothermal heat treatment as well as for isothermal conditions using large size glass tubes.

4.4. Thermal stability of pyrolusite and Mn_5O_8

Comparison of the thermal stability of Mn_5O_8 nanocrystals (~18 nm) with that of β-MnO_2 nanocrystals (~20 nm) was achieved by means of TGA/DSC analyses (Figure 13).
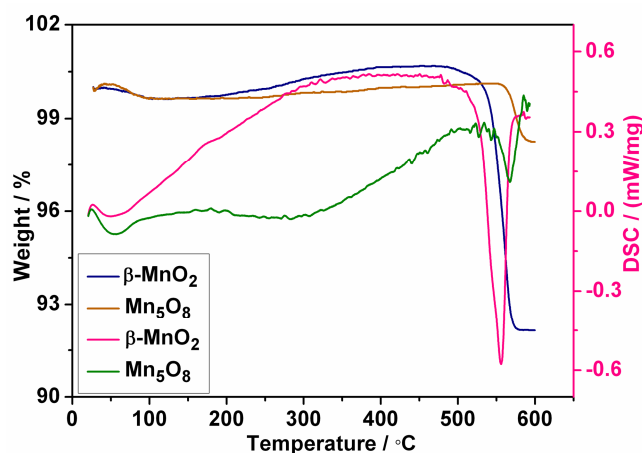
Figure 13. *TGA/DSC of β-MnO₂ and Mn₅O₈ under air flow (heating rate of 5 K/min).*

TG curves reveal that the inflection point located at 486 °C in the TG curve of β-MnO_2 may be taken as a characteristic temperature T_i at which the decomposition process takes place. For Mn_5O_8 the point of inflection for decomposition is monitored at about 558 °C. These results indicate that Mn_5O_8 is more stable than β-MnO_2. Taking into account that both, Mn_5O_8 and β-MnO_2, can be considered as metastable states relative to γ-MnOOH and α-Mn_2O_3, yet no clear evidence was reported for the metastibilty of Mn_5O_8. DSC results show that endothermic peaks are recognized in both cases. For the decomposition of Mn_5O_8 the enthalpy change is found ~22.1 kJ/mole whereas for β-MnO_2 the enthalpy change is 24.5 kJ/mole. Mass losses in both cases are listed in Table 6 along with their grain sizes and the values of T_i.

Table 6. Calculated, found mass losses and their assignments of the decomposition products of β-MnO_2 (<d> ~20 nm) and Mn_5O_8 (<d> ~18 nm), T_i values are taken from TGA/DSC performed under air flow.

Sample	*Calcd. / %*	*Found / %*	*T_i / °C*	*assignment*
β-MnO₂	9.19	7.95	486	α-Mn_2O_3
Mn₅O₈	1.98	1.73	558	α-Mn_2O_3

4.5. Thermal behaviour of manganite under argon atmosphere

As it is apparent from TG curve shown in Figure 14, TGA/DSC analysis for manganite under argon flow revealed that manganite decomposes upon heating in a two-step process.
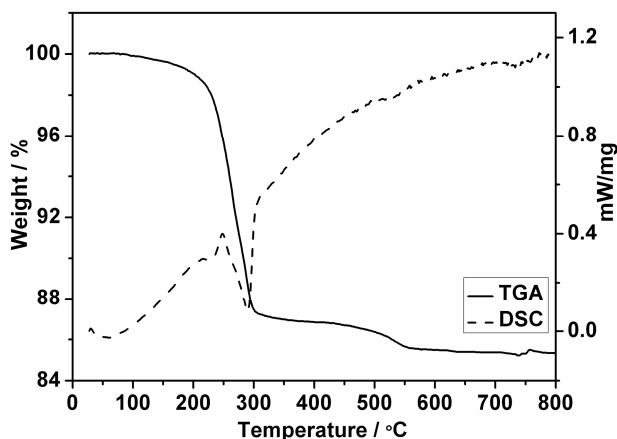
Figure 14. *TGA/DSC of γ-MnOOH under argon flow, heating rate of 5 K/min was used.*

The interpretation of these mass losses is not obvious by taking into account equation (3).[3] Accordingly, the first mass loss is expected to be 10.22% (found 11.9%) and the second mass loss should be 10.12% (found 1.4%) in contrast to what we detected. This difference reflects the fact that the decomposition of manganite under argon does not proceed according to equation (3). Therefore, we suggest a revised reaction scheme for the decomposition of manganite which can be represented by the equations 4 and 5.

$$8\ \gamma\text{-MnOOH} \rightarrow \text{Mn}_5\text{O}_8 + \alpha\text{-Mn}_3\text{O}_4 + 4\,\text{H}_2\text{O} \tag{3}$$

$$20\ \gamma\text{-MnOOH} \rightarrow \text{Mn}_5\text{O}_8 + 5\ \alpha\text{-Mn}_3\text{O}_4 + 10\,\text{H}_2\text{O} + \text{O}_2 \tag{4}$$

$$\text{Mn}_5\text{O}_8 \rightarrow 5/3\ \text{Mn}_3\text{O}_4 + 2/3\ \text{O}_2 \tag{5}$$
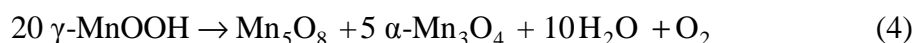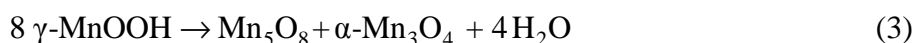
According to equation (4), the estimated mass loss of the 1st step is 12.05% (evolved as a mixture of water vapour and oxygen gas), which is in a good agreement with the found value (11.9%). The second mass loss corresponds also to what equation (5) predicts. Results of TGA/DTA are listed in Table 7 which reflects the matching between found and calculated mass losses according to our suggestion. This hypothesis was further proven by XRD measurements (Figure 15) for the products obtained at the end of each decomposition step which revealed the presence of a mixture of both, Mn_5O_8 and $\alpha\text{-Mn}_3\text{O}_4$ (end of 1st step). Rietveld refinement for such product was made (Figure 16) taking into account that we have a mixture of two oxides, i.e., Mn_5O_8 and Mn_3O_4. Estimation of the content of each component

was done from TGA and compared to that extracted from refinement; the results showed a very good agreement between them as observed in Table 8 indicating that our suggestion was correct. See Table 9 for refinement data.

Table 7. Calculated and found mass losses for decomposition products of γ-MnOOH extracted from TGA/DSC performed under argon atmosphere.

Step	Calcd. / %	Found / %	Assignment
1st	12.05	11.90	$Mn_5O_8 + 5\ Mn_3O_4$
2nd	1.38	1.40	Mn_3O_4
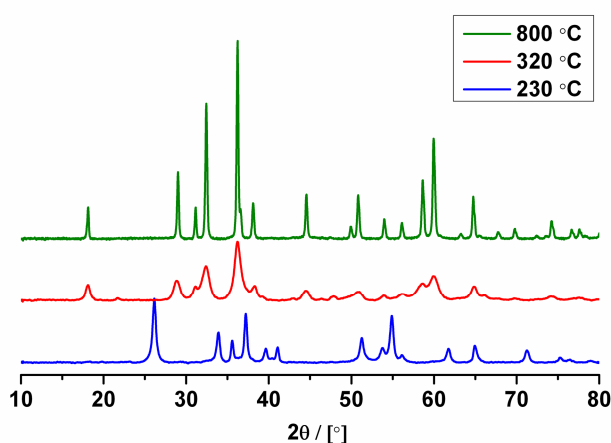
Figure 15. *XRD patterns of γ-MnOOH and its decomposition products obtained at the end of each decomposition step via TGA (Ar, 5 K/min).*
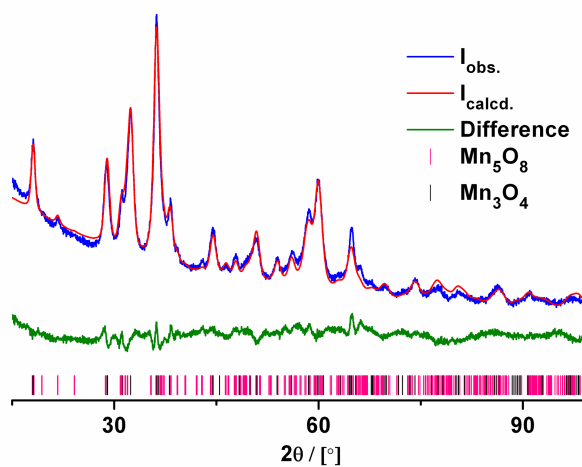
Figure 16. *Rietveld analysis for the residue obtained at the end of first mass loss, 320 °C from thermal decomposition of γ-MnOOH via TGA under argon flow using heating rate of 5 K/min.*

Table 8. Estimation of Mn_5O_8 and α-Mn_3O_4 contents for the residue obtained at the end of the first mass loss, derived from TGA of γ-MnOOH under argon atmosphere and Rietveld analysis for XRD data of that residue.

	Wt % / TGA	*Wt % / XRD*
Mn_5O_8	26.0	26
Mn_3O_4	74.0	74

Table 9. Measurement parameters, structure and refinement data for the residual product obtained at the end of the first mass loss whilst γ-MnOOH is heat-treated under Ar (5 K/min).

	Mn_5O_8	Mn_3O_4
Z	2	4
Formula mass / g/mol	805.37	915.25
Space group (No.)	C 1 2/m 1 (12)	I 4_1/a m d (141)
a / Å	10.388(7)	5.7645(8)
b / Å	5.743(4)	5.7645(8)
c / Å	4.878(3)	9.456(2)
α / °	90	90
β / °	109.55(4)	90
γ / °	90	90
V/ 10^6 pm^3	274.214	314.199
ρ / g/cm^3	4.88	4.84
V	0.6(3)	2.8(1)
W	0.5(1)	-0.02(3)
R (expected) / %	1.259	1.259
R (profile) / %	1.129	1.129
R (weighted profile) / %	1.431	1.431
R (Bragg) / %	1.293	0.938
GOF	1.394	1.293

4.6. Rationalization of thermal behaviour of manganite

From the previous results of the heat treatment of manganite we can conclude that the relative vapour pressure of oxygen gas in contact with manganite precursor is a crucial parameter that prompts such transformations. As well as for an inert gas which contains contaminants of oxygen, the quantity of oxygen admixed to it is a decisive factor for such reactions. Quantification of the impact of oxygen amount on transformations of γ-MnOOH to various manganese oxides was established via annealing manganite under nitrogen gas containing a well-defined amount of oxygen (5%). The results of XRD analyses for the heat-treated manganite precursors under different flow rates of nitrogen, i.e., 3.5 and 1.0 mL/min are shown in Figure 17.
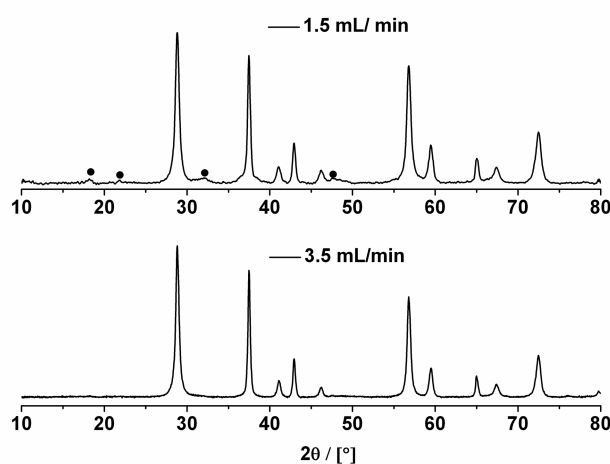
Figure 17. *XRD diffractograms for the decomposition products obtained by annealing of γ-MnOOH under nitrogen flow (contains 5% oxygen) using different flow rates, closed circles represent Mn_5O_8.*

A very careful insight for the XRD patterns reveals that at higher flow rate where much oxygen is flowing over the precursor, x-ray single phase β-MnO$_2$ is formed. In contrast, lower flow rate implicates low oxygen stream passing over the precursor but not low enough for formation of clean Mn_5O_8. In this case a mixture of both Mn_5O_8 and β-MnO$_2$ is produced. The content of Mn_5O_8 is very low at this condition which is evidenced by the existence of tiny peaks in the powder pattern of the product that are related to the presence of Mn_5O_8 as minors admixed to β-MnO$_2$.

4.7. Microstructural analysis

Microstructural analysis of manganite precursor and its calcination products was implemented via scanning electron microscopy. SEM image of manganite (Figure 18a) indicates that it has a rod-like morphology. These rods are uniform throughout and have a mean diameter of 30 nm and average length up to 1 μm with an aspect ratio up to 30. Actually, this fibrous-like structure is an indication for anisotropic growth of γ-MnOOH nanocrystals. Obviously, manganite transforms topotacticaly at lower temperature or in the presence of higher oxygen amount to pyrolusite that inherit the original rod-like morphology. The diameter of β-MnO_2 nanorods in this case is thinner than that of manganite as it is manifested by the SEM image shown in Figure 18b. Antecedent discussion have pointed out that such topotactic conversion from γ-MnOOH to β-MnO_2 is mainly an ordinary consequence of elimination of hydrogen rather than inflow of oxygen.[12] Seemingly, as it is apparent from SEM observations, manganite transforms at higher annealing temperatures (350-520 °C) and in the presence of extremely low amount of oxygen to Mn_5O_8 that preserves the initial rod-like morphology. Investigations of SEM pictures indicate that heat treatment of either β-MnO_2 or Mn_5O_8 results in production of α-Mn_2O_3 with conservation of shape; α-Mn_2O_3 maintains the fibrous structure in this case.
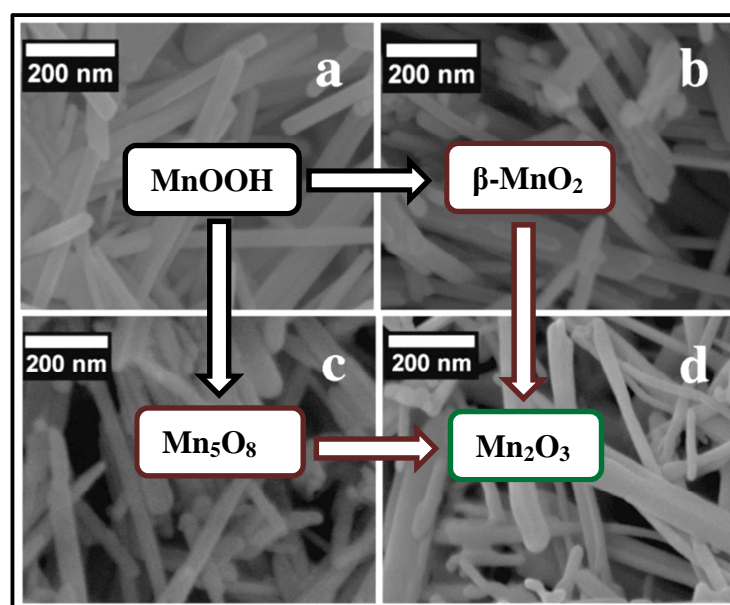
Figure 18. SEM images of MnOOH and its calcination products: a) γ-MnOOH, b) β-MnO₂, c) Mn₅O₈ and d) α-Mn₂O₃.

4.8. Structural analysis of Mn_5O_8

Rietveld analysis of the XRPD was made to ascertain some structural manifestation of the so obtained Mn_5O_8 sample (prepared by calcination of manganite at 350 ºC, ~16 nm). The calculated and the experimental patterns along with the difference pattern extracted from Rietveld refinement are shown in Figure 19.
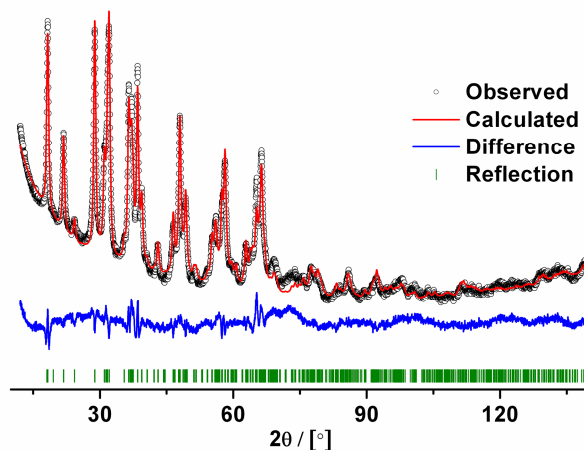
Figure 19. *Rietveld analysis results deduced from XRD data of Mn_5O_8, <d> ~16 nm.*

Obviously, the fitting between both patterns as well as the absence of any additional reflection are good signs inferring that we have a single phase Mn_5O_8 sample. Reasonable R values were obtained (Table 10). The SOF values for Mn atoms occupying various Wyckoff sites are all equal to 1 which implies that we have a non-deficient Mn_5O_8 structure. No excess mass is existing over the surface of this Mn_5O_8 sample as established by TG curve shown in Figure 13.

The measured density for this sample was 4.69(0.03) g/cm^3 which matches with the calculated one from Rietveld refinement (4.89 g/cm^3). The difference between them may be due to an error occurs as a result of using insufficient amount for the measurement (~18 mg).

Mn_5O_8 structure has monoclinic symmetry with space group C 1 2/m 1.[13] The calculated lattice parameters are in a good accordance with those found in literature,[13] non-appreciable difference (< 2 pm) can be seen as shown in Table 10. Atomic fractional coordinates and isotropic displacement parameters are illustrated in Table 11.

Table 10. Measurement parameters, structure and refinement data of Mn_5O_8 (prepared by calcination at 350 ºC).

	Mn_5O_8	*16956-ICSD*[13]
Z	2	2
Space group (No.)	C 1 2/m 1 (12)	C 1 2/m 1 (12)
a / Å	10.398(1)	10.347
b / Å	5.7322(5)	5.724
c / Å	4.8715(5)	4.852
β / •	109.520(5)	109.41
V/ 10^6 pm^3	273.680	273.033
ρ / g/cm^3	4.89	4.93
V	0.18	–
W	0.25	–
R (expected) / %	1.174	–
R (profile) / %	1.071	–
R (weighted profile) / %	1.386	–
R (Bragg) / %	0.774	–
GOF	1.394	–

Table 11. Wyckoff positions, atomic fractional coordinates and isotropic displacement parameters B of Mn_5O_8.

Atom	*Wyck.*	*x*	*y*	*z*	$B / 10^4$ pm^2
Mn1	2c	0.0	0.0	0.5	1.5(1)
Mn2	4g	0.0	0.2663(5)	0.0	0.61(7)
Mn3	4i	0.7186(3)	0.0	0.6504(8)	1.89(7)
O1	8j	0.1084(6)	0.229(1)	0.386(2)	1.93(9)
O2	4i	0.108(1)	0.0	0.925(3)	1.93(9)
O3	4i	0.613(1)	0.0	0.910(3)	1.93(9)

It is obvious from the data obtained and shown in Table 12 that Mn_5O_8 can adopt the formula $Mn_2^{2+}Mn_3^{4+}O_8$. The crystal structure of Mn_5O_8 (Figure 20) consists of octahedral sheets in bc planes, Mn^{IV} atoms are occupying two different Wyckoff sites, i.e., Mn1 and Mn2. The octahedrons formed around Mn1 atoms are distorted and consisting of four equal Mn-O bonds that are shorter (192.9 pm) than the other two (199.7 pm) which are equal as well. All Mn-O distances are elongated compared to those of the bulk Mn_5O_8 (Table 12).[13]

The octahedral coordination of Mn2 exhibits three equal sets of Mn-O bonds that are different in length (Mn-O distances are 185.3, 192.8 and 200 pm). All sets are increased in length if compared to bulk Mn_5O_8.[13] One-fourth of the octahedral sites is vacant, above and below the empty sites Mn^{II} are located (Mn3). Mn3 (oxidation state II) exhibits a rare trigonal presimatic coordination of oxygen atoms with two equal sets of Mn-O bonds (209.7 and 228.2 pm) and the other two Mn-O have different lengths (193 and 224.6). The distances between Mn and O in the trigonal prisms get shorten relative to those of the bulk material (Table 12). The estimated average interatomic Mn-O distances show differences from those of bulk Mn_5O_8 (the difference for Mn^{IV}-O is ~5-9 pm and Mn^{II}-O is ~15 pm). Furthermore, comparison of these distances with those of other manganese oxide/hydroxide phases (different oxidation states, Table 13) reveals that Mn1-O and Mn2-O have distances located between those of Mn^{IV}-O and Mn^{III}-O. Similarly, Mn3-O has a distance located between that of Mn^{II}-O and Mn^{III}-O. This finding indicates that we may have a partly charge-disordered Mn_5O_8 structure, trivalent Mn might be present. The way how these Mn^{III} atoms are distributed within Mn_5O_8 structure is not obvious, extensive study is needed for this purpose.
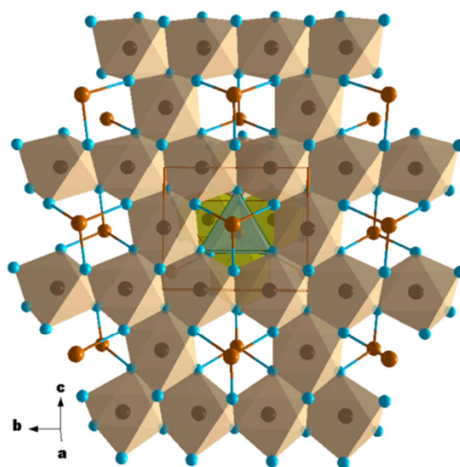

Figure 20. *Crystal structure of Mn₅O₈ projected along [100].*

Table 12. Coordination of atoms and bond distances of Mn_5O_8.

Atom	Coordination	Distance	Literature[12]	Number
Mn1	O1	192.9(7)	185.29	4x
	O2	199.7(1.2)	187.9	2x
	Mn2	287.5(2)		4x
	Mn3	324.5(4)		2x
	O2	335.0(2)		2x
	O3	346.6(7)		4x
Mn2	O1	185.3(7)	184.92	2x
	O3	192.8(1.1)	189.34	2x
	O2	200.0(9)	191.89	2x
	Mn2	268.0(4)		1x
	Mn1	287.5(2)		2x
	Mn2	305.3(4)		1x
	Mn3	323.5(3)		2x
	O1	338.4(7)		2x
	O1	342.8(7)		2x
	Mn3	349.1(3)		2x
Mn3	O3	193.0(1.6)	204.66	1x
	O1	209.7(7)	216.66	2x
	O2	224.6(1.0)	228.26	1x
	O1	228.2(7)	231.44	2x
	Mn2	323.5(3)		2x
	Mn1	324.5(4)		1x
	Mn3	338.0(3)		1x
	O3	340.3(1.4)		1x
	Mn2	349.1(3)		2x

Table 13. Interatomic Mn-O distances of manganese oxide/hydroxide phases with various oxidation states.

	Oxidn. state	Mn-O distance / pm	No. of Mn-O	ICSD No.
MnO	II	222.2	6x	43459
γ-MnOOH	III	188.1, 189.3, 197.7, 198.2, 221.3, 233.7		84949
β-MnO₂	IV	187.9	4x	393
		189.8	2x	

4.9. Magnetic behaviour of Mn_5O_8

Magnetic studies of Mn_5O_8 samples were conducted using a SQUID magnetometer. Temperature-dependent measurements of the magnetization were performed. Figure 21 demonstrates the temperature-dependent magnetic susceptibility χ of Mn_5O_8 (sample 1, prepared by calcination of carefully washed precursor at 350 °C for 1 h) measured using various field strengths under field-cooled (FC) and zero field-cooled (ZFC) conditions.
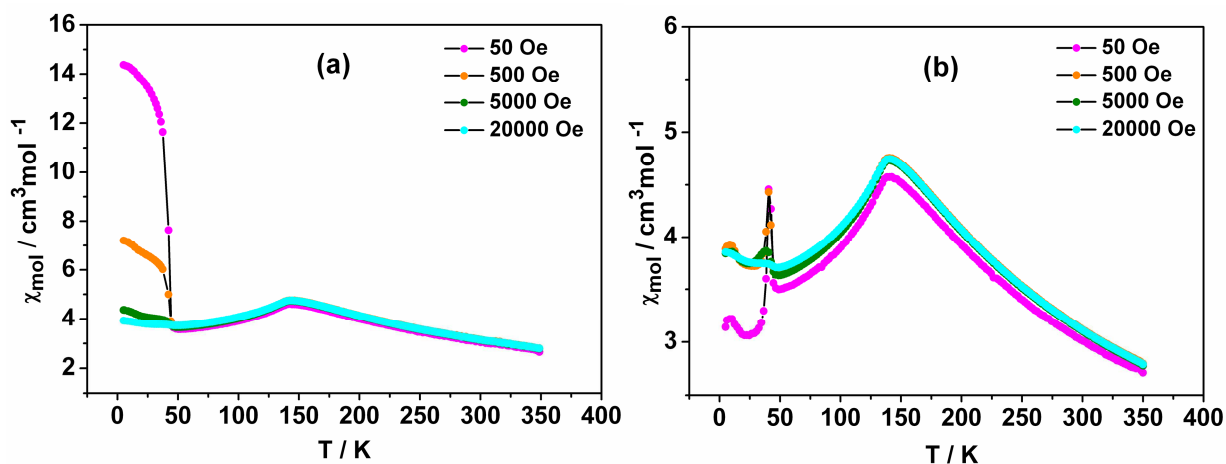

Figure 21. *Temperature-dependent magnetic susceptibility of Mn_5O_8 (sample **1**, 16 nm) measured under FC (a) and ZFC (b) conditions utilizing variable field strength.*

Distinctly, two peaks are notable in the χ-T plot. The 1st sharp one locates in χ near to 42 K which perfectly coincides with the Curie temperature of the hausmannite, Mn_3O_4 (exists as tiny impurities), the electronic spins in Mn_3O_4 order ferrimagntically. The existence of the spinel admixed to Mn_5O_8 sample (<d> ~16 nm) could not be monitored by XRD examination. The 2nd peak observed in χ-T plot sets in χ near 128 K and is attributed to antiferromagnetic ordering of the electronic spins in Mn_5O_8.

The invers χ versus T graph (Figure 22) was used to find out the value of effective magnetic moment μ_{eff}, a value of 4.71 μ_B was obtained for $\mu_{eff.}$, which is in good accordance with the estimated value 4.80 μ_B for charge ordered Mn_5O_8 structure. The difference between both μ_{eff} values may indicate the presence of subtle degree of structural disorder. Assuming spin–only contributions, the μ_{eff} can be calculated by the formula:

$$\mu_{eff. \ (Mn_5O_8)/5} = \sqrt{\frac{2}{5}\left[\mu_{Mn(II)}\right]^2 + \frac{3}{5}\left[\mu_{Mn(IV)}\right]^2}$$

Where, $\mu_{Mn\ (II)} = 5.916 \ \mu_B$ and $\mu_{Mn(IV)} = 3.873 \ \mu_B$

Curie-Weiss temperature (θ_{CW}) was detected from the invers χ-T plot (Figure 22) by extrapolation of the fitted line for the data till $\chi^{-1} = 0$, -116 K was found for θ_{CW}. Field-dependent measurements illustrated in Figure 23 exhibit no hysteresis even at very low temperature of 5 K that emphasizes the antiferromagnetic ordering for Mn_5O_8.
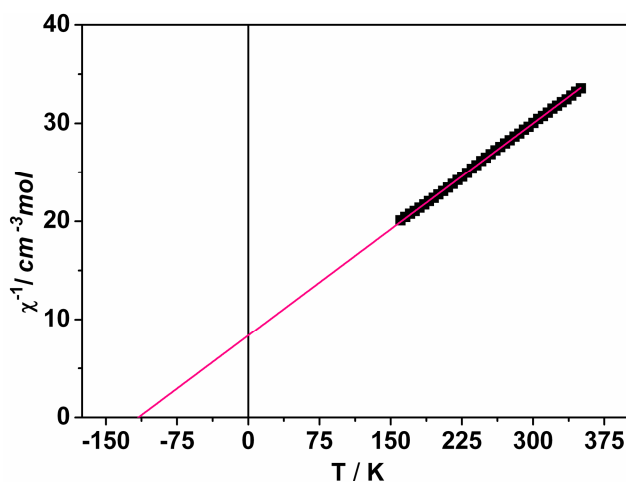
Figure 22. *Inverse magnetic susceptibility versus temperature plotted for Mn_5O_8 (sample **1**). Solid line is the fitting according to Curie-Weiss law.*
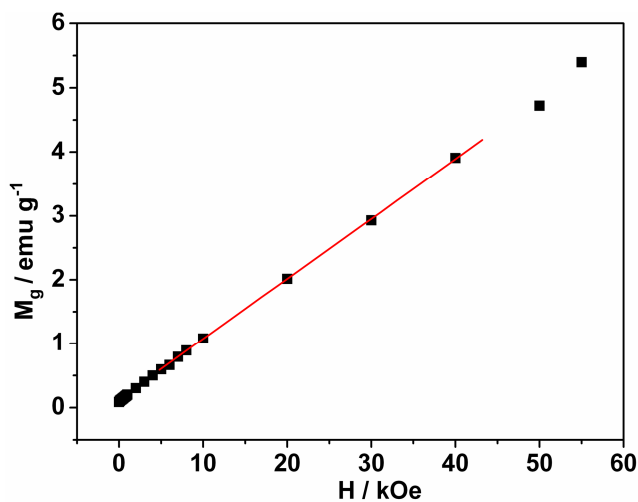
Figure 23. *Field-dependent magnetization of Mn_5O_8 (sample **1**) measured at a temperature of 5 K.*

The presence of tiny impurities of α-Mn_3O_4 could be explained on the basis of the presence of some unreacted manganese acetate adsorbed over the surface of the manganite precursor which in turn by annealing manganite at 350 °C produces the spinel, α-Mn_3O_4.

To substantiate our point of view, another sample of manganite was prepared by the same way and separated this time without further washing. It is expected that more manganese acetate is accumulated over the surface of the precursor. Manganite sample was then checked by XRD analysis which indicates a single phase manganite. Afterward, the sample was tested by IR analysis. The IR spectrum demonstrated in Figure 24 shows absorption bands located in the range of 1350-1670 cm^{-1}. They are attributed to symmetric and asymmetric carbonyl stretching vibrations of acetate group.[14]
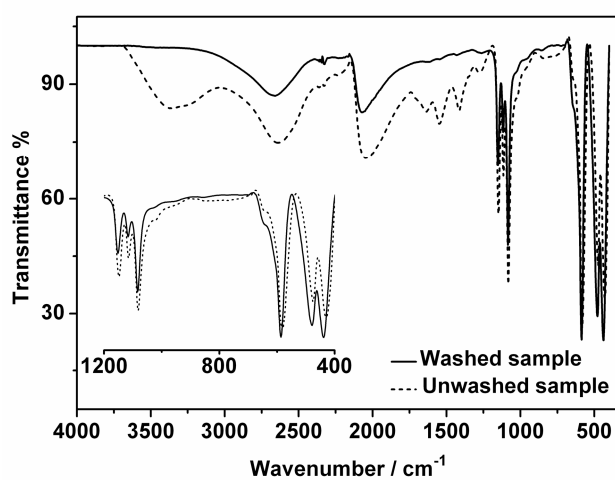
Figure 24. *IR spectra of two manganite precursors one carefully washed and the other is the unwashed one. The insight is their magnifications in the range of 400-1200 cm^{-1}.*

Thereafter, the manganite sample was heat-treated at a temperature of 350 °C and the calcination product was characterized via XRD analysis (Figure 25). From XRD patterns depicted in Figure 25 an additional reflection occurs at 2θ ~45° which is related to the (220) lattice plane of α-Mn_3O_4. This result indicates that we have Mn_5O_8 sample (sample 2) contaminated with appreciable amount of spinel. Magnetic measurements were performed for such Mn_5O_8 sample. From χ-T plot (Figure 26) we can observe that no saturation for the magnetic spins takes place even at extremely high field strength, reflecting a high contribution of the spinel spins to such sample.

It is noteworthy to demonstrate that calcination of manganite precursor under the certain conditions established before (i.e., 350-520 °C, in small size tubes), leads to formation of Mn_5O_8. Impurities of spinel exist even with a very careful washing for the precursor. We found that it is not possible to remove entirely the adsorbed and unreacted manganese acetate

over the manganite surface (main reason for the spinel formation) via repeated ultrasonic washing.
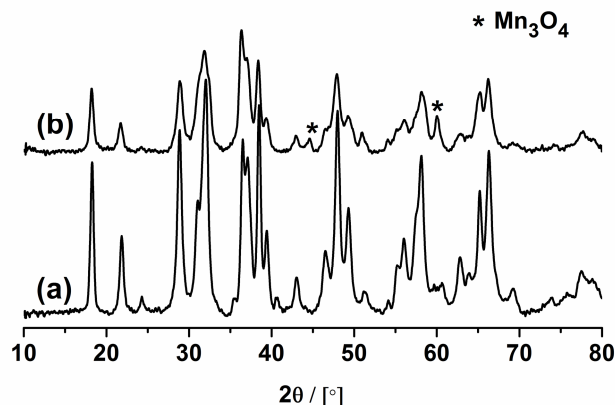
Figure 25. *XRD patterns of Mn_5O_8 samples prepared via a) calcination of washed manganite precursor at 400 °C using small size glass tube and b) calcination of unwashed manganite precursor using the same conditions.*
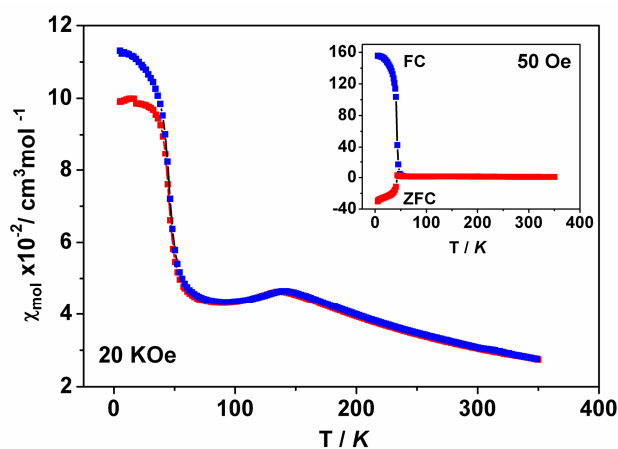
Figure 26. *Temperature dependent magnetic susceptibility of Mn_5O_8 (sample **2**, obtained from unwashed precursor) measured using higher field strength under FC and ZFC, inset represents the low field measurements.*

Assessment of the amount of spinel impurities admixed to Mn_5O_8 samples was carried out by comparing the value of saturation magnetization of each sample with that of pure spinel sample (Figure 27). The results spell out that subtle amount of α-Mn_3O_4 about 0.4-0.6% is coexisting within the Mn_5O_8 samples prepared from carefully washed precursor. Whereas, Mn_5O_8 sample prepared from unwashed precursor exhibits much spinel in content exceeding 13%.
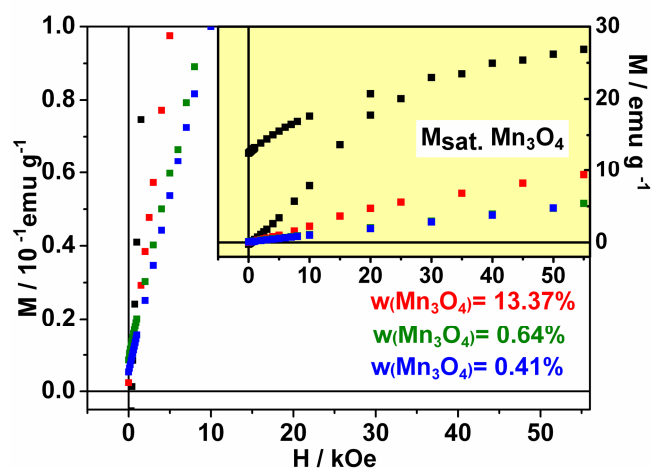
Figure 27. Evaluation of saturation magnetization from field-dependent magnetization measurements for three Mn₅O₈ samples prepared by calcination of 1) washed γ-MnOOH precursor at 350 °C (blue) and 400 °C (green) and 2) unwashed γ-MnOOH precursor by calcination at 350 °C (Red). As well as for pure α-Mn₃O₄ (black), measurements were performed at a temperature of 5 K.

4.10. Summary and conclusions

We can summarize our results as follow:

❖ The amount of oxygen accessible (i.e., oxygen partial pressure) to the manganite precursor is a crucial parameter for the transformation toward manganese oxides with different oxidation states either in air or in Ar (or N_2) atmosphere containing some oxygen.

❖ Formation of single phase Mn_5O_8 (in air) demands a high calcination temperature of 350-520 °C and low oxygen pressure, whereas β-MnO_2 is formed irrespective of the calcination temperature provided that a high amount of oxygen is accessible to manganite.

❖ γ-MnOOH transforms topotactically to β-MnO_2 which has the same rutile-type structure and isomorphously towards Mn_5O_8. Both of them are decomposed isomorphously to α-Mn_2O_3 preserving the same rod-like structure.

❖ Structural analysis of Mn_5O_8 sample (~16 nm) showed a non-deficient structure which is established by Rietveld refinement, density measurement and TGA.

❖ The estimated average interatomic Mn-O distances showed differences from those of bulk Mn_5O_8 (the difference for Mn^{IV}-O ~5-9 pm and Mn^{II}-O ~15 pm). This divergence indicates that we may have a partly charge-disordered Mn_5O_8 structure. Trivalent Mn might be present as well.

❖ Mn_5O_8 orders antiferromagnetically with Néel temperature of 128 K and $θ_{CW}$ of -116 K, the effective magnetic moment $μ_{eff}$ is 4.71 $μ_B$ which is in accordance with the estimated value 4.80 $μ_B$ for charge-ordered Mn_5O_8 assuming only contributions from the spin.

❖ Impurities of α-Mn_3O_4 which detected in the Mn_5O_8 samples can be ascribed to the presence of some unreacted manganese acetate over the surface of the precursor. The adsorbed manganese acetate cannot be removed completely via repeated washing for the precursor even by under sonication.

References

1. Hernan, L.; Morales, J.; Tirado, J. L. Relationships between composition and surface properties of the dehydration products of synthetic manganite. *Surf. Coat. Technol.* **1986,** *27* (4), 343-350.

2. Folch, B.; Larionova, J.; Guari, Y.; Guerin, C.; Reibel, C. Synthesis of MnOOH nanorods by cluster growth route from $[Mn_{12}O_{12}(RCOO)(16)(H_2O)(n)]$ (R = CH_3, C_2H_5). Rational conversion of MnOOH into Mn_3O_4 or MnO_2 nanorods. *J. Solid State Chem.* **2005,** *178* (7), 2368-2375.

3. Gao, T.; Norby, P.; Krumeich, F.; Okamoto, H.; Nesper, R.; Fjellvag, H. Synthesis and properties of layered-structured Mn_5O_8 nanorods. *J. Phys. Chem. C* **2010,** *114* (2), 922-928.

4. Novak, A. Hydrogen bonding in solids correlation of spectroscopic and crystallographic data. In *Large Molecules*, Structure and Bonding ed.; Springer Berlin Heidelberg: 1974; pp 177-216.

5. Kohler, T.; Armbruster, T.; Libowitzky, E. Hydrogen bonding and Jahn-Teller distortion in groutite, alpha-MnOOH, and manganite, gamma-MnOOH, and their relations to the manganese dioxides ramsdellite and pyrolusite. *J. Solid State Chem.* **1997,** *133* (2), 486-500.

6. Baur, W. H. Rutile-type compounds. V. Refinement of MnO_2 and MgF_2. *Acta Cryst. B* **1976,** *32* (7), 2200-2204.

7. Gao, T.; Krumeich, F.; Nesper, R.; Fjellvag, H.; Norby, P. Microstructures, surface properties, and topotactic transitions of manganite nanorods. *Inorg. Chem.* **2009,** *48* (13), 6242-6250.

8. Julien, C. M.; Massot, M.; Poinsignon, C. Lattice vibrations of manganese oxides: Part I. Periodic structures. *Spectrochim. Acta, Part A* **2004,** *60* (3), 689-700.

9. Li, L.; Chu, Y.; Liu, Y.; Dong, L. Synthesis and shape evolution of novel cuniform-like MnO_2 in aqueous solution. *Mater. Lett.* **2007,** *61* (7), 1609-1613.

10. Gillot, B.; El Guendouzi, M.; Laarj, M. Particle size effects on the oxidation-reduction behavior of Mn_3O_4 hausmannite. *Mater. Chem. Phys.* **2001,** *70* (1), 54-60.

11. Ferreira, O. P.; Otubo, L.; Romano, R.; Alves, O. L. One-dimensional nanostructures from layered manganese oxide. *Cryst. Growth & Des.* **2006,** *6* (2), 601-606.

12. Rask, J. H.; Buseck, P. R. Topotactic relations among pyrolusite, manganite, and Mn_5O_8 - A high-resolution transmission electron-microscopy investigation. *Am. Mineral.* **1986,** *71* (5-6), 805-814.

13. Oswald, H. R.; Wampetich, M. J. Die Kristallstrukturen von Mn_5O_8 und $Cd_2Mn_3O_8$. *Hev. Chim. Acta* **1967,** *50* (7), 2023-2034.

14. Spectral Database for Organic Compounds SDBS. *http://sdbs. db. aist. go. jp/sdbs/cgi-bin/direct_frame_top. cgi* **2015**. **(Last access 29-1-2015)**

Chapter 5

Self-template assisted synthesis of various manganese dioxide polymorphs

5. Introduction

Due to their unique physical properties and technological prominence, manganese dioxides have attracted extraordinary attention in technological applications, e.g., selective heterogeneous catalysts, battery materials and electrochemical capacitors.[1]

Various structural forms of MnO_2 occur in nature, e.g., α, β, γ, and δ-type. All are built from the same structural units MnO_6 octahedra. α, β, γ-MnO_2 (cryptomelane, pyrolusite and nsutite) consist of MnO_6 chains that are attached together in a way that 2x2, 1x1 and 1x2 1D channels are formed, respectively. δ-type (birnessite) has a layer structure, composed of edge-sharing MnO_6 octahedra.[2]

A lot of approaches were developed for the synthesis of the various forms of manganese dioxide.[2,3] Yet, no single approach has been developed for the synthesis of all manganese dioxide polymorphs. The frequently reported comproportionation reaction between Mn^{2+} and MnO_4^- has been used for the synthesis of α, β, γ, and δ-type (frequently under hydrothermal conditions)[4-7] but not for ε and not for birnessite with various intercalated cations (e.g., Cs-birnessite).

Intercalation of templates to the reaction system will markedly sophisticate the synthetic method, and raises the production cost, hence, increases the difficulty for scale-up fabrication of nanostructures with 1D tunnels. Consequently, it is worth to discover further techniques without involving templates (the same problems arise for the hydrothermal reactions).

The effect of using of different permanganate salts ($NaMnO_4$, $KMnO_4$ and $CsMnO_4$) as a self-template for the synthesis of different forms of manganese dioxide has been studied.[8] Under pH control (the medium acidified using either buffer solution or nitric acid), either single phase of cryptomelane or mixtures of manganese oxides were produced.

In this chapter, a simple and self-template approach is used for the synthesis of the various polymorphs of manganese dioxide (single phases), i.e., α, γ, ε and δ-types, merely from aqueous medium and under simple reflux process. Concentration of K cations (of $KMnO_4$) acts as a template for the production of α, γ and δ-types (by changing the Mn^{2+}/ MnO_4^- ratio). Variation of the reaction temperature is the key-parameter for the formation of ε-type.

To the best of our knowledge, Cs-birnessite is synthesized for the first time in this work. Template effect of the alkali metal cation of the permanganate salts associated with the

variation of the reaction pH (different Mn^{2+} salts will be used for this purpose) is of importance for this purpose.

Crystallographic data regarding MnO_2 and its structurally related compounds are shown in Table 1.

Table 1. Crystallographic data of MnO_2 and its structurally related compounds.

Compound	Mineral name	Crystal system	Cell parameters / Å	Features	Intercalated / Substituted species
β-MnO₂	Pyrolusite	Tetragonal ($P4_2$ / mnm)	a = 4.39 c = 2.87	1x1 tunnels	–
γ-MnO₂	Nsutite	Orthorhombic (*Pnam*)	a = 9.32 b = 4.46 c = 2.850	1x1 + 1x2 tunnels	e.g., OH⁻ or H_2O
R-MnO₂	Ramsdellite	Orthorhombic (*Pbnm*)	a = 4.53 b = 9.27 c = 2.87	1x2 tunnels	e.g., OH⁻ or H_2O
ε-MnO₂	Akhtenskite	Hexagonal $P\,6_3$ / $m\,m\,c$	a = 2.786 c = 4.412	No tunnels	–
α-MnO₂	Crytomelane	Tetragonal (I_4 / m)	a = 9.96 c = 2.85	2x2 tunnels	e.g., K, Ba, OH⁻ or H_2O
δ-MnO₂	Birnessite	Hexagonal $P\,6_3$ / $m\,m\,c$	a = 2.84 c = 14.64	1x∞ layers	e.g., Na, K, OH⁻ or H_2O

5.1. Effect of molar ratio of Mn^{2+}/MnO_4^-

XRD analysis

Comproportionation reaction between $KMnO_4$ and $MnCl_2$ was carried out in aqueous medium (100 mL) using three different molar ratios for Mn^{2+}/MnO_4^-, i.e., 5:1, 1:1 and 1:3, at the same experimental time of 17 h and under refluxing conditions (pH of the medium ~4, 6 and 9, respectively). Different forms of manganese dioxide are produced (Figure 1).
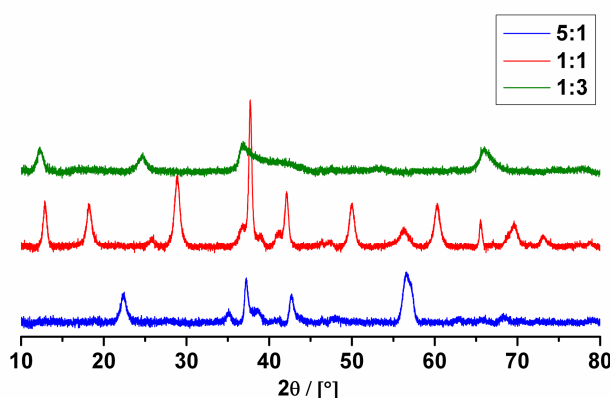

Figure 1. *XRD patterns of the samples prepared by refluxing $MnCl_2.4H_2O$ and $KMnO_4$ in aqueous medium (100 mL) for 17 h. Different molar ratios for Mn^{2+}/MnO_4^- were used; 5:1, γ-MnO_2 ; 1:1, α-MnO_2 and 1:3, δ-MnO_2.*

With low molar ratios, 1D tunnelled structures are obtained. When a molar ratio of 5:1 is used, nsutite is produced (a = 9.393(3) Å, b = 2.8280(8) Å and c = 4.419(2) Å). Nsutite, i.e., γ-MnO_2, is the result of the intergrowth between ramsdellite (R-form) with 1x2 tunnels and pyrolusite (β-form) with 1x1 tunnelled structure, space group $P6_3/mmc$.

Increase in the tunnel size to 2x2 occurs when the molar ratio is increased to 1:1, α-MnO_2 namely, cryptomelane is obtained which is stabilized by insertion of small amounts of K^+ cations into its tunnels (a = 9.794(1) Å and c = 2.8476(3) Å). Using molar ratio of 3:1, the tunnelled structures disappear and a new layer structure δ-MnO_2 is formed (mineral name; birnessite). The XRD patterns shown in Figure 1 are indexed to x-ray single phases of γ-MnO_2, α-MnO_2 and δ-MnO_2, respectively. Reference patterns for these phases are shown in Figure 2. Much broader reflections in the powder pattern of birnessite are associated with turbostratic disordered structures, i.e., each layer is translated and/or rotated randomly in relation to adjacent layers.[9]
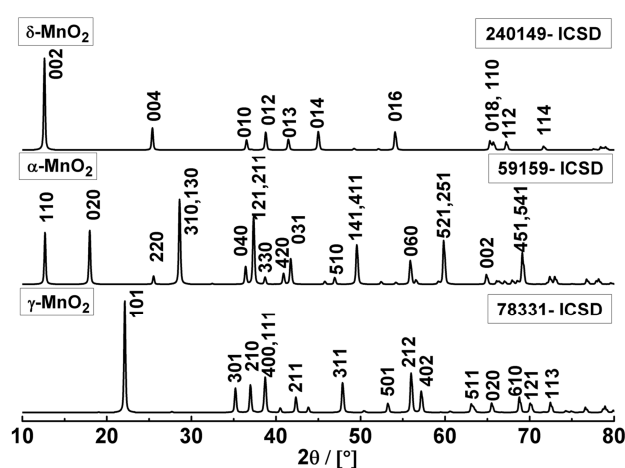
Figure 2. *Reference patterns of γ-MnO₂, α-MnO₂ and δ-MnO₂.*

It is know from the standard electrode potentials that $KMnO_4$ can oxidize Cl^- to Cl_2 gas. A parallel reaction of $KMnO_4$ with HCl at pH values of ~5 and ~2 was done to investigate whether or not at the given experimental conditions, $KMnO_4$ is able to oxidize Cl^- ions (Mn salt) and be reduced to MnO_2. Actually, no precipitation of MnO_2 occurs under these conditions which indicates that there is no redox reaction occurs. No side reaction of $KMnO_4$ with Cl^- ions occurs.

The mean particle size for all products was calculated using Scherrer's equation. The estimated particle size for γ-MnO_2 is ~13 nm (calculated using the reflections at $2\theta =$ 22.4°(101), 35.15° (301), 37.2° (210) and 42.6° (211)). Reflections at $2\theta = 12.88°$ (110) and 18.21° (020) were used for particle size calculation for α-MnO_2 (~14 nm). The reflections in the powder pattern of δ-MnO_2 sample located at $2\theta = 12.26°$ (002) and 24.52° (004) were used for the size estimation for which the mean grain size ~10 nm.

From the forgoing results it is very likely that the crucial factor for these transformations is the concentration of K^+ cations, acting as a template for the structure modification from one with low tunnel size to one with large tunnel size and finally to layered-type structure via adjusting its quantity.

The above results reveal that a control over the crystallographic structure of manganese dioxide can be achieved by variation of the molar ratio of Mn^{2+}/MnO_4^-. This conclusion matches with the report of Wang et al.[4] who observed that δ-MnO_2 can be produced at a higher K^+ concentration. This phenomenon can be explained as following:[4,7]

The aqueous solution of $KMnO_4$ and $MnCl_2$ was employed to carry out the reaction, and the whole reaction can be expressed by eqn. 1.

$$2\,KMnO_4 + 3\,MnCl_2 + 2\,H_2O \rightarrow 5\,MnO_2 + 2\,KCl + 4\,HCl \qquad (1)$$

$KMnO_4$ decomposes in the solution according to eqn. 2.

$$KMnO_4 + [(1\text{-}x\text{+}2y)\,/\,2]\,H_2O \rightarrow K_x MnO_2\,y\,H_2O + (1\text{-}x)\,KOH + [(3 + x)\,/\,4]\,O_2 \qquad (2)$$

At very low concentration of $KMnO_4$, γ-MnO_2 assumed to be obtained from eqn. 1. The measured pH value after termination of the reaction was ~1.8 which is correlated with HCl formation in eqn.1.

Wang et al.[4] found that δ-MnO_2 is produced as an intermediate during the formation process of α-MnO_2, which implies that reaction 2 occurs first. However, when a low concentration of K^+ is present, the layer structure directly and rapidly collapses into (2×2) tunnel formation process of α-MnO_2. At a higher molar ratio, mainly reaction 2 takes place and $K_x MnO_2 \cdot y H_2O$ is produced. So birnessite is obtained in this work when the molar ratio of 3:1 is used for MnO_4^-/Mn^{2+}.

IR analysis

The different forms of manganese dioxide were further characterized by IR analyses. IR spectra for the three forms are presented in Figure 3.
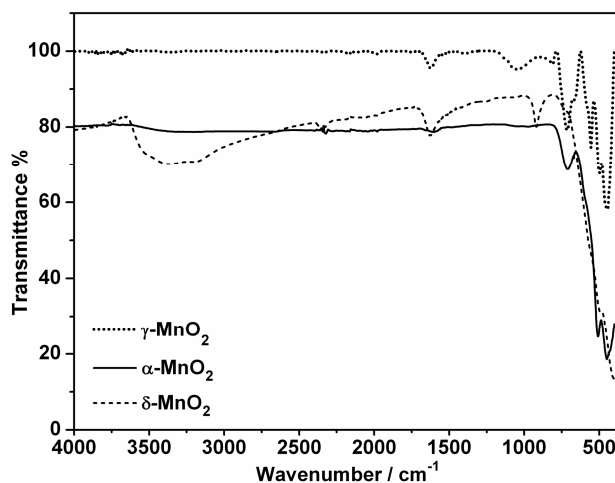
Figure 3. *IR spectra of γ-, α- and δ-MnO₂ samples.*

For γ-MnO_2 seven absorption bands are located at 443, 496, 555, 583, 663, 713 and 813 cm^{-1}. These are assigned to Mn-O lattice vibrations in MnO_6 octahedra and match with those found in literature.[10] Whereas the absorption band located at 1626 cm^{-1} is ascribed to O–H vibration.[11] The band appeared at 1050 cm^{-1} represents vibration due to interaction of Mn with OH.[11]

Cryptomelane shows three vibrations at 449, 508 and 709 cm^{-1} that are ascribed to the vibrations of the MnO_6 octahedral framework and which are consistent with those reported in literature.[12] The absorption band at 449 cm^{-1} is assigned to the vibration due to the displacement of the oxygen anions relative to the manganese ions along the direction of the octahedral chains. The absorption at 709 cm^{-1} is attributed to the stretching mode of MnO_6 octahedral along the double-chain.[12]

For birnessite, the IR spectrum shows bands at 411 and 495 cm^{-1} arising from Mn-O stretching modes. Characteristic bands at 3385 and 1620 cm^{-1} are assigned to stretching and bending vibrations of the –OH group of adsorbed and/or crystallization water.[13]

Positions of the absorption bands for the three forms of the structurally related MnO_2 forms along with their assignment are listed in Table 2.

Table 2. IR data of γ-, α- and δ-MnO_2 samples along with their assignment.

Structure	*Peak position / cm^{-1}*	*Assignment*
γ- MnO$_2$	443, 496, 555, 583, 663, 713 and 813	Mn-O stretching
	1620	OH vibration
α- MnO$_2$	449, 508 and 709	Mn-O stretching
δ- MnO$_2$	411, 495 and 918	Mn-O stretching
	1620 and 3385	OH vibrations

EDX analysis

Elemental analyses were performed for γ-, α- and δ-MnO_2 samples using EDX analyses. The results are presented in Figure 4. The data obtained from EDX analyses are listed in Table 3.
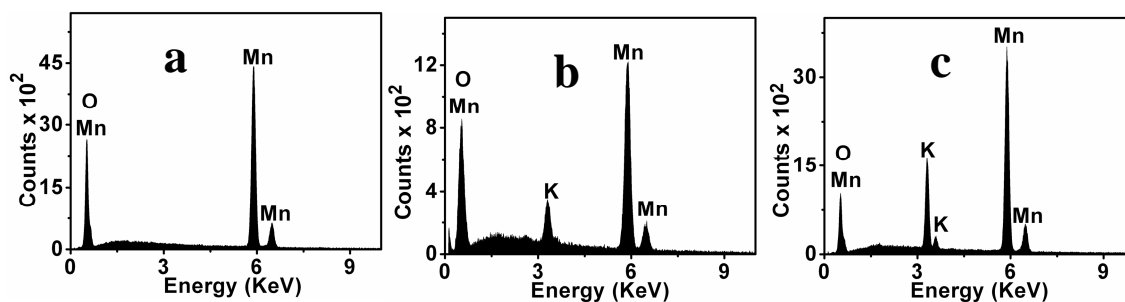

Figure 4. *EDX analyses of MnO$_2$ samples: a) γ-MnO$_2$, (b) α-MnO$_2$ and c) δ-MnO$_2$.*

Table 3. Elemental analysis data of γ-, α- and δ-MnO_2 samples derived from EDX analyses. The standard deviations for the measurements are shown in the parentheses.

Structure	%K	%Mn	%O
γ- MnO₂	0	30(4)	70(5)
α- MnO₂	3(0.3)	30(3)	66(3)
δ- MnO₂	6(1)	27(3)	66(4)

For nsutite, the smaller tunnel size (0.24 nm x 0.48 nm) cannot be occupied by the large K^+ cations. As a consequence, K cations insertions in such tunnels are not expected. Indeed, no characteristic peak corresponding to presence of K cations can be observed in the EDX spectrum of nsutite, the elemental analysis for Mn and O atoms is typical for MnO_2 formula. Cryptomelane has 2x2 tunnels (0.46 nm x 0.46 nm), the size of which is large enough to accommodate the K^+ cations. Intercalation of K cations into such tunnels gives rise to structural stability of cryptomelane. The K/Mn ratio is about 0.1:1, but because EDX is a semi-quantitative technique, the exact molecular formula needs to be determined by other methods. Birnessite (δ-MnO_2) with a layer-type structure can accommodate more K^+ cations, which are located between the layers (inter-layer distance of 0.7 nm). This can be proven by an EDX spectrum in which a more intense K^+ peaks exist compared to those found in case of cryptomelane. For this sample the K content is approximately twice that found in case of cryptomelane. The K/Mn ratio is about 0.22:1.

Morphological investigations

Morphological shapes of the obtained manganese dioxide phases were investigated by using SEM. The images are shown in Figure 5.
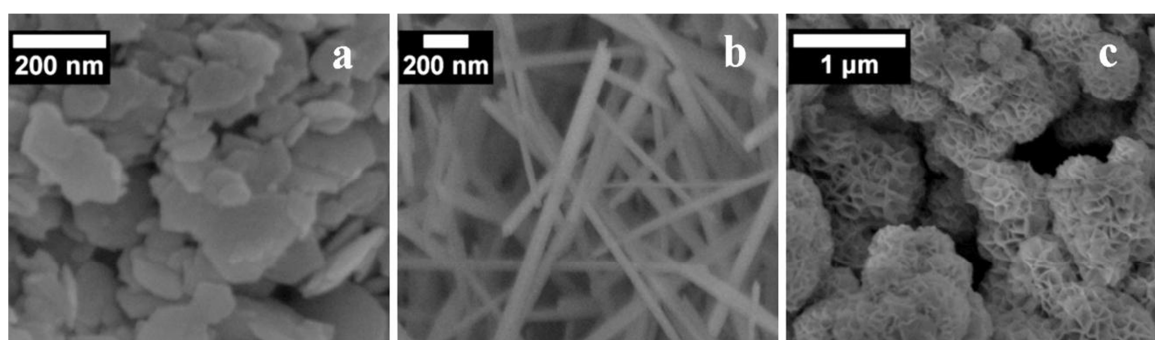

Figure 5. SEM images of MnO₂ samples: a) γ-MnO₂, b) α-MnO₂ and c) δ-MnO₂.

For nsutite, a plate-like morphology was adopted, the thickness of the plates is about 5 nm. These plates are irregularly shaped as illustrated in Figure 5a. Cryptomelane (Figure 5b) shows a rod-like morphology with average diameter of about 25 nm and length of about 1-2 µm. The rods are uniform throughout the entire length. The rod-like morphology implies anisotropic growth of the cryptomelane nanocrystals. The diameters of these nanorods estimated from SEM images were very close to the particle size calculated using Scherrer's formula for diffraction peak (310). As we can see from Figure 5c, the morphology of δ-MnO$_2$ is a flower-like or sponge-like spherical aggregate with diameters of 1-1.5 µm. Each aggregate is composed of dozens of ultrathin nanoflakes with a thickness of ~10 nm.

5.2. Surface area measurements

N$_2$ adsorption–desorption isotherms of the different forms of manganese dioxide (Figures 6a, c and e) exhibit type IV adsorption isotherms classified according to IUPAC.[14] These isotherms are characterized by hysteresis loops that can be considered as H3 type, indicating slit-like pores.[15] No limiting adsorption at high p/p° can be observed. A drastic increase in the volume of N$_2$ adsorption in the domain of P/P° = 0.9–1.0 is representative of capillary condensation in the mesopores. At very low P/P° ~0.1, it is not possible to remove entirely the adsorbed N$_2$ gas (Figure 6a, c and d), which may indicate a strong adsorbate-adsorbent interactions. The measured BET surface area for γ-MnO$_2$, α-MnO$_2$ and δ-MnO$_2$ samples is 17, 18 and 14 m^2 g^{-1}, respectively. Pore width-pore volume and pore width-pore area relationships are shown in Figures 6b, d and f. The corresponding BJH average pore diameters are located between 2-50 nm (Table 4) which indicate the presence of mesoporous structures in the obtained samples.

Table 4. Specific surface area, average pore width and total pore volume of γ-, α- and δ-MnO$_2$ samples.

	γ-MnO$_2$	*α-MnO$_2$*	*δ-MnO$_2$*
\<d\> / nm from XRD	13[a]	14[b]	10[c]
S$_{BET}$ / m^2.g^{-1}	17	18	14
Average pore width / nm	13	7	13
Total pore Volume / cm³/g	0.06	0.03	0.045

a; the corresponding plate diameter ~100-300 nm, b; the corresponding rod diameters is ~25 nm (length ~1-2 µm) and c; diameter of spherical agglomerates ~1-2 µm.
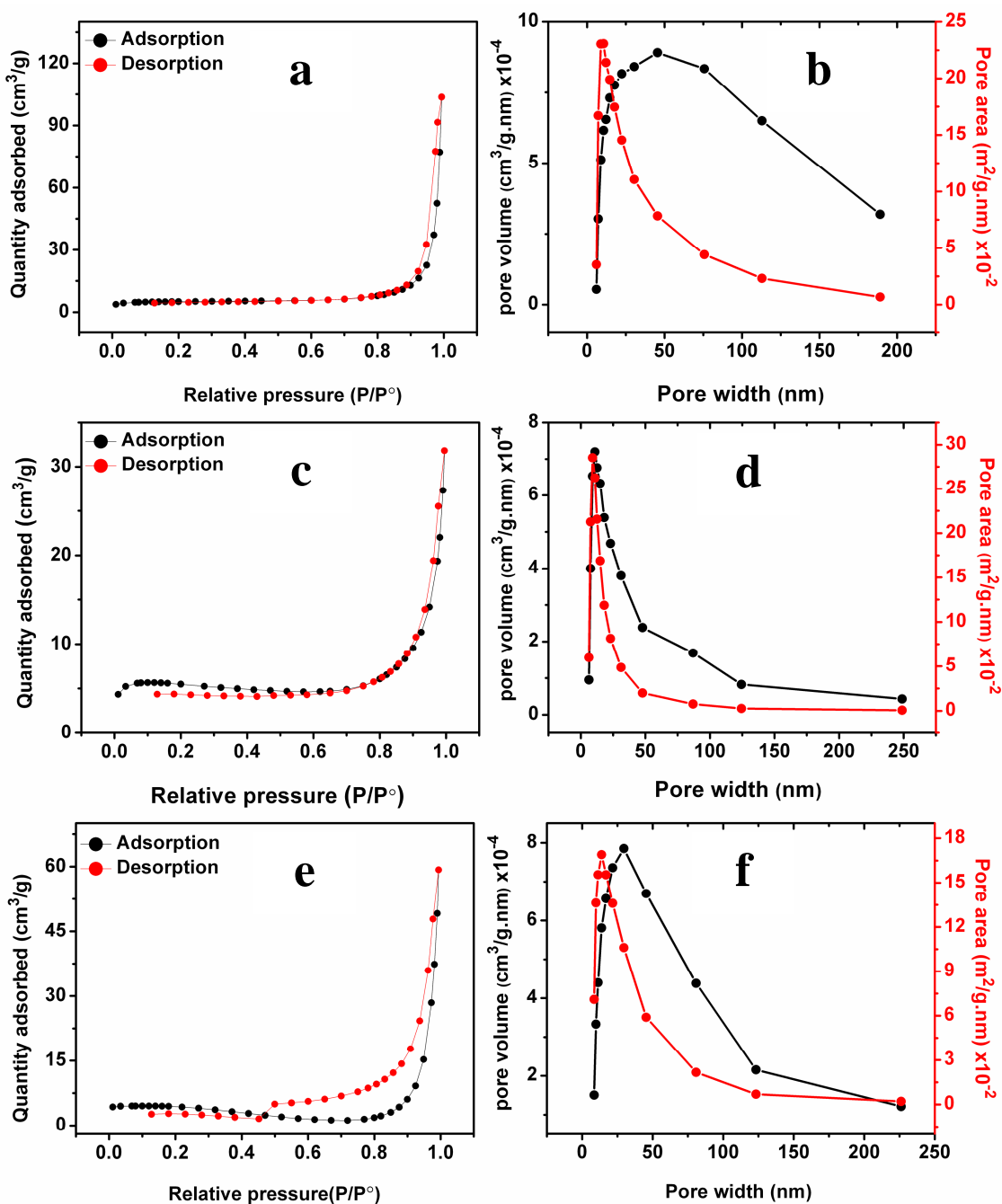
Figure 6. *a, c and e) represent adsorption-desorption isotherms for γ-, α- and δ-MnO₂ samples, respectively. b, d and f) represent their pore width-pore volume and pore width-pore area relationships.*

5.3. Effect of time on phase formation

The effect of the reflux time was studied at the three different molar ratios of Mn^{2+}/MnO_4^-, the time was varied from 1 to 72 h. Using 5:1 molar ratio and irrespective of the reaction time the product was found to be γ-MnO_2 as shown in Figure 7, all reflections are matched consistently with those of single phase γ-MnO_2. The broadening and the intensity of the bands nearly remain the same which means that the particle size is not significantly affected by changing the time. It is located in the range 12.3-14.3 nm. Table 5 lists the impact of time on the phase of the product and its particle size.
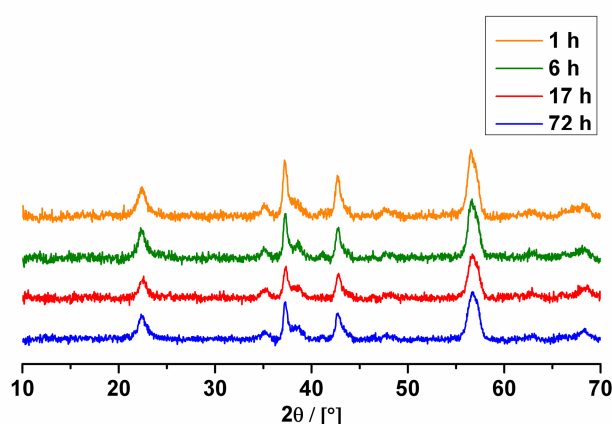
Figure 7. XRD patterns of γ-MnO₂ samples prepared by refluxing MnCl₂.4H₂O and KMnO₄ (5:1) in aqueous medium for different times of 1, 6, 17 and 72 h.

Table 5. Effect of time on the mean grain size of γ-MnO_2 samples.

Time / h	1	6	17	72
<d> / nm	12.6	14.3	12.6	13.1

Morphological studies were carried out for two samples prepared at 1 and 72 h (Figure 8). A plate-like morphology is adopted by the sample obtained at 1 h (Figure 8a). These plates are assembled to a flower-like morphology. By increasing the time to 72 h some rods are appeared and spread over these plates (Figure 8b). Existence of these rods may be due to formation of α-MnO_2. Nevertheless, no indication for its formation can be observed in XRD patterns.
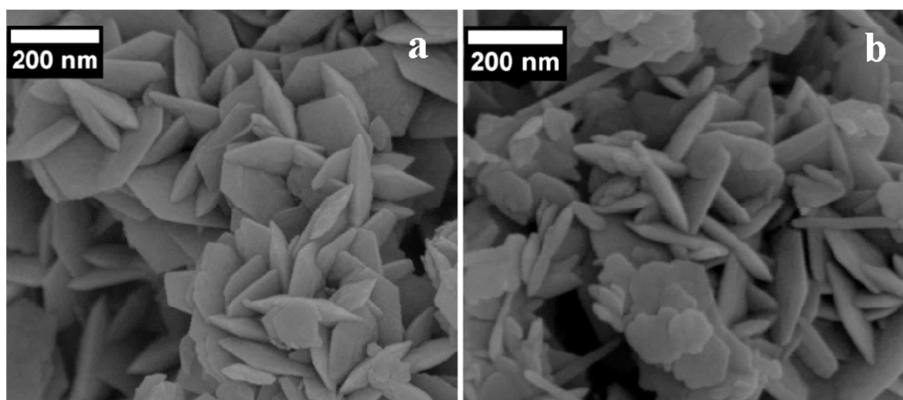
Figure 8. *SEM images of γ-MnO₂ samples prepared at different times: a) 1 h and b) 72 h.*

XRD patterns depicted in Figure 9 show the impact of reflux time whilst 1:1 molar ratio is used. At lower time of 1 h layered-type MnO_2, birnessite with turbostratically disordered structure[9] is formed initially. The powder pattern exhibits essentially two reflections at $2\theta = 37.26°$ and $66.5°$ the other two reflections at $2\theta = 12.3°$ and $24.6°$ are completely absent referring to low crystallinty; the particle size calculated from these two reflections is about 8 nm. Increasing the time to 17 h leads to formation of the tunnelled structure of α-MnO_2 and disappearance of layered-type structure. This can be explained by taking into consideration that the layer structure directly and quickly collapses into 2×2 tunnelled structure giving rise to formation of α-MnO_2. Further increase in the reflux time does not result in variation of the product phase. Cryptomelane with approximately the same mean particle size of ~14 nm is obtained. Sponge-like morphology is found for birnessite whereas rod-like morphology is adopted by cryptomelane as shown in Figure 10.
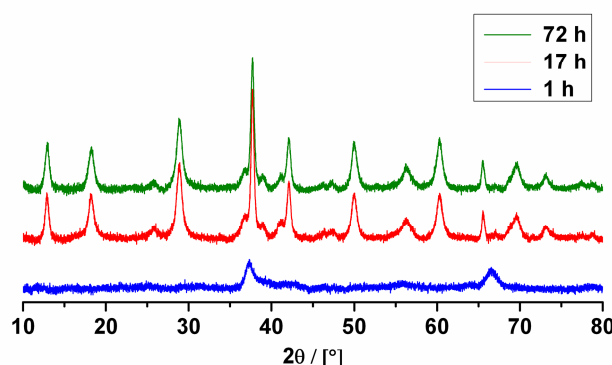
Figure 9. *XRD patterns of the samples prepared by refluxing MnCl₂.4H₂O and KMnO₄ (1:1) in aqueous medium for different times of 1, 17 and 72 h. Blue: δ-MnO₂; red and green: α-MnO₂.*
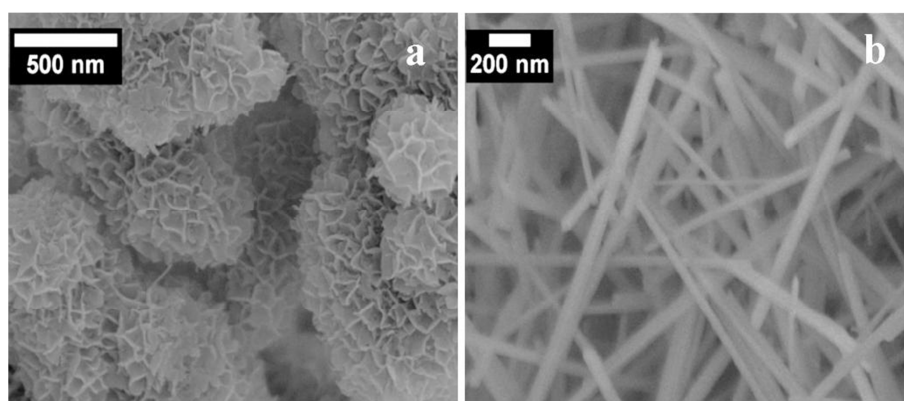
Figure 10. *SEM images of the samples prepared using different refluxing times: a) 1 h, δ-MnO$_2$ and b) 17 h, α-MnO$_2$.*

When a molar ratio of 1:3 is used for the redox couple Mn^{2+}/ MnO$_4^-$, the time has not any effect on the phase purity; δ-MnO$_2$ is produced as depicted by XRD patterns shown in Figure 11. Time affects only the mean grain size. By extending the reflux time the size increases from 10 nm (1 h) to 15 nm (72 h), which is estimated from the reflections widths.

The morphological shape was investigated for two birnessite samples prepared by reflux for two different times of 1 and 17 h. Sponge-like spherical agglomerates were found for both as illustrated by SEM images shown in Figure 12. At shorter time these agglomerates consist of many regular spheres rather than those obtained at longer time. The average diameter of these spheres was estimated for the two birnessite samples, it is in the range of 0.4-0.8 µm for the sample obtained at 1 h and about 1.0 -1.5 µm for the sample obtained at 17 h.

Figure 11. *XRD patterns of δ-MnO$_2$ samples (K-type) prepared by refluxing MnCl$_2$.4H$_2$O and KMnO$_4$(1:3) in aqueous medium for different times of 1, 17 and 72 h.*
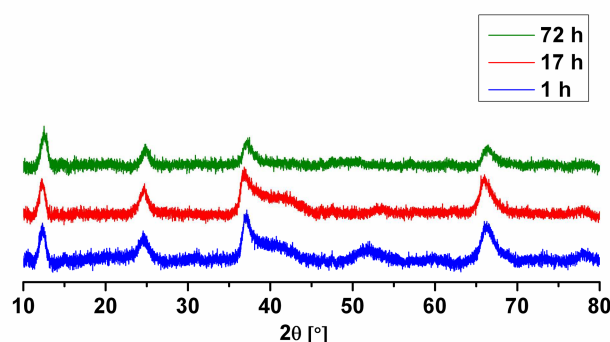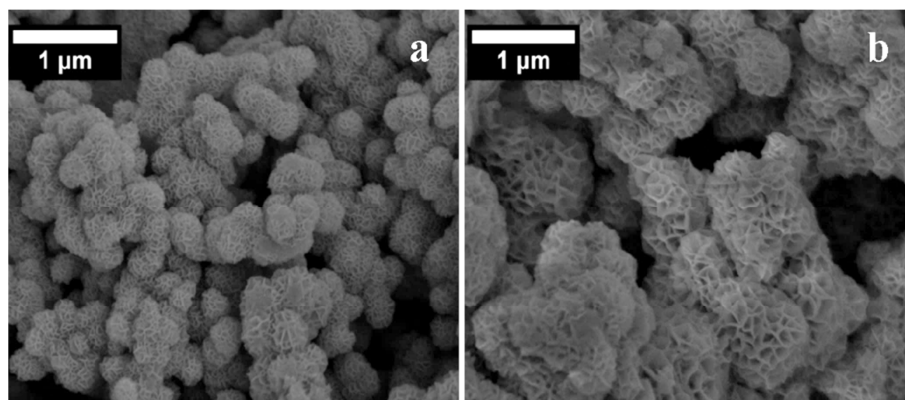
Figure 12. SEM images of birnessite (K-type) samples prepared using different refluxing times: a) 1 h and b) 17 h.

5.4. Impact of temperature

Synthesis of akhtenskite (ε-form)

The influence of the reaction temperature on the product phase and its grain size was studied using a 5:1 molar ratio. Two different temperatures, i.e., room temperature (RT) and 110 °C were used at times of 1 h and 72 h. The results are shown in Figure 13, assignment of the obtained phases as a function of both reaction temperature and time are listed in Table 6. The most important observation is the formation of ε-MnO_2 (akhtenskite, space group $P6_3/mmc$) by aging at RT for 1 h. The lattice parameters for this sample are a = 2.829(1) Å, c = 4.408(2) Å and γ = 120°, according to literature they should be as a = 2.786(1) Å, c = 4.412(1) Å and γ = 120°.[16]

According to Chabre and Pannetier[17] who presented the defects of ''microtwinning'', ε-MnO_2 is a result of the microtwinning of γ-MnO_2 with De Wolff defects.[18] The symmetry is hexagonal as a result of an utmost twinning (the twinning not being rely upon the De Wolff defects). The double chains of ramsdellite (R) and/or single chains of pyrolusite (r), parallel to the c-axis suffer numerous modifications of direction at ca. 60/120° upon twinning resulting in a mean hexagonal structure.[17] Increasing of either the reaction temperature or the aging time results in an arrangement of ε-MnO_2 structure to γ-MnO_2.

IR data for both phases are introduced in Table 7 (see Figure 14). For akhtenskite, there are six absorption bands located in the range 400-800 cm^{-1}; these are related to the vibrations of Mn-O within MnO_6 octahedrons. The absorption peaks are shifted relative to those of nsutite, which gives a hint about structural-diverge between them.

The bands located at ~3400 and 1620 cm^{-1} in the IR spectrum of akhtenskite are ascribed to stretching and bending modes of the –OH group of adsorbed and/or crystallization water.[13] The main constituents of akhtenskite sample are Mn and O as proven by EDX analysis. There are no indications for the presence of either K or Cl ions by EDX analysis.

Table 6. Product phase and its mean particle size as a function of time and temperature.

Time / h	*1*		*72*	
Temperature / °C	*RT*	*110*	*RT*	*110*
Phase	ε-MnO$_2$	γ-MnO$_2$	ε-MnO$_2$+γ-MnO$_2$	γ-MnO$_2$
<d> / nm	8.50	12.5	10.0	13.0
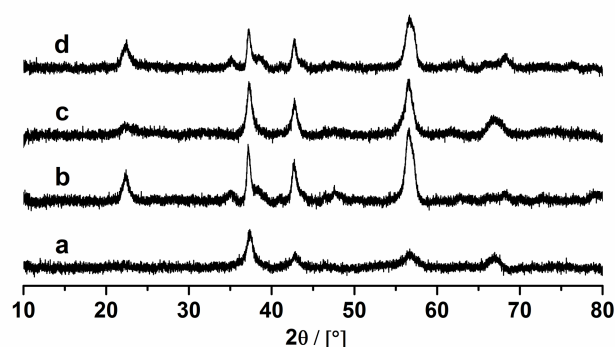
Figure 13. *XRD patterns of the samples prepared by the reaction of MnCl$_2$.4H$_2$O and KMnO$_4$ (5:1) in aqueous medium: a) 1 h at room temperature; ε-MnO$_2$, b) 1 h at 110 °C; γ-MnO$_2$, c) 72 h at room temperature; ε-MnO$_2$+γ-MnO$_2$ and d) 72 h at 110 °C; γ-MnO$_2$.*
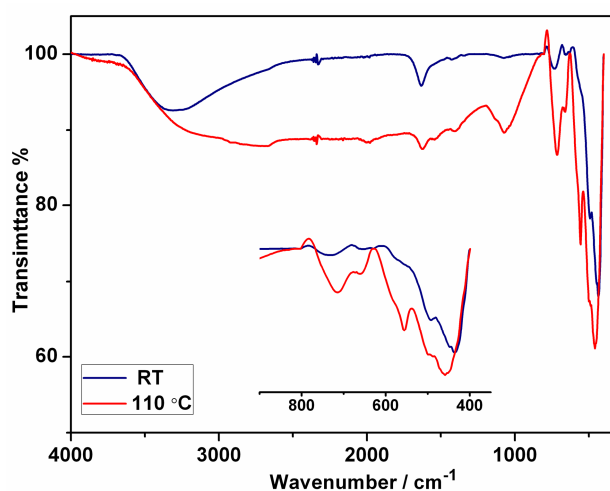
Figure 14. *IR spectra of ε-MnO$_2$ (RT, 1 h) and γ-MnO$_2$ (110 ºC, 1 h) samples.*

Table 7. IR data of ε-MnO$_2$ and γ-MnO$_2$ samples.

Temp.	*Mn–O str. / cm^{-1}*					
RT	437	449	492	571	647	730
110	459	492	556	581	658	714

Investigation of the morphological shape of ε-MnO$_2$ sample prepared at room temperature revealed spherical-like aggregates (Figure 15a) with diameter in the range of 500-750 nm. Each sphere consists of many nanosheets (~9 nm in thickness) that are inclined to each other. The nsutite sample adopts flower-like morphology; its petals are formed from hexagonal plates with thickness of ~12 nm (Figure 15b).
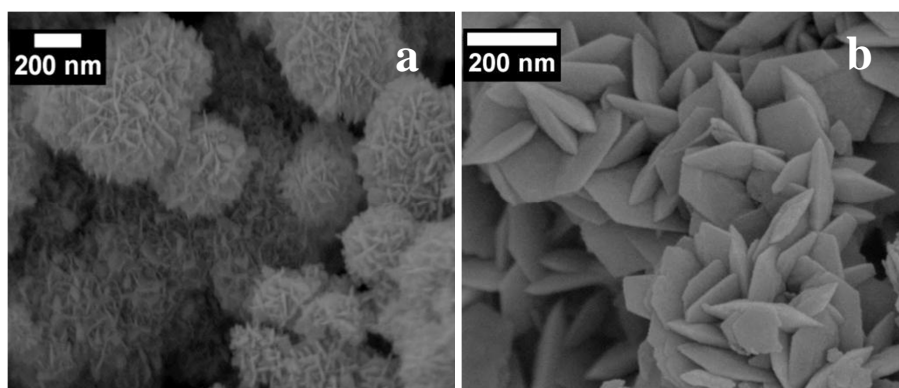
Figure 15. *SEM images of ε-MnO$_2$ (a) and γ-MnO$_2$ (b) samples prepared at room temperature and 110 °C, respectively under reflux for 1 h.*

As we observed before variation of the molar ratio of Mn^{2+}/ MnO_4^- from 5:1 to 1:1 (while the other experimental parameters are kept unchanged) leads to a change in the reaction pathway, cryptomelane is obtained instead of nsutite. The impact of temperature on the reaction pathway in case of using of 1:1 molar ratio was also studied. When the reaction temperature is set at 60 ℃ or 90 °C, birnessite phase is obtained (Figure 16). Two broad reflections at $2\theta = 36.4°$ and $66.6°$ are apparent. The band broadening indicates a low crystallinity of the birnessite samples. The estimated average crystallite size from these two reflections is ~10 nm for both samples. Increasing the reaction temperature to 110 °C results in a collapse of birnessite with a layered-type structure to 2x2 tunnelled structure. Cryptomelane is produced as obvious from the XRD pattern.

Morphological investigations (Figure 17) showed that the birnessite samples have sponge-like spherical agglomerates with diameters of 0.5-1 μm. Each flower is composed of dozens of ultrathin nanoflakes with a thickness of ~10 nm. Cryptomelane has the normal rod-like morphology. The average diameter of the nanorods is ~25 nm and the length is ~1-2 µm.
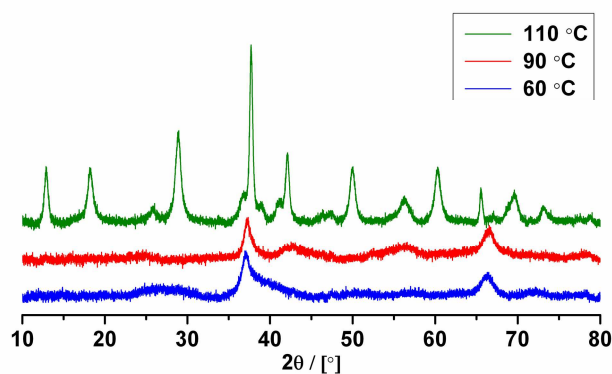
Figure 16. *XRD patterns of the samples prepared by refluxing $MnCl_2.4H_2O$ and $KMnO_4$ (1:1) in aqueous medium for 17 h at different temperatures of 60, 90 and 110 °C.*
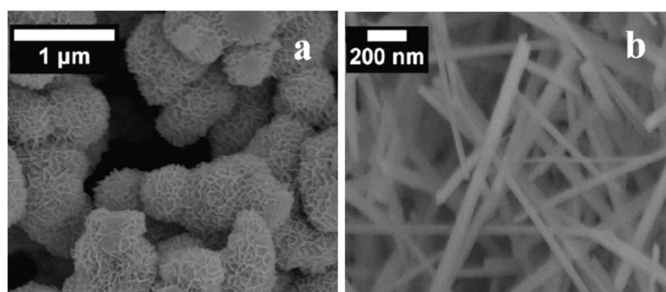
Figure 17. *SEM images of the samples prepared at: a) 60 °C, δ-MnO_2 and b) 110 ℃, α-MnO_2.*

No significant change arises in case of using molar ratio of 1:3. Birnessite is obtained irrespective of the reaction temperature (Figure 18). The temperature affects only on the mean particle size. Sample with lowest crystallite size is obtained at lower reaction temperature (~8 nm) whereas the largest size sample (~10 nm) is formed at higher reaction temperature. SEM analyses revealed the same sponge-like agglomerates for birnessite samples obtained at 60 and 110 °C, the diameter is affected by temperature. At lower temperature the diameter is in the range of 0.2- 0.8 µm whereas 0.5-1.5 µm range is found for the sample obtained at higher temperature as one can see from SEM images (Figure 19).
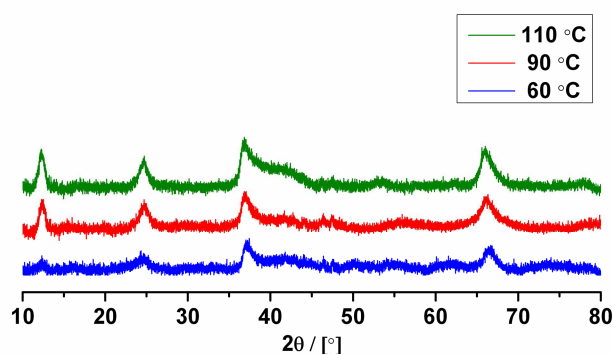
Figure 18. *XRD patterns of birnessite samples prepared by refluxing $MnCl_2.4H_2O$ and $KMnO_4$ (1:3) in aqueous medium for 17 h at different temperatures of 60, 90 and 110 °C.*
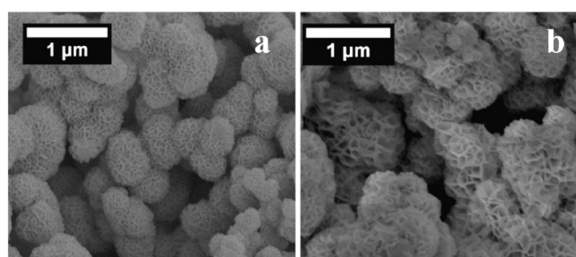
Figure 19. *SEM images of birnessite samples prepared at a) 60 °C and b) 110 °C.*

5.5. Effect of alkali metal cations

The influence of the alkali-metal cations of the permanganate salts on the reaction pathway was investigated. The comproportionation reaction was performed between $MnCl_2$ and different permanganate salts, i.e., $NaMnO_4$, $KMnO_4$ and $CsMnO_4$. The other experimental parameters were kept unchanged (molar ratio of 5:1 for Mn^{2+}/MnO_4^-, reflux for 17 h and total Mn concentration ~62.0 mmol L^{-1}). No change in the reaction product occurs using various permanganate salts. XRD measurements revealed that all patterns correspond to that of γ-MnO_2 as shown in Figure 20. The estimated particle size for all samples is ~12 nm.

SEM examination for the obtained nsutite samples was done. It is clear from Figure 21 that, γ-MnO_2 sample prepared using $KMnO_4$ has a plate-like morphology with large diameter of 100-300 nm. Nsutite samples with deformed plates are obtained using either $NaMnO_4$ or $CsMnO_4$. Much smaller and deformed plates are observed for the sample prepared using $CsMnO_4$. For this sample the particles are aggregated together to form hollow structures.
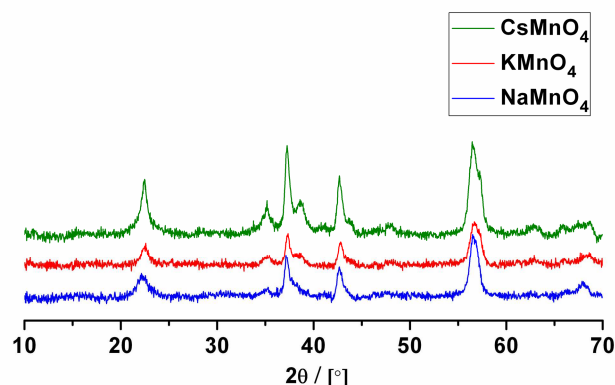
Figure 20. *XRD patterns of the nsutite samples prepared by refluxing $MnCl_2.4H_2O$ and $XMnO_4$ (5:1) for 17 h, where X = Na, K or Cs.*
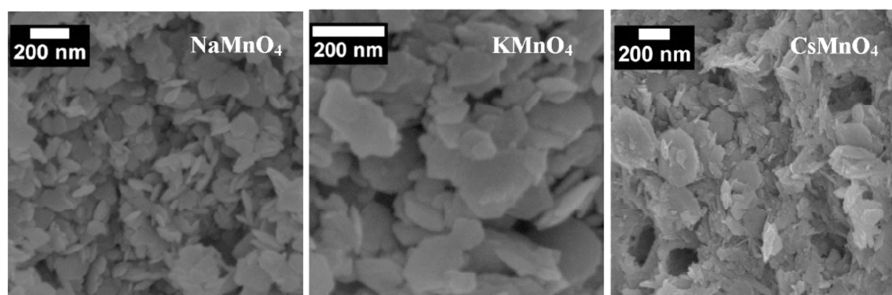
Figure 21. *SEM images of nsutite samples obtained using different permanganate salts.*

A marked effect of the alkali metal cations is observed when 1:1 molar ratio is used for Mn^{2+}/MnO_4^-. Using either sodium or cesium permanganate, γ-MnO_2 (1x2 + 1x1 tunnels) is produced, whereas utilizing of $KMnO_4$ results in formation of cryptomelane, α-MnO_2 (2x2 tunnelled structure). Apparently, potassium in this case is acting as a template for the structural modifications from one with small tunnel size to one with large tunnel size (Figure 22).

EDX analyses were performed, the results showed that in case of cryptomelane with large tunnel size the accommodation of K^+ cations (3 $\pm$ 0.3%) is the case. Certainly, these tunnels are smaller in size in the case of nsutite. Accordingly, nsutite cannot insert Na^+ or Cs^+ cations.

(See the discussion section to understand why K results in formation of cryptomelane whereas Na and Cs lead to formation of nsutite).
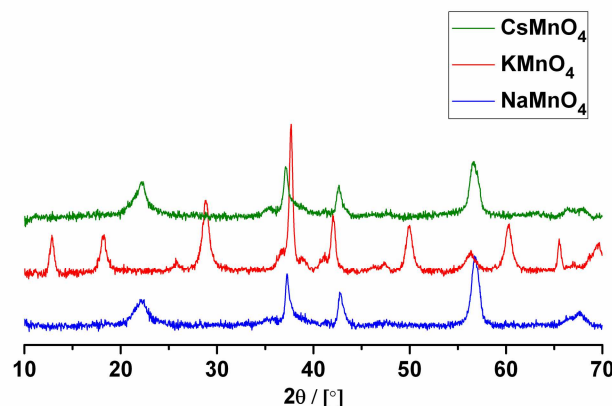
Figure 22. *XRD patterns of the samples prepared by refluxing MnCl$_2$.4H$_2$O and XMnO$_4$ (1:1) for 17 h, where X = Na, K or Cs.*

SEM investigations (Figure 23) showed that the cryptomelane sample has a rod-like morphology with average diameter of 25 nm. Nsutite samples with plate-like shape can be observed (left and right pictures). Well-shaped plates with approximately hexagonal edges can be seen for the sample obtained using CsMnO$_4$. This observation indicates a uniform growth of these plates in case of CsMnO$_4$.
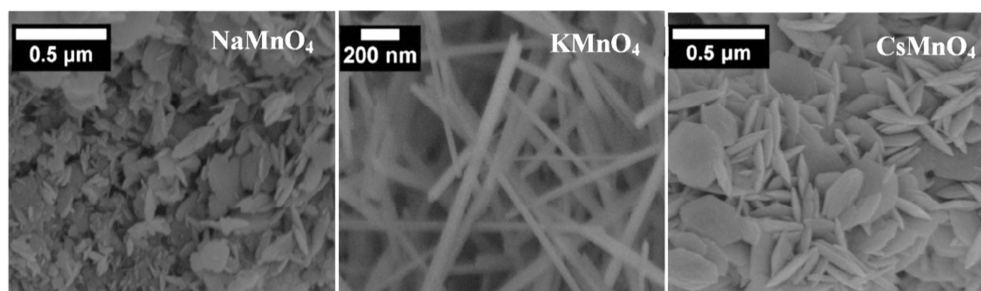
Figure 23. *SEM images of MnO$_2$ samples, the left and right one for γ-MnO$_2$ and the one in the middle represents α-MnO$_2$.*

In chapter 3 we have seen that when the reactions are performed under otherwise equal conditions using Mn(OAc)$_2$ instead of MnCl$_2$ whilst 5:1 molar ratio is used for Mn^{2+}/MnO$_4^-$, variation of the permanganate salt does not result in variation of the reaction product. Manganite nanorods were obtained regardless of the type of the permanganate salt. The morphological shape is the only factor that is affected in this case.

A complety different case exists when 1:1 molar ratio is used for Mn^{2+}/MnO$_4^-$, the templating effect of alkali metal cations of the permangante salts is quite obvious. Signifacant

varition in the reaction pathways toward the formation of different forms of MnO_2 is monitored by XRPD (Figure 24). In case of using $NaMnO_4$, nsutite (γ-MnO_2) is formed, which is a small tunnel size (1x2 + 1x1) manganese dioxide. Hence, tunnels can not insert Na cations. Average particle size calculated for this sample using Scherrer's formula is ~14 nm. Once the cation is changed from Na to K, large tunnel size manganese dioxide is formed which is characterized as crytomelane (α-MnO_2) with 2x2 tunnelled structure. The average grain size is 14 nm. Intercalation of K^+ cations is anticipated in this case. Indeed cryptomelane is stabilized by insertion of K^+ cations. When larger size Cs cations are used as a template, transition from the tunnel structure to the layer-type birnessite takes place. With an interlayer distance of 7 Å it is possible for the large size Cs cations to reside between the layers.
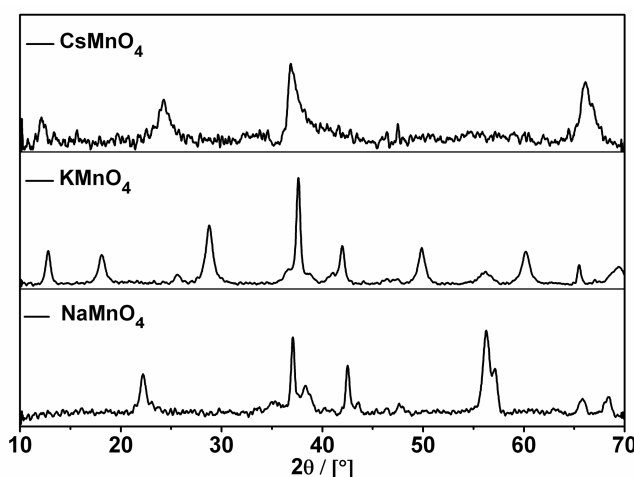
 Figure 24. *XRD patterns of the products of the redox reaction between Mn(OAc)₂ and XMnO₄ (1:1), where X=Na, K or Cs, the reaction lasts 17 h.*

EDX measurements were accomplished for the as-prepared samples, the results showed for nsutite with a smaller tunnel size that the residence of Na cations is not likely. Actually, there is no indication from EDX (Figure 25) hinting to the existence of Na as interstitial cations or even as excess cations over the surface of the prepared γ-MnO_2 sample. Tiny amount of Na cations exists (atomic percent of about 0.2%), this may be related to some unreacted cations placed over nsutite surface (can be removed by extra-washing for the sample). From Table 8, the found atomic percent values for Mn and O atoms are typical for MnO_2 structure without foreign cations in its tunnelled structure. With cryptomelane having 2x2 tunnels, the insertion of K cations is reasonable. Actually, EDX graph (Figure 25) reveals its presence, corresponding peaks exist. In this case a large amount of K cations is located into these tunnels, the found atomic percent of K about 5%. For the layered-type birnessite structure

with the large interlayer distance it is possible for the large size Cs cations to locate between its layers giving rise to a structural stability. EDX measurements displayed peaks corresponding to Cs (Figure 25). To the best of our knowledge this the first time that Cs-birnessite is prepared by our method.

Table 8. Atomic percent values obtained for γ-, α- and δ-MnO$_2$ samples. Standard deviations are shown in parenthesis.

Sample	*Atomic percent / %*		
	Mn	*O*	*X*
γ-**MnO$_2$**	33(3)	67(4)	0.2(0.1) [a]
α-**MnO$_2$**	35(2)	60(2)	5(0.5) [b]
δ-**MnO$_2$**	32(4)	64(5)	4(1) [c]

a; X= Na, b; X= K and c; X= Cs
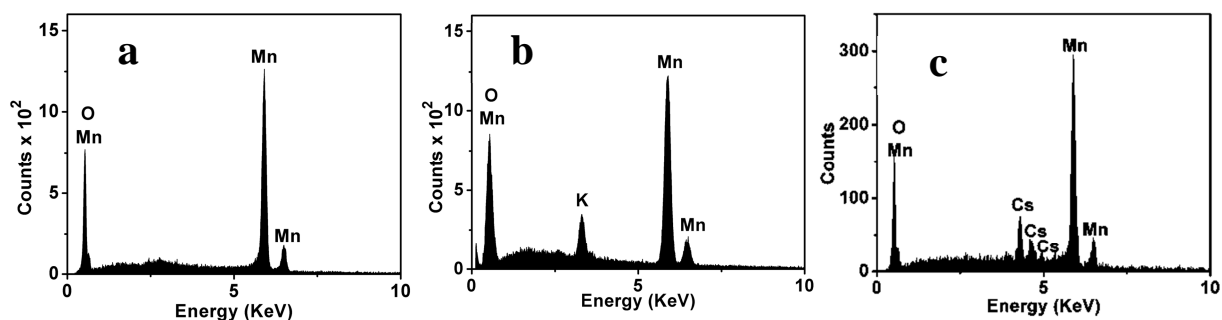
Figure 25. *EDX analyses of a) γ-MnO$_2$, b) α-MnO$_2$ and c) δ-MnO$_2$ (Cs-birnessite), respectively.*

Radius ratio tolerance factor

Formation of manganese dioxides with variable crystal structure can be explained by taking into considerations so-called Tolarence Factor. The question now why K containing permangante salt steer the reaction toward the formation of cryptomelane (Hollandite structure) whereas Na or Cs does not?

In 1983 Kesson and White geometrically demonstrated the relation between the 2 x 2 tunnel dimensions and the size of the central cation.[19] They extended a simple "radius ratio tolerance factor" t_H that can be given by the equation 3. Assessment of this factor is most convenient to prognosticate the stability of a large variety of hollandite structures with different tunnel ions and a variety of elements other than manganese constructing the octahedral framework. According to thier results, t_H values of 0.93–1.16 indicate a stable hollandite structure.

$$t_H = \frac{[(r_A + r_O)^2 - 0.5(r_B + r_O)^2]^{0.5}}{\sqrt{1.5}(r_B + r_O)} \hspace{3cm} (3)$$

r_A = radius of the tunnel cation, r_B = radius of the octahedral center-ion, r_O = radius of oxygen.

In hollandites, tunnel ions are surrounded by eight oxygen atoms. For the tunnel ions A located within the (2 x 2) tunnels in eightfold coordination of oxygen with, A = Na, K and Cs, the ionic radii (Table 9)[20] were used to calculate the tolerance factors. It is assumed that 100% Mn^{4+} with coordination number six which possesses an ionic radius of 67 pm and O^{2-} ions with coordination number two and an ionic radius of 126 pm.[20] Calculation of the factor t_H for potassium results in $t_H = 1.03$. This value locates in the range appropriate for the formation of stable manganese oxide with 2x2 tunnels.

For Na and Cs cations the values are 0.85 and 1.17, respectively. Both values are located out of the previousely mentioned range, hence, the formation of stable cryptomelane structure with these cations is not possible.

Table 9. Ionic radii of tunnel ions (A) and the corresponding tolerance factors t_H.

Ion (A)	Radius (K=8) pm	t_H
Na	116	0.85
K	152	1.03
Cs	181	1.17

SEM investagations for the obtained samples revealed different morphological shapes. This divergence in morphology arises mainly from the variation in the crystal structure of each form and the way in which the atomes are arranged within this structure. For nsutite with a hexagonal unit cell, very thick plates (about 40 nm in thickness) are formed as shown in Figure 26b. These plates have somewhat sligh uniform hexagonal shapes. The dimensions of which fall in the range 300-400 nm. Rod-like morphology is apparent for the cryptomelane (α-form) sample that have a tetragonal unit cell, these rods are uniform throughout. Two arrays of nanorods are apparent in the SEM image (Figure 26c) one with large average diameter of 35-50 nm and length of 2-3 μm and the other is thinner and has average diameter of ~10-15 nm. For Cs-birnessite (δ-form) sample a flower-like morphology is a characteristic shape, with thickness of the petals ~10 nm (Figure 26f).
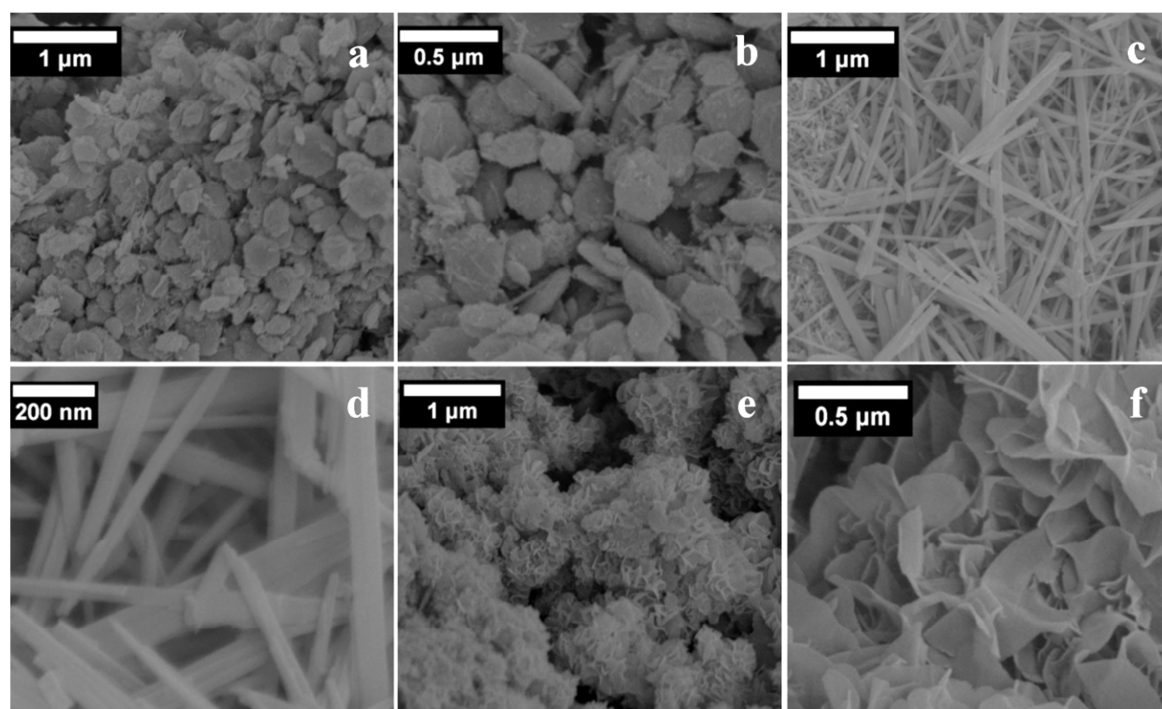
Figure 26. *Low and high magnification SEM images of a-b) γ-MnO$_2$, c-d) α-MnO$_2$ and e-f) δ-MnO$_2$, respectively, formed by refluxing of different permanganate salts with Mn(OAc)$_2$ (1:1) in aqueous medium for 17 h.*

5.6. Structural analysis of akhtenskite (ε-MnO$_2$)

Rietveld refinement for the akhtenskite sample (<d> ~8.5 nm) was used to identify some structural properties. There is a good agreement between the theoretical and calculated patterns (Figure 27) as indicated by R values shown in Table 10. The cell parameters spell out the hexagonal symmetry, trivial differences exist in comparison to the reported values (< 5 pm).[16] Akhtenskite has regular MnO$_6$ octahedrons with 6 equal Mn-O bonds, the distances between Mn and O atoms are 197.01(0.06) (reported Mn-O distance was 195.22).[16]

From the refinement (Table 11), the SOF value of Mn^{4+} is found to be 0.431(9) which refers to deficiency in Mn^{4+} sites (~14%) in accordance with SOF = 0.5 for clean ε-MnO$_2$.[16] The deficiency results in formation of cationic vacancies, Mn^{4+} may be reduced to Mn^{3+} or even to Mn^{2+} (yet, no proof). Actually, further analytical methods are necessary to identify the presence of various oxidation states of manganese in the akhtenskite structure. These cationic vacancies can be compensated by existence of species such as H$_2$O or OH$^-$.

IR spectrum of akhtenskite presented before (Figure 14) showed two pronounced absorption bands locate at 1620 and 3400 cm^{-1} which are assigned to OH bending and

stretching modes, respectively. Presence of OH^- or H_2O (could not be distinguished from IR) may compensate for such cationic defects.

The measured density for this akhtenskite sample is 4.05(0.06) g/cm^3 which is lower than the calculated from Rietveld analysis (4.24 g/cm^3). Both are lower than the density for the bulk material which should be 4.78 g/cm^3.

Integration of all results from Rietveld analysis, IR and density measurement we can realize that akhtenskite with a defected structure is obtained.
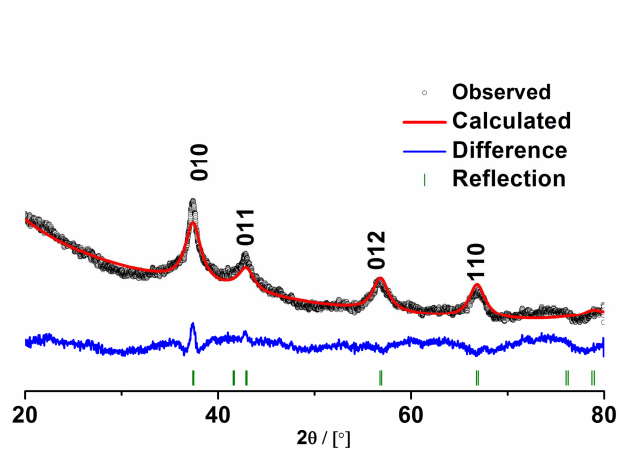
Figure 27. *Refinement analysis of ε-MnO₂ sample using Rietveld method.*

Table 10. Measurement parameters, structure and refinement data for akhtenskite based on ICSD-76430 data as starting set of the calculations.[16]

Akhtenskite sample	$<d> = 8.5\ nm$
Formula sum	$Mn_{0.86}O_{2.00}$
Z	1
Formula mass / g/mol	79.35
Space group (No.)	$P6_3/mmc$ (194)
a = b / Å	2.829(1)
c / Å	4.408(2)
$\gamma^\bullet$	120
ρ / g/cm³	4.31
V/ 10^6 pm³	30.549
R (expected) / %	1.348
R (profile) / %	0.969
R (weighted profile) / %	1.230
R (Bragg) / %	0.633
GOF	0.832

Radiation is Cu-$K\alpha$ and the type of profile fit is Pseudo-Voigt

Table 11. Wyckoff positions, occupancy, atomic fractional coordinates and isotropic displacement parameters B of akhtenskite (ICSD-76430).

Atom	*Wyck.*	*s.o.f*	*x*	*y*	*z*	*B / 10^4 pm²*
Mn	2a	0.431(9)	0.0	0.0	0.0	2.74
O	2c	1.0	0.33329	0.6667	0.25	4.80994

5.7. Summary and conclusions

Different polymorphs of manganese dioxides are prepared from the comproportionation reaction between divalent manganese and different permanganate salts. Control over the experimental conditions is the key parameter for such reaction, e.g., time, temperature, molar ratio of Mn^{2+}/MnO_4^-, pH and the alkali metal in the permanganate salt.

Room-temperature synthesis of akhtenskite; ε-MnO_2 ($<d>$ ~8.5 nm) was developed for the first time from such comproportionation reaction. Akhtenskite adopted a sponge-like spherical morphology with a mean diameter of 500-750 nm.

The structural analysis of akhtenskite via Rietveld refinement revealed deficiencies in cationic sites. This result was proven by the dropping of the measured density value for this sample from that of the bulk material, i.e., measured value of 4.05 g/cm^3 is found compared to 4.78 g/cm^3 for the bulk (calculated density from the refinement ~4.24 g/cm^3). IR results indicate the existence of OH groups which may compensate for the cationic vacancies.

Self-template method is a promising technique for synthesis of various manganese dioxide polymorphs, particularly, birnessite type containing large-size Cs cations intercalated between its layers.

The prepared oxides possess different morphological shapes, i.e., plates, rods, sponge-like spheres or flowers. The various routes for obtaining the different polymorphs of manganese dioxide can be summarized according to the following diagrams:
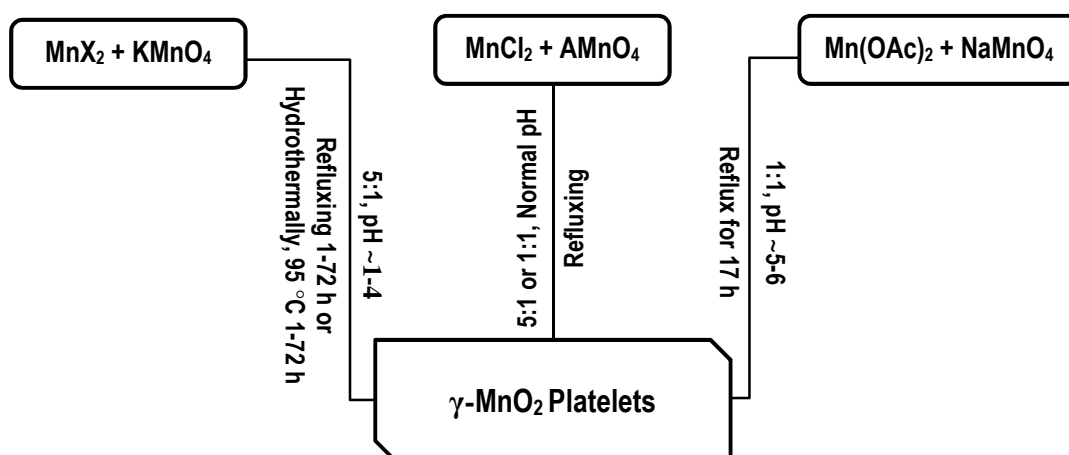
Scheme 1. *The various routes of synthesis of nsutite (γ-MnO$_2$); X = OAc$^-$, Cl$^-$ or SO$_4^{-2}$; A = Na or Cs.*
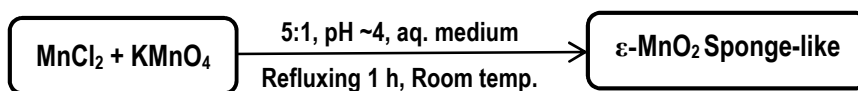
Scheme 2. *Synthesis of akhtenskite, ε-MnO₂.*
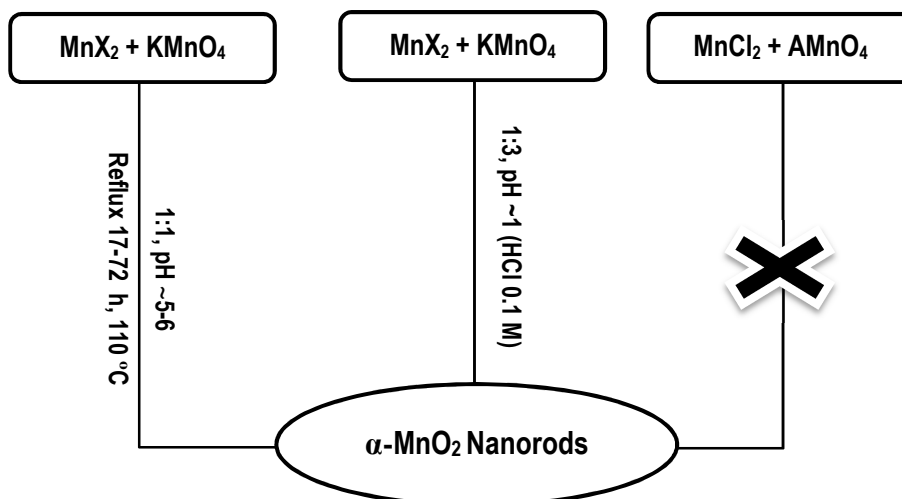
Scheme 3. *The various routes of synthesis of cryptomelane (α-MnO₂); X = OAc⁻, Cl⁻ or SO₄⁻²; A = Na or Cs.*
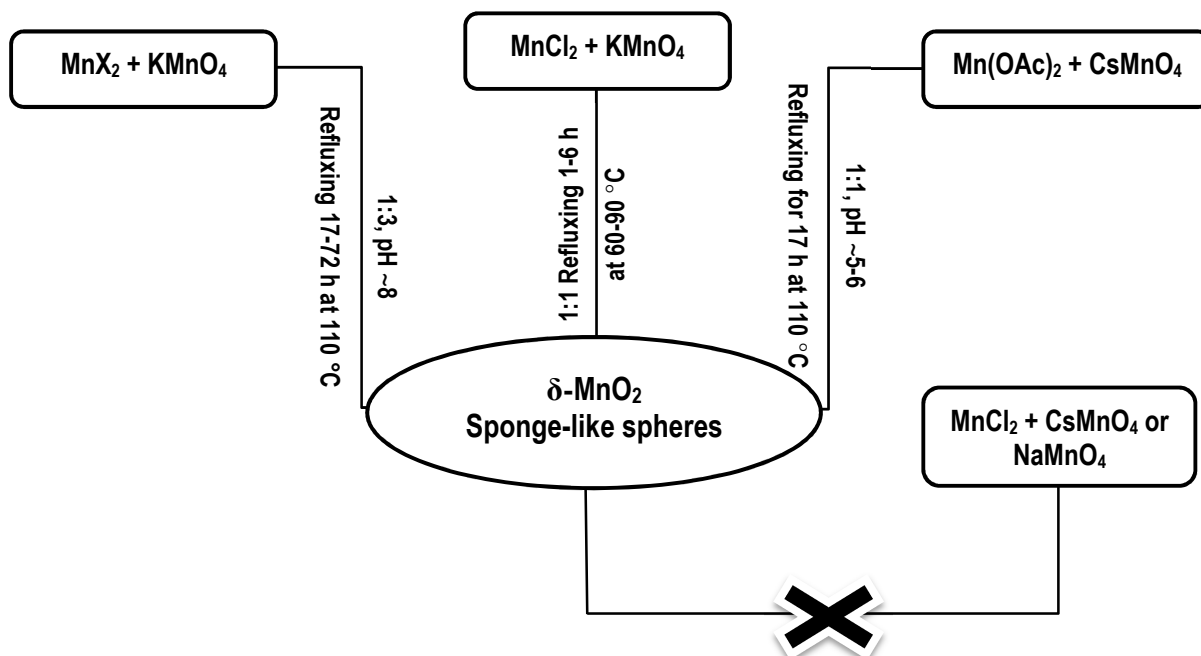
Scheme 4. *The various routes of synthesis of K- and Cs-birnessite (δ-MnO₂), X = OAc⁻, Cl⁻ or SO₄⁻².*

References

1. Hashemzadeh, F.; Mehdi Kashani Motlagh, M.; Maghsoudipour, A. A comparative study of hydrothermal and sol−gel methods in the synthesis of MnO_2 nanostructures. *J. Sol-Gel Sci. Technol.* **2009,** *51* (2), 169-174.

2. Umek, P.; Zorko, A.; Arcon, D. Magnetic properties of transition-metal oxides: From bulk to nano. In *Ceramics Science and Technology*, Wiley-VCH Verlag GmbH & Co. KGaA: 2010; pp 791-833.

3. Brock, S. L.; Duan, N.; Tian, Z. R.; Giraldo, O.; Zhou, H.; Suib, S. L. A review of porous manganese oxide materials. *Chem. Mater.* **1998,** *10* (10), 2619-2628.

4. Wang, X.; Li, Y. D. Synthesis and formation mechanism of manganese dioxide nanowires/nanorods. *Chem. Eur. J.* **2003,** *9* (1), 300-306.

5. Qiu, G.; Huang, H.; Dharmarathna, S.; Benbow, E.; Stafford, L.; Suib, S. L. Hydrothermal synthesis of manganese oxide nanomaterials and their catalytic and electrochemical properties. *Chem. Mater.* **2011,** *23* (17), 3892-3901.

6. Chen, Y.; Duan, Z.; Min, Y.; Shao, M.; Zhao, Y. Synthesis, characterization and catalytic property of manganese dioxide with different structures. *J. Mater. Sci. : Mater. Electron.* **2011,** *22* (8), 1162-1167.

7. Yang, Y.; Huang, C. Effect of synthetical conditions, morphology, and crystallographic structure of MnO_2 on its electrochemical behavior. *J. Solid State Electrochem.* **2010,** *14* (7), 1293-1301.

8. Santos, V. P.; Pereira, M. F. R.; Órfão, J. J. M.; Figueiredo, J. L. Synthesis and characterization of manganese oxide catalysts for the total oxidation of ethyl acetate. *Top. Catal.* **2009,** *52* (5), 470-481.

9. Holland, K. L.; Walker, J. R. Crystal structure modeling of a highly disordered potassium birnessite. *Clays Clay Miner.* **1996,** *44* (6), 744-748.

10. Julien, C. M.; Massot, M.; Poinsignon, C. Lattice vibrations of manganese oxides: Part I. Periodic structures. *Spectrochim. Acta, Part A* **2004,** *60* (3), 689-700.

11. Ananth, M. V.; Pethkar, S.; Dakshinamurthi, K. Distortion of MnO_6 octahedra and electrochemical activity of Nstutite-based MnO_2 polymorphs for alkaline electrolytes− an FTIR study. *J. Power Sources* **1998,** *75* (2), 278-282.

12. Tian, H.; He, J.; Zhang, X.; Zhou, L.; Wang, D. Facile synthesis of porous manganese oxide K-OMS-2 materials and their catalytic activity for formaldehyde oxidation. *Microporous Mesoporous Mater.* **2011,** *138* (1−3), 118-122.

13. Nakamoto, K. Infrared and Raman Spectra of Inorganic and Coordination Compounds: Applications in coordination, organometallic, and bioinorganic chemistry; Wiley: 1997.

14. Everett. D. H. Manual of symbols and terminology for physicochemical quantities and units. Appendix II. Definitions, terminology, and symbols in colloid and surface chemistry. *Pure Appl. Chem.* **1972,** *31* (4), 577-638.

15. Sing, K. S. W.; Everett, D. H.; Haul, R. A. W.; Moscou, L.; Pierotti, R. A.; Rouquerol, J.; Siemieniewska, T. Reporting physisorption data for gas/solid systems with special reference to the determination of surface area and porosity. *Pure Appl. Chem.* **1985,** *57* (4), 603-619.

16. Kondrashev, Yu. D.; Zaslavskii, A. I. The structure of the modifications of manganese oxide. *Izvestiya Akademii Nauk SSSR, Seriya Fizicheskaya* **1951,** *15*, 179-186.

17. Chabre, Y.; Pannetier, J. Structural and electrochemical properties of the proton / γ-MnO_2 system. *Prog. Solid State Chem.* **1995,** *23* (1), 1-130.

18. De Wolff, P. M. Interpretation of some γ-MnO_2 diffraction patterns. *Acta Cryst.* **1959,** *12* (4), 341-345.

19. Kesson, S. E.; White, T. J. Radius ratio tolerance factors and the stability of hollandites. *J. Solid State Chem.* **1986,** *63* (1), 122-125.

20. Shannon, R. D. Revised effective ionic radii and systematic studies of interatomic distances in halides and chalcogenides. *Acta Cryst. A* **1976,** *32* (5), 751-767.

Chapter 6

Simple preparative method for tunable size Mn$_3$O$_4$ nanocrystals:

Characterization and defect chemistry

6. Introduction

Hausmannite has a stoichiometry corresponds to a normal spinel AB_2O_4. The unit cell comprises 32 oxide ions and there are 8 Mn^{2+} ions occupying the tetrahedral (A) and 16 Mn^{3+} ions located in the octahedral (B) sites.[1-3]

References to hausmannite reveals that hausmannite has some trends toward nonstoichiometry through the formation of oxygen-rich compounds compared to the normal Mn:O ratio in stoichiometric Mn_3O_4.[4-7] These deviations from stoichiometry result in a defect structure and substitution of Mn^{3+} for Mn^{2+} giving rise to formation of cation vacancies.

The distribution of Mn^{3+} cations and cationic vacancies in the hydrous hausmannite was studied (single particle size).[8] It has been found that the cationic vacancies in hydrohausmannite are mainly due to the presence of structural OH^- groups.

Actually, the identification of the defect chemistry for substances is the key factor for understanding many intrinsic properties of the materials. Similarly, the variation of particle size gives rise to the variation of many properties of such materials. Accordingly, we will extend the former study on the defect chemistry of hydrous hausmannite to comprise size-dependent defect chemistry on the basis of Reitveld refinement to XRD intensity profile.

Wang et al., synthesized the Mn_3O_4 nanocrystals (~5 nm). They used ethanol as a solvent, precipitated the hydroxide with KOH and heated to 60 °C for 24 h.[9] We followed the same experimental procedures as them (i.e., amounts of $Mn(OAc)_2$ and KOH, time and temperature) and we could not obtain a clean phase hausmannite. Accordingly, in our work we will prepare the hydrous hausmannite in a similar way but with some modifications for this method. The hydroxide gel will be precipitated by using either NaOH or NH_3 solution. Mixtures of ethanol-water will be used with a purpose of tuning the particle size for the obtained nanocrystals.

The report of Shchukarev et.al.,[10] about the solubility of oxygen in ethanol-water mixtures revealed that, the amount of dissolved oxygen significantly affected by the content of ethanol in water. Solutions with high ethanol content can dissolve oxygen much easier than those with low ethanol content. The quantity ι (Ostwald distribution coefficient, i.e., the number of volumes of gas dissolved per unit volume of solvent) for dissolved oxygen in pure water, pure ethanol and in a mixture of both was determined experimentally. The distribution coefficient is dependent on the temperature; the corresponding coefficients at 25 ºC were found for pure water 0.031 and 0.283 for pure ethanol.

Based on the former, we can identify the goals for our research study in this chapter as follow:

⇨ Identification of the influence of ethanol/water ratio (i.e., changing of solvent polarity) on the grain size of the as-prepared Mn_3O_4 nanoparticles.

⇨ The amount of dissolved oxygen in the reaction medium is a critical parameter that can affect the product phase hence studying the factors affecting the dissolved oxygen such as solvent polarity, temperature and time are of significance.

⇨ Investigation of the size-dependent sorption properties, i.e., surface area, pore width and total pore volume.

⇨ Finally, as many intrinsic properties are function of the material structure so it is of interest to study the defect chemistry of the spinel structure as a function of grain size.

6.1. NaOH as a precipitating agent

In such reaction manganese (II) is precipitated using NaOH (~0.08 mol L^{-1}, $c(Mn^{2+})/c(OH^-)$ $\approx$ 1:2) as $Mn(OH)_2$ which subsequently undergoes air oxidation to Mn_3O_4 (Hausmannite), the reaction was performed in pure water at first. All reflections for the obtained product (Figure 1) match consistently with those of hausmannite (ICSD-31094). Hausmannite sample with average grain size of 21 nm (calculated from the band broadening using Scherrer's formula) was produced. The reflections used for determination of the average particle size <d> are (112), (013), (121), (220), (231) and (224)). In pure water the formation of the spinel can be represented by the following equations:

$$Mn(OAc)_2 + 2\ NaOH \rightarrow Mn(OH)_2 + 2\ NaOAc \tag{1}$$

$$3\ Mn(OH)_2 + 1/2\ O_2 \rightarrow Mn_3O_4 + 3\ H_2O \tag{2}$$
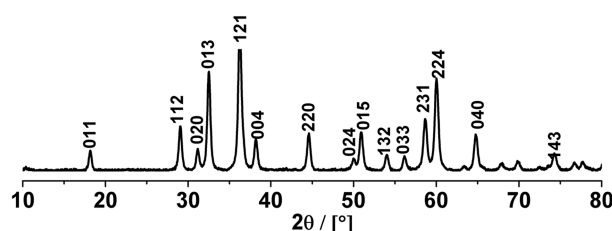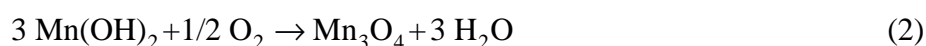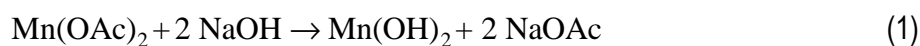
Figure 1. *Diffractogram of nc-Mn₃O₄ precipitated from pure water using sodium hydroxide at 40 °C after 6 h, Miller indexes are assigned.*

6.1.1. Variation of ethanol content

Various ratios of $EtOH/H_2O$ were used: 0%, 50%, 85% and 95%. The reactions were carried out under reflux at 40 °C for 1 h. The results of XRPD analyses for the products (Figure 2) revealed that the content of ethanol in water has a great impact on the phase purity and the mean grain size of nc-Mn_3O_4 samples. By increasing the ethanol content from 0 to 50%, the grain size of the so obtained Mn_3O_4 sample (X-ray single phase) falls by about 57% of its original value where the size drops from ~21 to ~12 nm. For the sample prepared in pure water, a tiny reflection appears at 2θ ~18.75°. This can be assigned to the presence of subtle amount of un–oxidized $Mn(OH)_2$,[11] which means that shorter reflux time of 1 h is insufficient for complete air oxidation of $Mn(OH)_2$. Band broadening and less intense peaks are general features for the powder patterns of the samples obtained with increasing ethanol content, reflecting reduction in the grain size of the products. By increasing the %EtOH up to

85 and 95% impure hausmannite samples were produced, the drop in size in such cases is not significant. Trace amounts of β-MnOOH were observed in the products that can be identified by the presence of a small peak appeared at 2θ ~19.2° (feitknechtite, JCPDS 18-0804) as reported by Portehault et al.,[12] summary of the impact of ethanol content in water on the product phase, its mean grain size and the lattice parameters is listed in Table 1.

Table 1. Impact of variation of %EtOH on the reaction product, its mean grain size and the lattice parameters, NaOH was used as a precipitant.

%EtOH	*0*	*50*	*85*	*95*	*100 [a]*
Phase	Mn_3O_4+A	Mn_3O_4	Mn_3O_4+B	Mn_3O_4+B	-
<d> / nm	21	12	11	10.5	-
a / Å	5.7645(2)	5.7660(5)	5.7674(5)	5.770(1)	
c / Å	9.4423(4)	9.439(1)	9.416(1)	9.411(3)	

A: $Mn(OH)_2$; B: β-MnOOH; a: no precipitation.
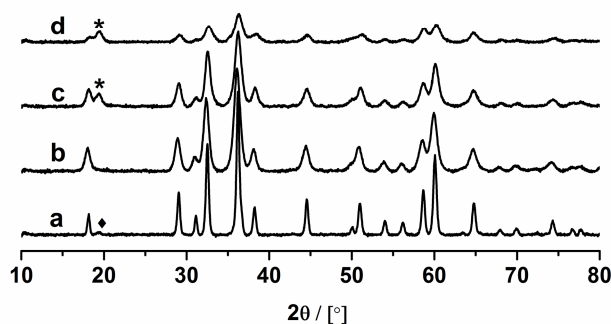
Figure 2. *XRD patterns of the hausmannite samples obtained using different %EtOH, the reactions were performed under reflux at 40 °C for 1 h using NaOH as a precipitant. a) 0%, b) 50%, c) 85% and d) 95%, stars: β-MnOOH and diamond: un-oxidized Mn(OH)$_2$.*

The remarkable fall of the particle size with increasing the content of ethanol can be explained as follows: Ethanol is a less polar solvent than water, thus the solvation energy of the oxide/hydroxide phase is lower than in pure water. This leads to a higher initial energy of the oxide/hydroxide before nucleation, so decreasing the energy barrier that has to be overcome for crystallization.[13] Consequently, the nucleation rate is higher in ethanol-rich solutions, so the available manganese oxide is consumed quickly which prevents the growth of bigger crystallites.

IR analyses were done for the products, the spectra are shown in Figure 3. Magnifications in the range of 400-1200 cm^{-1} are shown for two samples produced using either pure water or 95% EtOH. The results are shown in Table 2.
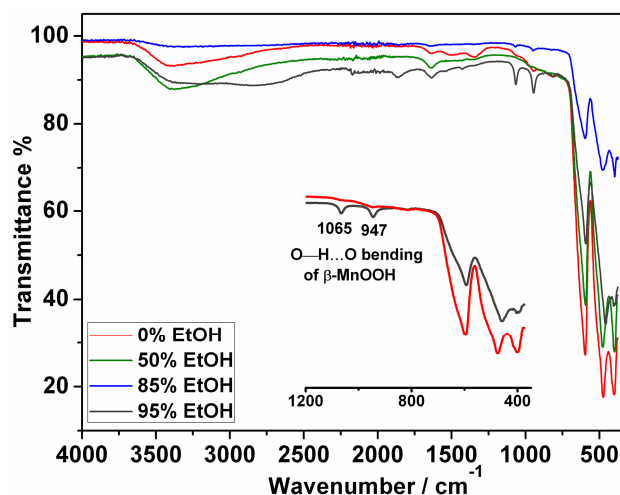
Figure 3. *IR spectra of the samples prepared by precipitation of Mn(OH)$_2$ followed by air oxidation in the presence of different ratios of ethanol/water solutions at 40 °C for 1 h. The inset is the magnification of IR spectra in the region 400-1200 cm^{-1} for the samples prepared in pure water and in 95% EtOH.*

Table 2. Impact of variation of %EtOH on the vibrational modes of the samples obtained using NaOH as a precipitant.

%EtOH	*Peak positions / cm^{-1}*	*Assignment*
0	402, 475, 597	Mn-O vibrations
50	400, 477, 594	Mn-O vibrations
85	400, 476, 596	Mn-O vibrations
	949, 1067	O—H…O bending of β-MnOOH
95	400, 459, 594	Mn-O vibrations
	947, 1065	O—H…O bending of β-MnOOH
	2700	OH stretching of β-MnOOH

IR spectrum of the sample obtained in pure water (also the hausmannite sample obtained using 50% EtOH) exhibits three absorption bands at ~400, 477 and 594 cm^{-1}, which are consistent with the bands described in literature for bulk Mn$_3$O$_4$.[14] The bands locate at 594 and 477 cm^{-1} are commonly related to the coupling between the Mn-O stretching modes of the octahedral and tetrahedral sites, whereas the band locates at 400 cm^{-1} is correlated to the bond

stretching modes of the octahedral sites. Absorption bands located at 1638 and 3416 cm^{-1} are attributed to bending and stretching vibrations of the –OH group of absorbed and/or crystallization water molecules.[15] No shifts in the positions of the absorption bands were monitored as a function of size modification. Instead a decrease in the intensity of the absorption peaks corresponding to Mn-O vibrations with increasing of the amount of ethanol is found, probably arising from the decreasing in the grain size.

For the samples synthesized whilst 85% and 95% EtOH solutions were utilized the IR spectra display characteristic peaks at 947 and 1065 cm^{-1}, which are assigned to the deformation vibrations of O—H…O for β-MnOOH.[16] These peaks are more pronounced in case of using 95%EtOH solution. The broad band at ~2700 cm^{-1} is attributed to OH stretching vibration due to hydrogen bond O—H…O.

6.1.2. Impact of time and temperature

Time-dependent experiments were performed by carrying out the reactions at variable times of 1, 6, 24 and 72 h using either pure water or 95% EtOH as reaction solvents. The summary of this study is listed in Table 3. In pure water (Figure 4), at shorter time of 1 h tiny impurities of un-oxidized Mn(OH)$_2$ coexist with hausmannite as indicated by too less intense peak at 2θ ~18.75º,[11] pristine hausmannite is produced while the reaction is set at times between 6-24 h. Extension of the time up to 72 h results in an additional phase combined with Mn$_3$O$_4$ which is indicated by the presence of less intense peak at 2θ ~26º, this peak is assigned to γ-MnOOH (JCPDS 41-1379).[17] This can be explained by taking into account the kinetics of the oxidation process; by extending the time up to 72 h air oxidation process will have enough time permitting partial oxidation of so obtained Mn$_3$O$_4$ to γ-MnOOH.

Table 3. Impact of time on the reaction product and its mean grain size, NaOH was used as a precipitant and the reaction temperature is fixed at 40 ºC.

Time/ h	**0% EtOH**		**95% EtOH**	
	Phase	*<d>/ nm*	*Phase*	*<d>/ nm*
1	Mn$_3$O$_4$ + A	21.0	Mn$_3$O$_4$ + C	10.5
6	Mn$_3$O$_4$	20.0	Mn$_3$O$_4$ + C	12.0
24	Mn$_3$O$_4$	18.0	Mn$_3$O$_4$ + C	12.0
72	Mn$_3$O$_4$ + B	20.0	Mn$_3$O$_4$	8.50

A: Mn(OH)$_2$; B: γ-MnOOH; C: β-MnOOH
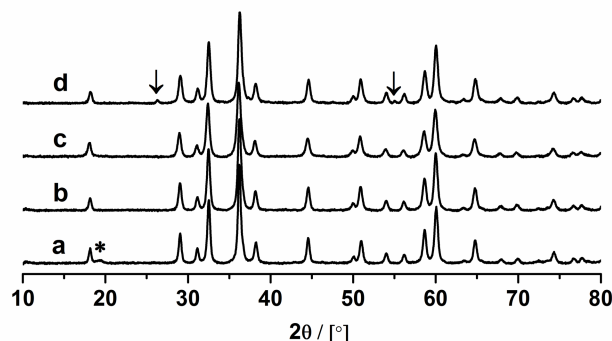
Figure 4. XRD patterns revealing the impact of time on the phase purity of hausmannite samples obtained at 40 °C, the reactions were performed in pure water. a) 1 h, b) 6 h, c) 24 h and d) 72 h. Star: un-oxidized $Mn(OH)_2$ and arrows: γ-MnOOH.

Using 95% EtOH as a reaction solvent (Figure 5) and at shorter time of 1 h, tiny impurities of β-MnOOH are admixed to Mn_3O_4 sample. These impurities get more by increasing the time up to 6 h which is manifested by more intense reflection at 2θ ~19.2° (JCPDS 18-0804). When the time reaches 24 h the amount of impurities start to decrease. Extending the time to 72 h releases β-MnOOH from the product. Taking into consideration that the partial pressure of atmospheric oxygen enclosed in the round flask (where the reaction is performed) is nearly fixed since a closed system is used. Accordingly, these results can be explained by taking into account the amount of dissolved oxygen in the reaction solution.

It is known that ethanol-rich solutions have much dissolved oxygen in comparison to pure water.[10] Therefore, the possibility to steer the oxidation of $Mn(OH)_2$ (layered type structure) directly to β-MnOOH becomes reasonable at shorter times (spinel is the major product). Consumption of the dissolved oxygen in the oxidation processes gets larger with increasing time, at a time of 72 h dissolved oxygen is merely, enough for oxidation of $Mn(OH)_2$ to Mn_3O_4.

Grain size for hausmannite samples remains to some extent unchanged (see Table 3); slight variation is recorded by increasing the reflux time. This reflects that the processes of seed formation and grain growth take place at earliest time and further extension of the time does not result in any grain growth.
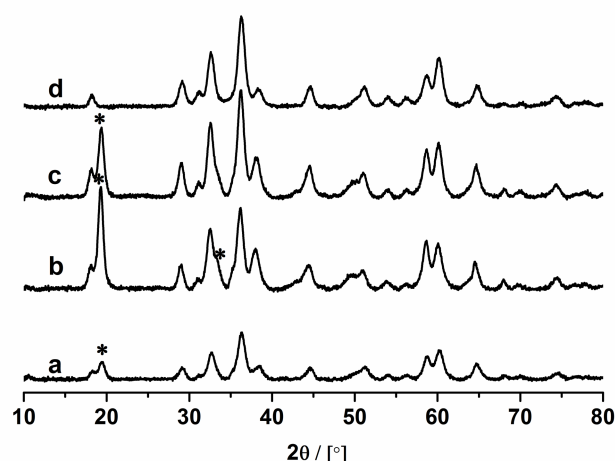
Figure 5. *XRD patterns revealing the impact of time on the hausmannite samples obtained at 40 °C using 95% EtOH solution. a) 1 h, b) 6 h, c) 24 h and d) 72 h, stars: β-MnOOH.*

Reaction temperature is a substantial key for most of chemical processes, control of the reaction temperature is a precondition preceding commencement of any chemical approach. Four different reaction temperatures were chosen, i.e., 25, 40, 60 and 80 °C. The other experimental conditions were kept unchanged, the reactions were done in 95% EtOH solution (Table 4). At lower temperatures of 25 and 40 °C, a strong reflection occurs in the powder pattern of hausmannite sample locating at 2θ ~19.2º (Figure 6) which correspond to the presence of β-MnOOH impurities. By rising the reaction temperature up to 60 and 80 °C evanescence of β-MnOOH is observed and x-ray single phase hausmannite samples are produced.

Table 4. Impact of reaction temperature on the purity of hausmannite samples and their mean grain sizes whilst 95% EtOH was used, the time was set at 24 h.

Temp. / ºC	*25*	*40*	*60*	*80*
Phase	Mn_3O_4+A	Mn_3O_4+A	Mn_3O_4	Mn_3O_4
<d> / nm	10.5	12.0	12.0	13.0

A: β-MnOOH
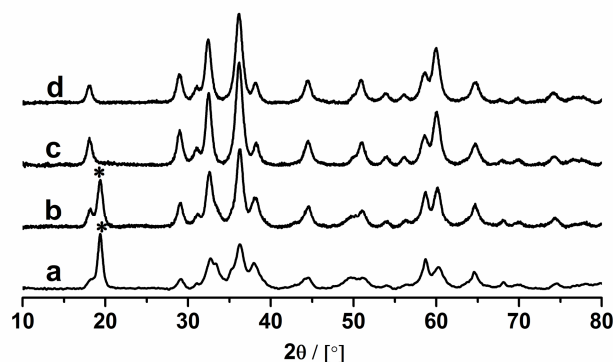
Figure 6. XRD patterns of the hausmannite samples obtained after 24 h under different reaction temperatures of a) RT, b) 40 °C, c) 60 °C and d) 80 °C, utilizing 95% EtOH. Stars: β-MnOOH.

The former findings can be explained based on an oxygen-temperature relationship. It is known that the amount of dissolved oxygen in the solutions significantly changes with temperature.[10] The higher the temperature, the lower is the amount of oxygen dissolved. Therefore, at lower reaction temperatures the amount of dissolved oxygen is higher, hence, there is an expectation for forthright oxidation of $Mn(OH)_2$ to β-MnOOH. When the reaction temperature is raised up to 60 °C (also for 80 °C), a decrease in the amount of dissolved oxygen takes place which is just enough for oxidation of $Mn(OH)_2$ to Mn_3O_4.

6.1.3. Variation of the ratio of $c(Mn^{2+})$ / $c(OH^-)$

Different concentrations of NaOH, i.e., 0.08, 0.16 and 0.24 mol L^{-1} were used for the purpose of investigation of the effect of NaOH concentration on phase purity of the product and on its grain size (concentration of Mn^{II} salt and the other reaction parameters were held at constant). The corresponding ratios of $c(Mn^{2+})/c(OH^-)$ are 1:2, 1:4 and 1:6, respectively. XRD patterns for the samples obtained by variation of %EtOH and utilizing 0.08 mol L^{-1} NaOH (Figure 7) show a transition from pure hausmannite sample whilst solutions of low contents of EtOH are used to impure ones using 95% EtOH, (β-MnOOH contaminants coexist).
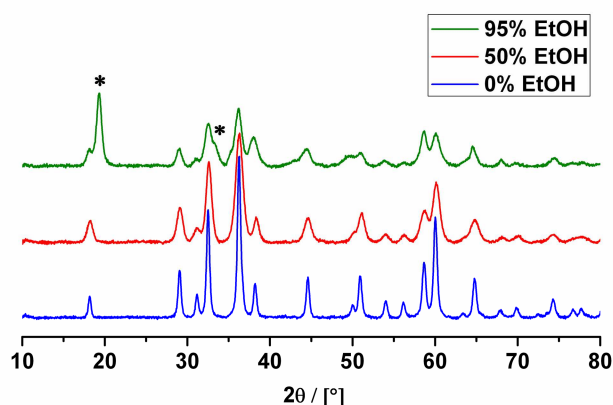
Figure 7. XRD patterns of the hausmannite samples prepared using different EtOH contents, employing 0.08 mol L^{-1} NaOH (40 °C, 6 h). Stars: β-MnOOH.

With 0.16 mol L^{-1} NaOH (c(Mn^{2+})/c(OH$^-$) = 1:4) and employing various ratios of EtOH/H$_2$O (Figure 8), formation of Mn$_3$O$_4$ predominates in pure water whereas formation of birnessite (layered type structure MnO$_2$) commence with rising the content of ethanol in water. Using 50% EtOH; a mixture of birnessite and hausmannite is produced, a single phase birnessite δ-MnO$_2$ (Na-type) is produced whilst 95% EtOH solution is used.

Two important parameters are acting together and inducing the formation of layered-type birnessite, firstly, the presence of excess sodium hydroxide that stimulate the formation of birnessite through the role of the excess sodium cations acting as a template assisting the formation of layer-type structure MnO$_2$. Secondly, the amount of dissolved oxygen (large in ethanol-rich solutions) induces the oxidation of Mn(OH)$_2$ straightforward to δ-MnO$_2$.
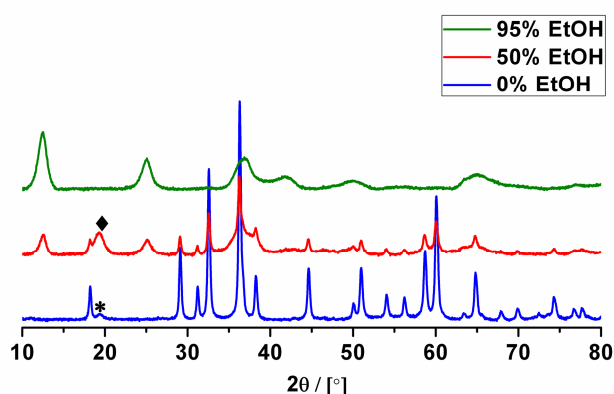
Figure 8. XRD patterns of the samples prepared using solutions with different EtOH content, 0.16 mol L^{-1} NaOH was used and the system was heated to 40 °C for 6 h. Blue: α-Mn$_3$O$_4$, red:α-Mn$_3$O$_4$ + δ-MnO$_2$ and green: δ-MnO$_2$ (Na-birnessite). Star: un-oxidized Mn(OH)$_2$ and diamond: β-MnOOH.

Our results show that variation of NaOH concentration not only changes the product phase but also its average grain size as illustrated in Table 5. This can be accounted for the change of the pH of the reaction medium, increasing the pH leads to an increase in the crystallite size of the hausmannite products.

Table 5. Impact of base concentration on the reaction product and its grain size, 50% EtOH was used, the time was set at 6 h.

C_{NaOH}/ mol L^{-1}	0.08	0.16	0.24
pH_f	6.8	12.2	13.5
Phase	Mn_3O_4	Mn_3O_4+A	Mn_3O_4+A
<d> / nm	13.0	21.0	23.0

Where pH_f: pH measured at the end of reaction. A: δ-MnO_2.

6.2. Ammonia as a precipitating agent

In an attempt to obtain single phase hausmannite samples, another set of experiments was conducted using ammonia solution as a precipitating agent. The aim of this study is to investigate the influence of using ammonia as a precipitant (compared to the use of NaOH) on the phase purity and mean particle size of the obtained hausmannite samples. Precipitation of $Mn(OH)_2$ occur firstly, followed by air oxidation giving rise to formation of pure spinel Mn_3O_4. The mean particle size for the hausmannite sample prepared in pure water at 40 ºC (calculated from band broadening using Scherrer's equation) was found to be about 25 nm which is larger than that obtained at the same condition using NaOH (21 nm). The explanation for this could be related to the difference in pH values for both reaction media (same molar concentration of both NaOH and NH_3 solution). Indeed, measurements of pH values after termination of both reactions showed that the final pH for the solution of the first sample was ~9.0. A value of ~7.5 was monitored for the solution of the second sample prepared using NaOH.

Formation of hausmannite using ammonia as a precipitant can be represented by the following equations:

$$Mn(OAc)_2 + 2\,NH_3 + 2H_2O \rightarrow Mn(OH)_2 + 2\,NH_4OAc \qquad (3)$$

$$3Mn(OH)_2 + 1/2\,O_2 \rightarrow Mn_3O_4 + 3\,H_2O \qquad (4)$$
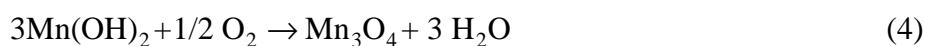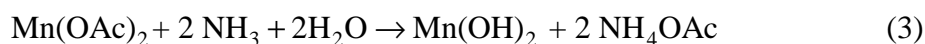
   Once again the influence of variation of ethanol content in the reaction solution was studied. Unlike the case of using NaOH, it is found that very clean hausmannite samples are produced while ammonia solution is used as a precipitant (40 ℃, 1 h), irrespective of the ethanol content in the solution (Figure 9). Shrinkage of the particle size is a characteristic feature; it drops from 25 nm in pure water to 9.3 nm in 85% solution. No precipitation is observed (in contrast to the use of NaOH where a mixture of hausmannite and β-MnOOH is precipitated using 95% EtOH) when the ethanol content in the solution reaches 95% (at 40 ℃, 1 h). Table 6 shows the variation of the mean grain size as well as the lattice parameters of the hausmannite samples with ethanol content.

Table 6. Influence of variation of %EtOH on the average grain size and lattice parameters of hausmannite samples when ammonia is used as a precipitant, the reaction temperature set at 40 ℃ for 1 h.

EtOH/H$_2$O	*0%*	*50%*	*85%*	*95% [a]*
Phase	Mn$_3$O$_4$	Mn$_3$O$_4$	Mn$_3$O$_4$	-
<d> / nm	25	15.5	9.3	-
a / Å	5.7639(1)	5.7642(2)	5.7709(6)	
c / Å	9.4602(3)	9.4432(5)	9.409(1)	

  a: no precipitation
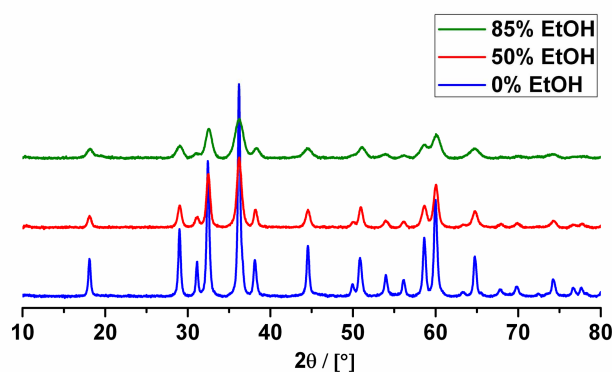
Figure 9. XRD diffractograms of hausmannite samples obtained using different EtOH contents and 0.08 mol L^{-1} ammonia, the system was heated to 40 °C for 1 h. Blue: 25 nm, red:15.5 nm and green: 9.3 nm.

IR analyses (Figure 10) were done, the spectra indicate that all absorption bands fall in the range of 400-600 cm^{-1} are assigned to the coupling between the Mn-O stretching modes of the octahedral and tetrahedral sites and to the bond stretching modes of the octahedral sites. Peaks at 1630 and 4300 cm^{-1} refer to the presence of water incorporated into these samples either structurally or just adsorbed on the surface.[15] Obviously, there is no shift in the peak positions as a result of changing the particle size, merely; the peaks get more intense with increasing of the grain size. The big difference in the peak positions can be seen by comparison with bulk Mn_3O_4 (Table 7).
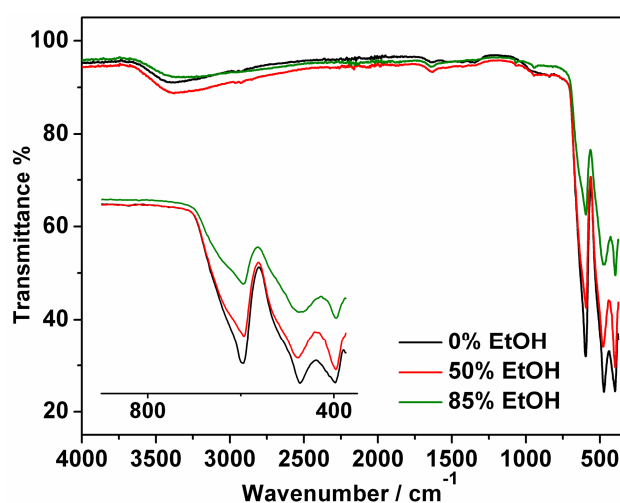
Figure 10. *IR spectra of hausmannite samples obtained using different %EtOH.*

Table 7. Comparison of the locations of the absorption bands of Mn_3O_4 samples *obtained using different %EtOH*.

%EtOH	<d> / nm	Mn–O stretching modes /cm^{-1}		
0	25	398	473	597
50	15.5	396	479	592
85	9.3	396	475	592
-	Bulk[14]	412	502	612

The diffractograms (Figure 11) for the products obtained at reaction temperatures of 25, 40, 60 and 80 °C (using 95% ethanolic solution and keeping the other experimental conditions unchanged) indicate that x-ray single phase hausmannite samples are produced even at room temperature. Average crystallite sizes calculated from band broadening using Scherrer's formula reveal that variation of the reaction temperature does not noticeably change the size. The grain size scatters between 10.8, 10.0, 10.3 and 9.6 nm at 25, 40, 60 and 80 °C,

respectively. This may be explained as follow; after nucleation of hausmannite from $Mn(OH)_2$ at room temperature no significant growth of the particles with temperature occurs. Ostwald ripening is not observed here, that is the case which associated with too low molar solubility of hausmannite in the reaction solvent. Table 8 shows the effect of temperature on the grain size and lattice parameters of hausmannite. We can see that, there is no general trend for variation of the lattice parameters with temperature.
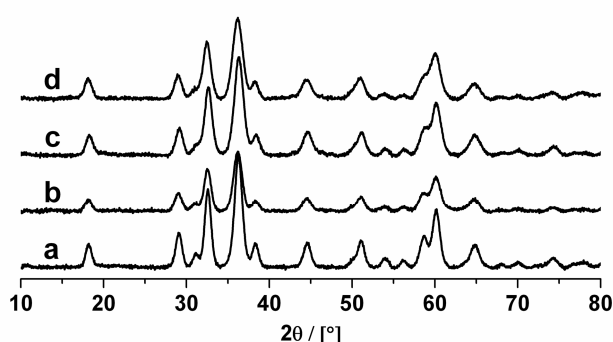
Figure 11. *Impact of reaction temperature on phase purity of hausmannite obtained using 95% EtOH (0.08 mol L^{-1} NH_3 solution, 24 h). a) 25 °C, b) 40 °C, c) 60 ºC and d) 80 °C.*

Table 8. Influence of variation of reaction temperature on the average grain size and lattice parameters of hausmannite samples prepared using 95% EtOH, 24 h.

Temp. / °C	*25*	*40*	*60*	*80*
<d> / nm	10.8	10.0	10.3	9.6
a / Å	5.7701(5)	5.7647(9)	5.7753(7)	5.7641(7)
c / Å	9.418(1)	9.395(2)	9.425(1)	9.419(1)

Pristine hausmannite samples were prepared at room temperature irrespective of the ethanol content in water (Figure 12). Larger size hausmannite sample is obtained in pure water, shrinkage of the average crystallite sizes takes place with increasing of the content of ethanol for the same reason mentioned before in case of using NaOH as a precipitant.[13] Elongation of the unit cell in a direction and contraction in c direction occur with increasing of %EtOH (Table 9).
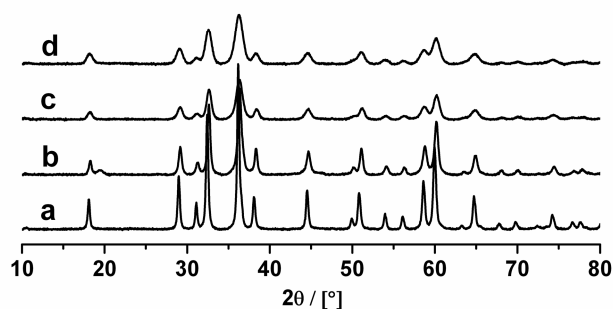
Figure 12. *XRD diffractogram of hausmannite samples prepared using different %EtOH and NH₃ as a precipitant at room temperature for 24 h. a) 0%, b) 50%, c) 85% and d) 95%.*

Table 9. Influence of variation of %EtOH on the average grain size and lattice parameters of hausmannite samples prepared at room temperature, 24 h.

EtOH/H$_2$O	*0%*	*50%*	*85%*	*95%*
<d> / nm	26.5	17	13	11
a / Å	5.7642(1)	5.7656(3)	5.7677(4)	5.7701(5)
c / Å	9.4647(3)	9.4465(6)	9.418(1)	9.417(1)

To the best of our knowledge this is consider as a new, simple and green chemical method for synthesis of hausmannite at room temperature with variable grain size. Variation of the average crystallite size of hausmannite samples (obtained at room temp.) with %EtOH is illustrated in Figure 13.
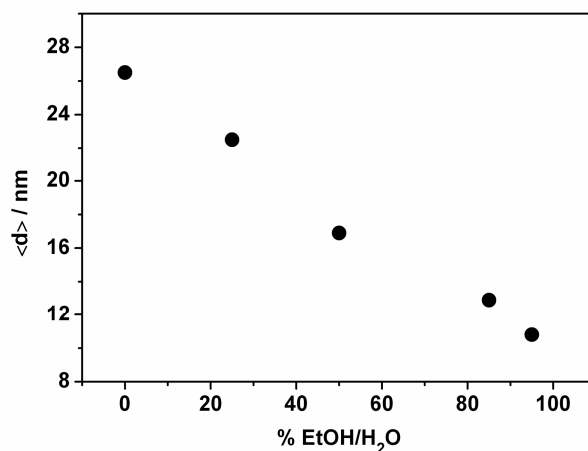
Figure 13. *Variation of particle size with %EtOH for the pristine hausmannite samples prepared at room temperature, the other experimental conditions are kept constant.*

Seemingly, increasing of the molar concentration of NH_3 solution does not affect the type of the product obtained. XRD analysis for the samples prepared (Figure 14) using ~0.16 mol L^{-1} ammonia solution ($(c(Mn^{2+})/c(OH^-)$ is 1:4) shows that whatever the content of ethanol in the reaction solution, the products are characterized to be hausmannite. Noticeably, the crystallite size doesn't suffer any significant change as a function of the pH change (see Table 10). A small difference in the final pH value is seen and this is associated with a slight change in the particle size even with high molar concentration of ammonia ~0.24 mol L^{-1}.

Table 10. Impact of ammonia concentration on the grain size of hausmannite whilst 50% EtOH is used (6 h, 40 ºC).

C_{NH3}/ mol L^{-1}	0.08	0.16	0.24
pH_f	7.6	9.0	9.3
Phase	Mn_3O_4	Mn_3O_4	Mn_3O_4
<d> / nm	16.9	16.3	18.0
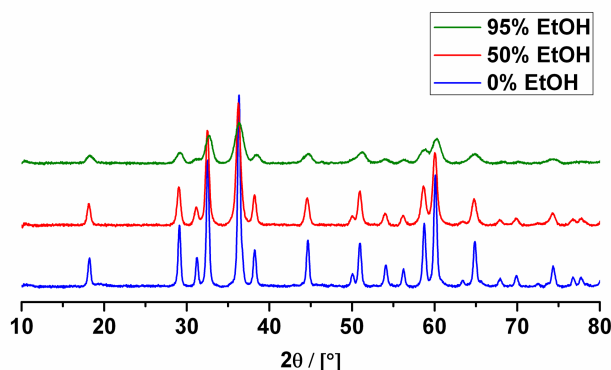
Figure 14. *XRD patterns of the hausmannite samples prepared using different %EtOH (0.16 mol L^{-1} NH_3 solutions, 40 °C and 1 h).*

6.3. Adsorption-Desorption Isotherms

The surface areas for nc-Mn_3O_4 samples with average particle sizes of about 20, 14 and 10 nm were measured in order to see how microstructural parameters change with mean particle size. Nitrogen adsorption-desorption using the BET method was measured, see Figure 15. The isotherms can be classified as type IV isotherms.[18] Hysteresis is a characteristic feature for this kind of isotherms. This type is correlated with the presence of mesopores. The capillary condensation occurring in the mesopores restricts adsorption above a high P/P°. The first part of the isotherms is related to monolayer-multilayer adsorption. The hysteresis observed in

isotherms I and II for Mn_3O_4 samples with large particle size can be classified as H3 type which does not show any limiting adsorption at high p/p°. By IUPAC definition the hysteresis observed in isotherm III (Mn_3O_4 sample with smallest particle size) is classified as H2 type which suggests pores with narrow necks and wide bodies (normally referred to as 'ink bottle' pores).[19]

The BET surface area can be roughly estimated by assuming the nanocrystallites as spheres with diameter equivalent to the average particle size. The estimated values for the different nc-Mn_3O_4 samples and their experimental counterparts are shown in Table 11. The experimental values are in the order of the theoretical estimations, except for the largest particles. Pore size distribution curves are introduced in Figure 16 which suggests that these pores are distributed in a monomodal fashion, which is observable for the three hausmannite samples, the mean pore sizes are listed in the Table 11.
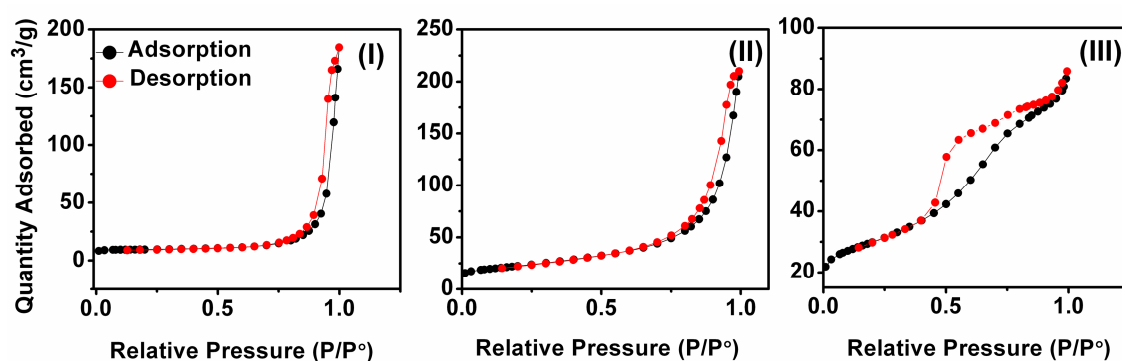
Figure 15. *Adsorption-desorption isotherms of hausmannite samples (obtained using 0.08 mol L^{-1}NaOH) having different mean grain sizes; I) <d> ~20 nm, II) <d> ~14 nm and III) <d> ~10 nm.*
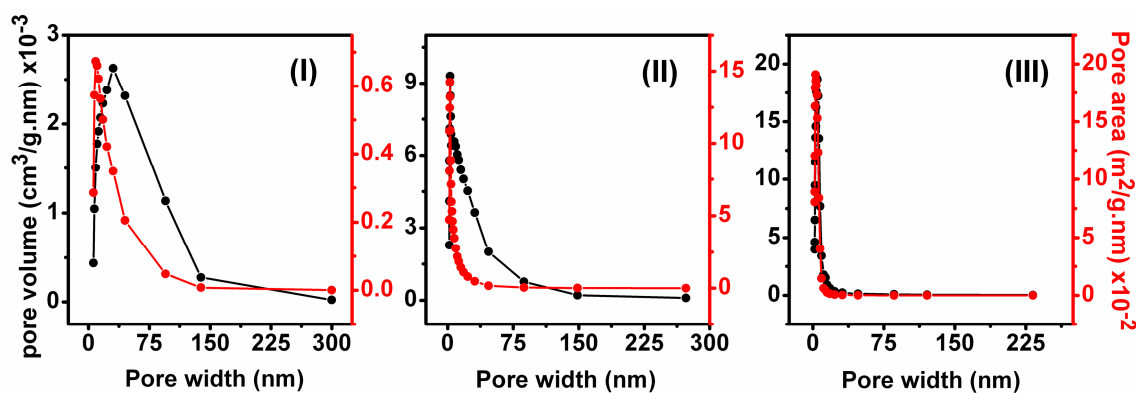
Figure 16. *Pore width-pore volume and pore width-pore area relationships of hausmannite samples; I) <d> ~20 nm, II) <d> ~14 nm and III) <d> ~10 nm.*

If the surface area and the average pore width are plotted as a function of the average particle size, the relation given in Figure 17 is received. Approximately, linear dependence of the surface area on the inverse of the average particle size ($1/<d>$) can be seen.

Table 11. Expected and found surface areas of nc-Mn_3O_4 samples, average pore width as well as total pore volume as a function of the mean particle size.

<d> / nm	*Surface area as spheres m^2/g*	*S_{BET} m^2/g*	*Average pore width /nm*	*Total pore volume cm^3/g*
20	65	32	23	0.19
14	90	79	13	0.26
10	128.5	103	4.7	0.12
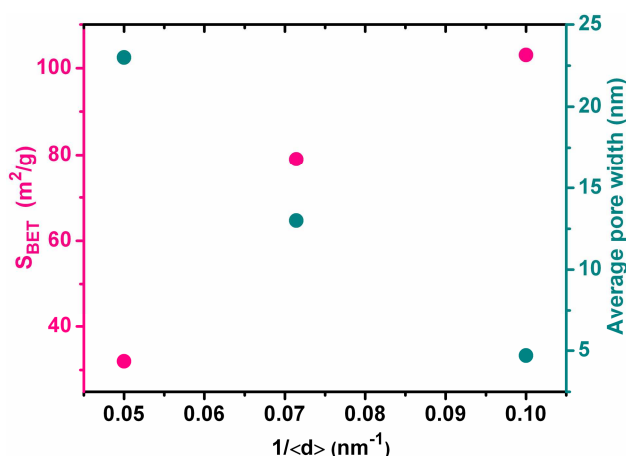
Figure 17. *BET surface area and average pore width as a function of the grain size of nc-Mn_3O_4 samples.*

6.4. Average crystallite size (XRD Vs. TEM)

In order to compare the average particle sizes determined from XRD (calculated from band broadening using Scherrer's formula) and to study the morphology of the obtained nanocrystals, three hausmannite samples (prepared by using ammonia as a precipitant and different %EtOH, 24 h) were examined by transmission electron microscopy (TEM).

As visible from TEM images shown in Figure 18a-c, the Mn_3O_4 nanoparticles are a mixture of cubes and spheres that are all distorted in one direction, thus representing the tetragonal distortion of the unit cell. Shape control cannot be achieved via this synthetic route. In order to obtain particle size distributions about 300 particles were measured for each sample. This was done by measuring the longest and shortest possible diagonal through each particle.

Figure 18d shows particle size distribution curves for all samples, Gaussian function was used to fit particle size distribution curves. Characteristic features that can be extracted from TEM distribution curves are, symmetry of the distribution curves about the average values of the particle size and the particle sizes are distributed in a monomodal fashion. Table 12 shows the comparison between the average particle size deduced from XRPD and that extracted from TEM distribution curves, slight difference is observed between them.

Table 12. Comparison of the mean particle size from XRD and TEM.

Method	*Mean particl size <d> / nm*		
XRD	24	15	10
TEM	22.5	14	8
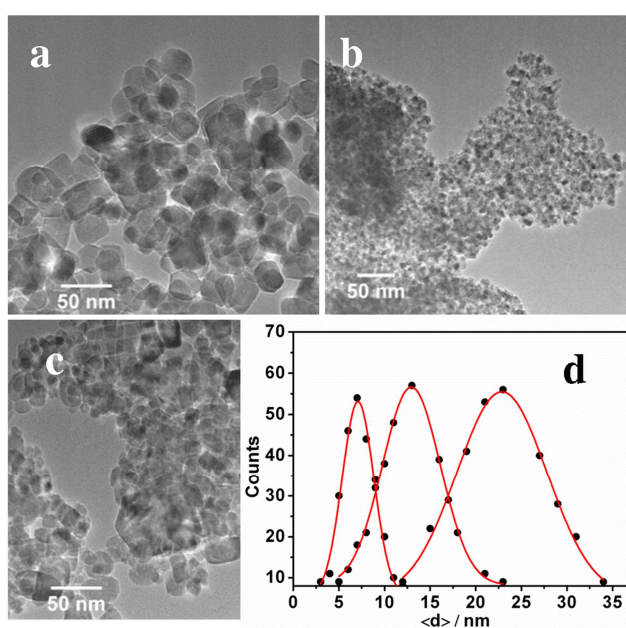
Figure 18. TEM images of Mn₃O₄ samples: a) <d> ~24 nm, b) <d> ~15 and c) <d> ~10 nm. d) Their corresponding size distribution curves from right to left, respectively.

6.5. Structural analysis

Size-dependent structural analyses were made using Rietveld analyses for three selected Mn_3O_4 samples with different grain sizes, their profile fits depicted in Figure 19. The observed and calculated patterns are fitted well as indicated by R values (Table 13). Obviously, all reflections match well; there is no other reflection that can be assigned for the presence of any other phase of manganese oxides.
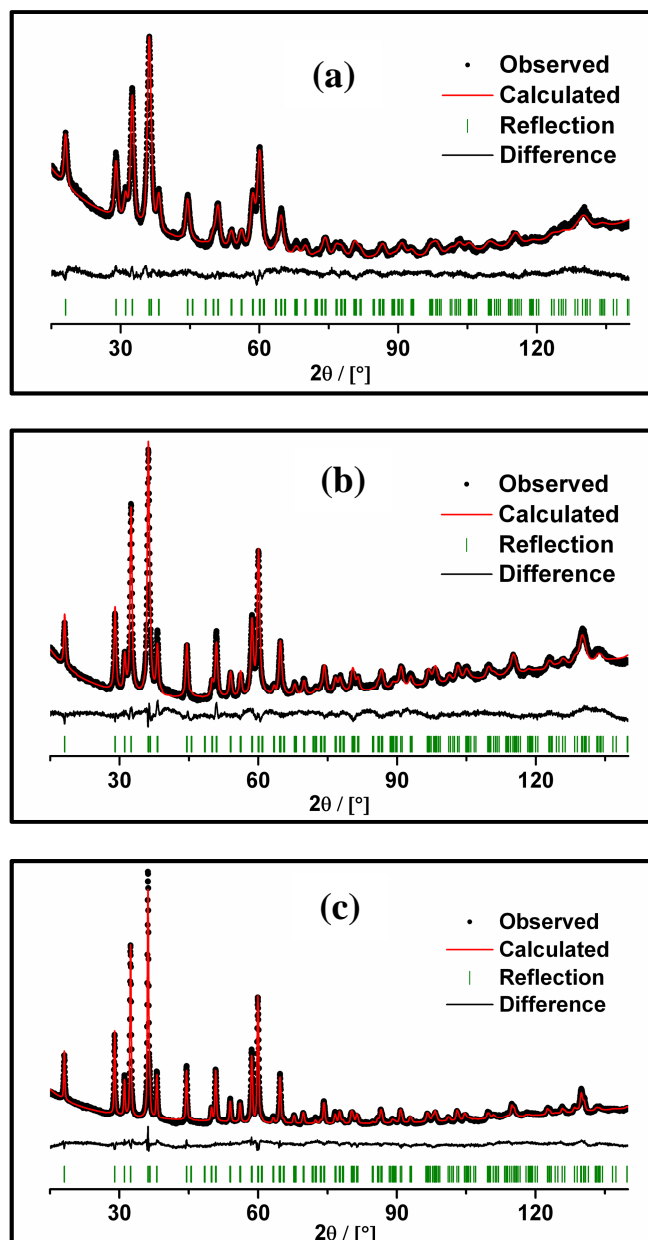
Figure 19. *Refinement analyses of three Mn₃O₄ samples with different particle size using Rietveld method; a) <d> = 10 nm, b) <d> = 16 nm and c) <d> = 25 nm.*

The results of refinement (Table 13) indicate the great influence of the particle size on the tetragonal cell parameters, a contraction of the unit cell occurs in "a" direction and elongation in the direction of "c" axis take place by increasing the mean particle size <d>.

Table 13. Measurement parameters, structure and refinement data for three different size spinel samples.

Sample	*<d> = 10 nm*	*<d> = 16 nm*	*<d> = 25 nm*
Formula sum	$Mn_{11.63}O_{14.77}$	$Mn_{11.95}O_{16.00}$	$Mn_{12.08}O_{16.00}$
Formula mass / g/mol	875.20	912.23	919.64
Space group (No.)	$I\,4_1/a\,m\,d$ (141)	$I\,4_1/a\,m\,d$ (141)	$I\,4_1/a\,m\,d$ (141)
a = b / Å	5.7684(5)	5.7658(2)	5.7639(1)
c / Å	9.420(1)	9.4507(5)	9.4602(3)
c/√2 a	1.1547	1.1590	1.1606
ρ / g/cm³	4.64	4.82	4.86
V/ 10⁶ pm³	313.44	314.17	314.29
R (expected) / %	1.154	1.203	1.110
R (profile) / %	0.819	0.983	0.972
R (weighted profile) / %	1.018	1.255	1.290
R (Bragg) / %	0.504	0.770	1.127
GOF	0.778	1.090	1.351

Radiation is Cu-$K\alpha$ and the type of profile fit is Pseudo-Voigt

The degree of tetragonal distortion of the unit cell, taking the ratio $c/\sqrt{2}\,a$ as a measure, is plotted versus the mean particle size for several hausmannite samples (Figure 20). It is obvious from the plot that the release of distortion increases with decreasing of particle size. The degree of distortion is plotted versus the 1/<d> (Figure 21). A straight line can be fitted which indicates that the distortion decreases linearly with the reciprocal particle size 1/<d>, which in turn is proportional to the surface area of the particles. 1/<d> can be related to the surface area as follow:

$$S_{BET} = \frac{A}{m} \qquad (m^2 / g)$$

Where; S_{BET} is the specific surface area, A and m are the surface area and mass of the particles, respectively.

For spherical particles the area $A = 4\pi r^2$ and $m = \rho.V = \rho(4/3\pi r^3)$, where r is the diameter of the sphere which is taken as <d> in this case. So the mean diameter <d> can be related to the surface area by the following relation:

$$S_{BET} = \frac{4\pi r^2}{\rho(4/3\pi r^3)} \alpha \frac{1}{\prec d \succ}$$
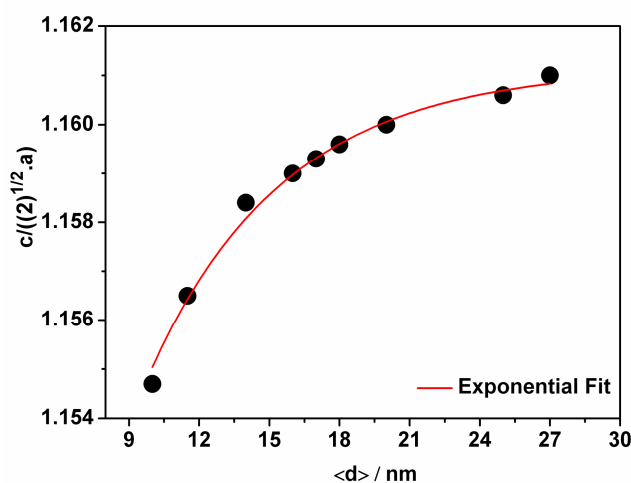
Figure 20. *Tetragonal distortion of the unit cell versus the mean particle size of hausmannite samples.*
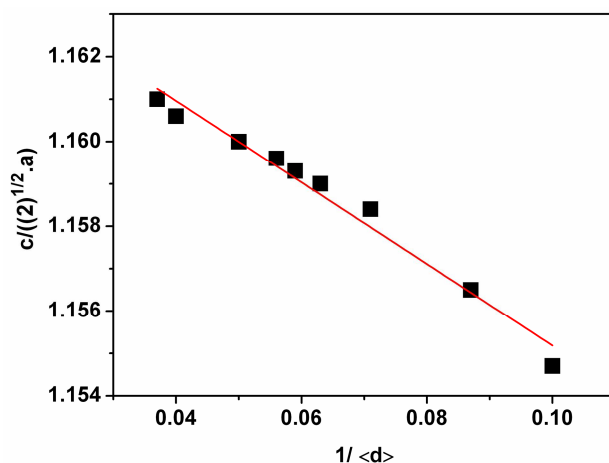
Figure 21. *Tetragonal distortion plotted against invers particle size of hausmannite samples.*

Figure 22 shows elongation of the tetragonal unit cell of hausmannite in "c" direction with increasing of the mean particle size, whereas the cell parameter "a" fluctuates, generally with a contraction with increasing of the particle size (Table 14). Nevertheless, the unit cell volume increases with increasing of the mean particle size (Figure 23). Mn-O tetrahedral bond

distances are increased compared to those of bulk Mn_3O_4 (Table 15). Whereas, the Mn-O distances of the MnO_6 octahedrons are shorten.[20]
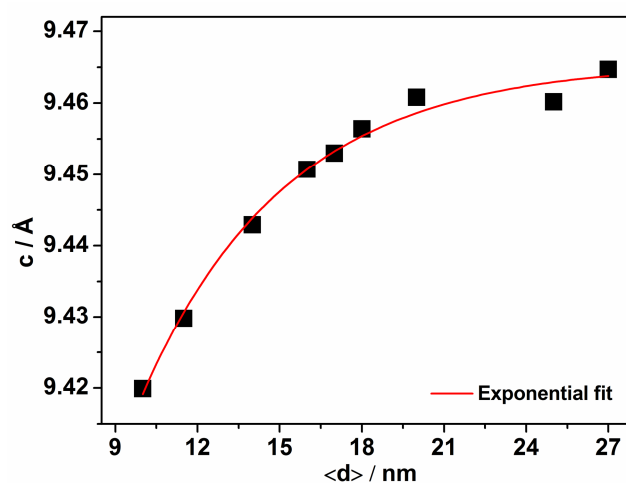
Figure 22. *Variation of the cell parameter c with mean particle size.*
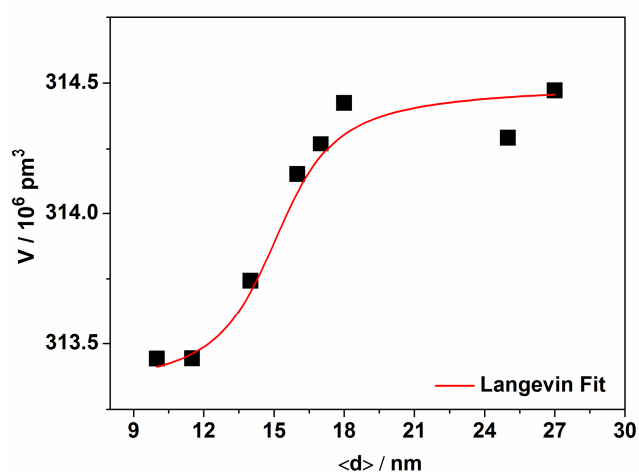
Figure 23. *Variation of the volume of unit cell with mean particle size.*

Table 14. Variation of cell parameters with the mean particle size for several hausmannite samples.

\<d\>	*a / Å*	*c / Å*	$c/\sqrt{2}\,a$	*V / 10⁶ pm³*
10	5.7685	9.4199	1.1547	313.443
11.5	5.7654	9.4298	1.1565	313.444
14	5.7641	9.4429	1.1584	313.743
16	5.7658	9.4507	1.159	314.15
17	5.7659	9.453	1.1593	314.267
18	5.7663	9.4564	1.1596	314.424
20	5.767	9.4608	1.16	314.64
25	5.7639	9.4602	1.1606	314.292
27	5.7642	9.4647	1.161	314.472

Table 15. Coordination of atoms and bond distances.

Sample	*Atom*	*Coordination*	*Distance*	*Number*
<d> = 10 nm	*Mn1*	*O1*	200.7(3)	4x
	Mn2	*O1*	195.1(2)	4x
		O1	228.9(3)	2x
<d> = 16 nm	*Mn1*	*O1*	198.6(3)	4x
	Mn2	*O1*	195.5(2)	4x
		O1	232.2(2)	2x
<d> = 25 nm	*Mn1*	*O1*	200.8(1)	4x
	Mn2	*O1*	195.6(2)	4x
		O1	228.9(2)	2x
Literature:[20] Mn1-O1; 186.2, Mn2-O1; 203.7 and Mn2-O1; 235.9				

Mn_3O_4 sample with the smallest particle size showed a defect in its structure, SOF value for Mn^{2+} (Table 16) indicates a defect in the cationic sites. The refinements were done assuming that the octahedral sites are fully occupied by Mn^{3+}. Also the SOF value for oxygen atoms reflects an anionic defect. Approximately, 9% deficiency exists in cationic sites containing Mn^{2+} that can arise from partial oxidation of Mn^{2+} to Mn^{3+} leading to formation of cationic vacancies. These can be compensated by either the deficiency in the anionic sites (~9%) through formation of anionic vacancies or via presence of interstitials (e.g., OH^-).

The calculated density for such sample from Refinement data reveals a defected spinel structure, a value of 4.64 g/cm^3 was found compared to 4.86 g/cm^3 for the ideal spinel structure (bulk material).[20] The density for this sample was measured and a value of 4.29(0.03) g/cm^3 was found (Table 17), which is too low compared to the calculated one and strongly emphasizes such structural deficiency. The difference between the measured and calculated values may be due to presence of water adsorbed over its surface (proven by TGA).

With increasing the particle size such type of anionic deficiency vanish and just quite small deficiency in Mn^{2+} sites exists, the calculated density for the larger size hausmannite sample (~16 nm) is found 4.82 g/cm^3 whereas the measured one is 4.59(0.01) g/cm^3. Ideal spinel structure was found for the largest hausmannite sample with mean particle size of 25 nm, no deficiency could be recognized from SOF values which is indicated by the values of the calculated and measured densities, 4.86 and 4.68(0.04) g/cm^3, respectively.

Table 16. Wyckoff positions, occupancy, atomic fractional coordinates and isotropic displacement parameters B for three different size hausmannite samples (refined according to 31094-ICSD).[20]

Atom	*Sample 1 (<d> = 10 nm)*					
	Wyck.	*s.o.f*	*x*	*y*	*z*	*B / 10^4 pm^2*
Mn1	4b	0.91(1)	0.0	0.25	0.375	0.54(6)
Mn2	8c	1.0	0.0	0.0	0.0	0.27(5)
O1	16h	0.92(4)	0.0	0.9774(6)	0.2426(3)	1.0(2)
	Sample 2 (<d> = 16 nm)					
Mn1	4b	0.988(9)	0.0	0.25	0.375	0.4
Mn2	8c	1.0	0.0	0.0	0.0	0.18(3)
O1	16h	1.02(4)	0.0	0.9790(5)	0.2454(3)	1.0(1)
	Sample 3 (<d> = 25 nm)					
Mn1	4b	1.02(1)	0.0	0.25	0.375	1.81(5)
Mn2	8c	1.0	0.0	0.0	0.0	1.00(3)
O1	16h	1.00(1)	0.0	0.9790(4)	0.2416(2)	1.0

Table 17. Measured and calculated density values of various hausmannite samples.

<d> / nm	**10**	**16**	**25**
Measured Density g/cm^3	4.29(0.03)	4.59(0.01)	4.68(0.04)
Calculated Density g/cm^3	4.65	4.82	4.86

TG analyses were performed for the hausmannite samples with different particle sizes under air flow (heating rate 5 k/min). For the temperature range 25 - 800 ºC, the thermogramms shown in Figure 24 reveal two mass losses occurring initially followed by a mass gain.
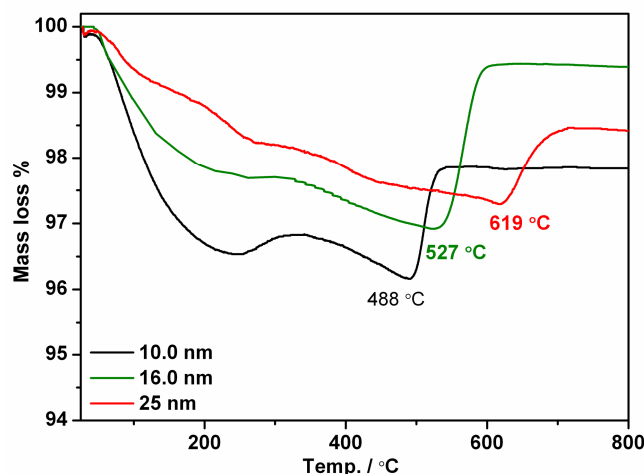
Figure 24. TG thermogramms of different size hausmannite samples obtained under air flow with heating rate of 5 K/ min.

The first mass loss in all thermogramms is assigned to removal of adsorbed water molecules over the surfaces of hausmannite samples (~250-275 ºC). It is apparent that the quantity of adsorbed water is high for the smallest size hausmannite sample and decreases with increasing of the size (result of decreasing of surface area). The second mass loss can be ascribed to loss of the excess mass (may be structural water or OH⁻). Quit small losses of 0.6-1% are detected in the TG curves (250-620 ºC) of the hausmannite samples. This matches with a non-appreciable deficiency in the structure of the hausmannite samples with larger sizes. This result indicates also that the cationic deficiency for the smallest size sample is compensated mainly by the presence of anionic vacancies.

From IR analysis, it is not straightforward to distinguish between the existence of water and OH⁻. Mass gain observed in the third step certainly corresponds to oxidation of hausmannite (α-Mn_3O_4) to bixbyite (α-Mn_2O_3). Theoretically this transformation should be accompanied by mass gain of 3.49% (for ideal Mn_3O_4 structure). A characteristic feature from the TG curves of the different size hausmannite samples, that is the transformation temperature of hausmannite to bixbyite significantly affected by its particle size. Hausmannite sample with lowest particle size can be transformed at low temperature to bixbyite compared to the largest

size hausmannite sample (see Figure 24). These results reflect an increase in thermal stability of hausmannite samples with increasing of the particle size.

To prove the former expectations of TGA, TG measurements were performed for a hausmannite sample (~10 nm) under static air conditions (5 K/min). The analyses were made in different temperature ranges 25-350 °C, 25-480 °C, 25-600 °C and 25-1000 °C. The solid products remained after the termination of the TGA were characterized by XRD analyses (Figure 25). The products remained after stopping the measurements at 350 and 480 °C were identified as Mn_3O_4, this result confirms the stability of such hausmannite sample till 480 °C which is matched with the result of TGA (Figure 24). At 600 °C the residue was characterized as bixbyite, α-Mn_2O_3.
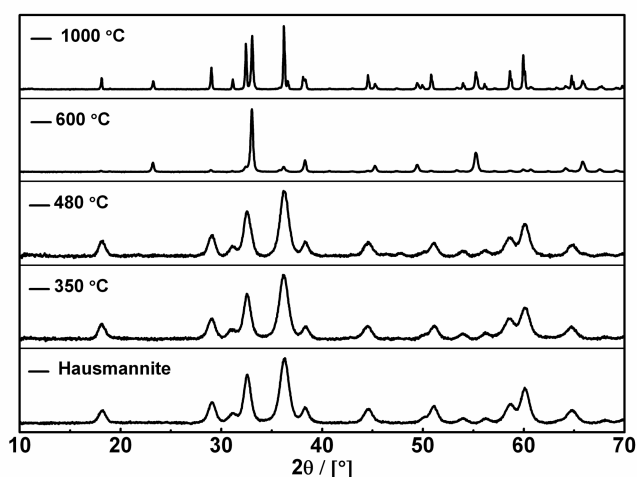
Figure 25. XRD patterns of the residual products of a hausmannite sample obtained by termination of TGA at different temperatures under static air (heating rate 5 K/min). Hausmannite sample has <d> = 10.4 nm, at 350 ºC; hausmannite (<d> = 9.9 nm), at 480 ºC; hausmannite (<d> = 10.2 nm), at 600 ºC; α-Mn₂O₃ (<d> = 30 nm) and at 1000 ºC; Mn₃O₄ + Mn₂O₃.

6.6. Summary and conclusions

- Control of the particle size of hausmannite can be achieved by variation of the ethanol/water ratio, increasing of the ethanol content leads to a drop in the particle size.

- Irrespective of the reaction temperature and Mn^{2+}/OH^- ratio, ammonia was found to be superior to NaOH for preparation of x-ray single phase hausmannite whereas NaOH is most useful for synthesis of δ-MnO_2, which is a sodium template directing process.

- Variation of reaction temperature and time has no significant influence on the growth of spinel nanocrystals,

- Room temperature synthesis of hausmannite sample was achieved for the first time in this work; size-selective synthesis was done by controlling the ethanol content in water.

- Surface area, pore size, total pore volume and thermal stability of hausmannite samples are size-dependent properties.

- Degree of tetragonal distortion for hausmannite unit cell increases with increasing of particle size and exhibits linear relation with the surface area of the samples.

- The smallest size sample showed a deficiency in the cationic sites (for Mn^{2+}) which can be compensated by the deficiency in the anionic sites. This result was proven by the quite low density value (measured). TGA indicate a slight excess mass over its surface (0.6%).

- No deficiency can be recognized for the larger size samples as indicated by Rietveld refinement, density measurement and TGA.

References

1. Chardon, B.; Vigneron, F. Mn_3O_4 commensurate and incommensurate magnetic structures. *J. Magn. Magn. Mater.* **1986,** *58* (1−2), 128-134.

2. Driessens, F. C. M. Place and valence of the cations in Mn_3O_4 and some related manganates. *Inorg. Chim. Acta* **1967,** *1* (0), 193-201.

3. Burns, R. G. *Mineralogical Applications of Crystal Field Theory;* Cambridge University Press: 1970.

4. Feitknecht, W.; Marti, W. Über die oxydation von mangan(II)-hydroxyd mit molekularem sauerstoff. *Hev. Chim. Acta* **1945,** *28* (1), 129-148.

5. Feitknecht, W.; Brunner, P.; Oswaldw, H. R. Über den einfluß der feuchtigkeit auf die oxydation von manganhydroxid durch molekularen sauerstoff. *Z. Anorg. Allg. Chem.* **1962,** *316* (3-4), 154-160.

6. Hem, J. D. Rates of manganese oxidation in aqueous systems. *Geochim. Cosmochim. Acta* **1981,** *45* (8), 1369-1374.

7. Murray, J. W.; Dillard, J. G.; Giovanoli, R.; Moers, H.; Stumm, W. Oxidation of Mn(II): Initial mineralogy, oxidation state and ageing. *Geochim. Cosmochim. Acta* **1985,** *49* (2), 463-470.

8. Kaczmarek, J.; Wolska, E. The defect structure and vacancy distribution in the low-temperature hausmanite. *Solid State Ionics* **1993,** *63−65* (0), 633-638.

9. Wang, N.; Guo, L.; He, L.; Cao, X.; Chen, C.; Wang, R.; Yang, S. Facile synthesis of monodisperse Mn_3O_4 tetragonal nanoparticles and their large-scale assembly into highly regular walls by a simple solution route. *Small* **2007,** *3* (4), 606-610.

10. Shchukarev, S. A.; Tolmacheva, T. A. Solubility of oxygen in ethanol - water mixtures. *J. Struct. Chem.* **1968,** *9* (1), 16-21.

11. Christensen, A. N.; Ollivier, G. Hydrothermal preparation and low temperature magnetic properties of $Mn(OH)_2$. *Solid State Commun.* **1972,** *10* (7), 609-614.

12. Portehault, D.; Cassaignon, S.; Baudrin, E.; Jolivet, J. P. Evolution of nanostructured manganese (oxyhydr)oxides in water through MnO_4^- reduction. *Cryst. Growth & Des.* **2010,** *10* (5), 2168-2173.

13. Rollett, A.; Humphreys, F. J.; Rohrer, G. S. *Recrystallization and Related Annealing Phenomena;* Elsevier Science: 2004.

14. Ishii, M.; Nakahira, M.; Yamanaka, T. Infrared absorption spectra and cation distributions in $(Mn, Fe)_3O_4$. *Solid State Commun.* **1972,** *11* (1), 209-212.

15. Nakamoto, K. Infrared and Raman Spectra of Inorganic and Coordination Compounds: Applications in coordination, organometallic, and bioinorganic chemistry; Wiley: 1997.

16. Feng, X.; Tan, W.; Liu, F.; Huang, Q.; Liu, X. Pathways of birnessite formation in alkali medium. *Sci. China Ser. D-Earth Sci.* **2005,** *48* (9), 1438-1451.

17. Kohler, T.; Armbruster, T.; Libowitzky, E. Hydrogen bonding and Jahn-Teller distortion in groutite, alpha-MnOOH, and manganite, gamma-MnOOH, and their relations to the manganese dioxides ramsdellite and pyrolusite. *J. Solid State Chem.* **1997,** *133* (2), 486-500.

18. Everett. D. H. Manual of symbols and terminology for physicochemical quantities and units. Appendix II. Definitions, terminology, and symbols in colloid and surface chemistry. *Pure Appl. Chem.* **1972,** *31* (4), 577-638.

19. Sing, K. S. W.; Everett, D. H.; Haul, R. A. W.; Moscou, L.; Pierotti, R. A.; Rouquerol, J.; Siemieniewska, T. Reporting physisorption data for gas/solid systems with special reference to the determination of surface area and porosity. *Pure Appl. Chem.* **1985,** *57* (4), 603-619.

20. Aminoff, G. Ueber die kristallstruktur von hausmannit (Mn Mn$_2$ O$_4$). *Z. Kristallogr.* **1926,** *64*, 475-490.

7. Summary

Manganese possesses numerous oxidation states (II, III, IV and VII are the most common ones) consequently, various manganese oxide/hydroxide phases are known. Although, the research field about manganese oxide/hydroxide nanocrystals is so spacious, nevertheless, many interesting research points are still obscure. Size-dependent physical properties are of importance.

A detailed overview about various manganese oxide/hydroxide phases including their structure, synthesis, properties and applications is given in chapter 1. In this chapter we also highlight the shortage of the reported studies about manganese oxide/hydroxide nano-particles that motivated us to do this research study with an eye on size-selective synthesis and size-dependent surface, thermal, and structural properties.

In chapter 3, γ-MnOOH (namely, manganite) nanorods were synthesized from the comproportionation reaction between Mn^{2+} and MnO_4^- in aqueous medium using molar ratio of 5:1. Actually, this reaction is a promising and versatile one since it provides many experimental parameters to modify the reaction pathway. Size-selective synthesis of γ-MnOOH nanorods was accomplished by modifying the synthesis parameters such as time, temperature and total Mn concentration in the solution. As a result γ-MnOOH samples with average grain size $<d>$ as low as 14 nm (1 h, 39 mmol L^{-1}) and as large as 36 nm (27 h, 156 mmol L^{-1}) are produced. Under otherwise unchanged experimental parameters, it was found that manganite nanocrystals grow with time according to the equation: $<d> = k(t+a)^{1/n}$ where, $<d>$: the average particle size, t: the reaction time, k: temperature-dependent time constant, a: additional parameter, corresponding to the quotient d_0^n/k with d_0 as the particle size at time $t = 0$ and n: the order of growth of particles with time ranging from ~6-9.

The impact of the anions of manganese salts and alkali metal cations of the permanganate salts on the rod shape of as-prepared manganite samples was studied. Significant effects of the anions (OAc^-, SO_4^{-2} and Cl^-) on the shape of the nanorods were established by SEM investigations. Ultra-long γ-MnOOH nanorods (4-5 µm) were obtained for the first time in this work via the redox reaction between $MnCl_2$ or $MnSO_4$ and $KMnO_4$ and modification of the pH of the reaction medium (pH of 6-8). Shorter nanorods (1-2 µm) were obtained using manganese acetate.

The alkali metal cations (K, Na and Cs) were proven to have an enormous influence on the shape of manganite nanorods. Regular shape nanorods were produced while $KMnO_4$ was used. However, Na- or Cs-permanganate hinders the uniform growth of such nanorods resulting in formation of manganite samples with deformed rod-like morphology.

A careful survey about feitknechtite β-MnOOH, with a layer-type structure revealed that a modest work has been done. Limited preparative methods were reported for feitknechtite synthesis. Successively, a new synthetic route was developed for feitknechtite nanorods (~10 nm diameter) from the solvothermal reaction of manganese acetate and $KMnO_4$ (5:1 molar ratio). The replacement of water entirely by acetone is the key for feitknechtite synthesis. Feitknechtite was characterized by XRD and IR analyses. The powder patterns showed a sharp reflection at 2θ ≈ 22.6º, additional low intensity reflections consistent with feitknechtite also exist. Feitknechtite has a trigonal symmetry (space group $P\bar{3}m1$ (164)) with cell parameters as a = 3.428 (3) Å, c = 4.919 (1) Å and β =120º. IR spectrum of feitknechtite showed absorption bands located at 745, 947 and 1070 cm^{-1} which are assigned to O—H…O deformation modes of β-MnOOH. The measured density value for the sample obtained at 95°C (1 h) using 70 mL acetone was 3.7 g/cm^3 typical for feitknechtite (3.8 g/cm^3). EDX analysis for this sample revealed that the main constituent atoms are Mn and O (H not detectable).

Size-dependent sorption properties were studied for four manganite samples of different mean particle size. The isotherms showed type IV characterized by distinct hysteresis loops indicating mesoporous microstructures. The loops follow H3 type isotherms which do not exhibit any limiting adsorption at high p/p°. Monomodal pore size distribution curves were obtained with average pore sizes in the range of 10-12 nm. The specific surface area S_{BET} of manganite samples was increased as the grain size decreased (from 13 to 47 m^2/g).

Size-dependent thermal stability of manganite nanoparticles (as well as its decomposition products) was also investigated. The larger the particle size, the higher the thermal stability.

According to the issued reports about manganite, it is not so obvious, why and how the decomposition of γ-MnOOH can pursue various pathways upon heating under different conditions. Therefore, we present in chapter 4 a clarification of the thermal behavior of manganite in air and in an inert gas atmosphere. Actually, the amount of oxygen accessible to manganite precursor is a crucial parameter for its transformation towards manganese oxides

with different oxidation state either in air (β-MnO_2 or Mn_5O_8) or even under N_2 or argon atmospheres with low oxygen partial pressure.

A modified preparation method of Mn_5O_8 nanorods was developed by calcination of manganite nanorods (~28 nm) in air in a temperature range of 350-520 °C for 1 h. The same amounts of the precursor (30 mg) were used. Calcinations were performed in the same size glass tubes each with ℓ = 10 cm and Φ =1 cm. It was established that the size of the glass tube is a crucial parameter for formation of Mn_5O_8. Otherwise β-MnO_2 is formed when a large size tube is used.The structure of the precursor was identified by Rietveld refinement, IR, TGA (excess mass) and density measurements. The results revealed a well ordered manganite structure without apparent defects. X-ray single phase Mn_5O_8 samples (mean particle size of 16-18 nm) were prepared by our method. Rietveld analysis was made to ascertain some structural manifestation of the so obtained Mn_5O_8 sample (16 nm, prepared by calcination of manganite at 350 ºC). Assuming that the oxygen sites are fully occupied, the site occupation factors (SOF) for Mn atoms occupying various Wyckoff sites are found to be 1 which implies that we have a well ordered Mn_5O_8 structure. The measured density for this sample was 4.69(0.03) g/cm^3 which matches with the calculated one from Rietveld refinement (4.89 g/cm^3).The estimated average interatomic Mn-O distances showed differences from those of bulk Mn_5O_8 (the difference for Mn^{IV}-O ~5-9 pm and Mn^{II}-O ~15 pm). This divergence indicates that we may have a partly charge-disordered Mn_5O_8 structure. Trivalent Mn might be present as well.

The magnetic measurements for Mn_5O_8 samples revealed that Mn_5O_8 orders antiferro-magnetically at a Néel temperature of 128 K and Curie-Weiss temperature (θ_{CW}) of -116 K. The effective magnetic moment μ_{eff} for this sample derived from linear Curie-Weiss fit for $1/\chi$ –T graph is 4.71 μ_B which is in accordance with the estimated value 4.80 μ_B for charge-ordered Mn_5O_8 assuming only contributions from the spin. The difference between both μ_{eff} values may also indicate the presence of subtle degree of structural disorder. The measurements showed a detectable amount of α-Mn_3O_4 impurities (~0.4-0.6%) admixed to Mn_5O_8 as indicated by a sharp peak in χ-T plot near to 42 K. This temperature perfectly coincides with the Curie temperature of the spinel. A rationalization of the formation of minute spinel impurities admixed to Mn_5O_8 samples is given. Such impurities are ascribed to the presence of some adsorbed manganese acetate on the surface of the manganite precursor, which in turn by calcination of manganite leads to formation of the spinel. The adsorbed

manganese acetate cannot be removed completely via repeated ultrasonic washing for the precursor.

In chapter 5, different polymorphs of manganese dioxide; α, γ, δ and ε-MnO_2 are reported, they prepared from reactions of manganese chloride and $KMnO_4$ in aqueous media. Regarding the literature such reactions were hitherto performed essentially under hydrothermal conditions. The formation of the various polymorphs is not possible under these conditions according to our attempts. We have modified the synthetic method by performing the reaction under reflux at ambient pressure, consequently, the type of the polymorph and/or its morphological shape was amended. K-birnessite (δ-MnO_2) with a sponge-like morphology was obtained under reflux. It does not form hydrothermally. Nsutite, γ-MnO_2, with a plate-like shape was also obtained.

We tuned the experimental parameters, e.g., time, temperature, molar ratio of Mn^{2+}/MnO_4^-, pH, and the alkali metal of the permanganate salt. These parameters are the key for modifying the reaction pathway, eventually resulting in formation of various manganese dioxide polymorphs.

To the best of our knowledge a room-temperature synthesis of akhtenskite (ε-MnO_2) was developed for the first time from such comproportionation reaction. Akhtenskite adopts morphology of sponge-like spherical aggregates (500-750 nm diameters). The measured density of ε-MnO_2 sample was 4.05(0.06) g/cm^3 which is lower than the calculated one from Rietveld analysis (4.24 g/cm^3), both are less than that of the bulk material which is 4.72 g/cm^3. This divergence in the density values combined with low SOF value for Mn^{4+} sites (0.431(9)) is associated with a deficiency of Mn^{4+} at the given crystallographic sites. Two absorption bands located at 1620 and 3400 cm^{-1} are apparent in IR spectra of akhtenskite samples which are assigned to OH bending and stretching modes. The presence of OH^- may compensate for such cationic defects.

The self-template approach is a promising technique for syntheses of various manganese dioxide polymorphs. In particular, birnessite-type (δ-MnO_2) with large-size Cs cations intercalated between its layers can be produced. Not yet reported Cs-birnessite was synthesized from the reaction of manganese acetate and $CsMnO_4$ using 1:1 molar ratio for Mn^{2+}/MnO_4^-. Flower-like morphology was adopted by the Cs-birnessite. EDX measurements revealed that the Cs:Mn ratio is ~0.125.

In chapter 6, tunable size hausmannite (α-Mn_3O_4) nanoparticles were prepared. Manganese (II) is precipitated using NaOH or NH_3 (~0.08 mol L^{-1}, $c(Mn^{2+})/c(OH^-) \approx 1:2$) as $Mn(OH)_2$ in water which subsequently undergoes air oxidation to hausmannite. Control of the particle size of hausmannite was achieved by replacing water partially by ethanol. Increasing of the ethanol content leads to shrinkage in the particle size. Hausmannite samples with sphere/cube-like morphology were obtained, the mean particle sizes <d> for which cover the range from 10 to 25 nm. Variation of the reaction temperature and time has no significant influence on the particle size of spinel nanocrystals.

Size-dependent structural analyses were made using Rietveld refinements for three selected hausmannite samples of different grain sizes. The results of refinement indicate measurable influence of the particle size on the tetragonal cell parameters. With increasing mean particle size a contraction of the unit cell occurs in "a" direction and an elongation in the "c" direction is found. The degree of tetragonal distortion of the unit cell – taken $c/\sqrt{2}\,a$ as a measure – increases steadily with increasing of particle size. The degree of distortion shows a linear decrease with increasing of the reciprocal particle size 1/<d>, which in turn is proportional to the surface area of the particles.

For the smallest size hausmannite sample (<d> ~10 nm) the SOF value of Mn^{2+} was found to be 0.91. The refinement was performed based on the assumption that the octahedral sites are fully occupied by Mn^{3+}. Approximately, 9% deficiency in the cationic sites containing Mn^{2+} was detected. The deficiency may arise from at least partial oxidation of Mn^{2+} to Mn^{3+} resulting in formation of cationic vacancies. The SOF value (0.92) of oxygen atoms indicates also an anionic defect. The measured density for this sample was ~4.29 g/cm^3, which is significantly lower than that calculated from refinement data (4.64 g/cm^3). Both features point to structural defects in agreement with a significantly reduced density compared to that of the bulk spinel structure (4.86 g/cm^3).

With increasing of the particle size such anionic deficiency vanish. Merely, insignificant deficiency on the Mn^{2+} site was detected (SOF is 0.988). The ordered spinel structure was found for the largest hausmannite sample (<d> ~25 nm), no deficiency could be recognized from the analysis of refined SOF values. The value of the measured density (4.68(4) g/cm^3) approaches that determined by x-ray analysis (4.86 g/cm^3). IR spectra for the samples showed two absorption bands at ~1620 and 3400 cm^{-1} that are ascribed to OH bending and stretching modes of either adsorbed or crystallization water. According to the TGA results for the

hausmannite samples there is no significant excess mass. Mass losses of ~0.6-1 % are found (temperature ranges of 250-620 °C) which may correspond to structural water.

Nitrogen adsorption-desorption using the BET method was measured for three hausmannite samples of different mean particle sizes. The isotherms were classified as type IV isotherms. Hysteresis is a characteristic feature for this kind of isotherms. This type is correlated with the presence of mesopores. The hysteresis observed in isotherms for Mn_3O_4 samples with large particle size was classified as H3 type which does not show any limiting adsorption at high $p/p°$. The hysteresis observed in the isotherm obtained for hausmannite sample with smallest particle size is classified as H2 type which suggests pores with narrow necks and wide bodies. Pore size distribution curves suggested that these pores are distributed in a monomodal fashion with a width varying between 4.7 nm for the smallest size sample and 23 nm for the largest one.

Finally, to be highlighted as an important outcome of the work that it is possible to synthesize most of nanocrystalline manganese oxide/hydroxide phases with size-selective and size-related physical properties by this facile and economic synthetic approach via precipitation from aqueous or aqueous/ethanolic solutions and in the case of feitknechtite from acetone for application-relevant research.

8. Zusammenfassung

Mangan kann viele verschiedene Oxidationsstufen wie etwa +II, +III, +IV und +VII einnehmen, die auch von verschiedenen Manganoxiden und Manganoxidhydroxid-Phasen her bekannt sind. Obwohl das Forschungsfeld der nanokristallinen Manganoxide/hydroxide sehr weitläufig ist, ergeben sich dennoch viele interessante Forschungsfelder, bei denen noch Unklarheit herrscht. Partikelgrößenabhängige physikalische Eigenschaften sind dabei von Bedeutung.

Ein detaillierter Überblick über die verschiedenen Manganoxid/hydroxid-Phasen einschließlich ihrer Struktur, Synthese, Eigenschaften und Anwendungen ist in Kapitel 1 aufgezeigt. In diesem Kapitel wird auch hervorgehoben, welche Fragestellungen sich aus ausgewählten publizierten Studien ergeben. Sie motivierten zu dieser Arbeit, die unter anderem die größenselektiven Synthese und die Untersuchung der größenabhängigen Änderungen hinsichtlich der Oberflächen sowie der thermischen und strukturellen Eigenschaften behandelt.

In Kapitel 3 wird aufgeführt, wie nanokristallines γ-MnOOH, Manganit-Nanostäbchen, über eine Komproportionierungsreaktion von Mn^{2+} und MnO_4^- in wässrigem Milieu bei einem molaren Verhältnis von 5:1 zugänglich gemacht werden kann. Tatsächlich ist dies eine aussichtsreiche und vielseitige Reaktion, da sie viele experimentelle Parameter ausweist, über deren gezielte Variation der Reaktionsweg und die Produktbildung beeinflusst werden kann. Die größenselektive Herstellung der γ-MnOOH-Nanostäbchen wurde über Variation der Syntheseparameter wie Zeit, Temperatur und Mn-Konzentration der Lösung realisiert. Es wurden so γ-MnOOH-Partikel mit mittlerer Partikelgröße <d> von 14 bis 36 nm erhalten. Unter isothermen Reaktionsbedingungen zeigen die Manganitpartikel ein zeitabhängiges Wachstum, das gemäß der allgemeinen Partikelwachstumsgleichung $\langle d \rangle = k(t+a)^{1/n}$ quantifiziert werden kann. Hierbei sind: <d>: mittlere Partikelgröße, t: Reaktionszeit, k: Temperaturabhängige Zeitkonstante, a: zusätzlicher Parameter, der dem Quotienten d_0^n/k mit d_0 als Partikelgröße zum Zeitpunkt t = 0 entsprechen sollte und n: Ordnung des Wachstums der Partikel mit Zeit.

Untersucht wurde auch der Einfluss der Anionen der Mangansalze und der Alkalimetallkationen des Permanganatsalzes auf die Stäbchenform der hergestellten Manganitproben. Signifikante Einflüsse der Anionen (OAc^-, SO_4^{-2} und Cl^-) auf die Form der Nanostäbchen

wurden über SEM-Untersuchungen ermittelt. Sehr lange γ-MnOOH-Nanostäbchen (4-5 µm) wurden im Rahmen der Arbeit erstmals über die Komproportionierung von $MnCl_2$ oder $MnSO_4$ und $KMnO_4$ hergestellt, wobei der pH-Wert des Reaktionsmediums (pH von 6-8) angepasst wurde. Kurze Nanostäbchen (1-2 µm) wurden unter Verwendung von Mangan-acetat erhalten.

Die Alkalimetallkationen (K, Na, Cs) zeigen einen enormen Einfluss auf die Form der Manganit-Nanostäbchen. Regelmäßig geformte Nanostäbchen wurden unter Verwendung von $KMnO_4$ erhalten. Na- und Cs-Permanganat scheint das gleichmäßige Wachstum von solchen Nanostäbchen zu behindern und führt zur Bildung von Partikeln mit deformierter, stäbchen-artigen Morphologie.

Eine Sichtung der Literatur zu Feitknechtit (β-MnOOHergab, dass diese metastabile Phase des Manganits recht wenig untersucht wurde. Es wurden wenige präparative Methoden für die Synthese von Feitknechtit berichtet. Mittels einer Solvothermalreaktion von Manganacetat und $KMnO_4$ (molares Verhältnis 5:1) wurde erfolgreich eine neue Syntheseroute für Feitknechtitnanostäbchen (~10 nm im Durchmesser) entwickelt. Entscheidend für die Syn-these von Feitknechtit ist das gänzliche Ersetzen von Wasser durch Aceton. Die Pulver-diffraktogramme zeigen scharfe Reflexe bei $2\theta \approx 22.6°$, zusätzlich existieren auch Reflexe schwacher Intensität, welche konsistent mit denen von Feitknechtit sind. Feitknechtit kristallisiert mit trigonaler Symmetrie, Raumgruppe $P\bar{3}m1$ (164) mit den Gitterparametern a = 3.428(3) Å, c = 4.919(1) Å und γ = 120°. Das IR-Spektrum von Feitknechtit zeigt Absorptionsbanden bei 947 und 1070 cm^{-1}, die durch die Deformationsschwingung von O-H…O des β-MnOOH hervorgerufen werden. Die gemessene Dichte (3.7 g/cm^3) für bei 95 °C erhaltenen Probe ist typisch für Feitknechtit (ρ = 3.85 g/cm^3). EDX-Analysen liefern als Hauptbestandteile Mn und O. H ist EDX-analytisch nicht detektierbar.

Größenabhängige Sorptionseigenschaften wurden an vier Manganitproben unterschiedlicher Partikelgröße untersucht. Die Isothermen zeigen einen Typ IV-Verlauf, erkennbar an einer durch die mesoporöse Mikrostruktur hervorgerufenen Hystereseschleife im Sorptions-verhalten. Dieses Verhalten kann dem H3-Srptionstyp zugeordnet werden, welcher keine Sättigung der Adsorption bei hohem p/p° aufweist. Es wurde eine monomodale Poren-größenverteilung mit einer mittleren Porengröße im Bereich von 10-12 nm erhalten. Die spezifische Oberfläche der Manganitproben wird mit abnehmender Partikelgröße größer (S_{BET}

von 13 zu 47 m²/g). Ebenfalls untersucht wurde die thermische Stabilität in Abhängigkeit von der Größe der Manganitnanopartikel (sowie dessen Zersetzungsprodukte). Je größer die Partikel sind, desto höher ist thermische Stabilität.

Ausgehend von veröffentlichen Berichten über Manganit ist es nicht offensichtlich, warum und wie sich verschiedene Reaktionswege bei der thermischen Zersetzung von γ-MnOOH bei unterschiedlichen Bedingungen ergeben. Daher wird in Kapitel 4 ein Überblick über das thermische Verhalten von Manganit an Luft und in Inertgas-Atmosphäre gegeben. Es wird gezeigt, dass die Menge an Sauerstoff, welche für den Manganitpräkursor zugänglich ist, ein kritischer Parameter für die Bildung von Manganoxiden mit unterschiedlichen Oxidations-stufen ist, entweder bei Reaktion an Luft (β-MnO$_2$ oder Mn$_5$O$_8$) oder sogar unter Gas-gemischen aus N$_2$- oder Argon mit geringem Sauerstoffpartialdruck.

Weiterhin wird eine modifizierte Präparationsmethode von Mn$_5$O$_8$-Nanostäbchen, über die Kalzinierung von Manganit-Nanostäbchen (~28 nm) an Luft im Temperaturbereich 350 - 520 °C bei einstündiger Reaktionszeit vorgestellt. Es wurden dabei immer gleiche Mengen an Präkursor (30 mg) verwendet. Die Kalzinierung wurde in Reagenzgläsern mit einheitlicher Größe, mit l = 10 nm und Φ = 1 cm, durchgeführt. Es wird nachgewiesen, dass die Größe des Reagenzglases ein kritischer Parameter bei der Bildung von Mn$_5$O$_8$ ist. Wird ein größeres Reagenzglas verwendet, bildet sich direkt β-MnO$_2$. Der Präkursor wurde über Profilanpassun-gen an Röntgenpulverdiffraktogramme nach Rietveld, IR-, TGA- (Exzessmasse) und Dichte-messungen identifiziert. Die Ergebnisse zeigen eine wohlgeordnete Manganitstruktur ohne erkennbare Defekte. Röntgenographisch einphasige nc-Mn$_5$O$_8$-Proben (mittlere Partikelgröße von 16-18 nm) wurden so erstmals hergestellt. Eine Rietveldanalyse an einer Mn$_5$O$_8$-Probe (16 nm) wurde zur Überprüfung der strukturellen Eigenschaften durchgeführt. Unter der An-nahme, dass die Sauerstoffposition vollbesetzt ist, wurde ein Besetzungsfaktor (SOF) für Mn auf den verschiedenen Wyckoff-Lagen von 1 gefunden, welcher anzeigt, dass eine wohlge-ordnete Mn$_5$O$_8$-Struktur vorliegt. Die gemessene Dichte für diese Probe ist 4.69(5) g/cm³, in akzeptabler Übereinstimmung mit der aus den Strukturdaten berechneten Dichte von 4.83 g/cm³. Eine Abstandsanalyse und der Vergleich mit den aus den Literaturdaten zugänglichen Mn-O-Abständen liefert Hinweise darauf, dass nc-Mn$_5$O$_8$ teilweise ladungsfehlgeordnet ist und Mn(+III) enthalten könnte.

Magnetische Messungen an Mn_5O_8-Proben bestätigen, dass Mn_5O_8 antiferromagnetisch bei einer Néel-Temperatur von 128 K ordnet entsprechend einer Curie-Weiss-Temperatur von -116 K. Das aus der Steigung des linearen Teils des $1/\chi$-T-Diagramms bestimmte magnetische Moment ist 4,71 μ_B, in guter Übereinstimmung mit dem Spin-only-Erwartungswert von 4,80 μ_B. Die Abweichung beider Werte ist im Einklang mit teilweiser Ladungsfehlordnung. Die Messungen weisen außerdem auf sehr geringe, aber nachweisbare Mengen an α-Mn_3O_4-Verunreinigungen (~0,4-0,6%) im Mn_5O_8 hin, erkennbar an einem abrupten Magnetisierungsanstieg beim Einsetzen der ferrimagnetische Ordnung bei 42 K in einer $1/\chi$-T-Auftragung. Diese Temperatur stimmt mit der Curie-Temperatur des Spinells überein. Es wird eine Erklärung für die Bildung für die geringe Verunreinigung der Mn_5O_8- Proben mit Spinell gegeben. Zugeschrieben werden sie adsorbiertem Manganacetat auf der Oberfläche des Manganit-Präkursors, welches dann bei der Kalzinierung des Manganits zur Bildung des Spinells führt. Das adsorbierte Manganacetat kann auch durch wiederholtes Waschen des Präkursors selbst bei Ultraschallbehandlung nicht entfernt werden.

In Kapitel 5 wird gezeigt, wie unterschiedliche Polymorphe von Mangandioxid; α, γ, δ und ε-MnO_2, aus der Reaktion von Manganchlorid mit $KMnO_4$ in wässrigem Medium darstellbar sind. Literaturbekannt sind hauptsächlich Hydrothermalreaktionen. Die Bildung von verschiedenen Modifikationen von MnO_2 und verwandter Phasen ist nicht direkt nach der beschriebenen Methode möglich. Die Syntheseroute wurde dahingehend abgewandelt, dass die Reaktion unter Rückflussbedingungen durchgeführt wurde. Daraus ergab sich eine erhöhte Kristallinität des jeweiligen Polymorphs und/oder dessen Morphologie. K-Birnessit (δ-MnO_2), welches sich nicht unter hydrothermalen Bedingungen bildet, wurde mit einer schwammartigen Morphologie erhalten. Ebenfalls wurde blättchenförmiger Nsutit, γ-MnO_2, hergestellt.

Es wurden die experimentellen Parameter, wie z.B. Zeit, Temperatur, molares Verhältnis von Mn^{2+}/MnO_4^-, pH und das Alkalimetallkation des Permanganat-Salzes, geändert. Diese Parameter sind entscheidend dafür, welcher Reaktionsweg vollzogen wird und welche Mangandioxidmodifikation gebildet wird.

Nach unserem Wissensstand wird hier die erste Raumtemperatursynthese von Akhtenskit, ε-MnO_2, über eine Komproportionierungsreaktion beschrieben. Akhtenskit fällt hierbei in Form schwammartiger, sphärischer Aggregate (Durchmesser 500-750 nm) an. Die gemessene

Dichte von ε-MnO_2 ist 4.05(6) g/cm³, was niedriger ist als die aus den Strukturdaten der Rietveldanalyse berechnete Dichte von 4,24 g/cm³. Beide Werte sind geringer als die für das Volumenmaterial, die bei 4.72 g/cm³ beträgt. Die Abweichung der Dichtewerte spiegeln die Unterbesetzung der Mn^{4+}-Lage (0.437(8) anstatt 0,5) wider. Der nanokristalline Ashtenskit zeigt zwei zusätzliche Absorptionsbanden bei ~1620 und ~3400 cm^{-1}, die auf OH-Deformations- und Valenzschwingungen hinweisen. Vorhandenes Hydroxid könnte die Kationendefekte kompensieren.

Die Formsteuerung mittels der Templatmethode ist eine vielversprechende Technik für die Synthese von verschiedenen Mangandioxidmodifikationen. So kann Birnessit-Typ (δ-MnO_2) mit zwischen den Schichten interkalierten Cs-Kationen produziert werden. Cs-Birnessit ist über die Reaktion von Manganacetat und $CsMnO_4$ im molaren Verhältnis Mn^{2+}/MnO_4^- von 1:1 herstellbar, was bisher noch nicht berichtet wurde. Die blumenartige Morphologie wurde von dem Cs-Birnessit übernommen. EDX-Messungen zeigen ein Verhältnis Cs:Mn von ~0.125.

In Kapitel 6 wird die Synthese von Hausmannit, α-Mn_3O_4, mit verschiedener Partikelgröße $\langle d \rangle$ vorgestellt. Mangan (II) wird unter Verwendung von NaOH oder NH_3 (~0.08 mol L^{-1}, $c(Mn^{2+})/c(OH^-) \approx 1:2$) aus wässriger Lösung als $Mn(OH)_2$ gefällt, welches anschließend in Suspension durch Luftoxidation in Hausmannit übergeht. Die Einstellung der Partikelgröße des Hausmannits wurde durch das partielle Ersetzen von Wasser mit Ethanol erreicht. Es wurden Hausmannit-Proben mit einer sphärischen/kubischen Morphologie erhalten. Die so einstellbare Partikelgröße $\langle d \rangle$ liegt im Bereich von 10 bis 25 nm. Die Variation der Reaktionstemperatur und Zeit niimmt keinen merklichen Einfluss auf die Größe der Spinell-Nanopartikel, was darauf hindeutet, dass die Partikel nach der Keimbildung direkt in der letztlich detektierten Größe ausfallen.

Strukturanalysen wurden über Rietveld-Profilanpassungen an die Röntgendiffraktogramme dreier ausgewählter Hausmannit-Proben unterschiedlicher Partikelgröße durchgeführt. Die strukturellen Befunde deuten an, dass die Partikelgröße einen signifikanten Einfluss auf den tetragonalen Zellparameter hat. Mit Zunahme der mittleren Partikelgröße erfolgt eine Kontraktion der Einheitszelle in a-Richtung und eine Verlängerung in Richtung der c-Achse. Der Grad der tetragonalen Verzerrung der Einheitszelle, bestimmt über das partikel-

größenabhängige Verhältnis $c/\sqrt{2}\,a$, nimmt mit Abnahme der Partikelgröße ab. Die Verzerrung skaliert linear mit $1/d$ und somit mit der spezifischen Oberfläche der Partikel.

Für die kleinsten Hausmannitproben ($<d> \sim 10$ nm) wurde der Besetzungsfaktor SOF der Mn^{2+}-Lage mit 0.91 bestimmt. Dieses Defizit von ungefähr 9% auf der Mn^{2+}-Lage wird damit in Zusammenhang gebracht, dass Mn^{2+} zu Mn^{3+} oxidiert wird und so Kationenleerstellen entstehen. Der SOF-Wert der Sauerstoffatome (0.92) deutet auch darauf hin, dass Anionen-Defekte vorliegen. Die gemessene Dichte für diese Probe ist 4.29 g/cm³, somit signifikant kleiner als die röntgenografische Dichte von 4.64 g/cm³. Vergleicht man dies mit der Dichte der Volumenphase von 4.86 g/cm³, so deuten beide zuvor angeführten Dichtewerte auf strukturelle Defekte und somit auf Abweichungen in der chemischen Zusammensetzung in nc-Mn_3O_4 hin. Mit Zunahme der Partikelgröße verschwindet die Anionen-Unterbesetzung zunehmend. Lediglich ein geringes Defizit auf der Mn^{2+}-Lage (SOF von 0.988) ist noch detektierbar. Die vollständig geordnete Spinellstruktur liegt bei den größten Hausmannit-Proben ($<d> \sim 25$ nm) vor. Eine Abweichung der SOF-Werte von 1 ist nicht feststellbar, was auch in Übereinstimmung mit den Werten der röntgenographischen und gemessen Dichte, 4.86 und 4.68 (4) g/cm³ ist. Das IR-Spektrum für diese Probe zeigt zwei Absorptionsbanden bei ~ 1620 und ~ 3400 cm^{-1}, hervorgerufen durch OH-Deformations- und Valenzschwingungen von entweder adsorbiertem oder Kristallisationswasser. Den TGA-Ergebnissen der Hausmannit-Proben nach sind die Partikel mit keiner signifikanten Exzessmasse mehr behaftet. Massenverluste von ~ 0.6-1% (Temperaturbereich von 250-620 °C) werden auf Kristallwasser zurückgeführt.

Stickstoff Adsorption-Desorption wurde unter Verwendung der BET-Methode für drei Hausmannitproben unterschiedlicher mittlerer Partikelgröße gemessen. Die Isothermen wurden als Typ-IV-Isothermen klassifiziert. Hysterese ist ein charakteristisches Merkmal für diese Art der Isotherme und wird korreliert mit dem Vorhandensein von Mesoporen. Die Isothermen von Mn_3O_4-Proben mit großer Partikelgröße zeigen eine Hysterese, die als H3-Typ klassifiziert werden kann, welche kein Adsorptionsplateau Des hohem P/Pº zeigen. Die Isothermen der Hausmannit Proben kleiner Partikelgröße zeigen eine Hysterese des H2-Typs, welchen auf das Vorliegen von weiträumigen Poren mit engem Hals hindeutet. Die Porengrößenverteilungskurven zeigten eine monomodale Verteilung mit einer Größe von 4.7 nm für die Probe mit der kleinsten und 23 nm für die mit der größten Partikelgröße.

Schlussendlich soll als bedeutsames Ergebnis der Arbeit hervorgehoben werden, dass es möglich ist, über die beschriebene einfache und ökonomische Herstellungsweise die meisten Manganoxid/hydroxid-Phasen nanokristallin und größenselektiv mit größenabhängig änderbaren physikalischen Eigenschaften durch Fällung aus wässriger, wässrig-ethanolischer Lösung und im Fall von Feitknechtit aus Aceton für anwendungsrelevante Untersuchungen bereit zu stellen.

9. Appendix

Table 1. Synthesis of MnOOH nanocrystals under refluxing conditions.

Sample No.	Mn(OAc)$_2$	KMnO$_4$	H$_2$O	Time / h	Temp. / °C	Phase	Size
M7R5	1.201	0.1500	150	17	110	γ-MnOOH	23.9
M7R7	1.2003	0.1501	150	27	110	γ-MnOOH	26.2
M7R8	1.2005	0.15005	150	3	110	γ-MnOOH	19.3
SM1	0.6003	0.065	225	17	110	γ-MnOOH	21.5
SM2	0.60004[a]	0.10009	100	17	110	γ-MnOOH	24.2
SM3	0.5153[b]	0.1025	100	17	110	γ-MnOOH	23.9
M7R13	1.2002	0.15006	75	17	110	γ-MnOOH	25.66
M7R14	0.6001	0.0653	225	3	110	γ-MnOOH	16.47
M7R16	1.2002	0.15002	75	3	110	γ-MnOOH	18.76
M7R16RE	1.20016	0.15009	75	3	110	γ-MnOOH	19.76
M7R17RE	0.30027	0.028	300	3	110	γ-MnOOH	14.5
M7R19	2.4001	0.30008	75	3	110	γ-MnOOH	21.84
M7R20RE	0.3001	0.0281	300	17	110	γ-MnOOH	19.34
M7R21	1.20004	0.15022	75	27	110	γ-MnOOH	27.31
M7R22	0.60008	0.06501	225	27	110	γ-MnOOH	25.28
M7R28	2.4007	0.3003	75	17	110	γ-MnOOH	27.64
M7R30	2.4003	0.3001	75	27	110	γ-MnOOH	28.96
M7R36	0.30015	0.03007	300	27	110	γ-MnOOH	20.22
M7R40	0.60008	0.40002	225	3	110	δ-MnO$_2$	8
M7R43	0.60005	0.03018	225	3	110	γ-MnOOH	20.47
M7R46	0.60015	0.01006	225	3	110	mixture	-
M7R57	0.60003	0.1	225	3	110	mixture	-
M7R61	0.60001	0.06515	225	1	110	γ-MnOOH	11.6
M7R63	0.30023	0.032	300	1	110	γ-MnOOH	11.1
M7R65	1.2002	0.1505	150	1	110	γ-MnOOH	13.73
M7R67	1.2003	0.15015	75	1	110	γ-MnOOH	15.98
M7R78	0.41027	0.40006	225	17	100	α-MnO$_2$	14.54
SM4	0.60035	0.0663[Na]	100	17	110	γ-MnOOH	18
SM5	0.6003	0.1042[Cs]	100	17	110	γ-MnOOH	20
M7R100	2.4002	0.3004	75	1	110	γ-MnOOH	17.6

a: MnCl$_2$ and pH modification till ~8 with HCl (1 mol L^{-1}); b: MnSO$_4$, pH modification (~8)

Table 2. Synthesis of MnOOH nanocrystals under hydrothermal conditions.

Sample No.	Mn(OAc)₂	KMnO₄	H₂O	Time / h	Temp. / °C	Phase	Size
M7R12	0.6003	0.07502	70	25	115	γ-MnOOH	28.95
M7R15	0.60003	0.07504	70	3	115	γ-MnOOH	21.75
M7R18	0.60007	0.07503	70	72	115	γ-MnOOH	31.81
M7R23	0.60015	0.07505	70	3	140	γ-MnOOH	24.75
M7R25	0.60001	0.07504	70	3	95	γ-MnOOH	19.32
M7R27	0.6002	0.07503	70	25	140	γ-MnOOH	35.69
M7R29	0.60024	0.075	70	72	140	γ-MnOOH	36.06
M7R31	0.60003	0.07506	70	3	80	γ-MnOOH	13.62
M7R32	0.60005	0.07503	70	3	85	γ-MnOOH	15.04
M7R35	0.60016	0.07501	70	72	95	γ-MnOOH	28.8
M7R37	0.6007	0.075	70	25	85	γ-MnOOH	21.6
M7R38	0.60001	0.0751	70	25	95	γ-MnOOH	24.54
M7R41	0.60005	0.07504	70	72	85	γ-MnOOH	26.38
M7R42	0.6001	0.075	70	17	115	γ-MnOOH	26.85
M7R45	0.60003	0.07515	70	17	140	γ-MnOOH	30.88
M7R47	0.60002	0.07507	70	3	60	mixture	-
M7R50	0.60004	0.07504	70	17	95	γ-MnOOH	24.25
M7R52	0.59997	0.07513	70	17	85	γ-MnOOH	19.3
M7R53	0.59999	0.075	70	1	85	γ-MnOOH	12
M7R54	0.6002	0.07502	70	1	115	γ-MnOOH	20.21
M7R55	0.60008	0.075	70	1	95	γ-MnOOH	13.81
M7R55RE	0.60017	0.07509	70	1	95	γ-MnOOH	14.1
M7R58	0.60003	0.07505	70	1	140	γ-MnOOH	22.95
ED039	0.6003	0.07503	70^{acetone}	1	95	β-MnOOH	39

Table 3. Impact of variation of pH of the medium on the phase of the product prepared under hydrothermal conditions.

Sample No.	Mn(OAc)$_2$	KMnO$_4$	H$_2$O	Time / h	Temp. / °C	pHi	pHf	Phase	Size
M7RpH1	0.60024	0.07534	62	3	95	~ 2	1.4	A	12
M7RpH3	0.60012	0.07512	65	3	95	~ 4	2.2	A	12.7
M7RpH6	0.6001	0.07504	70	3	95	~ 6	3-4	B	19
M7RpH8	0.60041	0.0752	66	3	95	~ 8.5	5.8	B+C	-
M7RpH11	0.60024	0.0754	63	3	95	~ 11		C	21

A: γ-MnO$_2$; B: γ-MnOOH; C: α-Mn$_3$O$_4$.

Table 4. Impact of variation of reaction solvent on the product phase and its mean particle size prepared under hydrothermal conditions.

Sample No.	Mn(OAc)$_2$	KMnO$_4$	%EtOH	Time / h	Temp. / °C	Phase	Size
M7R24RE	0.60015	0.07504	0	3	160	A	27.3
M7REt10	0.6002	0.0751	10	3	160	A	24
M7REt20	0.60015	0.07544	20	3	160	A+B	-
M7REt40	0.60026	0.0755	40	3	160	A+B	-
M7REt60	0.6004	0.0755	60	3	160	A+B	-
M7REt80	0.6003	0.0753	80	3	160	B	26
M7REt100	0.6004	0.0752	100	3	160	B	9

A: γ-MnOOH; B: α-Mn$_3$O$_4$.

Table 5. Synthesis of various manganese dioxide polymorphs under reflux conditions.

Sample No.	MnCl$_2$	KMnO$_4$	H$_2$O	Time / h	Temp. / °C	pHi	pHf	Phase	Size
M14R2	0.6001	0.5001	100	17	110	~ 5-6	3-4	α	14.3
M14R5	0.6001	0.1	100	17	110	~ 3-4	~ 2	γ	12.6
M14R8	0.60027	0.50003	100	1	110	~ 5-6	-	δ, K-type	8.1
M14R13	0.60026	0.5003	100	17	90	~ 5-6	-	δ	10.1
M14R20	0.60028	0.10039	100	6	110	~ 3-4	~ 2	γ	14.3
M14R21	0.6006	0.1004	100	1	110	~ 3-4	~ 2	γ	12.6
M14R23	0.60033	0.5004	100	72	110	~ 5-6	1.4	α	16.3
M14R24	0.60011	0.10008	100	72	110	~ 3-4	1.8	γ	13.1
M14R25	0.60018	0.1004	100	1	RT	~ 3-4	1.8	ε	8.5
M14R27	0.60025	0.10032	100	72	RT	~ 3-4	1.8	ε + γ	-
M14R28	0.6003	0.5003	100	17	60	~ 5-6	1.6	δ	9.9
M14R32	0.60027	1.5001	100	17	110	~ 9	8.6	δ	10.3
M14R33	0.60015	1.5002	100	72	110	~ 9	8.1	δ	15.1
M14R60	0.6004	0.8036^{Cs}	100	17	110	~ 4	1.7	γ	12.5
M14R63	0.6004	0.1608^{Cs}	100	17	110	~ 4	2	γ	12.2
M14R66	0.60037	0.5074^{Na}	100	17	110	3-4	1.8	γ	12.4
M14R69	0.6004	0.1019^{Na}	100	17	110	~ 3-4	1.9	γ	11.9
M14R73	0.6004	1.5004	100	17	90	~ 9	8.4	δ	9.1
M14R74	0.6004	1.5004	100	17	60	~ 9	8.5	δ	8.2
M14R75	0.60039	1.5004	100	1	110	~ 9	8.3	δ	9.6
M7R80	0.6004^{OAc}	0.40016^{K}	225	17	110	~ 5-6	4.3	α	14
M7R93	0.6004^{OAc}	0.6425^{Cs}	100	17	110	~ 5-6	4.5	δ, Cs-type	8.2
M7R96	0.6003$^{OAc^-}$	0.4055^{Na}	100	17	110	~ 5-6	4.8	γ	12.3

Table 6. Synthesis of huasmannite nanocrystals using NaOH as a precipitant under reflux conditions.

Sample No	Mn(OAc)$_2$ / mmol	NaOH / mmol	%EtOH	Temp. / °C	Time / h	pHi	pHf	Phase	Size
ED001	4.09	8.37	0	40	6	~ 10-11	6.8	A	20
ED002	4.12	8.23	0	40	24	~ 10-11	6.4	A	17.6
ED003	4.10	8.24	100	40	6	~ 10	8.1	Amor.	-
ED004	4.09	8.28	100	40	24	~ 9-10	7.9	Amor.	-
ED005	4.07	8.28	50	40	6	~ 10-11	6.8	A	13
ED006	4.09	8.25	50	40	24	~ 10	6.7	A	14.4
ED010	4.09	8.27	95	60	24	~ 9	7.6	A	12.2
ED012	4.08	8.31	95	80	24	~ 8-9	7.6	A	13.4
ED014	4.08	16.6	0	40	6	>11	12.2	A	23.2
ED015	4.09	8.20	0	40	1	~ 10-11	7.5	A+B	20.7
ED017	4.07	16.6	50	40	6	>11	12.2	A+C	21
ED019	4.08	16.6	95	40	6	>11	12.4	C	12
ED021	4.08	8.29	95	40	1	~ 10	7.8	A+D	10.5
ED022	4.09	8.24	50	40	1	~ 10	7.4	A	11.9
ED025	4.08	8.28	95	40	24	~ 9-10	7.7	A+D	12
ED026	4.09	8.28	95	RT	24	~ 9	7.7	A+D	10.5
ED031	4.08	8.36	95	40	6	~ 9	7.7	A+D	12
ED038	4.09	8.30	0	40	72	~ 10-11	6.4	A+E	19.9
ED039	4.09	8.20	85	40	6	~ 9-10	7.2	A+D	12.4
ED040	4.08	8.28	85	40	24	~ 10	7.4	A+D	11.7
ED045	2.05	4.20	95	40	1	~ 8-9	7.8	A+D	9.6
ED047	4.08	8.22	85	40	1	~ 9-10	7.5	A+D	11
ED060	2.04	4.12	95	40	1	~ 9	8.6	A+D	10.7
ED074	4.08	8.26	95	40	72	~ 13.8	13.5	A	8.5
ED075	4.08	24.7	50	40	6	~ 13.5	13.2	A+C	23

A: hausmannite, B: un-oxidized Mn(OH)$_2$, C: δ-MnO$_2$, D: β-MnOOH and E: γ-MnOOH

Table 7. Synthesis of huasmannite nanocrystals using ammonia as a precipitant under reflux conditions.

Sample No.	Mn(OAc)$_2$ / mmol	NH$_3$(25%) / mmol	%EtOH	Temp. / °C	Time / h	pHi	pHf	Phase	Size
ED007	4.08	8.55	0	40	6	~ 10	6.8	A	20.1
ED008	4.10	8.28	0	40	24	~ 10	6.3	A	23.6
ED009	4.08	8.28	50	40	6	~ 8	7.6	A	16.9
ED011	4.08	8.28	95	40	24	~ 9	7.5	A	10
ED013	4.09	17.4	0	40	6	>11	9.2	A	24.6
ED016	4.09	17.4	50	40	6	~ 11	9.0	A	16.3
ED018	4.08	17.4	95	40	6	>11	8.6	A	12
ED020	4.08	8.28	95	40	1	~ 10	N.p.	N.p.	
ED023	4.09	8.28	0	40	1	~ 10	8.8	A	24.6
ED024	4.08	8.28	50	40	1	~ 9-10	8.5	A	15.5
ED027	4.07	8.28	50	40	24	10	6.9	A	15.5
ED028	4.08	8.28	95	RT	24	~ 9-10	7.7	A	10.8
ED029	4.08	8.28	95	60	24	~ 9-10	7.5	A	10.3
ED030	4.08	8.28	95	80	24	~ 9-10	7.2	A	9.6
ED032	4.08	8.28	95	40	6	~ 9-10	7.6	A	10.2
ED041	4.09	8.28	85	40	6	~ 9-10	7.5	A	12.6
ED042	4.09	8.28	85	40	24	~ 9-10	7.5	A	12.2
ED043	4.09	8.28	0	RT	24	~ 10-11	6.9	A	26.5
ED044	4.08	8.28	50	RT	24	~ 10	6.9	A	16.9
ED046	4.08	8.28	85	40	1	~ 9-10	8.0	A	9.3
ED055	4.07	8.28	85	RT	24	~ 10	8.1	A	12.9
ED056	2.05	4.14	95	RT	24	~ 9	8.1	A	10.1
ED076	4.08	24.9	50	40	6	~ 9.7	9.3	A	18
ED079	4.08	8.28	25	RT	24	~ 8-9		A	22.5

N.p.: no precipitation

Curriculum Vitae

1- <u>Personal Data</u>

Name: *Mohamed Abdel Megeed Ibrahim Said*

Date of Birth: *6/12/1978*

Place of Birth: *Assiut-Egypt*

Nationality: *Egyptian*

Address: *Assiut University, Faculty of Science, Chemistry Department*

Telephone: *06421 28 25680 & 017637512276*

Degree: *Master degree in Inorganic Chemistry from Faculty of Science- Assiut University 2008.*

Marital status: *Married with two children*

Employment Record: *Assistant Lecturer*

E-mail: *moh_chem1@yahoo.com*

ibrahimm@staff.uni-marburg.de

2- <u>Academic Degrees</u>

B. Sc. in Chemistry (1997 – 2002): Very good (Honor degree)

Master Courses (2003 – 2004): Very good

Master Thesis (2005-2008): Master degree in Inorganic Chemistry, Faculty of Science, Assiut University, Egypt.

3- <u>Previous and Current Positions</u>

12/2002 – 11/2008: Demonstrator of Chemistry, Faculty of Science, Assiut University, Assiut, Egypt and teaching assistant for undergraduate.

11/2008 – 10/2010: Assistant lecturer at the Department of Chemistry, Faculty of Science, Assiut University, Assiut, Egypt.

10/2010 – 5/2011: Exchange student at Philipps Universität Marburg.

5/2011 – to date: PhD student at Philipps Universität Marburg.

4- <u>Publications</u>

Mixed ligand Zinc (II) and Cadmium (II) complexes containing Ceftriaxone or Cephradine antibiotics and different donors. A. I. El-Said, A. A. M. Aly, M. S. El-Meligy (the late) and M. A. Ibrahim. The Journal of the Argentine Chemical Society Vol. 97 N ° 2, 149-165 (2009).

5- <u>Conferences</u>

- First Conference for Young Scientists, Basic Science & Technology (Assiut, May 5-6, 2007), Oral Presentation.

- Wöhler-Vereinigung für Anorganische Chemie (September 2012/ Göttingen), Poster.

- Hemdsärmelkolloquium, HÄKO (March 2013/Freiberg, March 2014/Köln).

- Wissenschaftsforum Chemie, Spetember 2013/Darmstadt, Poster.

- JCF-Frühjahrssymposium 2014, March 2014/Jena, Poster.

- Hirschegg Seminar, June 2014, Oral presentation.

7- <u>Membership</u>

- Member in the German Chemical Society (GDCh).

- Member in Marburg University Research Academy (MARA).

8- <u>Grants</u>

- STIBET Doctoral Program of the DAAD (Research Assistantship), April-July 2012.

- STIBET Doctoral Program of the DAAD (Research Assistantship), September-December 2013.